Supramolecular Derivatisation of New Anti-tubercular and Antimalarial Drug Leads

Laurelle Margaux Joseph

Dissertation presented for the degree of Master of Science

in the Department of Chemistry

University of Cape Town

October 2015

Supervisors: Professors Mino R. Caira and Kelly Chibale

Acknowledgments

My special thanks to:

Professor Mino Caira for his endless patience, support, kindness and excellent supervision.

Professor Kelly Chibale for his co-supervision, guidance, encouragement and support.

Dr Clive Oliver for his willingness to answer questions and give advice.

Dr Hong Su for the single crystal data-collection.

My colleagues at the Centre for Supramolecular Chemistry Research for their kindness and encouragement.

Dr Susan Winks, Dr Renier Van der Westhuyzen, Dr Tanya Paquet and everyone at the H3D Centre for synthesizing the drug leads used in this study.

The National Research Foundation and the HSBC for financial support.

Dr Natasha Strydom and her colleagues from the UCT Division of Pharmacology for the pharmacokinetic data.

Dr Sergio Wittlin and colleagues at the Swiss Tropical and Public Health Institute for conducting the *in vivo* efficacy testing.

Dr Nicholas Njuguna for assisting me with the turbidimetric solubility testing.

My family for their support and patience.

Abstract

The UCT Drug Discovery and Design Centre, H3D, provided anti-tubercular and antimalarial drug leads that display potent *in vitro* activity, but with unfavourable physicochemical properties. The primary objective of this study was to prepare supramolecular derivatives of the drug leads in an attempt to improve their physicochemical properties. Any new solid forms were to be characterized by a variety of analytical techniques, including X-ray analysis, spectroscopic and thermal techniques. Where possible, such derivatives would be tested for any enhancement in the aqueous solubility or biological activity of the drug lead. The second objective of this study was to employ supramolecular intervention in the early stages of the drug discovery and development process to help streamline the process by distinguishing between compounds that might be amenable to beneficiation via supramolecular modification and those that might not.

The crystal structure of a novel anti-tubercular drug lead, DL2, was solved and the compound was fully characterized using thermal and X-ray techniques. This compound displayed very poor solubility in both aqueous and organic media.

Phase solubility studies were performed with anti-tubercular drug lead DL3 and selected cyclodextrins (CDs). The apparent solubility of DL3 increased by a factor of more than 300 at the highest concentration of hydroxypropyl- β-CD (HPβCD) and β-CD investigated.

Three salts of antimalarial drug lead DL4 and carboxylic acids were prepared. The salts were characterized by X-ray and thermal techniques. A salt of citric acid and DL4 could be prepared by the liquid-assisted grinding method. The equilibrium solubility of this salt was 48 times greater than that of DL4.

An inclusion complex between DL4 and a partially methylated cyclodextrin (DIMEB) was prepared and fully characterized. Phase solubility analysis showed that the aqueous solubility of DL4 increased by a factor of 100 at the highest concentration of DIMEB investigated. Mice infected with *P. berghei* were dosed with capsules containing 5 mg kg^{-1} of inclusion complex for *in vivo* pharmacokinetic testing. The results are consistent with a slow release of DL4 from the inclusion complex, resulting in a longer sustained concentration of DL4 over time as seen from the increase in apparent half-life. *In vivo* efficacy studies showed that the antimalarial activity of the inclusion complex was more than double that of DL4 at a dose of 3 mg kg^{-1}.

Table of Contents

CHAPTER 1: INTRODUCTION

Supramolecular beneficiation of pharmaceuticals

The ability to manipulate solids through the control of crystal packing provides an enormous benefit to the pharmaceutical industry. Crystalline forms of drugs are favoured by the pharmaceutical industry because they are reproducible, they tend to be more stable than other forms and purification of crystalline forms can be achieved with much less effort than other types of solid forms. Over the past 50 years the understanding of intermolecular interactions as they relate to crystal packing has evolved[1] and crystal engineering has emerged as one of the main ways in which this knowledge of intermolecular interactions and crystals can be exploited to design new solids.[2] An in-depth understanding of the supramolecular chemistry of the functional groups present in a molecule is critical in crystal engineering.[3] An understanding of complementary hydrogen bonding is also vital for selecting molecules which may form supramolecular synthons with drug molecules (Figure 1).[4]

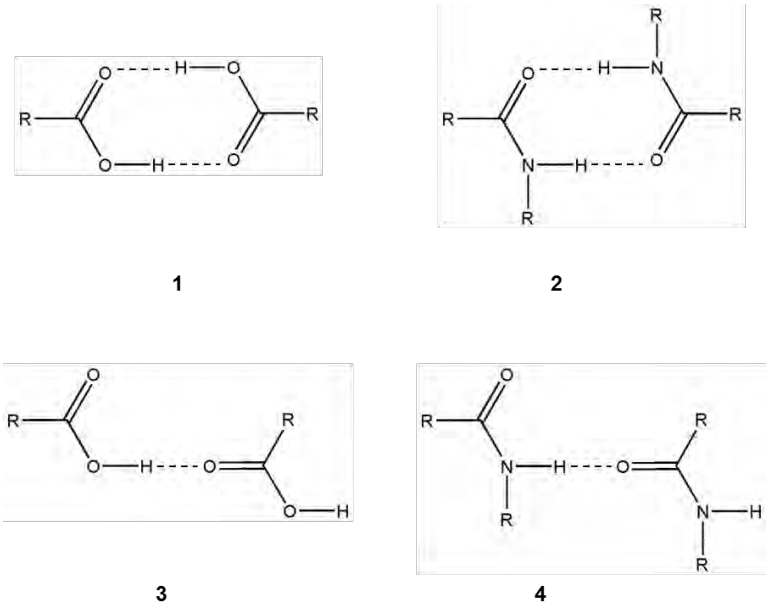

Figure 1: Common supramolecular synthons. 1 and 3 are acid-acid homosynthons with graph-set notation $R_2^2(8)$ and $C(4)$ respectively. 2 and 4 are amide-amide homosynthons with graph-set notation $R_2^2(8)$ and $C(4)$ respectively.

It has been shown that supramolecular derivatisation of drugs can result in new solid forms with improved solid-state properties such as enhanced aqueous solubility, more facile compressibility and reduced hygroscopicity.[3,5]

Pharmaceutical salts and co-crystals

Co-crystals are multi-component crystalline systems consisting of more than one chemical entity in the crystal. For a multi-component system to be considered a co-crystal, all of the components must be in neutral form and exist as solids at room temperature, according to one widely-used definition.[3] These criteria distinguish co-crystals from salts (where the components are in ionic form) and solvates (where at least one component is a liquid at room temperature). The different components in a co-crystal are linked by non-covalent interactions such as directed hydrogen bonding and the molecules are present in distinct stoichiometric ratios.[3]

Co-crystals can be prepared using the crystal engineering approach which typically involves the systematic selection of appropriate co-crystal formers followed by experimental work to synthesise the desired product. In the study described in this dissertation, all of the co-formers that were used appear on the Food and Drug Administration (FDA) “generally regarded as safe” (GRAS) database.[6]

An example of a co-crystal study from the literature can be found in the report by Caira *et al*, where five novel co-crystals of the antiretroviral drug Nevirapine were isolated. The study showed that the co-crystal of Nevirapine and maleic acid (Figure 2) had an aqueous solubility that was five times that of the untreated drug.[7]

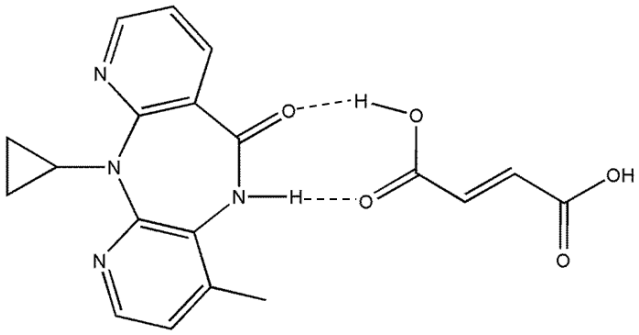

Figure 2: Complementary hydrogen bonding between Nevirapine and the maleic acid co-former.[7]

The formation of a salt is the result of an acid-base type of reaction that occurs when there is a proton transfer from an acidic to a basic component.[8] The components in a salt exist in ionic form and this is the major chemical feature that distinguishes a salt from a co-crystal. The pK_a values of the components are believed to play a role in the formation of salts or co-crystals. The difference in the pK_a values (ΔpK_a = [pK_a(base) – pK_a(acid)]) of the components is assumed to be the driving force behind proton transfer, with ΔpK_a = 3 generally corresponding to salt formation.[8] Although the ΔpK_a values do play a role in the formation of co-crystals vs. salts, these values should not be interpreted in isolation, but rather regarded as one of the factors to be considered in the crystal engineering process.

Cyclodextrins: general overview

Cyclodextrins (CDs) were first described by Villiers in the late 1800s and the term "cyclodextrin" was later coined by the Austrian chemist Franz Schardinger.[9-10] The native CDs are composed of six, seven or eight α-1,4 linked D-glucopyranose rings (α-, β- and γ-CD respectively) as shown in Figure 3. CDs have a narrower primary rim and a wider secondary rim, resulting in the molecule adopting a truncated cone shape [Figure 3(b)]. The primary rim possesses one primary hydroxyl group (O6–H) per glucose unit and the secondary rim has two hydroxyl groups (O2–H and O3–H) per glucose unit. α-, β- and γ-CD have comparatively low aqueous solubility at 25 °C (14.5, 1.85 and 23.2 g per 100 cm^3 respectively) relative to derivatised CDs. This is most probably a result of the strong binding of the CD molecules in the crystalline state. Furthermore, of the three native CDs, β-CD molecules form the strongest intramolecular O–H•••O hydrogen bonds that inhibit their ability to form hydrogen bonds with water molecules, thus resulting in this member of the series having the lowest solubility. Substituting any of the hydroxyl groups with a methoxy group can lead to significant physicochemical changes and the resulting derivatised CDs are generally more water soluble than native CDs. Despite this advantage, they are generally more toxic, although DIMEB and HPβCD and HPγCD have been used in formulations for pharmaceutical products.[11-13]

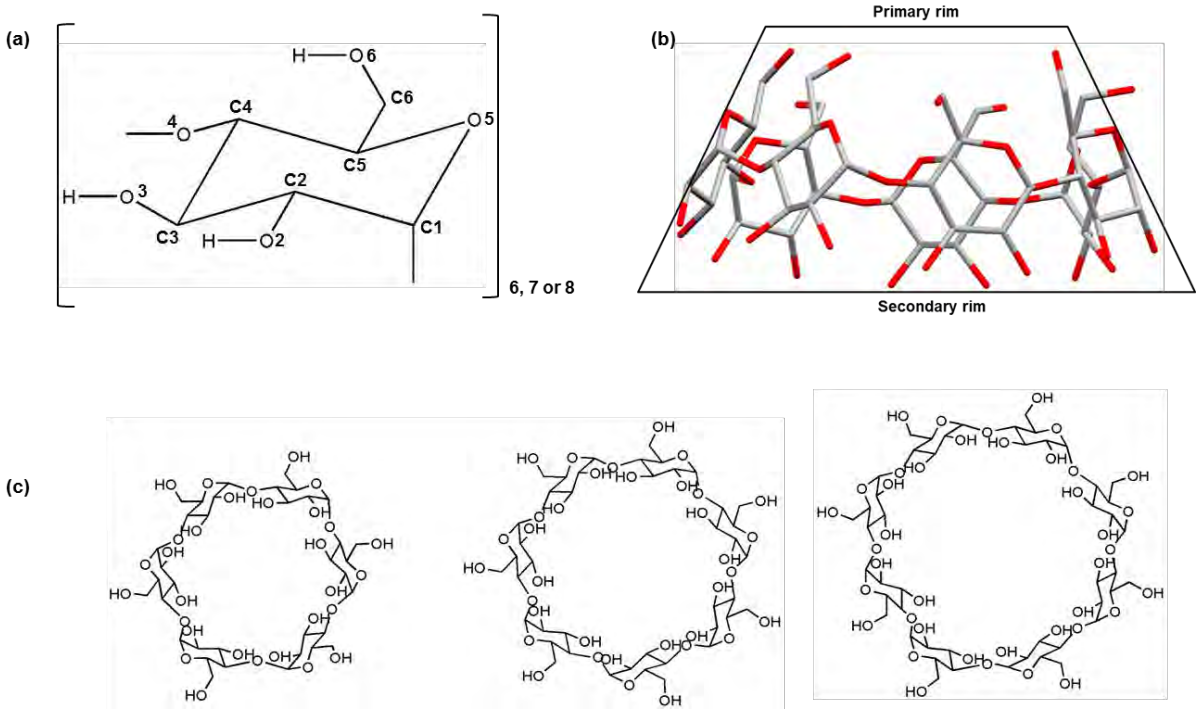

Figure 3: (a) an α D-glucopyranose unit, (b) the truncated cone shape showing the narrow primary rim and wider secondary rim, (c) left to right: macrocyclic rings of α-, β- and γ-CD.

Molecular geometry

A number of geometrical parameters are used to describe the macrocylic conformation of CDs. By comparing the conformation of complexed and uncomplexed hosts, one can obtain valuable information about the effect that the guest has on the conformation of the host. The geometric parameters, defined by Harata and Saenger, are based on the O4 atoms that are used to construct the O4-heptagon (in the case of β-CD and its derivatives) from which angles and distances can be measured.[14-15] The geometrical parameters that can be measured using the O4-heptagon (Figure 4) include the distance from the O4 atom to the centroid of the heptagon (l), the O4–O4′ distance (D), the O4–O4′–O4″ angle (ϕ) and the O4–O4′–O4″–O4‴ torsion angle (d). If the mean plane through the O4 atoms in an undistorted CD molecule were to be calculated, it would pass through all of the O4 atoms and all torsion angles (d) would be zero.

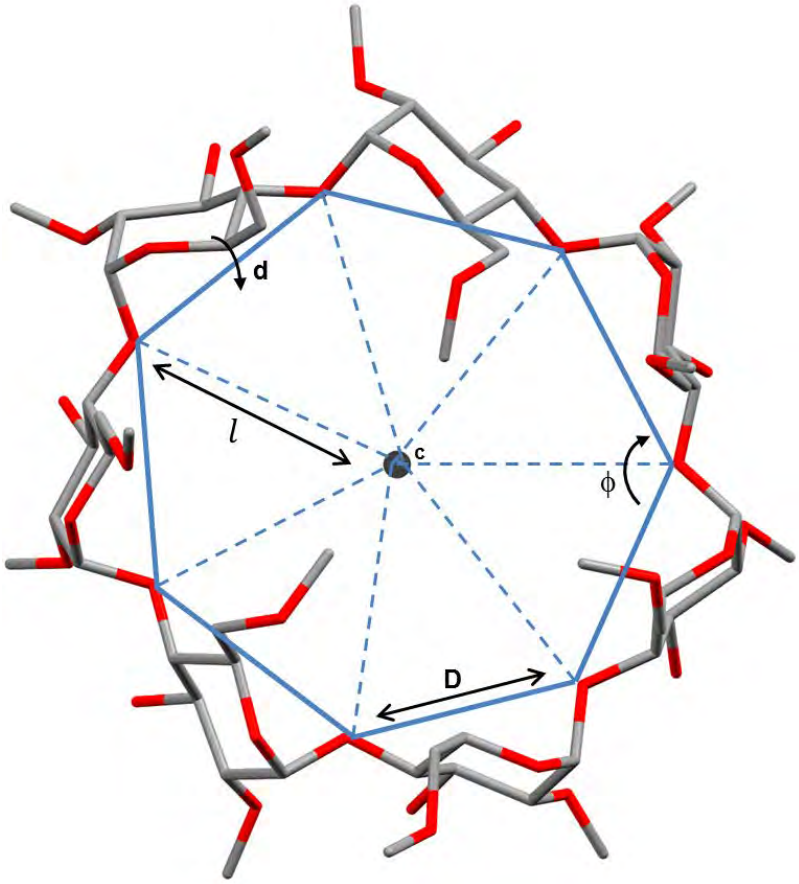

Figure 4: Principal geometric parameters of the O4-heptagon used to describe the conformation of each host molecule.

One geometrical parameter that is not directly defined by the O4-heptagon is the possible O2•••O3′ intramolecular hydrogen bond distance (D_3). It is possible to measure the deviation of each of the O4 atoms from the mean plane through the O4 atoms and this deviation is represented by the parameter α. The acute angle between the O4 mean plane and the plane through O4, C4, C1 and O4′ of a glucose ring in the CD is described by the parameter τ_2. The angle τ_2 is also referred to as the 'tilt angle' and it measures the relative inclination (or tilt) of each glucose unit relative to the O4 mean plane. Figure 5(a) shows the O4 mean plane through a β-CD host molecule and the planes defining the τ_2 angle for one of the glucose units have been shown in Figure 5(b).

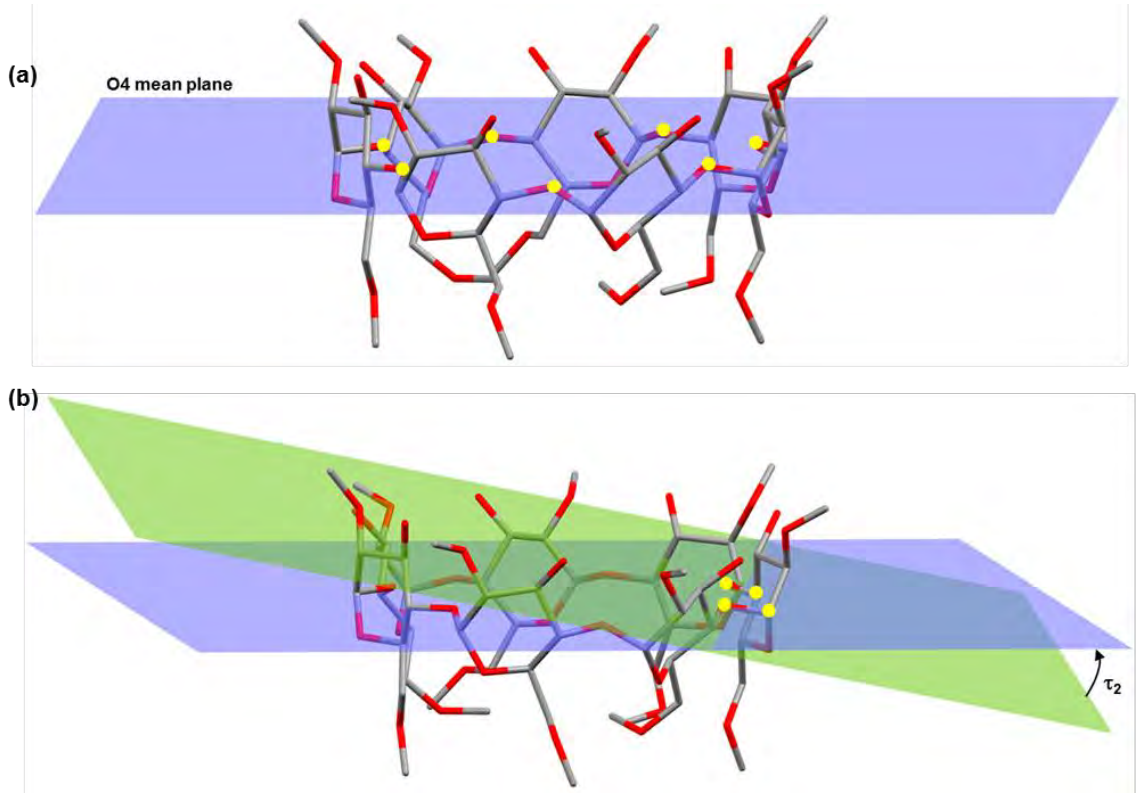

Figure 5: (a) O4 mean plane through a β-CD host molecule, (b) planes used to calculate τ_2 for one glucose unit in β-CD. Atoms that define a plane have been represented as yellow spheres.

Crystal packing arrangements for cyclodextrins

There are two types of packing arrangements that apply to both monomeric and dimeric CD complexes. This first is the channel type packing where the cavities of the CD molecules are aligned either head-to-head (dimeric) or head-to-tail (monomeric), creating infinite columns (Figure 6). Cage type packing occurs when the CD cavity is obstructed on both the primary and secondary rims by neighbouring CD molecules. Typical examples of monomeric cage type packing modes are the herringbone and brickwork arrangements.

The term isostructurality refers to two or more phases that have the same gross packing arrangement and hence similar arrangement of the molecules in the crystal, leading to similar unit cell dimensions.[16] The gross packing arrangement of cyclodextrin complexes is determined by the CD molecules, and thus it is possible for two or more complexes with different guest molecules to be considered isostructural. This was the subject of the review done by Caira in which he described

a series of isostructural PXRD patterns that exist for known CD complexes. It is now possible to compare the PXRD patterns from the isostructural series with any PXRD pattern resulting from a CD inclusion experiment and thereby determine if any complexation has occurred.[17]

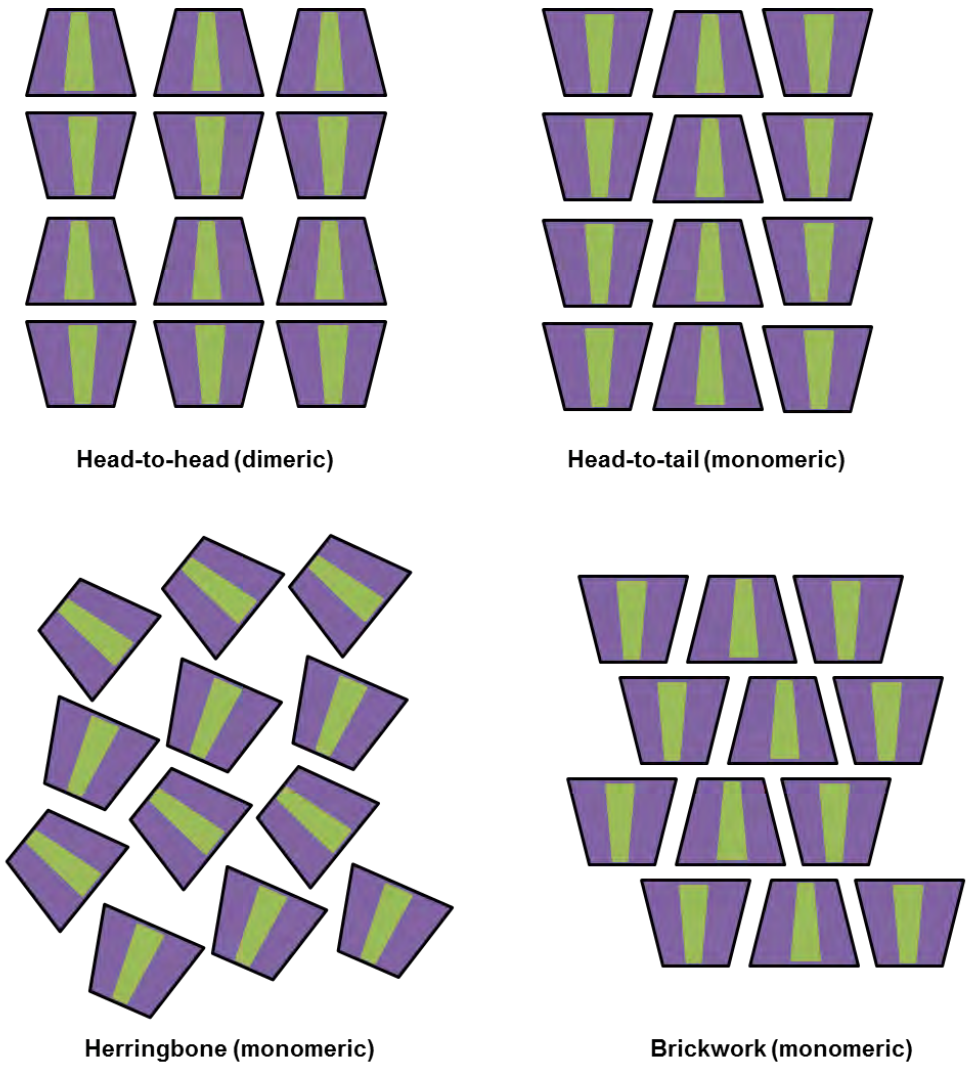

Figure 6: Examples of packing arrangements for CD complexes.

Inclusion complexes

The cavity of a CD molecule is able to accommodate guest molecules and reversibly bind to them, resulting in an inclusion complex. The central cavity of a CD is lipophilic and when a cyclodextrin inclusion complex is formed, lipophilic moieties on the guest molecule are involved in non-covalent interactions with the cavity.[5] Figure 7

is a graphical illustration of the reversible nature of CD inclusion, where $K_c = \frac{[CD \bullet G]}{[CD][G]}$.[18]

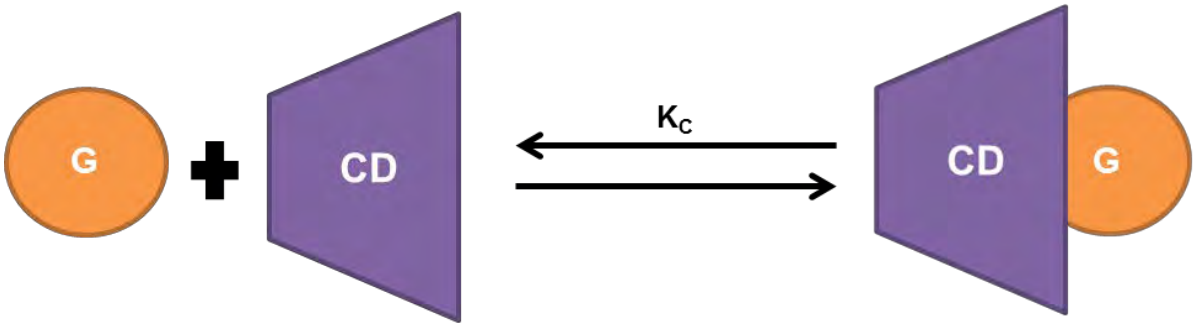

Figure 7: Reversible binding that can occur between a guest molecule (G) and a CD in solution.

Pharmaceutical applications of CDs

CDs are able to "mask" insoluble moieties on the guest molecule through the formation of inclusion complexes. Thus, poorly soluble compounds can be made soluble through the binding of an insoluble moiety to the lipophilic cavity of a CD and the favourable hydrogen bonding between the hydroxyl groups on the outer surface of the cyclodextrin with water molecules.[5] Studies have shown that the formation of cyclodextrin inclusion complexes can improve the bioavailabilities of FDA Class II drugs primarily i.e. drugs that have poor aqueous solubility and high permeability.[12]

CDs are almost non-toxic when they are administered orally, because they are generally not absorbed in the gastrointestinal tract.[19] Absorption studies have determined that 2-4% of CDs are absorbed in the small intestine with the remainder being degraded by α-amalyses and absorbed as glucose.[20] Their structures, molecular weights and low octanol/water partition coefficients are typical for compounds that do not easily cross biological membranes.[20-21] The fact that CDs are virtually non-toxic, do not readily cross biological membranes and are able to solubilise poorly soluble compounds makes them ideal for use in drug formulations.

Early supramolecular intervention in the drug discovery process

High throughput screening and combinatorial chemistry are just two of the techniques that have enabled drug discovery scientists to produce a large number of new chemical entities (NCEs). However, it is estimated that only 1 in 5000 NCEs actually enters the marketplace as a drug.[22] This is due to poor clinical efficacy, serious negative side effects, adverse drug reactions and unfavourable drug metabolism and pharmacokinetics, among other factors. A successful drug candidate should have good pharmacological activity, but safety and pharmacokinetics are also essential factors that will ultimately determine the success of a drug candidate.

Palucki *et al* have described strategies for implementing early formulation techniques during the drug discovery phase and emphasised the benefits of the early identification of an optimal phase in drug discovery.[23] In particular, their review emphasizes the importance of identifying an optimal crystalline phase during the drug discovery phase.

As seen in the schematic workflow in Figure 8, supramolecular intervention during the drug discovery stage can help to identify compounds that may present challenges during the formulation stage. It can also be used to identify compounds that have a combination of good pharmacological activity and favourable physicochemical properties for further development. Using supramolecular intervention in parallel with drug discovery can ultimately reduce the amount of resources, time and money spent on compounds that would inevitably be rejected during the preclinical stage.

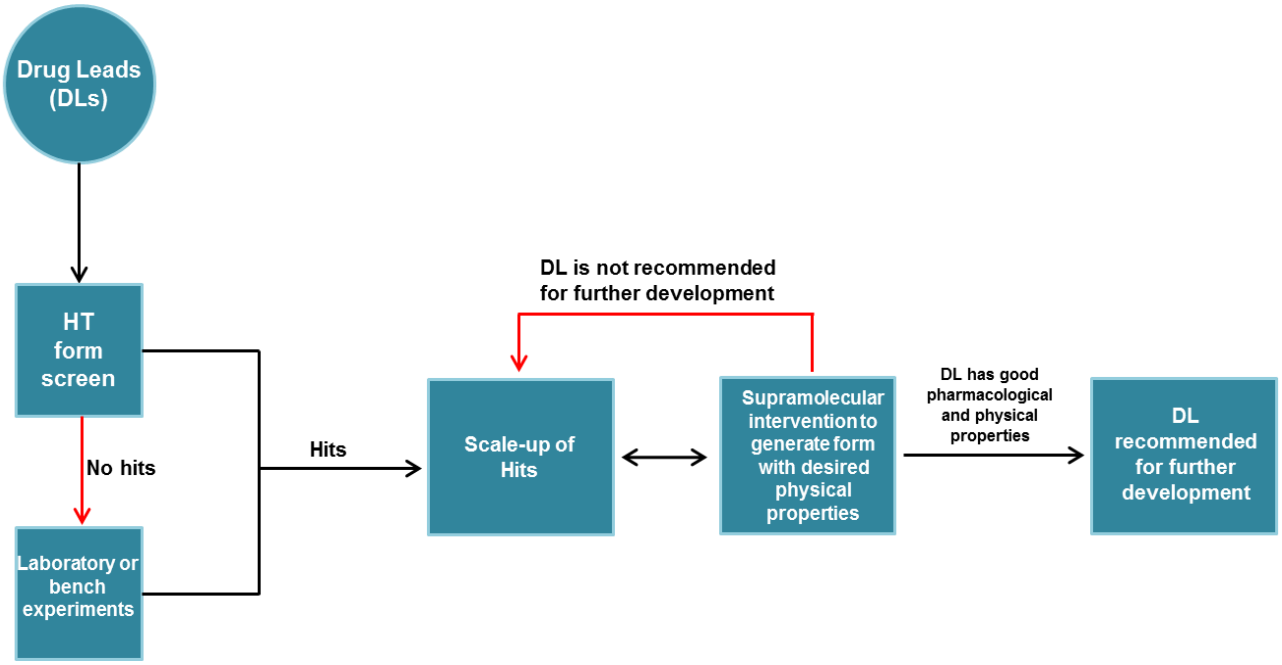

Figure 8: Schematic workflow for identifying a suitable drug lead for further development. Adapted from the review by Palucki *et al*.[23]

New drug leads to be investigated

Members of the UCT Drug Discovery and Development Centre, H3D, synthesized the four novel drug leads (DLs) that were investigated in this study. All of the drug leads displayed excellent *in vitro* activity (with compound also displaying good *in vivo* activity), but very poor aqueous solubility. The latter could potentially imply limited bioavailability and if this limitation is not addressed during the early stages of the drug discovery process, it could potentially cause major challenges during the development stage. In this study, supramolecular modification of the drug leads DL1 – DL4 was applied in an attempt to improve their aqueous solubility.

DL1

6-(methyl-4-(trifluoromethyl)benzylamino)-N-phenylpyrimidine-4-carboxamide (DL1, Figure 9) is an analogue of a "hit" compound that was identified from the screening of a BioFocus Softfocus Kinase library. DL1 is part of a novel series of anti-tubercular compounds. DL1 displayed excellent activity against the $H_{37}Rv$ strain of *Mycobacterium tuberculosis* (*Mtb*) with MIC_{99} (the minimum concentration required to inhibit 99% of *Mtb*) values of 1.2 – 2.3 µM and 9.4 µM in the GAST-Fe (glycerol-

alanine-salts-Tween-iron) and ADC (albumin-dextrose-catalase) medium respectively. The cytotoxicity against the VERO cells (African green monkey kidney cell line) was impressive with an IC_{50} (concentration required for 50% inhibition of *Mtb*) value greater than 259 μM. The solubility in phosphate buffer solution (PBS) at pH 7.4 was less than 5.0 μM at 25 °C.

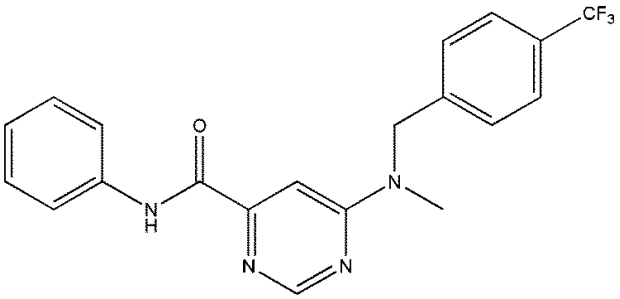

Figure 9: Structure of DL1.

DL2 and DL3

Ethyl 7-amino-2-benzyl-4-methyl-1,3-dioxo-2,3-dihydro-1*H*-pyrrolo[3,4-*c*]pyridine-6-carboxylate (DL2, Figure 10) and 7-amino-2-(3-chlorobenzyl)-4-methyl-6-(3-methyl-1,2,4-oxadiazol-5-yl)-1H-pyrrolo[3,4-c]pyridine-1,3(2H)-dione (DL3, Figure 10) are two drug leads from a novel series of anti-tubercular compounds. DL2 was identified as a "hit" from a high-throughput screening conducted by the Novartis Institute for Tropical Diseases (NITD, Singapore) and was further optimized to obtain DL3. Both compounds displayed good activity against the $H_{37}Rv$ strain of *MTb* with a MIC_{99} value of less than 0.16 μM in the GAST-Fe medium for DL2 and DL3. The cytotoxicity for both compounds was good with IC_{50} values greater than 295 μM and 261 μM against VERO cells for DL2 and DL3 respectively. Both compounds displayed poor solubility in PBS at pH 7.4 (7.7 μM and less than 5.0 μM at 25 °C for DL2 and DL3 respectively).

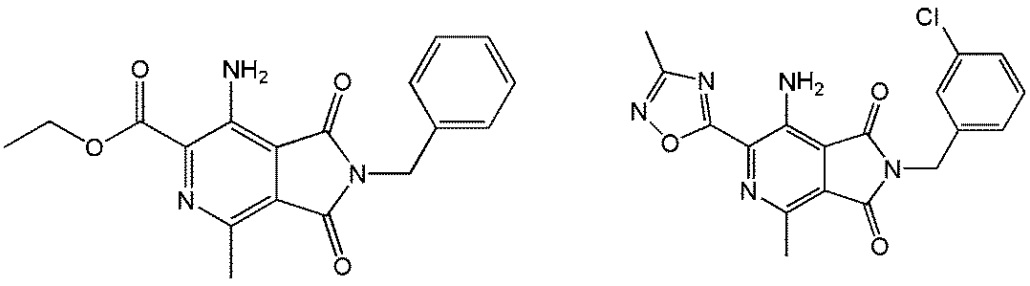

Figure 10: Structures of DL2 and DL3.

DL4

3-(6-Methoxypyridin-3-yl)-5-(4-methylsulfonylphenyl)-pyridin-2-amine (DL4, Figure 11) is a member of a novel series of antimalarial compounds.[25] DL4 showed potent *in vitro* activity against both the K1 (multi-drug resistant) and NF54 (sensitive) strains of the human malaria parasite *Plasmodium falciparum* with an IC_{50} value of 0.051 μM. It also displayed excellent *in vivo* antimalarial activity, with 99% reduction in parasitemia following the oral administration of a 30 mg kg^{-1} dose to *P. berghei* infected mice. However, DL4 displayed very poor aqueous solubility (0.121 μg cm^{-3} at pH 6.5 at 25 °C).

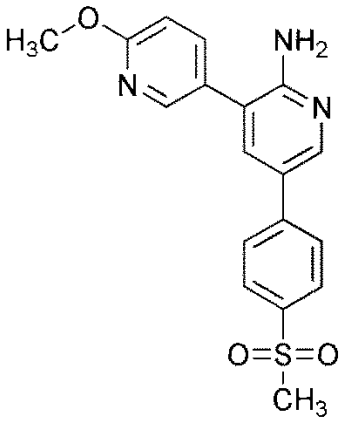

Figure 11: Structure of DL4.

Motivations and Objectives

The first motivation for this study was to use supramolecular intervention to obtain new solid forms of the selected drug leads with improved physicochemical properties, in particular aqueous solubility. The second was to demonstrate the effectiveness of employing supramolecular intervention during the early stages of the drug discovery process to prevent compound attrition during the later drug development stage.

The specific objectives were to:

1. perform co-crystal screening with each drug lead.
2. attempt CD inclusion with each drug lead.
3. where a new form was identified, obtain single crystals for X-ray structure determination.
4. characterize any co-crystals, salts or CD inclusion complexes using thermal, spectroscopic and X-ray techniques.
5. where possible, investigate whether the new solid forms display improved physicochemical properties or biological activity compared to the untreated drug lead.

References

1. G. R. Desiraju, *J. Am. Chem. Soc.*, 2013, **135**, 9952-9967.
2. G. R. Desiraju, *J. Chem. Sci*., 2010, **122**, 667-675.
3. N. Shan and M. J. Zaworotko, *Drug Discov. Today*, 2008, **13**, 440-446.
4. G. R. Desiraju, *Angew. Chem. Int. Ed. Engl.*, 1995, **34**, 2311-2327.
5. T. Loftsson and D. Duchêne, *Int. J. Pharm.*, 2007, **329**, 1-11.
6. SCOGS (Select Committee on GRAS Substances), http://www.accessdata.fda.gov/scripts/fdcc/?set=SCGOS (accessed February 2014).
7. M. R. Caira, S. A. Bourne, H. Samsodien, E. Engel, W. Liebenberg, N. Stieger and M. Aucamp, *CrystEngComm*, 2012, **14**, 2541-2551.
8. S. L. Childs, G. P. Stahly and A. Park, *Mol. Pharm.,* 2007, **4**, 323-338.
9. F. Schardinger, *Microben. Zentralbl. Bakteriol. Parasitenk. Abt. II,* 1911, **29**, 188-197.
10. F. Schardinger, *Zeitschrift für Lebensmitteluntersuchung und-Forschung A,* 1903, **6**, 865-880.
11. J. Szejtli, *Pure Appl. Chem.*, 2004, **76**, 1825-1845.
12. T. Loftsson, M. E. Brewster and M. Másson, *Am. J. Drug Deliv.*, 2004, **2**, 261-275.
13. T. Loftsson, P. Jarho, M. Másson and T. Järvinen, *Expert Opin. Drug Deliv.*, 2005, **2**, 335-351.
14. K. Harata, *Chem. Rev.,* 1998, **98**, 1803-1828.
15. W. Saenger, *Inclusion compounds*, ed. J. L. Atwood, J. E. D. Davies and D. D. MacNicol, Oxford University Press, London, 1984, vol. 5, ch. 9, 231-260.
16. A. Kálmán and L. Párkányi, *Advances in Molecular Structure Research*, JAI Press Inc., Greenwich, USA, 1997,189-226.
17. M. R. Caira, *Rev. Roum. Chim.*, 2001, **46**, 371-386.
18. T. Higuchi and K. A. Connors, *Adv. Anal. Chem. Instrum.,* 1965, **4**, 117-212.
19. T. Irie and K. Uekama, *J. Pharm. Sci.,* 1997, **86**, 147-162.
20. J. Szejtli, *Trends Biotechnol.,* 1989, **7**, 170-174.
21. C. A. Lipinski, F. Lombardo, B. W. Duminy and P. J. Feeney, *Adv. Drug Deliv. Rev.,* 2001, **46**, 3-26.

22. C. Prakash, *Drug Met. Lett.*, 2007, **1**, 1.
23. M. Palucki, J. D. Higgins, E. Kwong and A. C. Templeton, *J. Med. Chem.*, 2010, **53**, 5897-5905.
24. J. Higgins, *Am. Pharm. Rev.*, 2009, **12**, 42-46.
25. Y. Younis, F. Douelle, T. Feng, D. G. Cabrera, C. L. Manach, A. T. Nchinda, S. Duffy, K. L. White, D. M. Shackleford, J. Morizzi, J. Mannila, K. Katneni, R. Bhamidipati, K. M. Zabiulla, J. T. Joseph, S. Bashyam, D. Waterson, M. J. Witty, D. Hardick, S. Wittlin, V. Avery, S. A. Charman and K. Chibale, *J. Med. Chem.,* 2012, **55**, 3479-3487.

CHAPTER 2: EXPERIMENTAL

Materials

The three drug leads discussed in this dissertation, namely 3-(6-methoxypyridin-3-yl)-5-(4-methylsulfonylphenyl)-pyridin-2-amine ($C_{18}H_{17}N_3O_3S$),[1] ethyl 7-amino-2-benzyl-4-methyl-1,3-dioxo-2,3-dihydro-1*H*-pyrrolo[3,4-*c*]pyridine-6-carboxylate ($C_{18}H_{17}N_3O_4$) and 7-amino-2-(3-chlorobenzyl)-4-methyl-6-(3-methyl-1,2,4-oxadiazol-5-yl)-1*H*-pyrrolo[3,4-*c*]pyridine-1,3(*2H*)-dione ($C_{18}H_{14}N_5O_3Cl$), were synthesized and provided by the UCT Drug Discovery and Development Centre, H3D (University of Cape Town, South Africa). The compounds were used as received. Co-crystal formers were purchased from Sigma Aldrich (South Africa) and Acros Organics (Geel, Belgium). Cylodextrins were purchased from Cyclolab (Budapest, Hungary) and Sigma Aldrich (South Africa). All other materials and solvents used were of analytical reagent grade.

Co-crystal screening

Co-crystal screening with the drug leads was performed in three stages. The first stage involved selecting co-crystal formers with functional groups that had the potential to form supramolecular synthons with the functional groups present in the drug lead. The Cambridge Structural Database (CSD)[2] was used to investigate the frequency of these particular supramolecular synthons. All of the co-crystal formers that were used appear on the US Food and Drug Administration's "generally regarded as safe" (GRAS) database.[3]

The next step in the co-crystal screening process involved co-grinding the drug lead with the selected co-crystal formers. All of the co-grinding experiments were performed using 10 mg of the drug lead and grinding with an equimolar amount of the co-crystal former. In the case of dry co-grinding experiments, the drug lead and co-crystal former were ground with a mortar and pestle for 10-15 minutes. The product of the dry co-grinding experiment was then analysed using powder X-ray diffraction (PXRD) and its trace was compared with the PXRD traces of the two separate components. Liquid-assisted co-grinding (LAG) was used extensively as a means of generating potential co-crystals. During the LAG experiments, the drug

lead and co-crystal former were ground for 10-15 minutes while small drops of solvent were added to create and maintain a relatively dry paste-like texture. The products were analysed using PXRD.

All PXRD traces from the co-grinding experiments were compared with the PXRD traces of the separate components to try and identify any new solid phases that may have emerged. If the co-grinding experiments were unsuccessful in creating a new solid phase, the PXRD trace of the product would simply be the sum of the PXRD traces for the separate components, indicating the formation of a physical mixture of the components. If the PXRD trace of the product was found to contain new peaks, or if prominent peaks from one of the separate components were absent in the PXRD trace for the co-grinding product, then the trace was considered to be unique and indicative of the formation of a new solid phase.

Co-precipitation experiments were performed in the cases where LAG indicated that a new phase had emerged from the combination of a drug lead and a particular co-crystal former. In general, stoichiometric amounts of the drug lead and co-crystal former were dissolved separately in a common solvent while heating to just below the boiling point of the solvent. Once dissolved, the two components were combined and the resulting solution was then filtered through a 0.45 μm nylon filter into a clean vial. Vials were left on the bench to allow the solvent to evaporate slowly at ambient temperature. Suitable crystals were analysed using single crystal X-ray diffraction and all supramolecular derivatives were fully characterized.

Cyclodextrin inclusion

Kneading and co-precipitation experiments were carried out with the drug leads and cyclodextrins in an attempt to prepare inclusion complexes. For kneading experiments the drug leads were combined in a 1:1 molar ratio and kneaded with a small volume of water for 15-20 minutes. The products were analysed by PXRD and the resulting powder patterns were compared with known calculated patterns for common isostructural complexes. If the powder pattern for the kneaded product matched one of the calculated traces from the isostructural series,[4,5] it was considered to be a new inclusion complex with the same packing arrangement as the complex from the isostructural series.

For co-precipitation experiments with the native CDs, the CD was dissolved in 0.5-1 cm^3 Milli-Q^6 water at elevated temperature (40-50 °C) and the drug lead was added to this solution while stirring. In most cases a small volume of organic solvent (ethanol or acetone) had to be added to the solution to facilitate the dissolution of the drug lead in the CD solution.

After stirring at 40-50 °C for 5-24 hours the solutions were filtered through a 0.45 µm nylon filter into a clean vial and left on the bench to allow the solvent to evaporate slowly. Any suitable single crystals were submitted for unit cell determination to establish if an inclusion complex had formed.

For co-precipitation experiments with the derivatised cyclodextrins, the drug lead was dissolved in 1 cm^3 of ethanol or acetone while heating and the cyclodextrin was dissolved separately in 1 cm^3 Milli-Q^6 water at room temperature. The two components were combined while stirring at room temperature and the solution was filtered through a 0.45 µm nylon filter into a clean vial and placed in an oven at 60 °C. The vial was left uncapped in the oven for 1.5-2 hours to allow some of the organic solvent to evaporate. The solutions were left to crystallize at 50-60 °C. Single crystals were selected for unit cell determination.

Thermal analysis

The thermal methods used to characterise the drug leads and their supramolecular derivatives were Hot Stage Microscopy (HSM), Differential Scanning Calorimetry (DSC) and Thermogravimetric Analysis (TGA). These three techniques were used in combination to analyse the thermal behaviour of the materials.

Thermogravimetric analysis and differential scanning calorimetry

During thermogravimetric analysis a sample is exposed to a nitrogen atmosphere and a thermobalance measures the change in the mass of the sample as a function of temperature. This method allowed the observation of mass losses corresponding to particular components in a crystal. TGA was used extensively as a method to quantify the solvent present in crystals. Differential scanning calorimetry measures the difference in the energy input between a sample pan and a reference pan as a

function of temperature. During a DSC experiment the sample pan and the reference pan are maintained at a constant temperature and the heat required to maintain this state is measured. When the heat flow is plotted as a function of the temperature, it is possible to observe endothermic and exothermic peaks corresponding to thermal events such as melting, solvent loss or phase transitions.

A TA-Q500 Thermogravimetric Analyzer and DSC-Q200 Differential Scanning Calorimeter (TA instruments) with Universal Analysis 2000 software (v4.5A, TA Instruments-Waters LLC) were used. Both instruments were operated with a dry nitrogen purge gas flow rate of 60 cm^3 min^{-1} and samples were heated at a rate of 10 K min^{-1}. Samples in the range 1-5 mg were removed from their mother liquor, dried on filter paper and placed in an open aluminium crucible or a closed vented aluminium pan for TGA and DSC respectively.

Hot stage microscopy

Hot stage microscopy (HSM) was used to confirm the results from TGA and DSC. Colour changes, bubbling and changes in the opacity of crystals could be correlated with thermal events seen in the TGA and DSC traces. Due to the different sample sizes and conditions of the experiments, the temperatures recorded for the HSM images are somewhat different from the temperatures recorded for corresponding thermal events using TGA or DSC. Samples were monitored using a Nikon SMZ-10 stereoscopic microscope fitted with a Linkam THMS600 hot stage and a Linkam TP92 temperature control unit. Samples were placed on a cover slip with silicone oil and images were captured with a real-time Sony Digital Hyper HAD colour video camera and viewed using the Soft Imaging System program, analySIS.[7]

Liquid chromatography-mass spectrometry

The purity of each drug lead was determined using an Agilent® LCMS instrument equipped with a photodiode array (PDA) detector. The column was a X-bridge C18 5 µm (4.6 x 150 mm); organic phase: 10 mM ammonium acetate (pH 3.7) in HPLC grade methanol; aqueous phase: 10 mM ammonium acetate (pH 3.7) in HPLC grade water. The flow rate was 1.20 cm^3 min^{-1}.

NMR spectroscopy

Drug lead purity was confirmed by ^{1}H NMR and ^{13}C NMR spectroscopy. ^{1}H NMR spectroscopy was also used to determine the stoichiometry of CD inclusion complexes, co-crystals and salts that were prepared. Crystals were dissolved in deuterated DMSO (DMSO–d_6) and the ^{1}H NMR spectrum was recorded. For CD inclusion complexes the proton signals for the CD and drug lead were integrated to determine the host-guest stoichiometry. In the case of co-crystals or salts, the proton signals for each component were integrated to confirm the stoichiometry. The spectra were recorded on a Bruker 400 MHz spectrometer.

Fourier Transform Infrared (FTIR) spectroscopy

Fourier Transform Infrared (FTIR) spectroscopy was a useful way of establishing whether the product of a co-crystallization experiment was a co-crystal or a salt. By careful examination of the characteristic absorption bands of the acidic and basic functional groups present in the IR spectra, it was possible to establish whether a proton transfer had occurred between the two components. The IR spectra for putative co-crystals were recorded on a Bruker Tensor27 spectrometer with an ATR platinum Diamond 1 reflectance accessory for solid samples.

Powder X-ray diffraction

Powder X-ray diffraction patterns were recorded to establish whether a co-grinding or kneading experiment had resulted in a new crystalline phase. In the case of co-crystallisation experiments, the PXRD pattern of the product was compared with the PXRD patterns of the drug lead and the appropriate co-crystal former. The pattern of the product was examined for the emergence of new peaks or the disappearance of any peaks from the patterns of the individual components. For the kneading experiments the PXRD pattern of the product was compared with a library of reference patterns for a known series of isostructural inclusion complexes.[4,5] If the pattern did not match any of the isostructural patterns and also contained superimposed peaks of drug lead, it was concluded that no complexation had taken place.

The idealised PXRD patterns for the X-ray crystal structures that were determined were generated from the refined crystallographic data to see if the single crystal was representative of the bulk material. The program LAZY PULVERIX[8] was used to generate idealised PXRD patterns for all of the X-ray crystal structures. LAZY PULVERIX uses the formula $I(hkl) = mLp|F(hkl)|^2$, where $I(hkl)$ is the intensity of the reflection with indices *hkl*, *m* is the reflection multiplicity, L the Lorentz factor, *p* the polarisation factor, and *F(hkl)* the structure factor.

The powder X-ray diffraction measurements were recorded on a BRUKER D8 Advance X-ray diffractometer using Cu*Kα*-radiation (λ = 1.5406 Å). Samples were placed on a zero background sample holder and scanned over the 2θ-range 4 - 40° with a step size of 0.02° per second. The X-ray generator settings were 30 kV and 40 mA.

Crystal structure determination

For single crystal X-ray analysis, crystals of adequate size, quality and optical uniformity were removed from the mother liquor and dried on filter paper before being coated in Paratone N oil[9] and mounted on a nylon cryoloop. In the case of complexes of derivatised CDs, the crystals were maintained at 60 °C while being removed from the mother liquor and were then immediately dried on filter paper before being placed in Paratone N oil. The crystals had to be dried to prevent them from dissolving in the mother liquor at room temperature.

Single crystal intensity data were collected on one of two single crystal X-ray diffractometers. Either a Nonius KappaCCD (Charge Coupled Device) single crystal X-ray diffractometer, using graphite-monochromated MoKα radiation (λ = 0.71069 Å) generated by a Nonius FR590 generator operated at 50 kV and 20 mA was used, or a Bruker KAPPA APEX II DUO single crystal X-ray diffractometer using MoKα radiation (λ=0.71069 Å) generated by a Bruker K780 generator operated at 50 kV and 30 mA was used.[10] All single crystals were maintained at low temperature (173(2) K) during the data-collection by cooling with a constant stream of N_2 gas at a flow rate of 20 cm^3 min^{-1} with a Cryostream cooler (Oxford Cryostreams, UK). Unit cell refinement and data reduction were performed using the programs DENZO and

SCALEPACK[11] or the program SAINT[12] for all data-collections performed on the Nonius Kappa CCD diffractometer. Intensity data collected on the Bruker Apex II used the program SAINT[12] for unit cell refinement and data reduction. All intensity data were corrected for Lorentz-polarisation effects. The X-ray diffraction data obtained from crystals containing heavy atoms such as sulfur, phosphorus and chlorine were corrected for absorption using the program SADABS.[13] The crystal system was established from the observed Laue symmetry of the diffraction pattern and the space group was determined by examining systematic absences and matching the observed conditions to a known space group. The input files for structure solution were prepared using the program XPREP.[14] All crystal structures were solved by direct methods using SHELXS-97[15] and refined by full-matrix least-squares using SHELXH-97[15] operating within the X-SEED[16] interface.

SHELXH-97

The SHELXH-97[15] software program uses full-matrix least-squares fitting to minimize the value of $\sum w(F_o^2 - F_c^2)^2$ i.e. the sum of the squares of the differences between the observed and calculated intensities. The agreement between the observed (F_o) and calculated (F_c) structure factors is expressed by the residual index R_1, where a low R_1 value indicates a good model (1). A second residual index, wR_2, indicates the agreement between the observed and calculated intensities for the refinement against F^2 (2).

$$R_1 = \frac{\sum||F_o|-|F_c||}{\sum|F_o|} \qquad (1)$$

$$wR_2 = \left(\frac{\sum w(F_o^2-F_c^2)^2}{\sum w(F_o^2)^2}\right)^{\frac{1}{2}} \qquad (2)$$

The weighting scheme, w, used in (2) as well as the parameters a and b were refined for each structure using expressions (3) and (4) below. The value S (also referred to as the “Goodness of Fit” parameter) is defined in expression (5), with n equal to the number of reflections and p the total number of parameters. A well-refined structure will have S close to unity and a n/p ratio close to 10.

$$w = [\sigma^2(F_o^2) + (aP)^2 + bP]^{-1} \quad (3)$$

$$P = \frac{\max(0,F_o^2) + 2F_c^2}{3} \quad (4)$$

$$S = \left(\frac{\sum w(F_o^2 - F_c^2)^2}{n-p}\right)^{\frac{1}{2}} \quad (5)$$

The program PLATON[17] was used to calculate intramolecular and intermolecular geometrical parameters as well as the standard deviations for these values. Images of the crystal structures were created with POV-Ray for Windows.[18] The program LAYER[19] was used for the graphic display of intensity data as simulated precession photographs and this was useful when assigning space groups. The final crystallographic data files for each crystal structure described in this dissertation can be found in the Appendix. Table 1 lists the file types and information they contain.

Table 1: Crystallographic data files that can be found in the Appendix.

Extension	Details
.hkl	Reflection data
.res	SHELX co-ordinate data
.cif	Crystallographic information
.fcf	Observed and calculated intensities
.lis	Platon output
.xl	SHELX output
.sup	Tabulated supplementary data

Solubility studies

For phase solubility and equilibrium solubility studies, UV-visible spectroscopy was used to determine the concentration of the drug lead present in solution. Using the Beer-Lambert law (6) as it applies to the relationship between absorbance and concentration, it was possible to quantify the amount of the drug lead present in a given solution.

Expression (6) describes a linear relationship between the absorbance (A) and concentration (c) of an absorbing species with a constant path length (l) and extinction co-efficient (ε_o).

$$A = \varepsilon_o cl \qquad (6)$$

Calibration curves for the drug leads were constructed by preparing a stock solution of known concentration and then preparing solutions of varying concentrations from the stock solution. Due to the poor aqueous solubility of the drug leads a small, known amount of ethanol was added to the aqueous solutions to facilitate drug dissolution. All of the phase solubility and equilibrium solubility experiments were performed in a 1% ethanol/water [v/v] medium. The absorbance readings of the solutions were plotted against the molar concentration of the drug lead to obtain the calibration curve. The absorbance readings were recorded on a Cintra 20 UV-visible spectrometer and data were processed using the GBC Spectral computer program (v1.70, December 1998).

Equilibrium solubility studies

The equilibrium solubility of the drug leads, co-crystals or salts were determined by adding an excess amount of the material to 5 cm^3 of a 1% ethanol/water [v/v] solution in a polytop vial. The vial was capped and placed on a temperature controlled carousel and the solution was stirred at 500 rpm for 72 hours at 25 ± 0.5 °C. The solution was filtered through a 0.45 µm nylon filter and diluted appropriately before the UV spectrum was recorded. The concentration of the drug lead was determined from the respective calibration curve obtained as described above.

Phase solubility studies

Phase solubility studies were carried out by preparing serial dilutions of a cyclodextrin solution and adding excess amounts of the drug lead to each solution. An excess amount of the drug lead was added to a polytop vial containing 5 cm^3 of the cyclodextrin solution. The vials were capped and placed on a temperature

controlled carousel and stirred (500 rpm) at constant temperature (25 ± 0.5 °C) for 72 hours. The solutions were filtered through a 0.45 µm nylon filter and diluted appropriately before the UV-visible spectrum was recorded. The concentration of the drug lead was determined from the respective calibration curve obtained as described above.

Turbidimetric solubility assay

The aqueous solubility of the solvated adipic acid-DL4 salt was assessed using a turbidimetric solubility assay. This was performed by dissolving crystals of the salt in DMSO and then adding aliquots of the DMSO solution to 0.01M pH 7.4 Phosphate Buffered Saline (PBS) to obtain serial dilutions in a 96 well plate. Serial dilutions of DL4, the solvated adipic acid salt of DL4 (DL4ADI), reserpine and hydrocortisone were prepared in triplicate. Reserpine and hydrocortisone are standards of known solubility in the solvent medium. After preparing the serial dilutions the solutions were left to equilibrate for 2 hours. The approximate solubility of the salt was determined to be the concentration above which precipitation occurs, causing the solution to become turbid. The UV-visible absorbance of the solutions was recorded at 620 nm, because most compounds are not expected to absorb at this wavelength so any absorbance that was detected would be due to particles in solution. UV-visible spectra were recorded using a Molecular Devices SpectraMax 340PC 96 well plate reader and the data were analysed using the SoftMaxPro software package (v5.4.1).[20-24]

In vivo testing

An inclusion complex prepared during this study was submitted for *in vivo* biological testing to establish whether it showed any improved biological activity compared to the parent compound (drug lead).

In vivo pharmacokinetic testing

In vivo pharmacokinetic testing was carried out by Dr Natasha Strydom and colleagues from the Department of Pharmacology at the University of Cape Town (South Africa). Nine 6-week-old C57BL/6 mice were divided into an intravenous and

two oral dosage groups (*n* = 3). For the intravenous group, a single 2.5 mg/kg dose (formulation: DMSO, PEG, EtOH, PPG [2:6:1:7, v/v]) was injected into the penile dorsal vein. 20 µl of blood was collected from the tail tip at 0.08, 0.5, 1, 3, 8 and 24 hours and stored at - 80°C. Oral dosing was achieved using a single Torpac® capsule containing 5 mg kg^{-1} equivalent active dose of either the inclusion complex or the drug for oral groups A and B respectively. Blood samples were collected at 0.5, 1, 3, 5, 8 and 24 hours and stored at - 80°C for analysis.[25]

Whole blood concentration of the drug lead was quantified by an LC-MS/MS assay developed for a range of 2 – 3000 ng cm^{-3}. The samples were extracted by protein precipitation using 20 µl of whole blood and a 240 µl acetonitrile precipitation solution containing two internal standards. Samples were vortexed for 1 minute and centrifuged at 10 000 G for 5 minutes. For analysis 200 µl of the supernatant was collected, dried and reconstituted using a 100 µl 0.1% formic acid in acetonitrile/water [1:1, v/v] injection solution. Gradient chromatography was performed on a Phenomenex Kinetix PFP (2.1 × 50 mm, 2.4 µm) reverse phase column with mobile phase 0.1% formic acid in water [v/v] and 0.1% formic acid in acetonitrile at a flow rate of 200 µl min^{-1}. An AB Sciex API 4000Q mass spectrometer was operated at unit resolution in multiple reaction monitoring mode to monitor the transitions of the protonated molecular ions to their product ions for the compound of interest, i.e. 355.8 → 277.0 *m/z*. Non-compartmental analysis was performed using Summit PK solutions™ (Summit Research Services, Montrose, USA).[25]

In vivo efficacy testing

In vivo efficacy testing was carried out by Dr Sergio Wittlin and colleagues at the Swiss Tropical and Public Health Institute (Basel, Switzerland) according to the methodology described by Le Manach *et al*.[26] Mice (*n* = 3) were infected with a GFP-transfected *P. berghei* ANKA strain of malaria and parasitemia was determined using standard flow cytometry techniques with a detection limit of 0.1% (1 parasite in 1000 erythrocytes). The activity of the drug lead or inclusion complex was calculated as the difference between the mean percentage parasitemia for the control and treated groups expressed as a percentage relative to the control group. Compounds were suspended in a 4% Tween80 and 9% ethanol [v/v] suspension vehicle and orally

administered once per day on four consecutive days (4, 24, 48, and 72 h after infection). Blood samples were collected after 96 hours.

References

1. Y. Younis, F. Douelle, T. Feng, D. G. Cabrera, C. Le Manach, A. T. Nchinda, S. Duffy, K. L. White, D. M. Shackleford, J. Morizzi, J. Mannila, K. Katneni, R. Bhamidipati, K. M. Zabiulla, J. T. Joseph, S. Bashyam, D. Waterson, M. J. Witty, D. Hardick, S. Wittlin, V. Avery, S. A. Charman and K. Chibale, *J. Med. Chem.,* 2012, **55**, 3479-3487.
2. Cambridge Structural Database and Cambridge Structural Database system, Version 5.36 (updates to May 2015), Cambridge Crystallographic Data Centre, University Chemical Laboratory; Cambridge, England, 2014.
3. SCOGS (Select Committee on GRAS Substances), http://www.accessdata.fda.gov/scripts/fdcc/?set=SCGOS (accessed February 2014).
4. M. R. Caira, S. A. Bourne, H. Samsodien, E. Engel, W. Liebenberg, N. Stieger and M. Aucamp, *CrystEngComm,* 2012, **14**, 2541-2551.
5. M. R. Caira, *Rev. Roum. Chim,* 2001, **46**, 371-386.
6. Milli-Q water, Millipore Corporation, Billerica, Massachusetts, USA.
7. Soft Imaging System GmbH, *Digital Solutions for Imaging and Microscopy*, Version 3.1 for Windows (Copyright 1987-2000).
8. K. Yvon, W. Jeitschko and E. Parthé, *J. Appl. Crystallogr.*, 1977, **10**, 73-74.
9. Paratone N oil (Exxon Chemical Co., Texas, USA).
10. Bruker AXS Inc., APEX2, Version 1.0-27, Bruker AXS Inc., Madison, Wisconsin, USA.
11. Z. Otwinowski and W. Minor, *Methods in Enzymology*, eds. C.W. Carter and R.M. Sweet, Academic Press, New York, 1997, vol. 276, pp. 307-326.
12. Bruker AXS Inc., Program SAINT, Version 7.60a, Bruker AXS Inc., Madison, WI, USA, 2006.
13. G. M. Sheldrick, Program SADABS, Version 2.05, University of Göttingen, Germany, 2007.
14. Bruker AXS Inc., XPREP, Version 5.1, Bruker AXS Inc., Madison, WI, USA, 1997.
15. G. M. Sheldrick, *Acta Crystallogr. A.,* 2008, **64**, 112-122.
16. L. J. Barbour, *J. Supramol. Chem.,* 2001, **1**, 189-191.
17. A. L. Spek, *Acta Crystallogr.*, 2009, **D65**, 148-155.

18. C. Cason, T. Froehlich, N. Kopp and R. Parker, POV-Ray for Windows, Version 3.6.1a.icl8.win32, The Persistence of Vision Raytracer Pty. Ltd., 2003.
19. L. J. Barbour, *J. Appl. Crystallogr.*, 1999, **32**, 351-352.
20. C. A. Lipinski, F. Lombardo, B. W. Duminy and P. J. Feeney, *Adv. Drug Deliv. Rev.,* 2001, **46**, 3-26.
21. L. Pan, Q. Ho, K. Tsutsui and L. Takahashi, *J. Pharm. Sci.,* 2001, **90**, 521-529.
22. C. D. Bevan and R. S. Lloyd, *Anal. Chem.,* 2000, **72**, 1781-1787.
23. J. Alsenz and M. Kansy, *Adv. Drug Deliv. Rev.,* 2007, **59**, 546-567.
24. J. Pérez, C. Díaz, I. G. Salado, D. L. Pérez, F. Paláez, O. Genilloud and F. Vicente, *Adv. Biosci. Biotechnol.*, 2013, **4**, 628-639.
25. P. Melariri, L. Kalombo, P. Nkuna, A. Dube, R. Hayeshi, B. Ogutu, L. Gibhard, C. deKock, P. Smith, L. Wiesner, H. Swai, *Int. J. Nanomedicine*, 2015, **10**, 1493-1503.
26. C. Le Manach, T. Paquet, D. G. Cabrera, Y. Younis, D. Taylor, L. Wiesner, N. Lawrence, S. Schwager, D. Waterson, M. J. Witty, S. Wittlin, L. J. Street, K. Chibale, *J. Med. Chem.*, 2014, **57**, 8839-8848.

CHAPTER 3: Solid-state chemistry of ethyl 7-amino-2-benzyl-4-methyl-1,3-dioxo-2,3-dihydro-1*H*-pyrrolo[3,4-*c*]pyridine-6-carboxylate (DL2): a novel anti-tubercular drug lead

Introduction

At the start of the project, the UCT Drug Discovery and Development Centre, H3D, provided an anti-tubercular compound for supramolecular derivatisation, namely 6-(methyl-4-(trifluoromethyl)benzylamino)-N-phenylpyrimidine-4-carboxamide seen in Figure 1. This compound will be referred to as DL1 (drug lead 1) henceforth. DL1 was recrystallized from a variety of solvents using different crystallization techniques, but unfortunately none of the experiments yielded any single crystals and the crystal structure for this compound has not yet been elucidated. Liquid-assisted grinding experiments were performed with DL1 and a range of co-crystal formers as part of a co-crystal screening and the results indicated that all of the experiments produced only physical mixtures of DL1 and the co-crystal former. Attempts to include DL1 in both native and derivatised cyclodextrins were all unsuccessful except in the case of the kneading experiment with γ-cyclodextrin and DL1. The results of all the experiments carried out with DL1 can be found in the Appendix. DL1 was recrystallized from eight solvents, co-crystal screening was carried out using twelve co-formers and CD inclusion was attempted using the native CDs as well as three derivatised CDs. At first glance the experiments with DL1 appear to have been unsuccessful. However, from a drug discovery and design perspective these results highlight a very important concept. They demonstrate the ability of early supramolecular intervention to streamline this process. They also provide valuable information about which compounds are amenable to beneficiation via supramolecular modification, ultimately reducing wasted time, effort and money spent on compounds with poor physical properties.

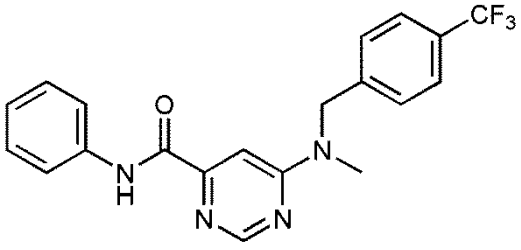

Figure 1: Molecular structure of DL1.

The drug lead that will be the focus of this chapter is ethyl 7-amino-2-benzyl-4-methyl-1,3-dioxo-2,3-dihydro-1*H*-pyrrolo[3,4-*c*]pyridine-6-carboxylate (Figure 2) which will be referred to as DL2 henceforth. The X-ray crystal structure of DL2 has been solved and will be discussed in this chapter. Co-crystal screening and CD inclusion experiments with DL2 will also be presented.

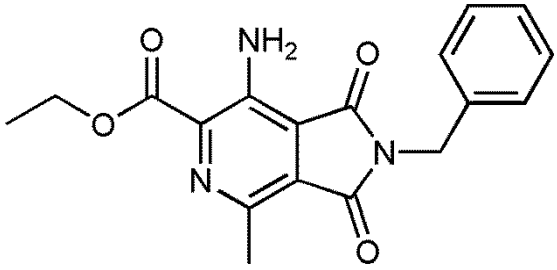

Figure 2: Molecular structure of DL2.

NMR and Mass Spectroscopy

The ^{1}H NMR and the LC-MS spectra for DL2 were provided by the H3D Centre and these data have been included in the Appendix.

Thermal analysis

HSM

Crystals of DL2 were heated at a rate of 10 K min^{-1} during a HSM experiment and the representative HSM photographs are shown in Figure 3. The photograph taken at 184 °C shows the crystals starting to melt and the entire sample has melted at 194 °C. Following melting, the vapour condensed onto the top glass cover slide of the HSM instrument, depositing crystals.

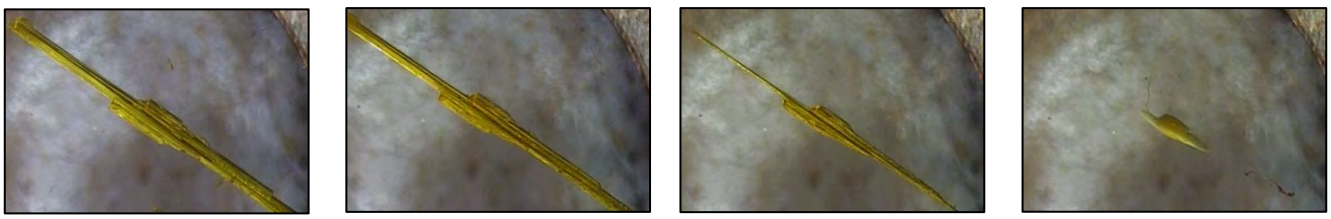

25 °C **157 °C** **184 °C** **194 °C**

Figure 3: Representative HSM photographs of DL2

TGA and DSC

The DSC trace of DL2 (Figure 4) shows the onset of melting occurring at 187 °C followed by a sharp endothermic peak corresponding to the melting point at 188 °C, with ΔH_{fus} = 37.37 kJ mol^{-1}.

The TGA trace in Figure 5 shows no significant mass loss until 228 °C when the melt vaporizes.

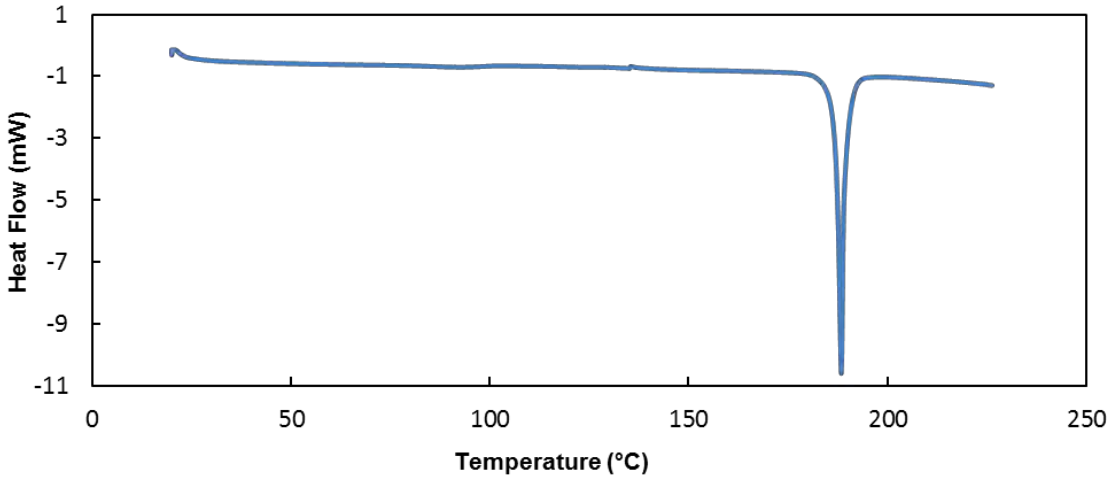

Figure 4: DSC trace for DL2

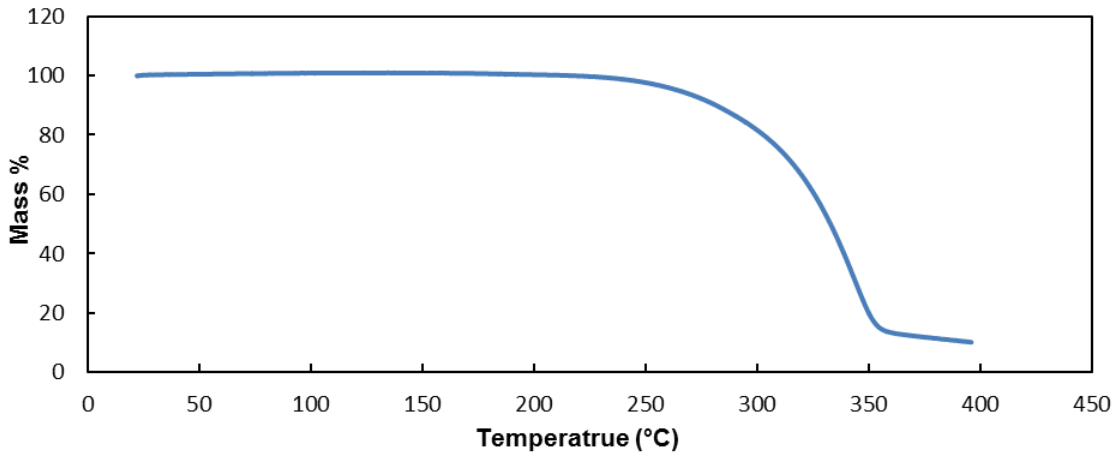

Figure 5: TGA trace for DL2

Preparation of single crystals

The recrystallization of DL2 was performed by dissolving 10 mg (0.03 mmol) of DL2 in approximately 1 cm^3 of acetone. The solution was gently heated to 40 °C while

stirring and then filtered through a 0.45 μm nylon filter into a clean vial and left to crystallize under ambient conditions. Crystals were obtained after 24 hours.

Crystal structure analysis

Data-collection and space group determination

Crystal intensity data were collected on a Bruker KAPPA APEX II DUO single crystal X-ray diffractometer. The data were corrected for absorption using the program SADABS.[1] The Laue symmetry was found to be *2/m* indicating the monoclinic crystal system and the space group $P2_1/n$ (an alternative setting of the space group $P2_1/c$) was identified from systematic absences. The crystal system and space group were subsequently confirmed by the program XPREP.[2]

Structure solution and refinement

Crystal and refinement data for DL2 are shown in Table 1 below. The unit cell refinement and data reduction were performed using the program SAINT.[3] After solving the structure using SHELXS-97[4] all of the non-hydrogen atoms were revealed. The non-hydrogen atoms were placed and refined isotropically using SHELXH-97.[4] None of the atoms displayed any disorder after being refined isotropically and subsequently they were all refined anisotropically. All of the hydrogen atoms were placed in idealised positions based on a riding model and were refined isotropically. The methylene and phenyl hydrogens were refined with U_{iso} values 1.5 times those of the carbon atoms to which they were attached. Methyl hydrogens were refined with U_{iso} values 1.2 times those of the parent atoms. The methyl hydrogens attached to C18 were found to be disordered over two positions and they were placed in idealised positions using an appropriate model. The hydrogens of the amine group appeared in difference Fourier maps and after the planar geometry of the NH_2 group was confirmed, they were allowed to refine freely.

Table 1: Data-collection and refinement parameters for DL2

Chemical Formula	$C_{18}H_{17}N_3O_4$
Formula weight (g mol^{-1})	339.35
Crystal system	Monoclinic
Space group	$P2_1/n$
a (Å)	4.774(2)
b (Å)	23.752(1)
c (Å)	14.869(8)
α (°)	90
β (°)	94.245(1)
γ (°)	90
V (Å^3)	1681.5(2)
Z	4
D_c (g cm^{-3})	1.340
μ (Mo Kα) (mm^{-1})	0.097
F(000)	712
Data collection temp. (K)	173(2)
Crystal size (mm^3)	0.06 × 0.11 × 0.60
Range scanned θ (°)	1.6 - 27.6
Index ranges ±*h*, ±*k*, ±*l*	h: -5, 6; k: -30, 30; k: -19, 19
Reflections (total)	18786
Independent reflections	3846
Reflections with I>2σ(I)	1818
No. of parameters	233
R_{int}	0.044
Goodness-of-fit, *S*	1.00
R_1 [*I*>2σ(*I*)]	0.0559
Reflections omitted	1
wR_2	0.1741
Parameters a, b in w = 1/[σ^2(F_o^2)+(aP)^2+(bP)]	0.0662, 0.4388
$(\Delta/\sigma)_{mean}$	< 0.001
$\Delta\rho_{min,\ max}$ (e Å^{-3})	-0.17, 0.31

Molecular structure

Figure 6 shows a diagram of the DL2 molecule with the labelling scheme. The fused pyridine-pyrrolidine ring system is planar with a maximum deviation of 0.008(2) Å from the least-squares plane (C9). The C-C bond lengths in the pyridine-pyrrolidine ring system range between 1.379(2) Å and 1.486(4) Å and the angles range between 105.9(2)° and 124.0(2)°. The phenyl ring is also planar with a maximum deviation of 0.008(4) Å from the least-squares plane (C22). The C-C bond lengths in the phenyl ring range between 1.336(4) Å and 1.413(6) Å and the angles range between 118.2(4)° and 122.0(4)°. The two torsion angles C2-N1-C19-C20 and N1-C19-C20-

C25 are 111.2(3) and 129.1(3)° respectively, defining the orientation of the phenyl ring with respect to the fused system. The chain of atoms C14-C17 is in an extended conformation. The three C=O carbonyl bond lengths range between 1.202(4) Å and 1.210(3) Å. All geometrical data can be found in the Appendix.

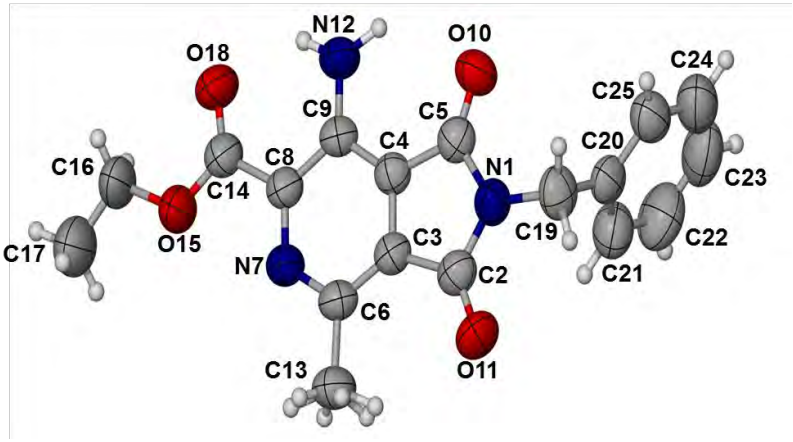

Figure 6: Molecular structure of DL2 showing thermal ellipsoids at the 50% probability level.

Hydrogen bonding

There are two intramolecular hydrogen bonds of type N-H•••O, namely N12-H12A•••O10 and N12-H12B•••O18. There are also two intramolecular hydrogen bonds of type C-H•••O, namely C13-H13D•••O11 and C19-H19A•••O11. An intermolecular hydrogen bond, N12-H12A•••O10[a] (a = 2-x, -y, 2-z) is also present. The molecules of DL2 form centrosymmetric hydrogen bonded dimers via two inversion-related N12-H12A•••O10 hydrogen bonds. The intermolecular N12-H12A•••O10 hydrogen bonds generate a $R_2^2(12)$ hydrogen bonding motif (Figure 7).

Table 2: Hydrogen bonding interactions for DL2.

Interaction	D-H (Å)	H•••A (Å)	D•••A (Å)	D-H•••A (°)
Intramolecular				
N12-H12A•••O10	0.96(4)	2.35(3)	3.024(4)	127(2)
N12-H12B•••O18	0.87(3)	2.00(3)	2.691(4)	136(3)
C13-H13D•••O11	0.98	2.48	3.226(4)	132
C19-H19A•••O11	0.99	2.55	2.919(4)	102
Intermolecular				
N12-H12A•••O10[a]	0.96(4)	2.17(3)	3.009(4)	145(2)

Symmetry codes: [a] 2-x, -y, 2-z

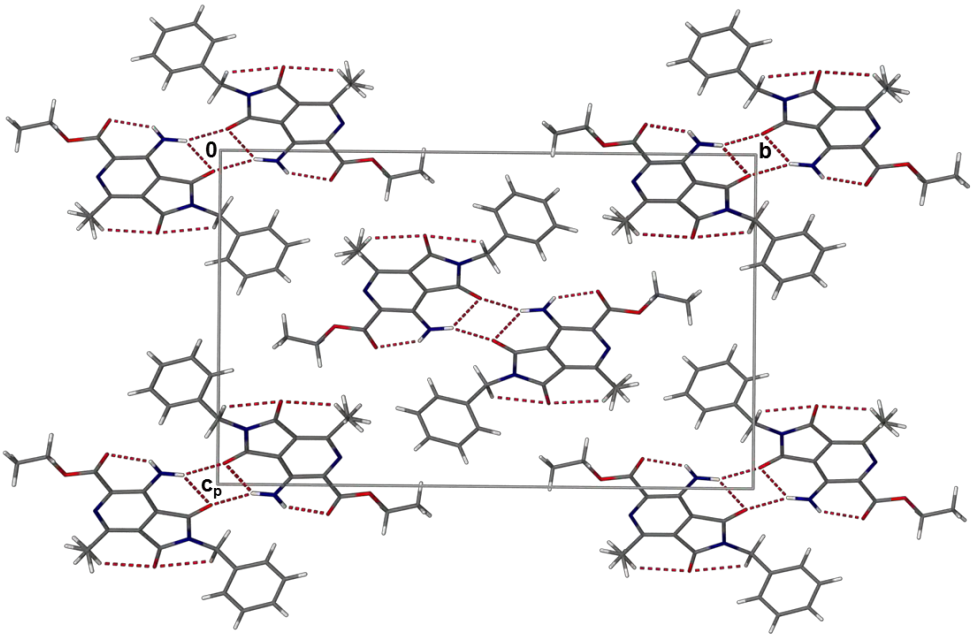

Figure 7: Crystal packing projected along [100].

Crystal packing

The centrosymmetric hydrogen bonded dimers are co-planar, resulting in a layered packing arrangement of the DL2 molecules. This can be seen very clearly when the structure is viewed down the *b*-axis (Figure 8). The program Mercury[5] was used to calculate the least-squares plane through two adjacent layers and the distance between the two planes was found to be 3.567 Å. This distance corresponds with the interplanar distance $d_{1\ 0\ -3}$ = 3.564 Å, resulting in an intense peak at 2θ position 24.99° in the PXRD trace for DL2 (Figure 9).

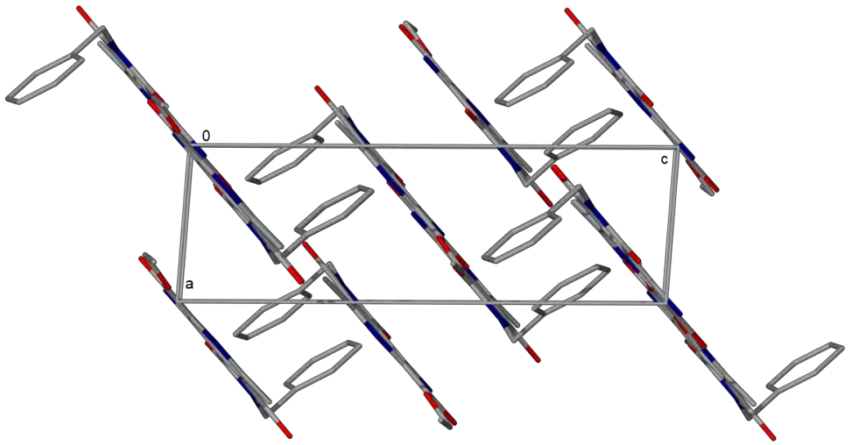

Figure 8: Crystal packing projected along [010] (hydrogens have been omitted for clarity).

Comparative PXRD

The calculated and experimental PXRD traces for DL2 are shown in Figure 9. The two patterns are practically indistinguishable and this high level of agreement confirms that the single crystal is representative of the bulk material.

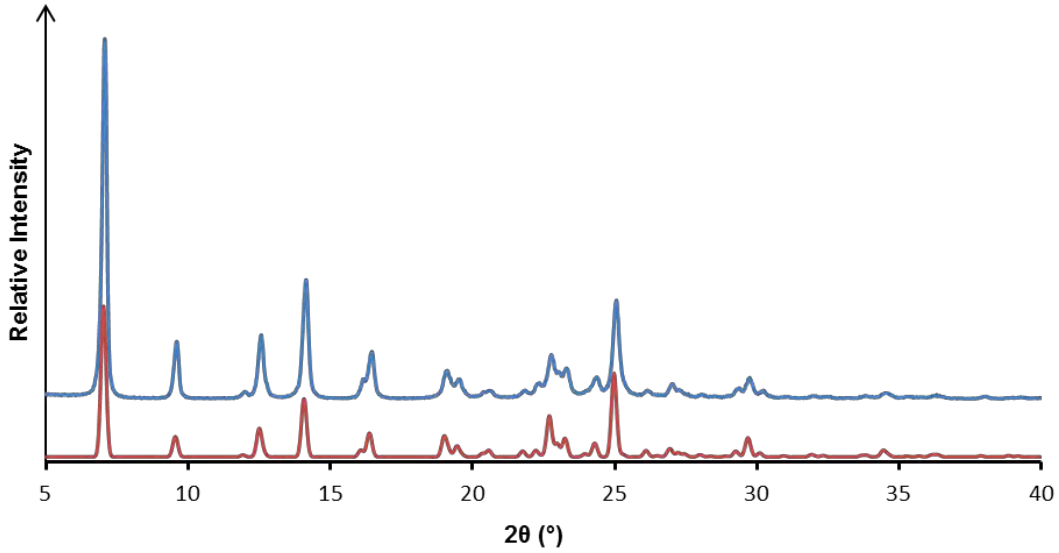

Figure 9: Calculated and experimental PXRD traces for DL2.

Co-crystal screening

The Cambridge Structural Database (CSD)[6] was searched for co-crystals or salts that contained similar functional groups to those in DL2. The results of the search were used as a guideline for the selection of the co-formers that were used in the co-crystal screening with DL2. The CSD was searched for common supramolecular synthons such as the ones shown in Figure 10. The results showed that the functional groups that were most likely to form supramolecular synthons with DL2 were the carboxylic acid (35 hits) and amide (36 hits) functional groups. Nine co-formers that contained the necessary functionalities were selected for co-crystal screening with DL2.

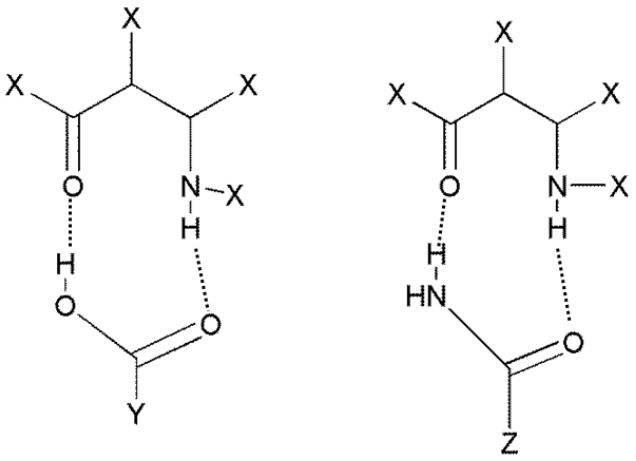

Figure 10: Supramolecular synthons that occur in the CSD.

The first stage of the co-crystal screening involved dry co-grinding with the co-former and DL2 and the results are summarised in Table 3. Dry co-grinding experiments were carried out as described in the previous chapter. The products were analysed by PXRD and the results indicated that all of the experiments resulted in physical mixtures of the two components. Figure 11 has been included as a representative PXRD trace to illustrate that the PXRD trace of the product was clearly a combination of the PXRD traces for the separate components and it was therefore concluded that no new phase had emerged as a result of the dry co-grinding experiments. All of the PXRD traces for the dry co-grinding experiments have been included in the Appendix.

Table 3: Summary of experimental outcomes for the dry co-grinding stage of co-crystal screening with DL2

Co-former	Molar ratio	Outcome
Adipic acid	1:1	Physical mixture
L-ascorbic acid	1:1	Physical mixture
Citric acid	1:1	Physical mixture
L-malic acid	1:1	Physical mixture
Fumaric acid	1:1	Results pending
Nicotinamide	1:1	Physical mixture
Propionamide	1:1	Physical mixture
Benzamide	1:1	Physical mixture
Uracil	1:1	Physical mixture

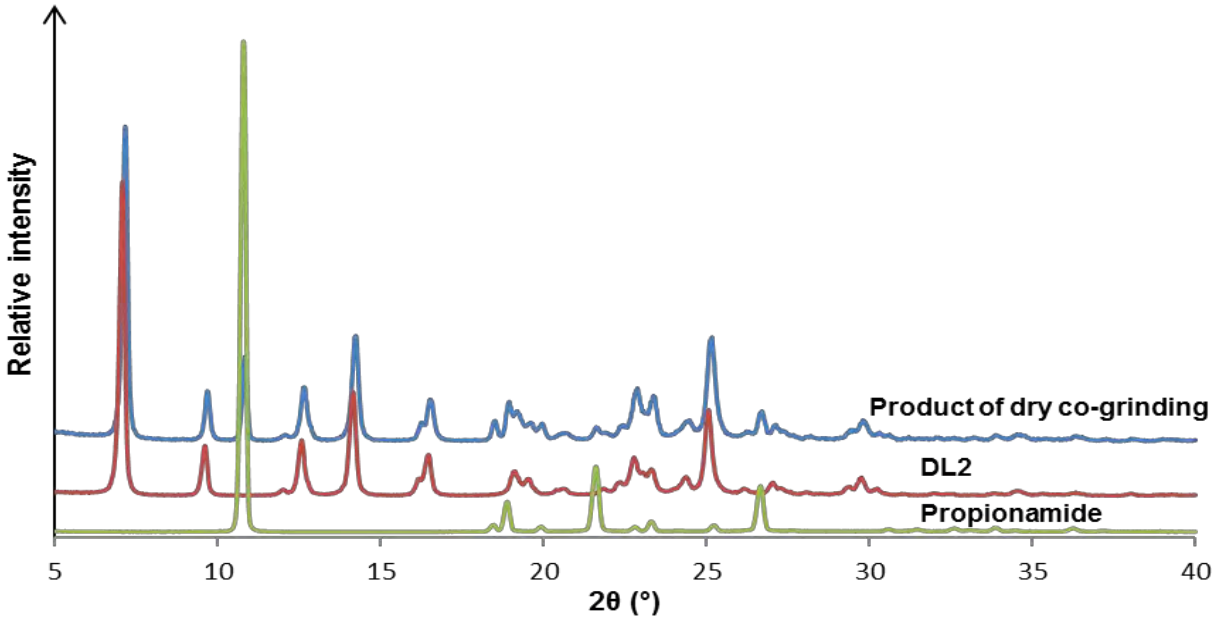

Figure 11: PXRD traces for DL2, propionamide and the product of the dry co-grinding experiment.

The next stage of the co-crystal screening involved liquid-assisted grinding (LAG) experiments. The co-former was ground for 15 minutes with DL2 while small drops of ethanol or acetonitrile were added. Ethanol was used as the solvent during LAG, because it appears on the FDA GRAS database.[7] The products of the LAG experiments were analysed by PXRD and the results (Table 4) indicated that all of the experiments resulted in only physical mixtures of DL2 and the co-former. The PXRD traces from the LAG experiments have been included in the Appendix.

Table 4: Summary of experimental outcomes for the liquid-assisted grinding stage of co-crystal screening with DL2.

Co-former	Solvent	Molar ratio	Product
Adipic acid	Ethanol	1:1	Physical mixture
L-ascorbic acid	Ethanol	1:1	Physical mixture
Citric acid	Acetonitrile	1:1	Physical mixture
L-malic acid	Ethanol	1:1	Physical mixture
Fumaric acid	Ethanol	1:1	Physical mixture
Nicotinamide	Ethanol	1:1	Physical mixture
Propionamide	Ethanol	1:1	Physical mixture
Benzamide	Ethanol	1:1	Physical mixture
Uracil	Ethanol	1:1	Physical mixture

The products of the LAG experiments were recovered after PXRD analysis and recrystallized from acetone. The unit cells of single crystals that resulted from the recrystallization were checked and in all of the cases DL2 crystallized separately from the co-former.

Cyclodextrin inclusion

Kneading and co-precipitation experiments were carried out in an attempt to include DL2 in CDs. In the case of the kneading experiments, DL2 and each of the native CDs were kneaded for 20 minutes while adding small drops of Milli-Q[8] water. The products were analysed using PXRD and the results are summarised in Table 5. The PXRD traces of the products indicated that all of the kneading experiments resulted in a physical mixture of DL2 and the CD. Figure 12 has been included as a representative PXRD trace for the kneading experiments. All of the PXRD traces from the CD experiments can be found in the Appendix.

Table 5: Kneading experiments with DL2.

CD	Solvent	Molar ratio	Method	Product
α-CD	H_2O	1:1	20 min kneading	Physical mixture
β-CD	H_2O	1:1	20 min kneading	Physical mixture
γ-CD	H_2O	1:1	20 min kneading	Physical mixture

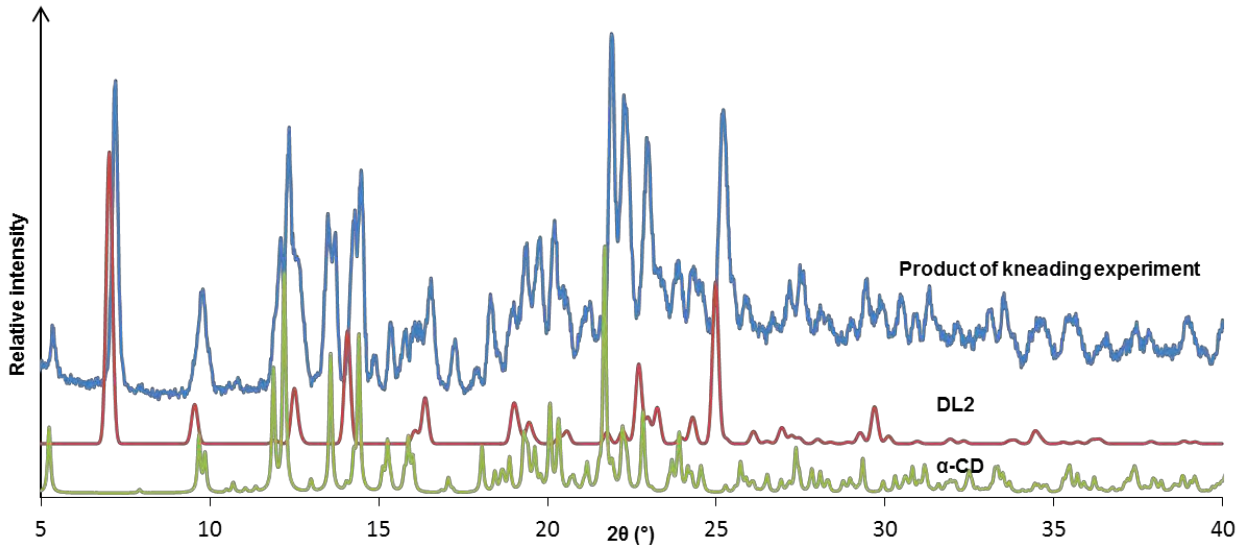

Figure 12: PXRD trace for α-CD, DL2 and the product of kneading DL2 and α-CD.

Co-precipitation experiments with DL2 and the native CDs as well as heptakis(2,6-di-*O*-methyl)-β-cyclodextrin (DIMEB), heptakis(2,3,6-tri-*O*-methly)-β-cyclodextrin (TRIMEB) and hexakis(2,3,6-tri-*O*-methyl)-α-cyclodextrin (TRIMEA) were unsuccessful. For co-precipitation with the native CDs, DL2 was added to a hot (50 °C) aqueous solution of the CD and ethanol was added to aid the dissolution of DL2. The solution was stirred for approximately 24 hours and then filtered. For the derivatised CDs, DL2 was dissolved separately in either ethanol or acetone and then added to an aqueous solution of the CD at room temperature. After filtering, the solution was placed in an oven at 60 °C. None of these experiments yielded any CD inclusion complexes.

Table 6: Co-precipitation experiments with selected CDs and DL2.

CD	Solvent	Molar ratio	Method	Product
α-CD	H_2O/Ethanol	1:1	Slow cooling from 50 °C	No complex
β-CD	H_2O/Ethanol	1:1	Slow cooling from 50 °C	No complex
γ-CD	H_2O/Ethanol	1:1	Slow cooling from 50 °C	No complex
DIMEB	H_2O/Ethanol	1:1	Recrystallization at 60 °C	No complex
DIMEB	H_2O/Acetone	1:1	Recrystallization at 60 °C	No complex
TRIMEB	H_2O/Ethanol	1:1	Recrystallization at 60 °C	No complex
TRIMEB	H_2O/Acetone	1:1	Recrystallization at 60 °C	No complex
TRIMEA	H_2O/Ethanol	1:1	Recrystallization at 60 °C	No complex
TRIMEA	H_2O/Acetone	1:1	Recrystallization at 60 °C	No complex

None of the desired products (co-crystals or inclusion complexes) were produced and the results indicate that DL2 may not be a favourable candidate for further drug development. In retrospect, the poor solubility could be explained by examining the crystal structure of DL2. Both of the hydrogens in the amine group are involved in intramolecular hydrogen bonding with the adjacent carbonyl oxygens. The third carbonyl oxygen is also involved in intramolecular hydrogen bonding with the adjacent methyl group. This suggests that the preferred configuration of the molecule is to have C19-H19B and the C14-C17 chain in positions that facilitate intramolecular hydrogen bonding with the fused pyridine-pyrrolidine ring system. It appears that these strong intramolecular and intermolecular hydrogen bonding systems in DL2 could preclude its ability to form new hydrogen bonds with other molecules.

Another observation was that DL2 displayed very poor solubility in both aqueous and organic media. The poor solubility of DL2 can present challenges not only in terms of bioavailability *in vivo*, but also for biological testing. If DL2 cannot be solubilized enough in aqueous media, it will be extremely difficult to accumulate relevant biological data for this drug lead. Therefore, an alternative approach will be required to improve the aqueous solubility. One alternative approach is the use of CDs to improve aqueous solubility of poorly soluble compounds. This approach will be explored in the next chapter, which will discuss the phase solubility studies that were carried out with various CDs and an analogue of DL2.

References

1. G. M. Sheldrick, Program SADABS, Version 2.05, University of Göttingen, Germany, 2007.
2. Bruker AXS Inc., XPREP, Version 5.1, Bruker AXS Inc., Madison, WI, USA, 1997.
3. Bruker AXS Inc., Program SAINT, Version 7.60a, Bruker AXS Inc., Madison, WI, USA, 2006.
4. G. M. Sheldrick, *Acta Crystallogr. A.,* 2007, **64**, 112-122.
5. C. F. Macrae, I. J. Bruno, J. A. Chisholm, P. R. Edgington, P. McCabe, E. Pidcock, L. Rodriguez-Monge, R. Taylor, J. van de Streek and P. A. Wood, *J. Appl. Cryst*., 2008, **41**, 466-470.
6. Cambridge Structural Database and Cambridge Structural Database system, Version 5.36 (updates to May 2015), Cambridge Crystallographic Data Centre, University Chemical Laboratory; Cambridge, England, 2014.
7. SCOGS (Select Committee on GRAS Substances), http://www.accessdata.fda.gov/scripts/fdcc/?set=SCGOS (accessed August 2014).
8. Milli-Q water, Millipore Corporation, Billerica, Massachusetts, USA.

CHAPTER 4: Phase solubility studies with 7-amino-2-(3-chlorobenzyl)-4-methyl-6-(3-methyl-1,2,4-oxadiazol-5-yl)-1H-pyrrolo[3,4-c]pyridine-1,3(2H)-dione (DL3): a novel anti-tubercular drug lead.

Introduction

7-Amino-2-(3-chlorobenzyl)-4-methyl-6-(3-methyl-1,2,4-oxadiazol-5-yl)-1H-pyrrolo-[3,4-c]pyridine-1,3(2H)-dione, ('DL3' henceforth), is an analogue of DL2, which was discussed in Chapter 3. These compounds are part of a novel series of anti-tubercular compounds identified by the H3D centre in collaboration with the Novartis Institute for Tropical Disease (NITD). DL2 was identified as a "hit" compound from a high-throughput screening conducted by NITD and was further optimized to obtain DL3. Both drug leads contain a fused pyridine-pyrrolidine ring system (Figure 1). As discussed in the previous chapter, DL2 displayed poor solubility in both organic and aqueous media and the same observation was made for DL3. It was therefore necessary to explore alternative ways of enhancing the solubility of DL3. One such approach is cyclodextrin (CD) inclusion, which has been shown to significantly improve the solubility of poorly soluble compounds.[1] This chapter will discuss the phase solubility studies performed with DL3 and various CDs. The crystal structure of DL3 was successfully elucidated and will also be presented.

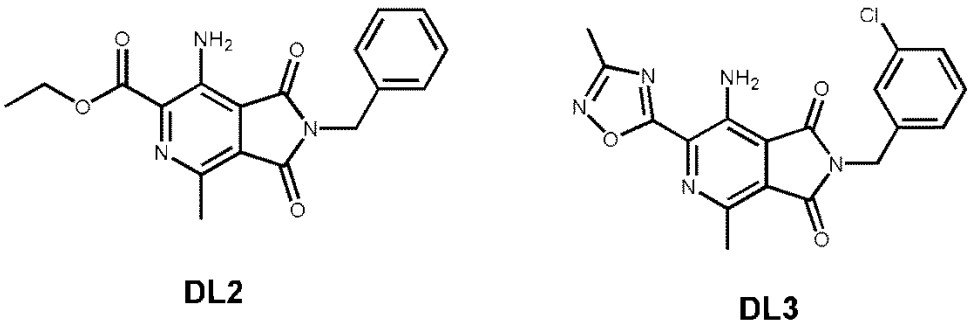

Figure 1: Structures of DL2 and DL3.

NMR and mass spectroscopy

The ^{1}H, ^{13}C NMR and LC-MS spectra for DL3 were provided by the H3D Centre and these data have been included in the Appendix.

Thermal analysis

HSM

Crystals of DL3 were heated at a rate of 10 K min^{-1} during a HSM experiment and the representative HSM photographs are shown in Figure 2. The crystals of DL3 start to melt at 191 °C and the entire sample is molten at 199 °C. No other significant thermal events were observed.

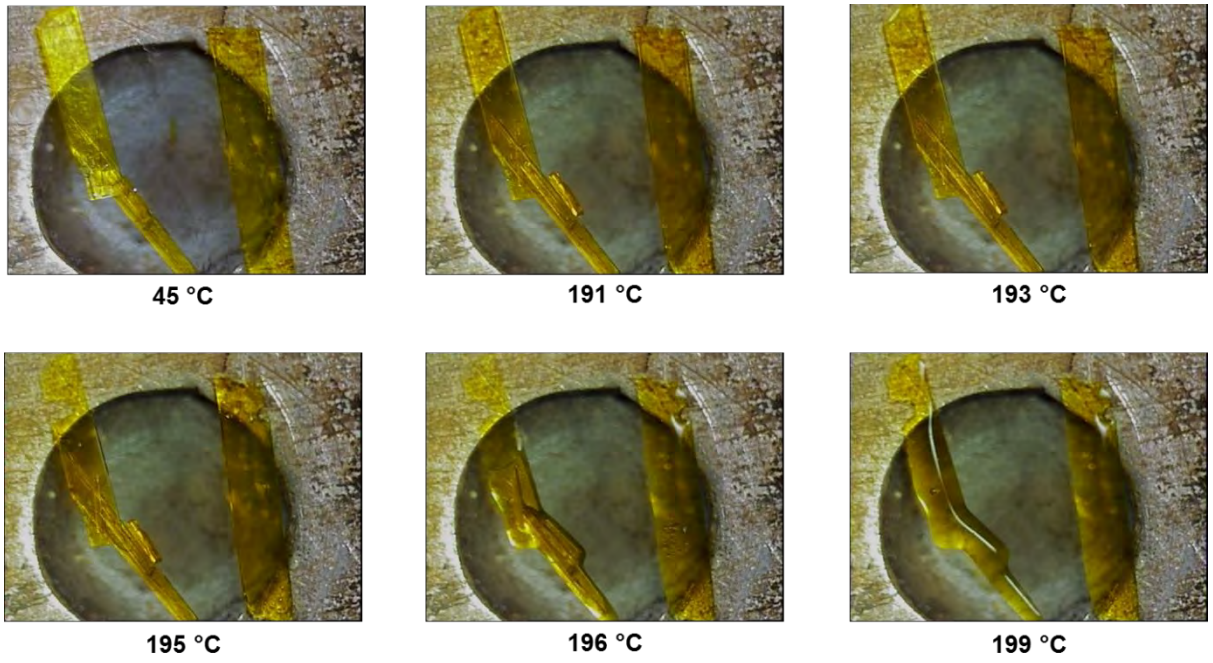

Figure 2: Representative HSM photographs of DL3.

TGA and DSC

The TGA trace of DL3 (Figure 3) shows no significant thermal events occurring before the onset of decomposition at 197 °C.

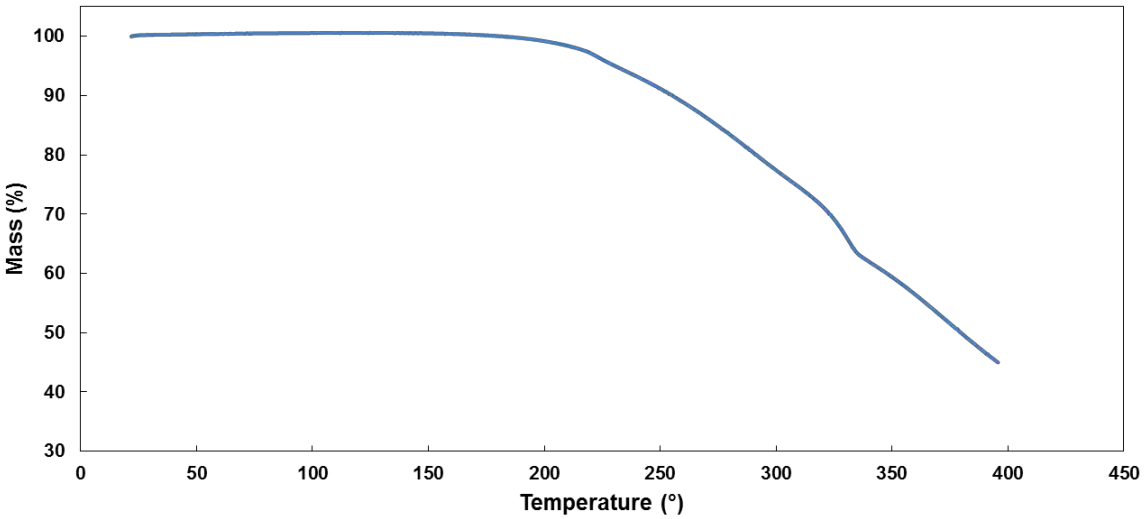

Figure 3: TGA trace for DL3.

The baseline of the DSC trace for DL3 (Figure 4) is sloped and this is most probably due to some irregularity with the DSC instrument at the time of recording. However, it is still possible to observe the endotherm (ΔH_{fus} = 18.20 kJ mol^{-1}) corresponding to the fusion of DL3, spanning the range 185 °C to 198 °C (peak at 187 °C).

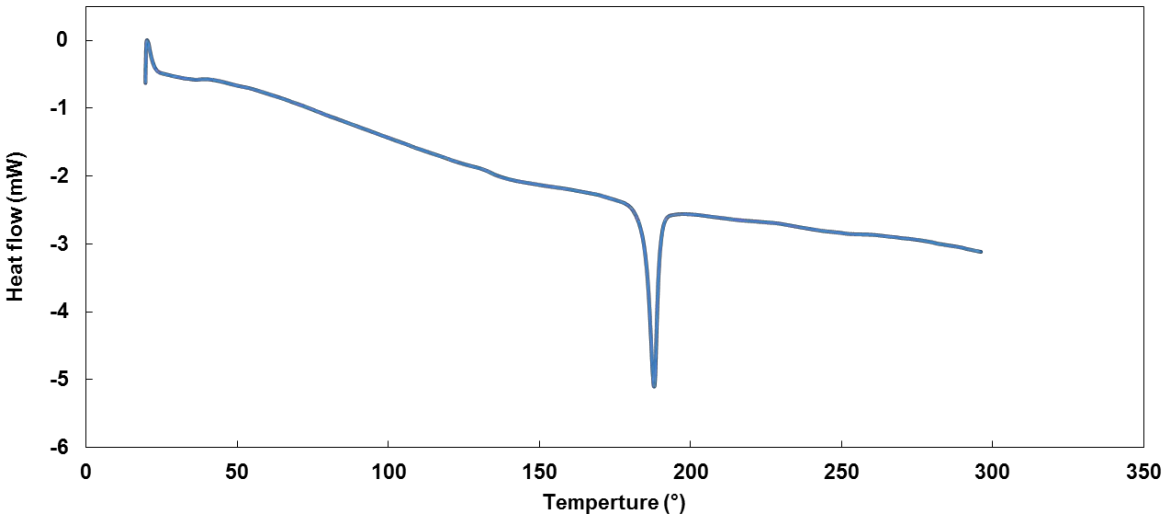

Figure 4: DSC trace for DL3.

Preparation of single crystals

Single crystals were obtained from the recrystallization of DL2. 10 mg of DL2 was dissolved in approximately 1 cm^3 acetone and gently heated to 40 °C while stirring.

The solution was filtered through a 0.45 µm nylon filter into a clean vial and left to crystallize under ambient conditions. Yellow plate-like crystals were obtained after 48 hours.

Crystal structure analysis

Data-collection and space group determination

Crystal intensity data for DL2 were collected on a Nonius KappaCCD single crystal X-ray diffractometer and corrected for absorption effects using the program SADABS.[2] Unit cell refinement and data reduction were performed using the programs DENZO and SCALEPACK.[3] The space group and crystal system of DL3 were determined using the program LAYER.[4] The Laue symmetry was found to be $\bar{1}$ indicating the triclinic crystal system and the mean $|E^2 - 1|$ parameter value of 0.956 obtained using the program XPREP[5] identified the space group as $P\ \bar{1}$.

Structure solution and refinement

Table 1 contains the crystal and refinement data for DL3. The structure was solved by direct methods using SHELXS-97,[6] which revealed all of the non-hydrogen atoms. The non-hydrogen atoms were placed and refined first isotropically and then anisotropically using SHELXH-97.[6] After confirming the planar geometry of both amino groups in the asymmetric unit, all of the hydrogen atoms were placed in idealised positions based on a riding model and were refined isotropically with U_{iso} values 1.2 – 1.5 times that of their parent atoms.

Table 1: Data-collection and refinement parameters for DL3.

Chemical Formula	$C_{18}H_{14}N_5O_3Cl$
Formula weight (g mol^{-1})	383.79
Crystal system	Triclinic
Space group	$P\ \bar{1}$
a (Å)	7.7740(3)
b (Å)	14.8745(8)
c (Å)	15.4291(8)
α (°)	102.988(2)
β (°)	91.816(3)
γ (°)	98.091(3)
V $(Å)^3$	1717.5(2)
Z	4
D_c (g cm^{-3})	1.484
μ (Mo Kα) (mm^{-1})	0.254
F(000)	792
Data collection temp. (K)	173(2)
Crystal size (mm^3)	0.03 × 0.09 × 0.45
Range scanned θ (°)	2.8 - 26.7
Index ranges ±*h*, ±*k*, ±*l*	h: -9, 9; k: -18, 18; k: -19, 19
Reflections (total)	39818
Independent reflections	7239
Reflections with I>2σ(I)	4931
No. of parameters	491
R_{int}	0.053
S	1.02
R_1 [*I*>2σ(*I*)]	0.0434
Reflections omitted	35
wR_2	0.1115
Parameters a, b in w = 1/[$\sigma^2(F_o^2)$+(aP)^2+(bP)]	0.0536, 0.4213
$(\Delta/\sigma)_{mean}$	<0.001
$\Delta\rho_{min,\ max}$ (e $Å^{-3}$)	-0.29, 0.25

Molecular structure

Figure 5 shows the asymmetric unit of DL3 with the labelling scheme. The asymmetric unit consists of two molecules of DL3 which have been labelled A and B. The fused pyridine-pyrrolidine ring system in molecule A is planar with a maximum deviation of 0.025(2) Å from the least-squares plane (C5A). The angle between the fused pyridine-pyrrolidine ring system and the oxadiazole ring is 0.53(8)°. The orientation of the phenyl ring with respect to the fused ring system is defined by the two torsion angles C2A-N1A-C20A-C21A and N1A-C20A-C21A-C26A and these are -103.5(2)° and 94.9(2)° respectively. In molecule B the fused pyridine-pyrrolidine ring

system is also planar with a maximum deviation of 0.023(2) Å from the least-squares plane (C4B) and the angle between this ring system and the oxadiazole ring is 4.09(9)°. The torsion angles C2B-N1B-C20B-C21B (-103.2(2)°) and N1B-C20B-C21B-C26B (96.4(2)°) define the orientation of the phenyl ring with respect to the fused ring system. All geometrical data can be found in the Appendix.

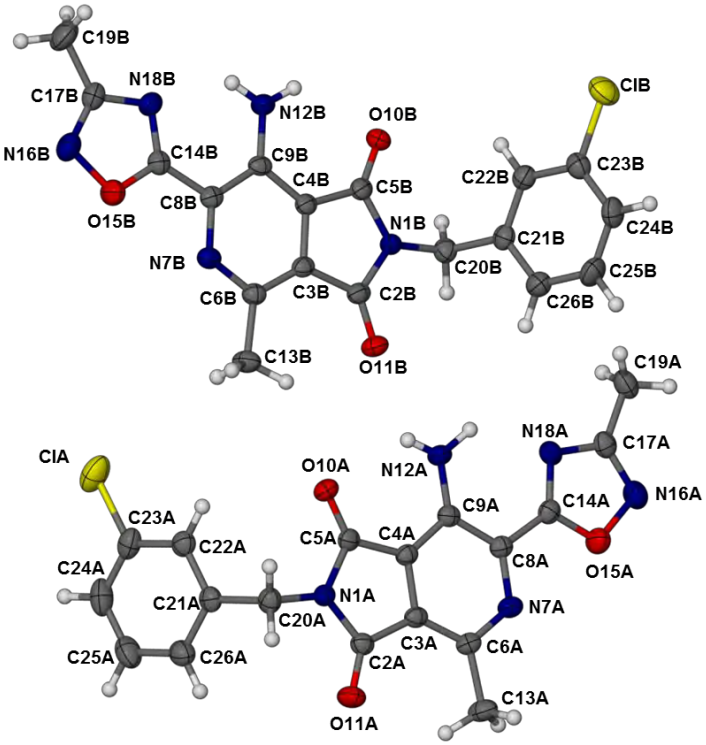

Figure 5: The asymmetric unit of DL3 showing thermal ellipsoids at the 50% probability level.

Hydrogen bonding and crystal packing

The hydrogen bonding interactions between molecules A and B are generated by two intramolecular (C13B-H13E•••O11B and N12A-H12A•••O10A) and two intermolecular (C13B-H13E•••O10A and N12A-H12A•••O11B) hydrogen bonds. These four bonds form a cyclic (quadrilateral) motif. There are also two intermolecular hydrogen bonding interactions, N12A-H12A•••O11B and C13B-H13E•••O10A, that propagate the quadrilateral hydrogen bonding motif parallel to the *c*-axis (Figure 6). The hydrogen bonding interactions are listed in Table 2.

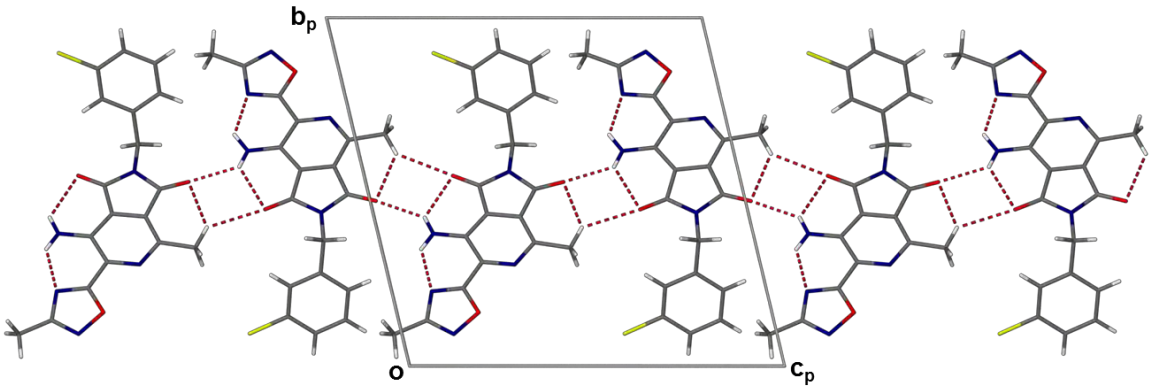

Figure 6: Hydrogen bonding interactions in DL3 viewed along [1 0 0].

Table 2: Hydrogen bonding interactions for DL3.

Interaction	D-H (Å)	H•••A (Å)	D•••A (Å)	D-H•••A (°)
Intramolecular				
N12A-H12A•••O10A	0.88	2.43	3.043(2)	127
N12B-H12C•••O10B	0.88	2.42	3.036(2)	128
N12A-H12B•••N18A	0.88	2.09	2.750(2)	131
N12B-H12D•••N18B	0.88	2.09	2.752(2)	131
C13A-H13B•••O11A	0.98	2.50	3.216(3)	129
C13B-H13E•••O11B	0.98	2.53	3.227(3)	128
Intermolecular				
N12B-H12D•••O11A[a]	0.88	2.15	2.824(2)	133
C13A-H13B•••O10B[b]	0.98	2.54	3.355(3)	141
C13B-H13E•••O10A	0.98	2.54	3.328(2)	138
N12A-H12A•••O11B	0.88	2.15	2.809(2)	131
C19A-H19C•••N7B[c]	0.98	2.60	3.401(3)	139

[a] x, y, -1+z; [b] x, y, 1+z; [c] 2-x, 1-y, 1-z

DL3 has a layered packing arrangement and there is a weak C19A-H19C•••N7B[c] (c = 2-x, 1-y, 1-z) between the layers (Figure 7). The layers lie very close to the (2 $\bar{3}$ 0) planes, resulting in an intense peak at the 2θ-angle 27.51° in the PXRD trace for DL3 (Figure 8).

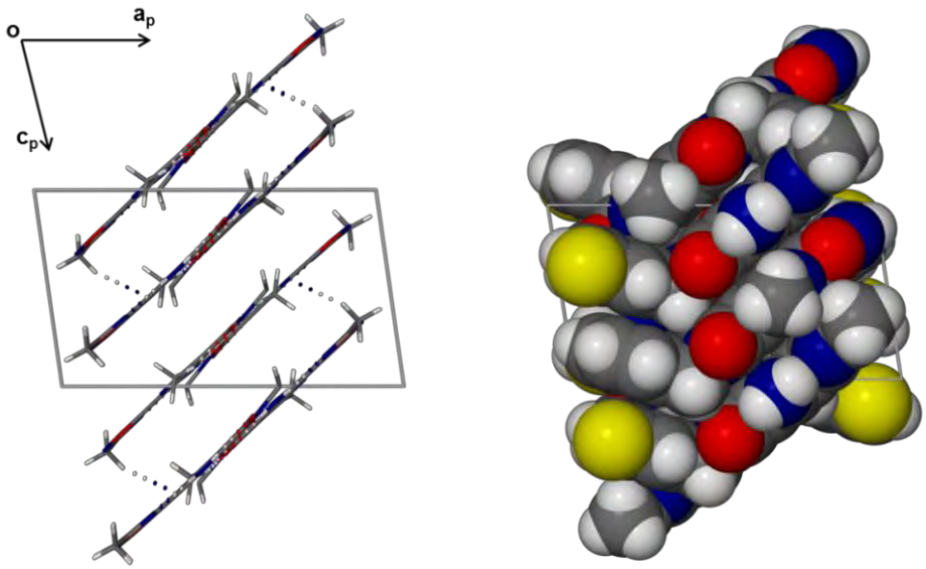

Figure 7: Packing diagram of DL3 viewed along [0 1 0]. The left image shows the weak C19A-H19C•••N7B^{c} hydrogen bonding interactions between the layers of DL3 molecules. The right image shows a space-filling view of the layers.

Comparative PXRD

The experimental and calculated PXRD traces for DL3 are shown in Figure 8. There is a high level of agreement between the experimental and the calculated traces which confirms that the single crystal is representative of the bulk material.

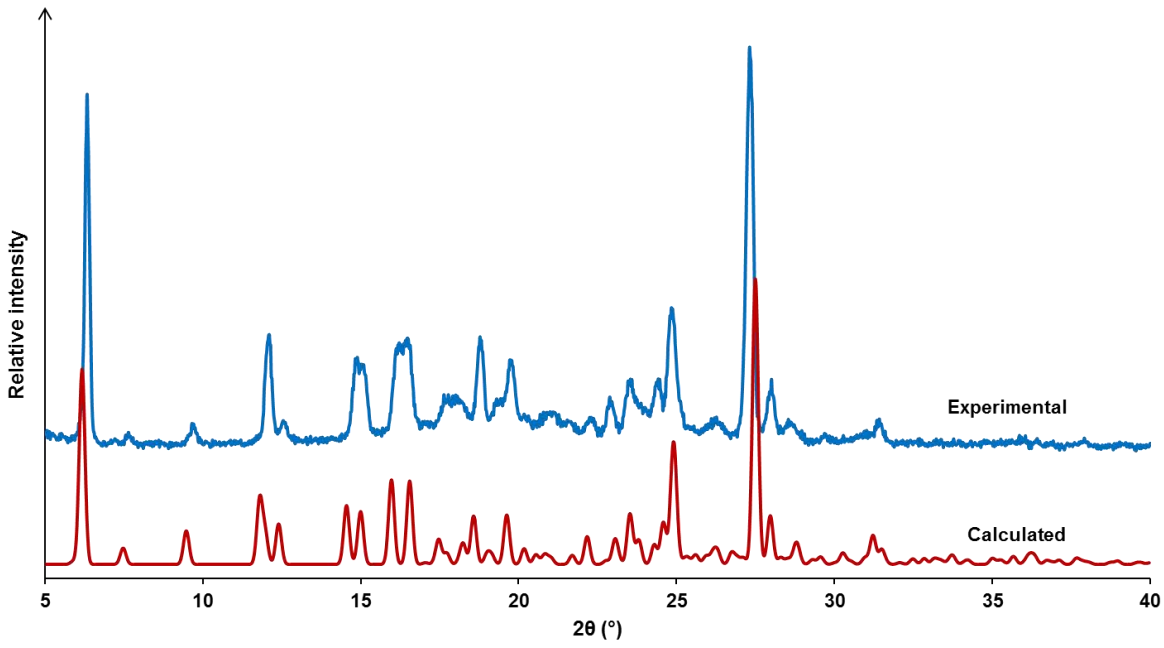

Figure 8: Experimental and calculated PXRD traces for DL3.

Phase solubility studies

Phase solubility studies were carried out with DL3 and seven different CDs: β-CD, hydroxypropyl-β-CD (HPβCD), β-CD polymer, γ-CD, hydroxypropyl-γ-CD (HPγCD), γ-CD polymer and randomly methylated β-CD (RAMEB) in an attempt to enhance its poor aqueous solubility (3.84 mg cm^{-3}, equivalent to 0.01 mM at 25 °C).

The phase solubility experiments were performed according to the method described by Higuchi and Connors.[8] Serial dilutions of each CD solution were prepared and an excess amount of DL3 was added to a polytop vial containing 5 cm^3 of each solution. The vials were stirred (500 rpm) at constant temperature (25 ± 0.5 °C) for 72 hours. The solutions were filtered through a 0.45 μm nylon filter and their UV-visible spectra were recorded. The concentration of DL3 was determined from a calibration curve (Figure 9) obtained as described in Chapter 2.

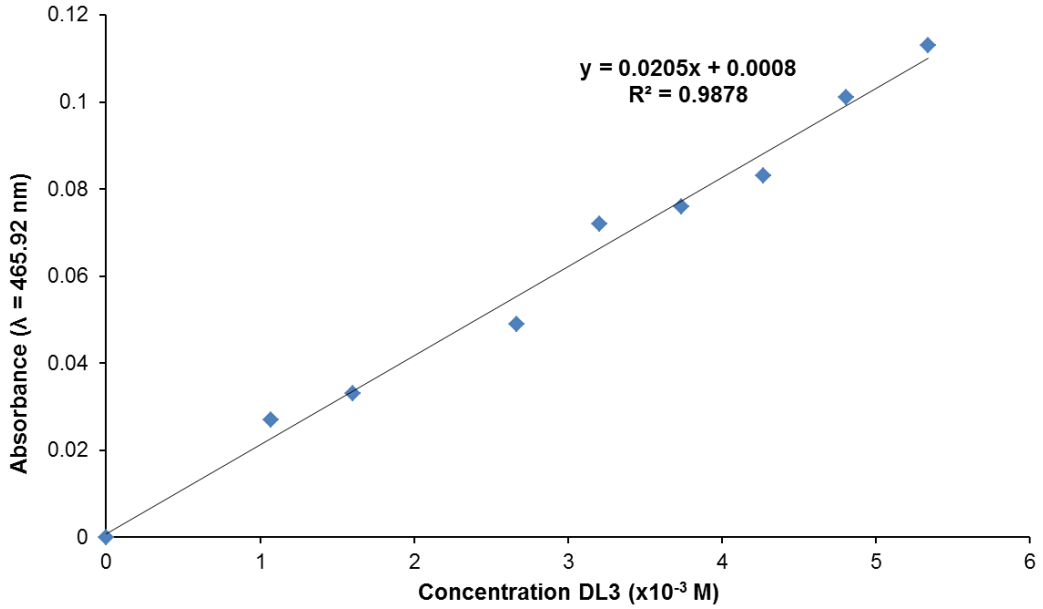

Figure 9: Calibration curve for DL3.

Expression (1) describes a linear relationship between the absorbance (A) and concentration (c) of an absorbing species with a constant path length (l) and extinction co-efficient (ε_o). Using equation (1) the extinction coefficient (ε_o) of DL3

was found to be 0.0205 mM^{-1} cm^{-1}, indicating that the compound is not particularly UV active. Any absorbance measurements that fell within the error of the instrument (less than 0.01 absorbance units) were not reported, because they were considered to be unreliable. Each CD solution containing DL3 was filtered directly into the cuvette before the UV spectrum was recorded. The solutions were not diluted and therefore the phase solubility profiles were constructed based on single measurements. This was done to ensure that the solution in the cuvette contained a maximum concentration of DL3 and that the resulting absorbance measurements were reliable i.e. at least 0.01 absorbance units.

$$A = \varepsilon_o cl \qquad (1)$$

The results of the phase solubility studies performed with γ-CD, hydroxypropyl γ-CD (HPγCD) and γ-CD polymer are not reported, because the UV measurements recorded during the experiments were unreliable (the values recorded for the UV-visible spectra were less than 0.01 absorbance units). Phase solubility studies with DL3 and RAMEB produced erratic results and these results have also been excluded.

Higuchi and Connors classified phase solubility profiles as either A- or B-type.[8] A-type behaviour is consistent with an increase in solubility of the compound with an increase in CD concentration. There are three sub-types of A-type behaviour: A_L-type curves show a linear increase in solubility with increasing CD concentration, whereas A_P- and A_N-type curves display a positive or negative deviation respectively due to a change in the physical nature of the solution. B-type behaviour indicates the formation of an insoluble complex in solution. The subtype B_S indicates the formation of an insoluble complex with limited solubility, while B_L indicates the formation of an insoluble complex.[8]

The phase solubility profile for β-CD (Figure 10) can be classified as A_P-type. This is due to the approximately linear increase in the apparent solubility of DL3 up to a β-CD concentration of 12 mM, after which there is a positive deviation. At the highest concentration of β-CD used the apparent solubility of DL3 increased to 3.6 mM, i.e. representing a solubility enhancement of 360-fold. It was not possible to quantify the

concentration of DL3 that was solubilized by a 20 mM β-CD solution, because the complex precipitated from the solution after only 24 hours. This can be attributed to the aggregation of β-CD molecules at this higher concentration.

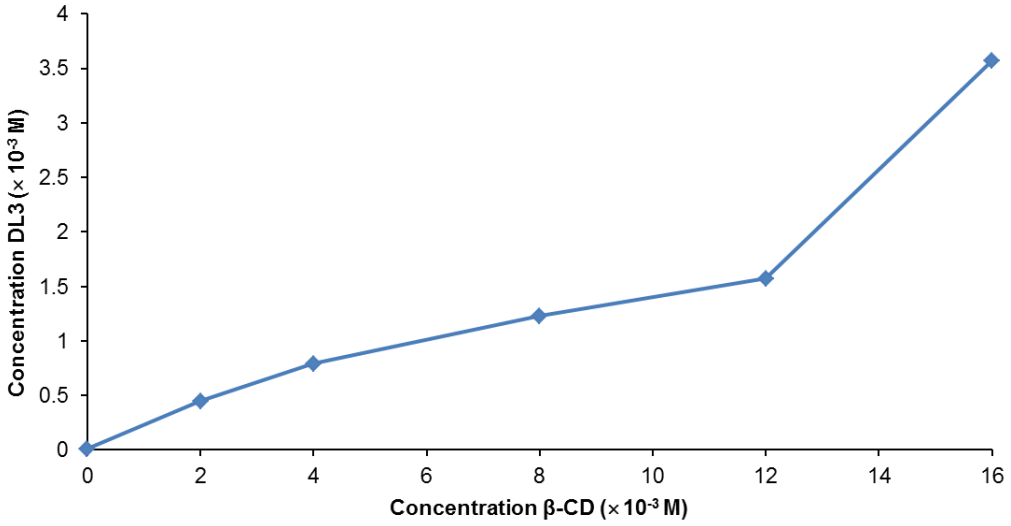

Figure 10: Solubility of DL3 as a function of [β-CD] at 25°C.

Figure 11 shows the phase solubility profile using HPβCD as host. There is a linear relationship between the concentration of DL3 and HPβCD concentration and this behaviour is classified as A_L-type. At the highest concentration of HPβCD used the apparent solubility of DL3 increased by a factor of more than 400.

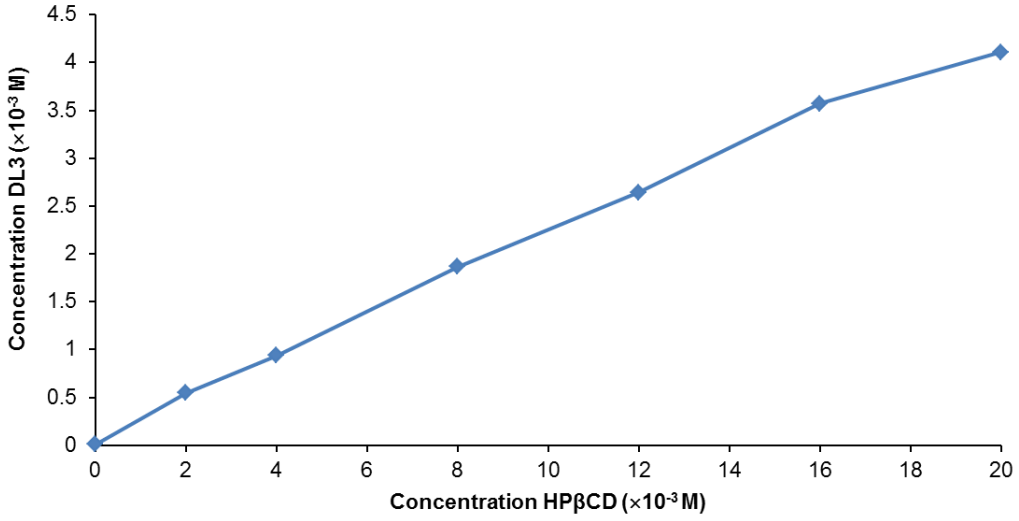

Figure 11: Solubility of DL3 as a function of [HPβCD] at 25°C.

The association constants for complex formation were calculated using Equation (2), where S_0 is the intrinsic solubility of DL3 at 25 °C and "slope" is the slope of the phase solubility profile. This equation is only valid for 1:1 host-guest complexes with the slope of the plot being less than 1. The initial slope of the β-CD profile was used to calculate K_C. The estimated apparent stability constants for complex formation with β-CD and HPβCD were found to be 14 700 M^{-1} and 26 780 M^{-1} respectively. These high values for K_C indicate very strong binding between DL3 and the CD in solution.

$$K_C = \frac{slope}{S_0\,(1-slope)} \qquad (2)$$

The results from the phase solubility studies demonstrate very clearly that it was possible to achieve a significant enhancement in the solubility of DL3 through the use of CDs. This result is also important in that it could have applications for drug delivery or biological testing where the liquid medium is a CD solution.

References

1. T. Loftsson, M. E. Brewster and M. Másson, *A. J. Drug Deliv.,* 2004, **2**, 261-275.
2. G. M. Sheldrick, Program SADABS, Version 2.05, University of Göttingen, Germany, 2007.
3. Z. Otwinowski and W. Minor, *Methods in Enzymology*, ed. C.W. Carter and R.M. Sweet, Academic Press, New York, 1997, vol. 276, pp. 307-326.
4. L. J. Barbour, *J. Appl. Crystallogr.*, 1999, **32**, 351-352.
5. Bruker AXS Inc., XPREP, Version 5.1, Bruker AXS Inc., Madison, WI, USA, 1997.
6. G. M. Sheldrick, *Acta Crystallogr. A.,* 2007, **64**, 112-122.
7. C. F. Macrae, I. J. Bruno, J. A. Chisholm, P. R. Edgington, P. McCabe, E. Pidcock, L. Rodriguez-Monge, R. Taylor, J. van de Streek and P. A. Wood, *J. Appl. Cryst.*, 2008, **41**, 466-470.
8. T. Higuchi and K. A. Connors, *Adv. Anal. Chem. Instrum.,* 1965, **4**, 117-212.

CHAPTER 5: Co-crystal screening with 3-(6-methoxy-pyridin-3-yl)-5-(4-methylsulfonylphenyl)-pyridin-2-amine (DL4): a novel antimalarial drug lead.

Introduction

3-(6-Methoxypyridin-3-yl)-5-(4-methylsulfonylphenyl)-pyridin-2-amine (DL4, Figure 1) is a novel antimalarial drug lead that has been reported in the literature.[1] DL4 displayed potent *in vitro* antiplasmodial activity against both the K1 (multi-drug resistant) and NF54 (sensitive) strains of the human malaria parasite *Plasmodium falciparum*, with an IC_{50} value of 0.051 μM for both strains. DL4 also showed 99.0% reduction in parasitemia following the oral administration of a 30 mg kg^{-1} dose to *P. berghei* infected mice. However, in terms of physicochemical properties, DL4 displays very poor aqueous solubility (0.121 mg cm^{-3} at pH 6.5) and this has been addressed in the literature by D. L. Cruickshank *et al* who reported five novel salts and one co-crystal of DL4.[2]

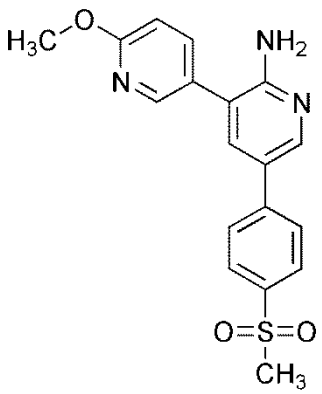

Figure 1: Chemical structure of DL4.

Previous co-crystal screening with DL4

The crystal structure of DL4 has been solved and Figure 2 shows two inversion-related molecules of DL4 that form a hydrogen bonded dimer. The 2-aminopyridine moieties in DL4 form a N–H•••N hydrogen bonding motif with graph-set notation $R_2^2(8)$, indicating an eight-membered ring with two acceptors and two donors.[2]

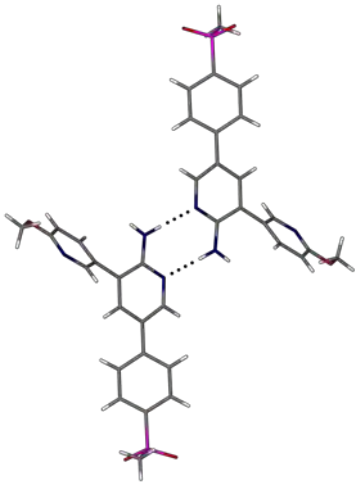

Figure 2: Inversion-related molecules of DL4 forming a hydrogen-bonded dimer.

In the study by D. L. Cruickshank *et al.* it was predicted that the 2-aminopyridine moiety in DL4 was the group that was most likely to form supramolecular heterosynthons with "generally regarded as safe" (GRAS) co-former molecules.[2] Their search of the Cambridge Structural Database revealed 177 hits for the ionic supramolecular heterosynthon [Figure 3(a)] between carboxylic acids and 2-aminopyridine groups and only nine hits for the neutral form [Figure 3(b)]. It had also been reported in a separate study that a proton transfer would be expected to take place when a 2-aminopyridine functional group is coupled to a carboxylic acid.[3]

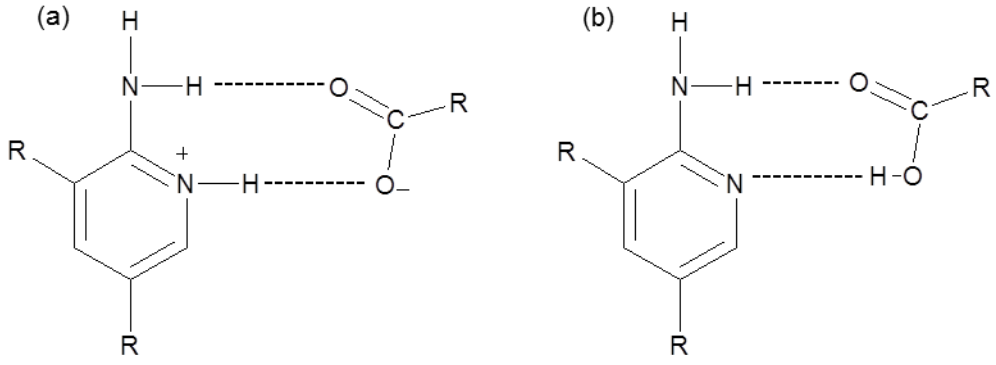

Figure 3: The ionic (a) and neutral (b) supramolecular heterosynthons that can form between 2-aminopyridine moieties and carboxylic acids.

Dry co-grinding and liquid-assisted grinding (LAG) experiments were performed with DL4 and four dicarboxylic acids (fumaric acid, oxalic acid, adipic acid and suberic acid) as well as saccharin and salicylic acid.[2] Dry co-grinding experiments did not reveal any hits, but LAG experiments with DL4 and fumaric acid, salicylic acid and

saccharin showed evidence for the formation of new phases. Recrystallization of the products of the LAG experiments yielded single crystals of the fumarate, salicylate and saccharinate salts of DL4. Two additional salts of DL4 (oxalate and suberate salts) were prepared by co-precipitation and a novel co-crystal of DL4 and adipic acid was prepared using the same method. A semi-quantitative turbidimetric solubility assay was used to assess the solubility of the salts in the 20 – 200 μM range. The results indicated that the saccharinate and fumarate salts as well as the adipic acid co-crystal displayed solubilities marginally greater than that of DL4.

Present study

This chapter will discuss the co-crystal screening experiments that were performed with DL4. LAG experiments with DL4 revealed three hits that indicated the formation of a new phase between DL4 and adipic acid, citric acid and orotic acid. Single crystals of the adipate, citrate and orotate salts were obtained by co-precipitation. The salts were fully characterised using thermal techniques, IR spectroscopy and X-ray structure analysis.

Co-crystal screening

Based on the success of the published co-crystal studies with DL4,[2] another series of GRAS co-formers containing a carboxylic acid functional group was selected for co-crystal screening with DL4. Additionally, co-formers containing an amide functional group were investigated. LAG was used as the first stage of co-crystal screening and the results of these experiments informed the choices for the co-precipitation stage. In general 10 mg of DL4 was ground with an equimolar amount of the co-former in the presence of a minimum amount of either methanol or acetonitrile. The results of the experiments (Table 1) indicated that a new phase had been formed between DL4 and adipic acid, citric acid and orotic acid.

Table 1: Co-formers, solvents and experimental outcomes for the LAG experiments with DL4. All experiments were performed using a 1:1 molar ratio of DL4 and the co-former.

Co- former	Solvent	Product
L-(-)-malic acid	Methanol	Physical mixture
Propionamide	Methanol	Physical mixture
Benzamide	Methanol	Physical mixture
Orotic acid	Methanol	New phase
Uric acid	Methanol	Physical mixture
Uracil	Methanol	Physical mixture
Nicotinic acid	Methanol	Physical mixture
L-ascorbic acid	Methanol	Physical mixture
Adipic acid	Methanol	Physical mixture
L-(+)-tartaric acid	Methanol	Amorphous
Isonicotinamide	Methanol	Physical mixture
Citric acid	Methanol	New phase
Propionamide	Acetonitrile	Physical mixture
Benzamide	Acetonitrile	Physical mixture
Uric acid	Acetonitrile	Physical mixture
Uracil	Acetonitrile	Physical mixture
Nicotinic acid	Acetonitrile	Physical mixture
L-ascorbic acid	Acetonitrile	Physical mixture
Adipic acid	Acetonitrile	New phase
L-(+)-tartaric acid	Acetonitrile	Amorphous
Isonicotinamide	Acetonitrile	Physical mixture
Citric acid	Acetonitrile	New phase

Co-precipitation experiments were performed in cases where the results indicated the formation of a new phase. Different solvent systems were used for each combination of DL4 and co-former, but in general equimolar amounts of DL4 and the co-former were dissolved separately in a common solvent. The solutions were combined while stirring and then filtered into a clean vial and allowed to crystallize under ambient conditions. The results are summarised in Table 2.

Table 2: Co-formers, solvents and experimental outcomes for the co-precipitation experiments with DL4. All experiments were performed using a 1:1 molar ratio of DL4 and the co-former.

Co-former	Solvent	Product
Adipic acid	Acetonitrile	Salt
Citric acid	Methanol	Salt
Citric acid	Ethanol	No crystal
Citric acid	Acetonitrile	No crystal
Citric acid	1,4-dioxane	No crystal
Citric acid	Ethyl acetate	No crystal
Orotic acid	Ethanol-water (50:50 v/v)	Salt

DL4ADI: DL4-adipic acid 2:1 salt

LAG and single crystal preparation

10 mg of DL4 and an equimolar amount of adipic acid were ground for 15 minutes with a mortar and pestle while small drops of acetonitrile were added. The product was analysed by PXRD and the results indicated that a new phase had formed. The PXRD traces for DL4, adipic acid and the product from the LAG experiment are shown in Figure 4. New peaks can be seen in the PXRD trace for the product at 2θ positions 6.78, 7.78, 9.03, 11.23, 13.62 and 15.11°. However, there are still peaks in the PXRD trace of the product that coincide with peaks of DL4, indicating that the new phase may not have formed in the 1:1 molar ratio that was employed for the LAG experiment.

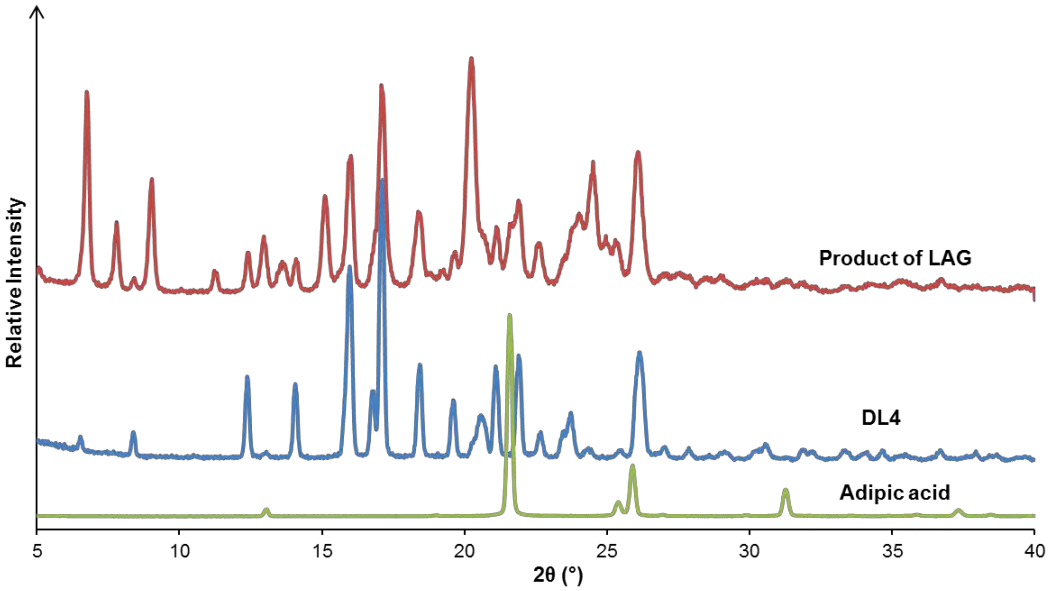

Figure 4: PXRD traces for adipic acid, DL4 and the product of LAG.

Single crystals of the DL4ADI salt were obtained by co-precipitation. 10 mg of DL4 and an equimolar amount of adipic acid were dissolved separately in a minimum amount of acetonitrile with gentle heating (~40 °C). The solutions were combined while stirring and then filtered through a 0.45 µm nylon filter into a clean vial and left on the bench to crystallize. Yellow-brown plate-like crystals appeared within 7 days.

Stoichiometry

Crystals of DL4ADI were dissolved in DMSO-d_6 and analysed using ^{1}H NMR spectroscopy. The spectrum and signal integrations are shown in Figure 5 and Table 3 respectively. The results suggest a 2:1:2 DL4:adipic acid:acetonitrile stoichiometry (the correct stoichiometry was subsequently determined to be 2:1:1:2 DL4 (protonated):adipate ion:adipic acid:acetonitrile).

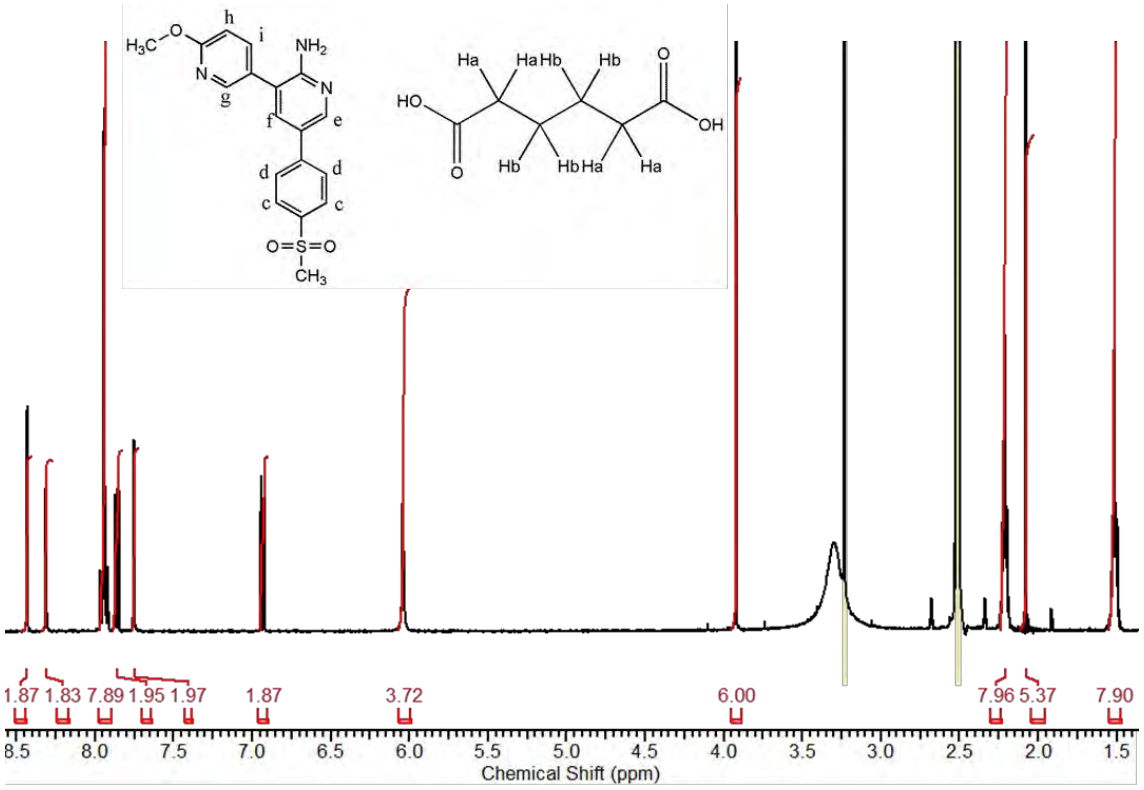

Figure 5: ^{1}H NMR spectrum of DL4ADI in DMSO-d_6.

Table 3: ^{1}H NMR integration for DL4ADI.

Proton	δ (ppm)	Multiplicity	J (Hz)	Integration	Experimental/ Theoretical
C-H_e	8.44	d	2.45	1.87	0.94
C-H_g	8.32	d	2.45	1.83	0.92
C-H_c + C-H_d	7.95	m		7.89	0.99
C-H_i	7.85-7.88	d of d	6.11, 2.45	1.95	0.98
C-H_f	7.75	d	2.45	1.97	0.99
C-H_h	6.94	d	9.29	1.87	0.94
2 x N-H_2	6.04	s (br)		3.72	0.93
3 x O-CH_3	3.92	s		*6.00	1
C-H_b	2.19-2.23	m		7.96	0.50
3 x C-H_3 (acetonitrile)	2.08	s		5.37	0.90
C-H_a	1.50-1.53	m		7.90	0.49

*reference integral

Infrared (IR) Spectroscopy

The IR spectra for DL4ADI and the desolvated form of the salt are shown in Figure 6. The IR spectrum for DL4ADI shows peaks in the range of 1400 –1600 cm^{-1} that correspond to the carboxylate stretching frequency. This suggests that an acid-base reaction had taken place, resulting in the formation of an adipate ion. The peaks associated with the carboxylate stretching frequency are also observed in the spectrum for the desolvated form of DL4ADI, indicating that the "salt-like" nature of the crystal structure was maintained after the solvent had been removed by controlled heating. This demonstrates that it is possible to eliminate the acetonitrile, which does not occur on the GRAS list, whilst leaving the residual salt intact.

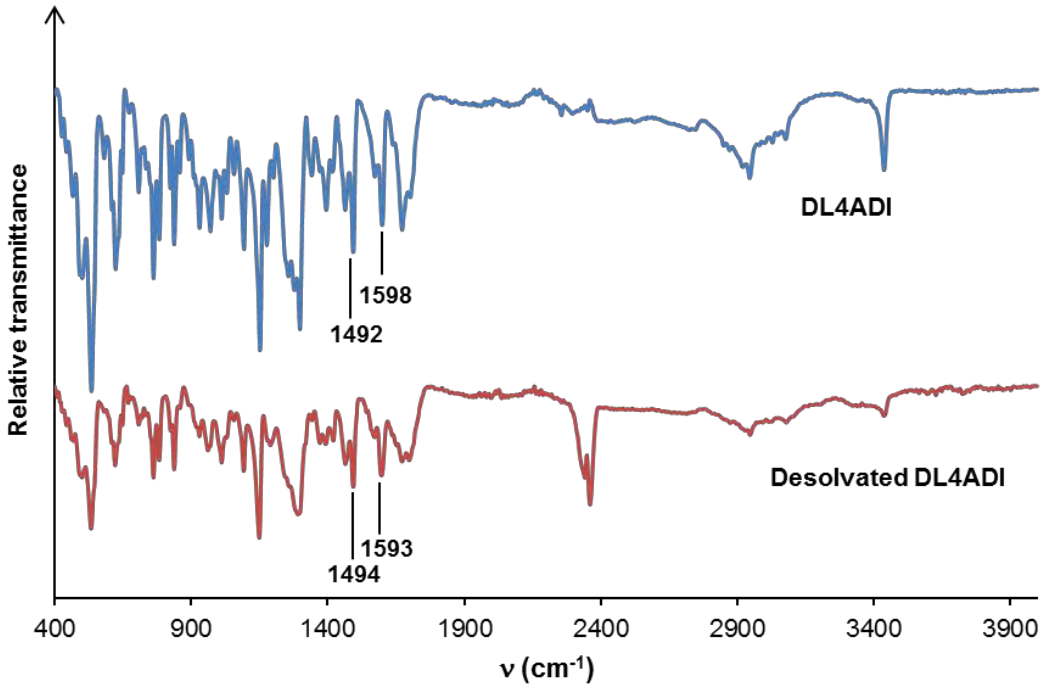

Figure 6: IR spectra for DL4ADI and the desolvated form of DL4ADI.

Thermal analysis

HSM

Representative photographs taken during a HSM experiment are shown in Figure 7. The crystals of DL4ADI were heated at a rate of 10 K min^{-1}. The photograph taken at 104 °C shows the first bubbles starting to appear, indicating the onset of desolvation.

The bubbling becomes more pronounced as the desolvation continues until 112 °C. The crystals start to melt at 108 °C and the entire sample is molten at 112 °C.

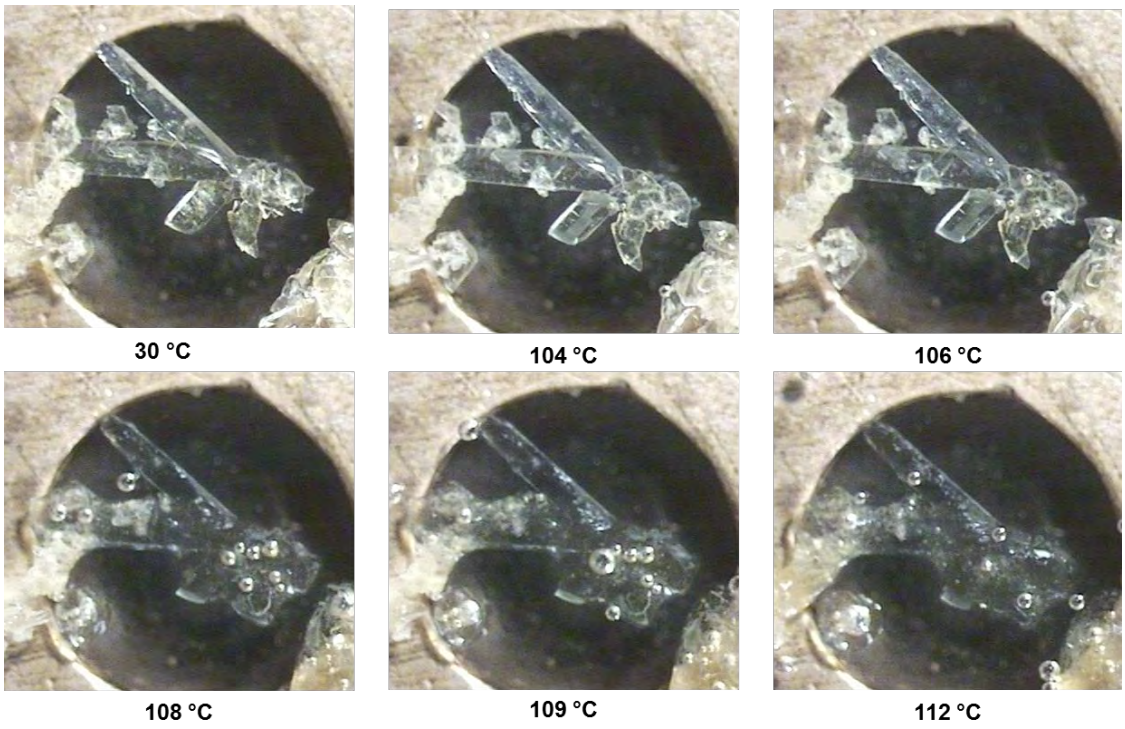

Figure 7: Representative HSM photographs for DL4ADI.

TGA and DSC

The TGA experiment with DL4ADI was performed in triplicate and a representative trace is shown in Figure 8. There is a mass loss of 7.4 ± 0.2% between 93 °C and 150 °C corresponding to the loss of two acetonitrile molecules [calculated 7.6% for a (DL4 cation)$_2$:adipate ion:adipic acid:(acetonitrile)$_2$ composition]. The second mass loss of 26.6 ± 0.3% that occurs between 150 °C and 250°C indicates the onset of decomposition and is most likely due to the loss of two molecules of adipic acid and (calculated 26.8%). Based on the ^{1}H NMR, IR and TGA data the chemical formula for the salt was determined to be $(C_{18}H_{18}N_3O_3S)^+ \bullet ½(C_6H_8O_4)^{2-} \bullet ½(C_6H_{10}O_4) \bullet (C_2H_3N)$.

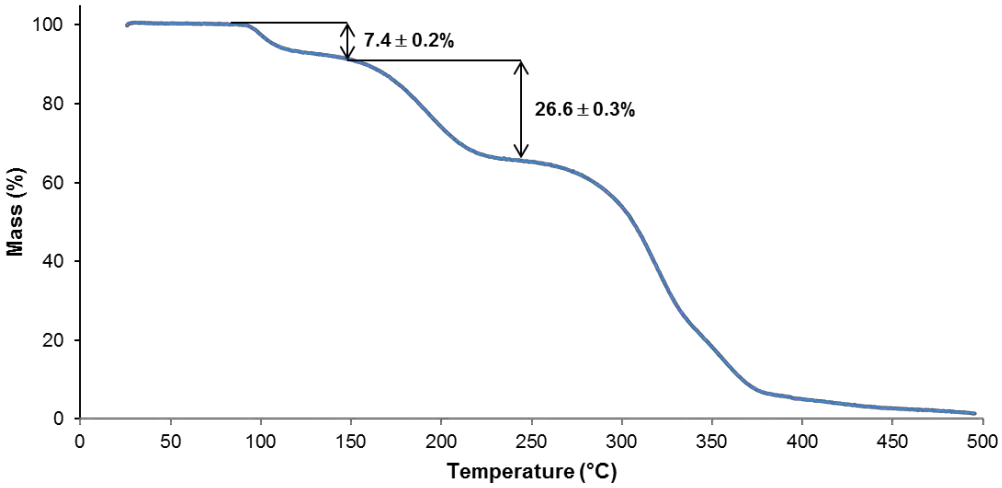

Figure 8: Representative TGA trace for DL4ADI.

The DSC trace seen in Figure 9 shows a sharp endotherm between 94 °C and 103 °C. This endotherm peaks at 97 °C and indicates the fusion of DL4ADI (ΔH_{fus} = 88.2 kJ mol^{-1}). The sample starts to decompose after fusion has occurred.

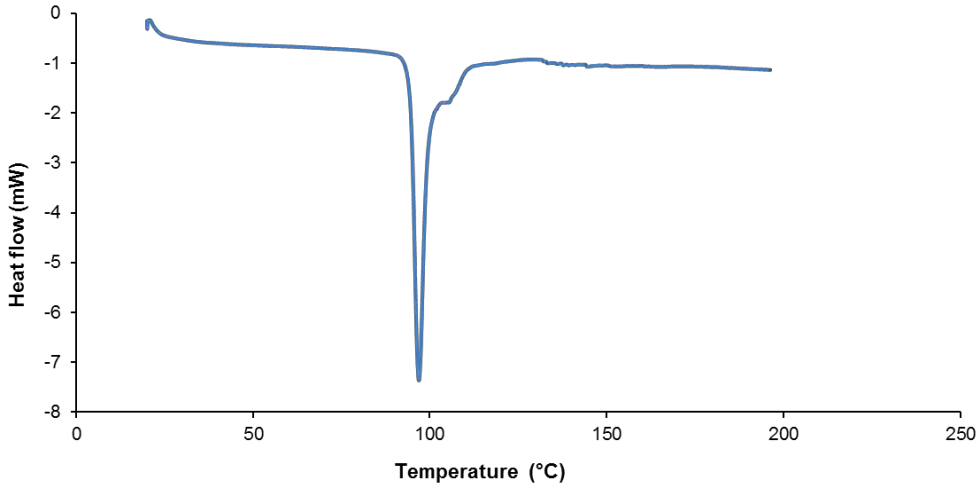

Figure 9: Representative DSC trace for DL4ADI.

Crystal structure analysis

Data-collection and space group determination

Crystal intensity data were collected on a Bruker KAPPA APEX II DUO single crystal X-ray diffractometer. The data were corrected for absorption effects using the program SADABS[4] and Lorentz-polarization corrections were applied using the

program SAINT.[5] The Laue symmetry was found to be $\bar{1}$ indicating the triclinic crystal system and the space group $P\bar{1}$ was identified from the mean $|E^2 - 1|$ parameter value of 1.244 (obtained using the program XPREP)[6] indicating centrosymmetry.

Structure solution and refinement

Crystal and refinement data for DL4ADI are shown in Table 4. The structure was solved by direct methods using program SHELXS-97[7] within the XSEED interface.[8] The structure was refined using full-matrix least-squares with SHELXH-97.[7] All of the ordered non-hydrogen atoms were refined isotropically initially and then anisotropically. All of the hydrogen atoms were initially located in difference Fourier syntheses and they were subsequently placed in idealised positions using a riding model and refined isotropically with U_{iso} in the range 1.2-1.5 times those of their parent atoms. The structure of DL4ADI displayed a high degree of disorder that proved to be challenging to model. Both of the acetonitrile molecules were disordered and after it became evident that applying a disordered model to these molecules would not be feasible, they were refined isotropically. The large residual electron density peak of 1.2 e $Å^{-3}$ is located close to one of the disordered acetonitrile molecules. The phenyl rings in both of the DL4 molecules were also found to be disordered over two orientations and were refined isotropically. The disordered phenyl rings were modelled using part numbers and their site-occupancies were treated as variables and allowed to refine, the major and minor components having s.o.f.s of *x* and *1-x*, *x* being a least-squares variable. The geometry of the disordered phenyl rings was very poor and an attempt to improve it involved imposing FLAT constraints. However, it was not possible to obtain a planar geometry for the phenyl rings. Despite the high degree of disorder, it was nevertheless possible to observe the main features of the structure, namely that it was a salt and not a co-crystal. The hydrogens on both pyridine nitrogen atoms were located in the difference Fourier maps and the CO bond lengths of the adipate ions were all in the range 1.228(6) to 1.290(6) Å, indicating that proton transfer had taken place. Furthermore, the CO bond lengths for the independent adipic acid moieties

were in the range 1.191(6) to 1.212(7) Å for the C=O bonds and 1.309(7) to 1.346(7) Å for the C–O bonds.

One possible reason for the high degree of disorder in the structure could be the effects of collecting the crystal intensity data at low temperature [173(2)K]. It is possible that upon cooling, small differences induced between the original chemical units caused the unit cell contents to double. The two halves of the ASU are practically identical and are related to each other by a translation of ~½ along the *a*-axis (i.e. ~5.3 Å). This doubling effect was also evident when the reflections were viewed using the program Layer[9], which showed strong/weak alternation in the intensities of the reflections in the reciprocal lattice levels *hkl* with $h = 2n$ and $h = 2n+1$ respectively.

Table 4: Data-collection and refinement parameters for DL4ADI.

Molecular formula	$(C_{18}H_{18}N_3O_3S)^+ \bullet ½(C_6H_8O_4)^{2-} \bullet ½(C_6H_{10}O_4) \bullet (C_2H_3N)$
Formula weight (g mol^{-1})	542.66
Crystal system	Triclinic
Space group	$P\bar{1}$
a (Å)	10.529(1)
b (Å)	14.370(2)
c (Å)	18.191(2)
α (°)	88.388(2)
β (°)	88.026(2)
γ (°)	81.527(2)
V (Å)^3	2720.0(5)
Z	4
D_c (g cm^{-3})	1.325
μ (Mo Kα) (mm^{-1})	0.170
F(000)	1144
Data-collection temp. (K)	173(2)
Crystal size (mm^3)	0.08 × 0.19 × 0.30
Range scanned θ (°)	1.1 - 28.4
Index ranges ±*h*, ±*k*, ±*l*	-14, 14 ; -19, 19 ; -24, 24
Reflections (total)	74180
Independent reflections	13602
Reflections with I>2σ(I)	7054
No. of parameters	638
R_{int}	0.058
S	1.10
R_1 [*I*>2σ(*I*)]	0.0976
Reflections omitted	0
wR_2	0.3062
a, b in w = 1/[σ^2(F_o^2)+(aP)^2+(bP)]	0.0949, 9.7998
$(\Delta/\sigma)_{mean}$	<0.001
$\Delta\rho_{min,max}$ (e Å^{-3})	-1.40 and 1.21

Molecular structure

The asymmetric unit of DL4ADI consists of two molecules of DL4 in protonated form, two half adipate ions, two half adipic acid molecules and two molecules of acetonitrile (Figure 10). The two independent cations of DL4 in the asymmetric unit possess a proton that has been fully transferred to each of the nitrogen atoms N15A and N15B (Figure 11). Each independent adipate ion is located on a centre of inversion. The same applies to the adipic acid molecules.

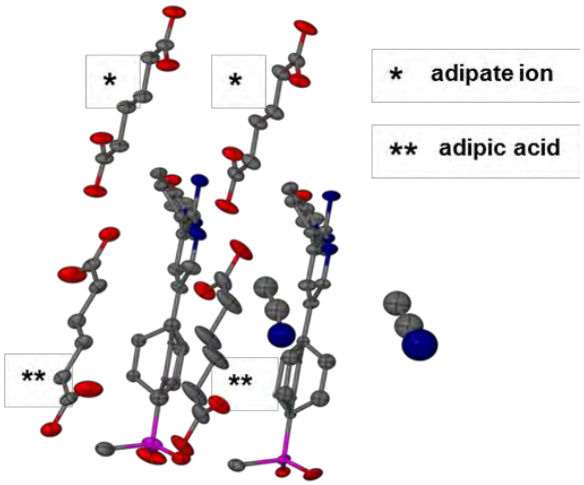

Figure 10: Asymmetric unit (ASU) of DL4ADI showing thermal ellipsoids at the 50% probability level. Hydrogen atoms have been omitted for clarity. The adipate ions and adipic acid molecules are located on centres of inversion and therefore only half of each of these moieties contributes to the ASU.

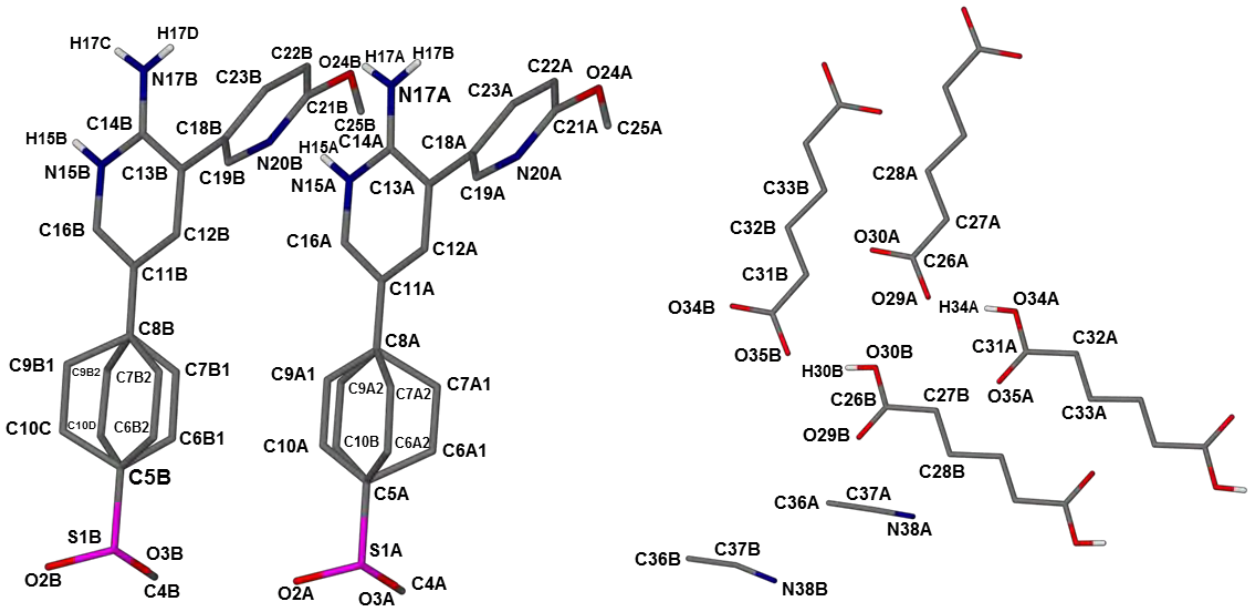

Figure 11: Left: labelling scheme for the two DL4 cations in DL4ADI. Right: labelling scheme for the acetonitrile molecules, adipic acid molecules and adipate ions. Only hydrogens involved in hydrogen bonding interactions have been displayed.

Hydrogen bonding and crystal packing

The N15B–H15A•••O35B and N17B–H17C•••O34B[a] (a = -1+x, y, z) intermolecular hydrogen bonding interactions between the DL4 molecule and the adipate anion generate a $R_2^2(8)$ hydrogen bonded motif (**1** in Figure 12). The N17B–H17D•••O24A[b] (b = 1-x, 1-y, 1-z) and N17A–H17B•••O24B[b] interactions generate a $R_2^2(18)$

hydrogen bonded motif (**2** in Figure 12). The adipic acid molecules and adipate anions are hydrogen bonded to each other via O30B–H30B•••O35B[a] and O34A–H34A•••O29A interactions. The principal hydrogen bonding interactions are listed in Table 5.

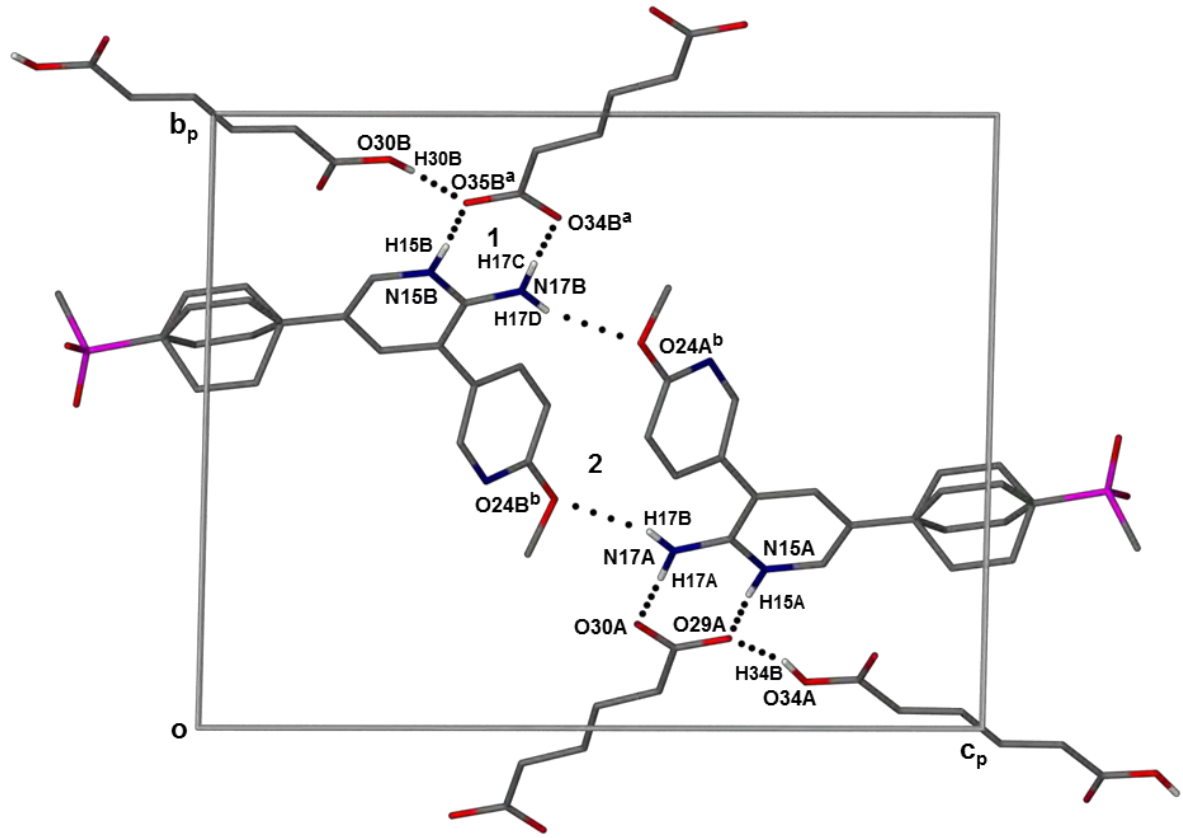

Figure 12: Packing diagram of DL4ADI viewed along [1 0 0] showing the principal hydrogen bonding interactions. Symmetry operators: a = -1+x, y, z; b = 1-x, 1-y, 1-z.

Table 5: Principal hydrogen bonding interactions in DL4ADI.

Interaction	D–H (Å)	H•••A (Å)	D•••A (Å)	D–H•••A (°)
N15A–H15A•••O29A	0.88	1.75	2.613(6)	167
N15B–H15B•••O35B[a]	0.88	1.73	2.597(5)	168
N17A–H17A•••O30A	0.88	1.97	2.834(6)	166
N17A–H17B•••O24B[b]	0.88	2.34	3.051(5)	138
N17B–H17C•••O34B[a]	0.88	1.97	2.832(6)	167
N17B–H17D•••O24A[b]	0.88	2.34	3.041(5)	137
O30B–H30B•••O35B	0.84	1.82	2.636(5)	163
O34A–H34A•••O29A	0.84	1.80	2.629(6)	167

[a]-1+x, y, z; [b]1-x, 1-y, 1-z

Figure 13 shows the packing diagram for DL4ADI viewed along [0 0 1]. The hydrogen bonded motifs pack in layers that straddle the (2 3 0) planes.

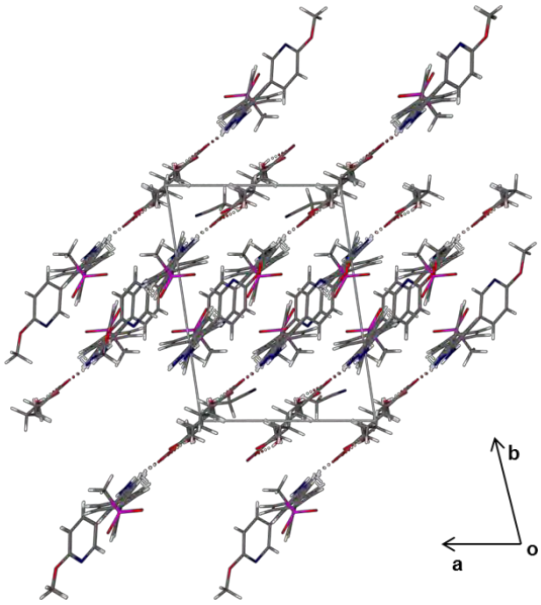

Figure 13: Packing diagram of DL4ADI viewed along [001].

Comparative PXRD

The high level of agreement between the experimental and calculated PXRD traces for DL4ADI (Figure 14) confirms that the single crystal which was analysed is representative of the bulk material. Differences in peak angular positions are due to the different temperatures involved (294 K and 173 K for the experimental and calculated patterns respectively).

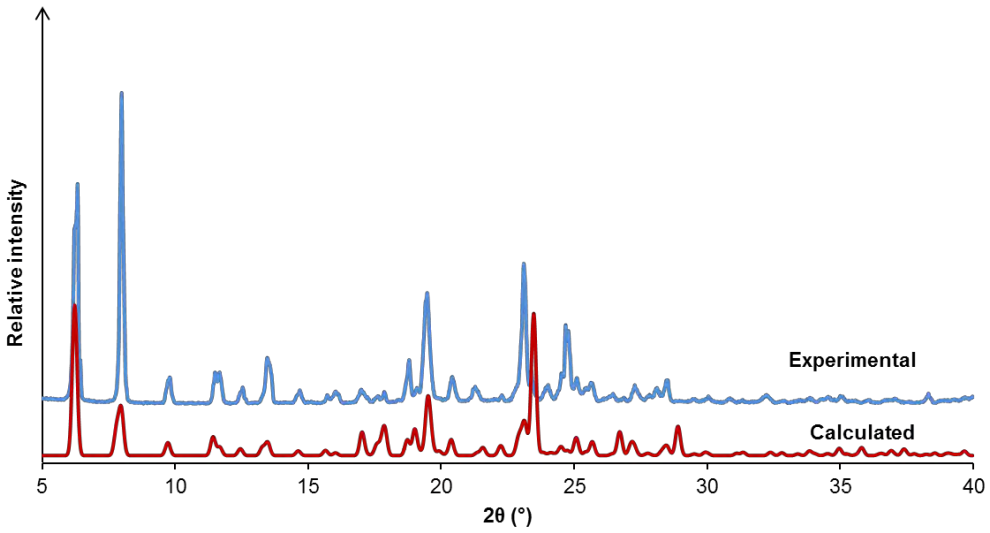

Figure 14: Calculated and experimental PXRD traces for DL4ADI.

Solubility assessment

A semi-quantitative turbidimetric solubility test in phosphate buffer solution (PBS) at 25 ± 0.5 °C was performed with DL4 and DL4ADI according to the method described by Pérez et al.[10] Although this method of solubility testing did not provide a discrete solubility value, it was useful in that the result could be compared with the apparent solubility of the co-crystal between adipic acid and DL4 reported in the literature.[2] Figure 15 is a plot of the average absorbance at 620 nm for three replicates of each sample for a concentration range spanning 20 – 200 µM. The approximate solubility can be defined as the concentration above which there is a significant positive deviation from the baseline. A line that does not deviate from the baseline indicates that no precipitation has occurred and therefore that the solubility is greater than 200 µM.

The results indicate that the apparent solubility of DL4ADI is lower than that of DL4. This is in contrast to the results reported for the co-crystal between adipic acid and DL4, where the co-crystal displayed an apparent solubility greater than that of DL4.

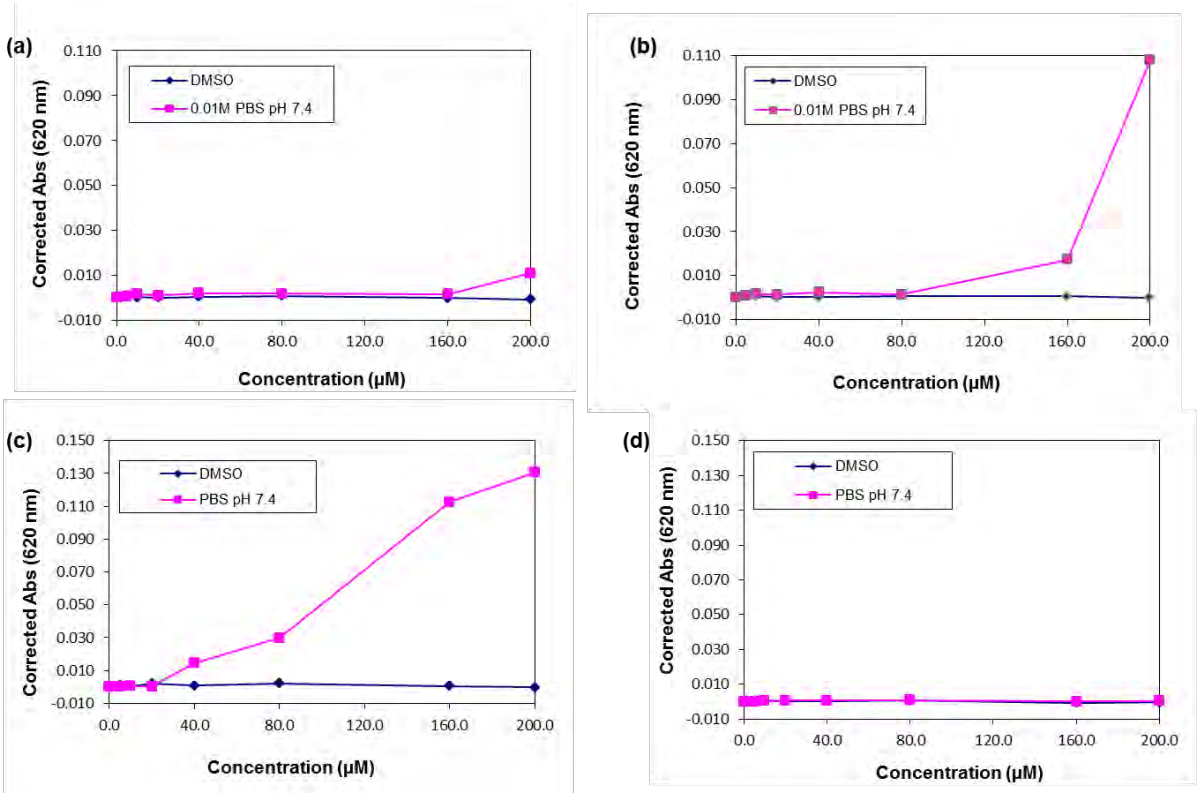

Figure 15: Plot of absorbance versus concentration for (a) DL4, (b) DL4ADI, (c) respirine and (d) hydrocortisone. Resperine and hydrocortisone are standards with known solubilities in PBS.

CITDL4: DL4-citric acid 1:1 salt

LAG and single crystal preparation

10 mg of DL4 was co-ground with an equimolar amount of citric acid for 15 minutes while small drops of either methanol or acetonitrile were added. The products were analysed using PXRD and the traces are shown in Figure 16. The PXRD traces for these products are very similar and clearly different from the component traces. This is a strong indication that the same new phase had formed during both LAG experiments. Single crystals of DL4CIT were obtained from a co-precipitation experiment where 10 mg DL4 and an equimolar amount of citric acid were dissolved separately in ~1 cm^3 of methanol. The solutions were combined while stirring and then filtered through a 0.45 µm nylon filter into a clean vial and left to crystallize on the bench. Crystals appeared after 2-3 weeks.

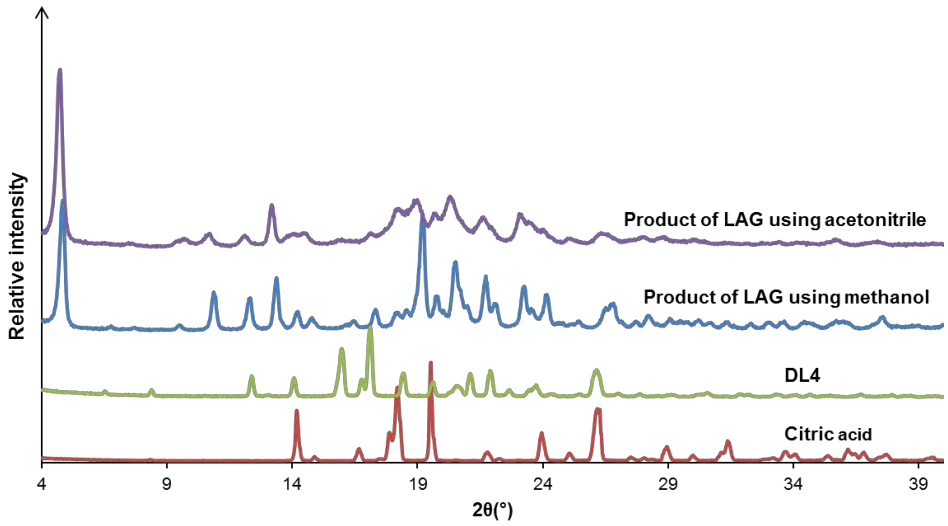

Figure 16: PXRD traces for citric acid, DL4, the product of LAG using methanol and the product of LAG using acetonitrile.

Stoichiometry

Crystals of DL4CIT were dissolved in DMSO-d_6 and analysed using ^{1}H NMR spectroscopy (Figure 17). The proton signals were integrated (Table 6) and the results confirmed the DL4:citric acid stoichiometry to be 1:1.

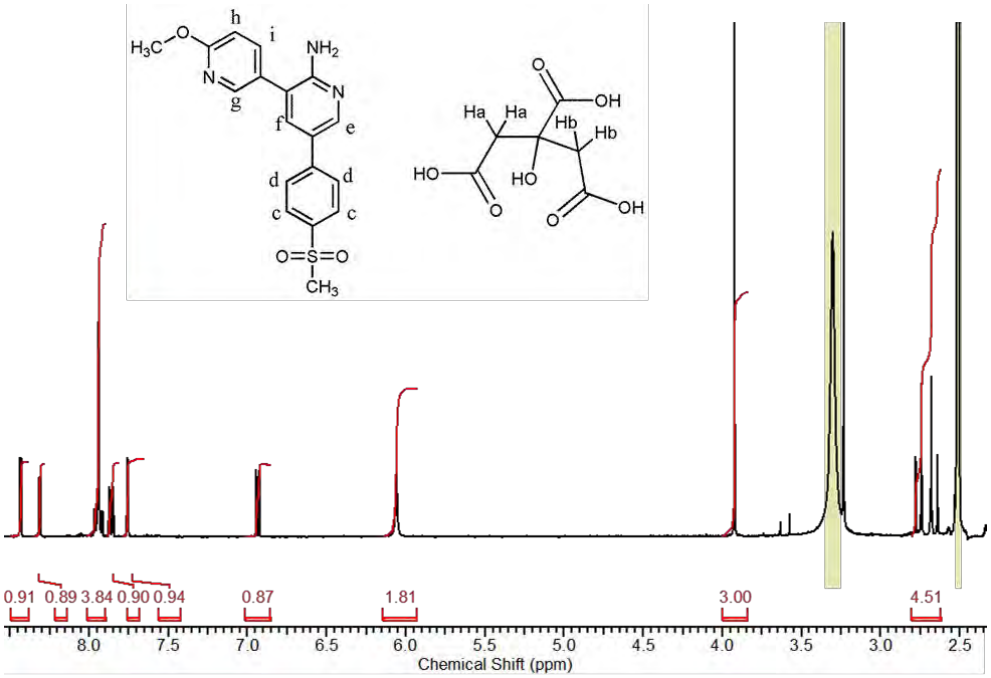

Figure 17: ^{1}H NMR spectrum of DL4CIT in DMSO-d_6.

Table 6: ^{1}H NMR integration for DL4CIT.

Proton	δ (ppm)	Multiplicity	J (Hz)	Integration	Experimental/ Theoretical
C-H_e	8.44-8.43	d	2.45	0.91	0.91
C-H_g	8.31	d	3.18	0.89	0.89
C-H_c + C-H_d	7.92-7.97	m		3.84	0.96
C-H_i	7.85-7.88	d of d	2.69, 5.87	0.90	0.90
C-H_f	7.76	d	2.45	0.94	0.94
C-H_h	6.92-6.95	d	9.29	0.87	0.87
2 x N-H_2	6.06	s (br)		1.81	0.91
O-CH_3	3.92	s		*3.00	1.00
H_a + H_b	2.64-2.78	q	15.41, 24.7	4.51	1.13

*reference integral

IR Spectroscopy

The IR spectrum of DL4CIT (Figure 18) provided evidence for the formation of a salt between citric acid and DL4. The peaks at 1421, 1492 and 1589 cm^{-1} are characteristic of the carboxylate stretching frequency, indicating that a proton has been transferred from the citric acid molecule to the DL4 molecule.

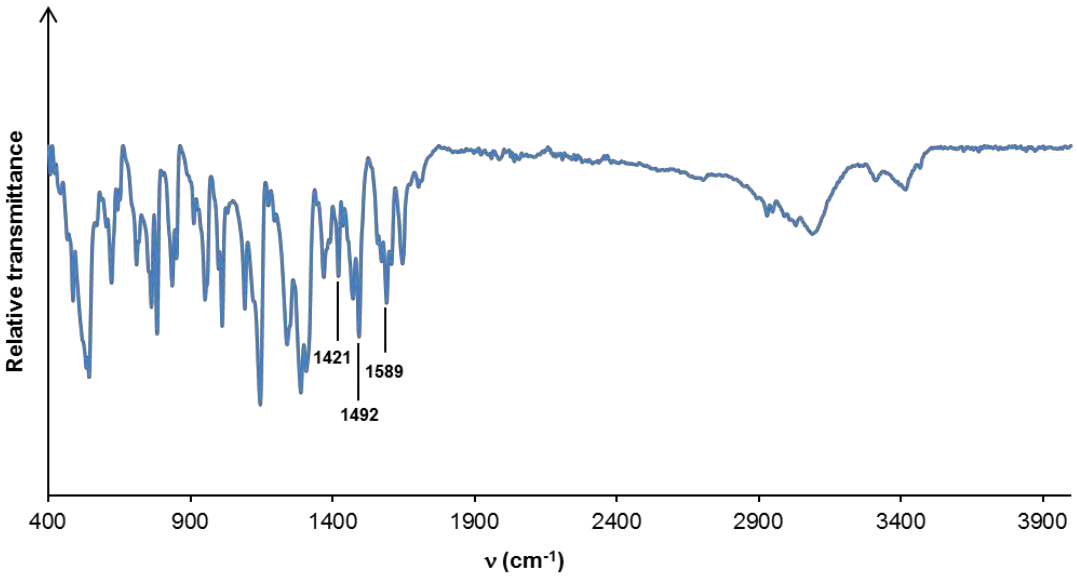

Figure 18: IR spectrum of DL4CIT.

Thermal analysis

HSM

The representative HSM photographs for DL4CIT are shown in Figure 19. Crystals of DL4CIT were heated at 10 K min^{-1}. The photograph recorded at 152 °C shows small bubbles appearing and this can be attributed to the loss of solvent. The bubbling continues until the sample melts at 169 °C.

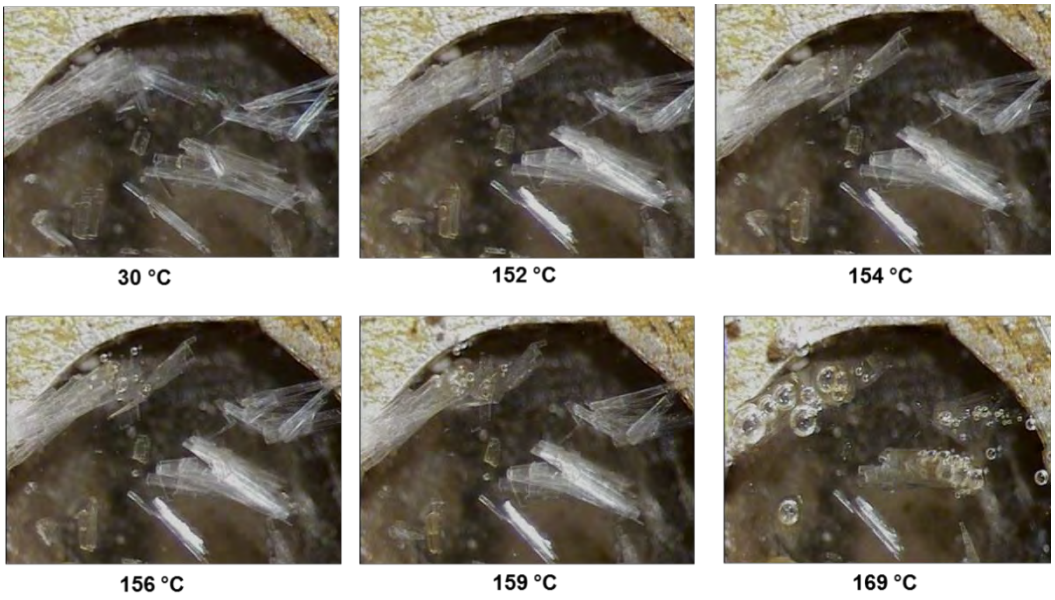

Figure 19: Representative HSM photographs of DL4CIT.

TGA and DSC

TGA was used to quantify the water content of DL4CIT. The TGA trace (Figure 20) shows an average mass loss of 3.2 ± 0.2% (n = 3) between 50 °C and 70 °C. This is consistent with the loss of one water molecule per ASU (calculated 3.2% for a 1:1:1 DL4:citric acid:water composition). Based on the ^{1}H NMR, IR and TGA data, the chemical formula for the salt was determined to be $(C_{18}H_{18}N_3O_3S)^{+}\bullet(C_6H_8O_7)^{-}\bullet(H_2O)$.

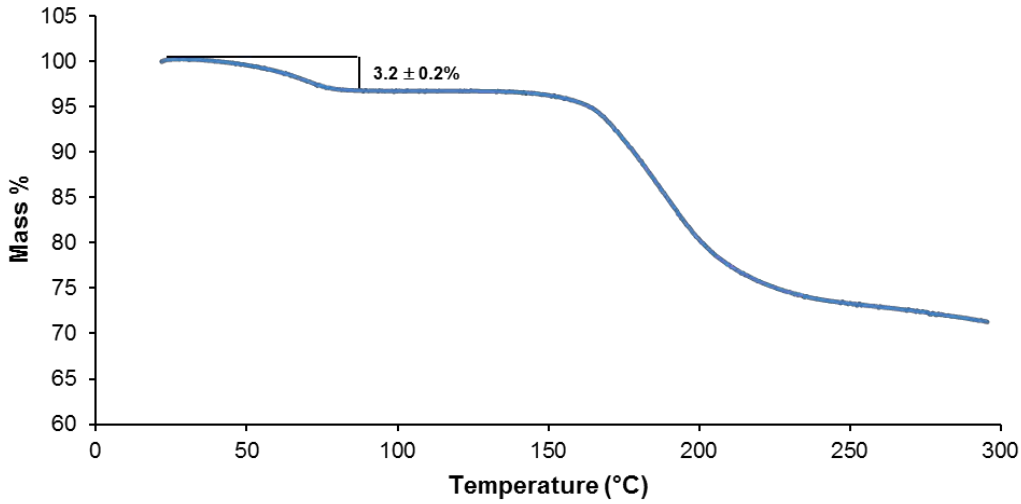

Figure 20: TGA trace for DL4CIT.

The DSC trace of DL4CIT (Figure 21) shows a broad endotherm spanning the temperature range 40 – 80 °C, which corresponds to dehydration. The endotherm between 153 °C and 165°C (peak 160°C) indicates the melting of the salt. ΔH_{fus} was estimated to be approximately 34.1 kJmol^{-1}, but this value is compromised by the fact that the baseline becomes very erratic with the onset of decomposition.

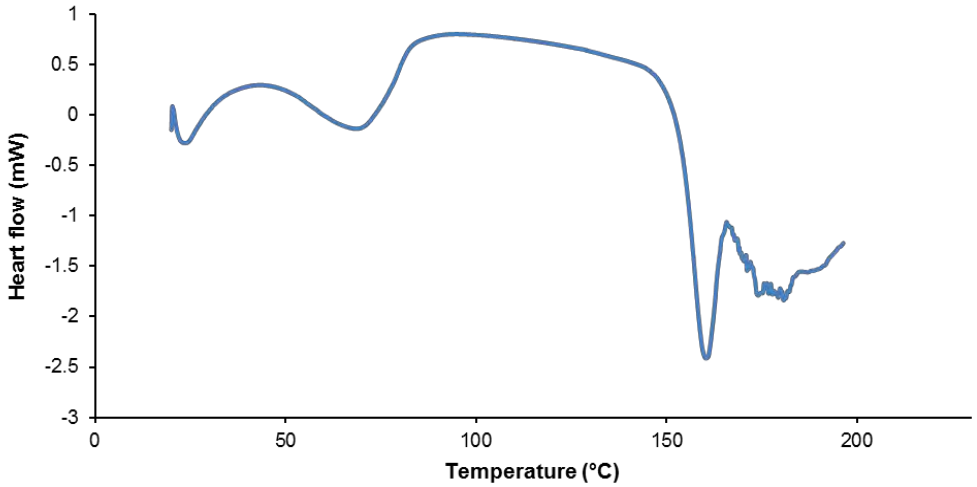

Figure 21: DSC trace for DL4CIT.

Crystal structure analysis

Data-collection and space group determination

Crystal intensity data were collected on a Bruker KAPPA APEX II DUO single crystal X-ray diffractometer. Lorentz-polarization corrections were applied using the program SAINT[5] and the data were corrected for absorption effects using the program SADABS.[4] The crystal system was found to be triclinic and the $|E^2 - 1|$ value of 0.951 obtained using the program XPREP[6] confirmed the space group as $P\ \bar{1}$.

Structure solution and refinement

The structure of DL4CIT was solved by direct methods using program SHELXS-97,[7] revealing all of the non-hydrogen atoms in DL4 and citric acid. These atoms were placed and following their refinement with isotropic thermal parameters they were refined anisotropically using SHELXH-97.[7] The difference Fourier maps revealed a hydrogen atom on the pyridine nitrogen atom of the DL4 molecule, indicating that a salt had been formed. Furthermore, the C–O bond lengths of one of the carboxyl groups on the citric acid moiety were found to be 1.260(2) Å and 1.249(2) Å, confirming the presence of a carboxylate ion and hence indicating that a proton transfer had taken place. All of the hydrogen atoms were located in difference Fourier syntheses and were placed in idealised positions using a riding model and refined isotropically with U_{iso} values 1.2 – 1.5 times those of their parent atoms. The difference Fourier maps revealed a large electron density peak that was initially attributed to the oxygen atom of one water molecule, as confirmed by TGA. Following several refinement cycles, however, it became clear that the oxygen atom was disordered over several positions and could not be modelled appropriately. Therefore, the tentative water oxygen components of the disordered O atom were deleted from the model and a new intensity data file (.hkl) was calculated using the SQUEEZE tool in the program PLATON.[11] SQUEEZE determines the contribution of the disordered water molecule to the intensities, which means that the intensity values in the new .hkl file would be adjusted to reflect the contribution from the water molecule. SQUEEZE also calculates the void accessible volume in the structure and

integrates the electron density in the void to give an electron count which can be used to quantify the solvent. The solvent accessible void was found to be 94.7 $Å^3$ and the electron density integrated for 32 electrons per unit cell. Z is 2 and therefore the electron count for the asymmetric unit would be 16, which corresponds to about 1.5 water molecules. Although there is a discrepancy between the number of water molecules determined using TGA and the number estimated from the electron count (1 and 1.5 respectively), more weight was accorded to the consistent estimate of water content using the TGA technique. After using the SQUEEZE tool, the structure was refined against the set of modified intensity data. The data-collection and refinement parameters for DL4CIT are shown in Table 7.

Table 7: Data-collection and refinement parameters for DL4CIT.

Molecular formula	$(C_{18}H_{18}N_3O_3S)^+•(C_6H_7O_7)^-$
Formula weight (g mol^{-1})	547.54
Crystal system	Triclinic
Space group	$P\bar{1}$
a (Å)	5.0688(4)
b (Å)	13.576(1)
c (Å)	18.955(2)
α (°)	82.164(2)
β (°)	85.900(2)
γ (°)	83.068(2)
V $(Å)^3$	1283.5(2)
Z	2
D_c (g cm^{-3})	1.417
μ (Mo Kα) (mm^{-1})	0.188
F(000)	572
Data collection temp. (K)	173(2)
Crystal size (mm^3)	0.05 × 0.14 × 0.45
Range scanned θ (°)	3.0 – 27.9
Index ranges ±*h*, ±*k*, ±*l*	-6, 6; -17, 17; -24, 24
Reflections (total)	21963
Independent reflections	6115
Reflections with I>2σ(I)	4968
No. of parameters	350
R_{int}	0.029
S	1.05
R_1 [*I*>2σ(*I*)]	0.0391
Reflections omitted	10
wR_2	0.1051
a, b in w = $1/[\sigma^2(F_o^2)+(aP)^2+(bP)]$	0.0571, 0.2609
$(\Delta/\sigma)_{mean}$	<0.01
$\Delta\rho_{min,max}$ (e $Å^{-3}$)	-0.32, 0.41

Molecular structure

The asymmetric unit (ASU) and labelling scheme of DL4CIT are shown in Figure 22. The ASU consists of one molecule of DL4 that has been protonated at N15 and one citrate ion that has been deprotonated.

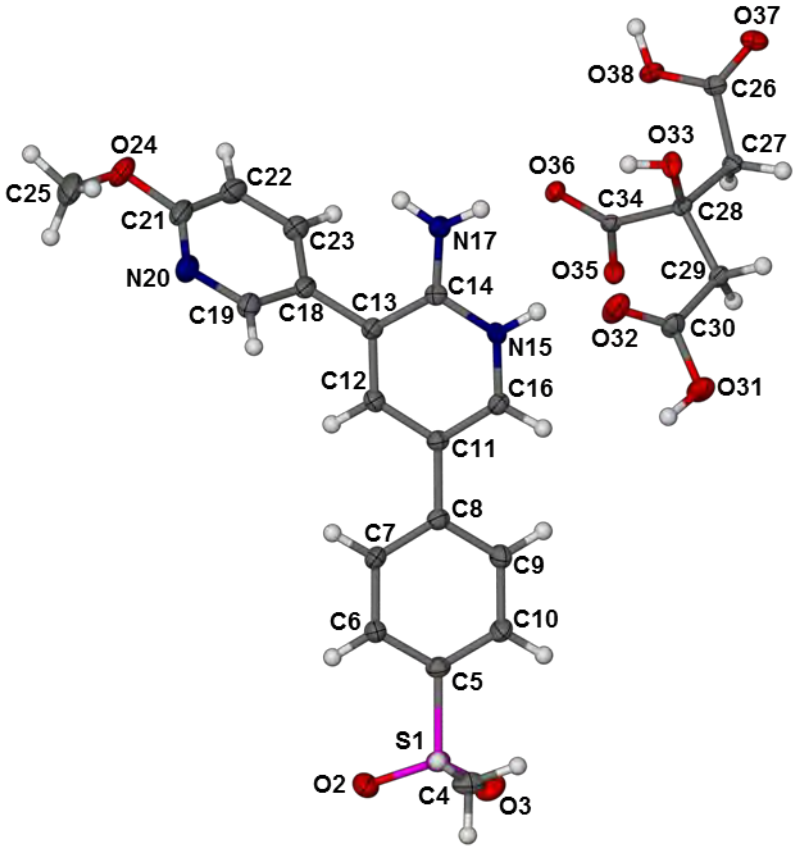

Figure 22: Asymmetric unit of DL4CIT showing thermal ellipsoids at the 50% probability level.

Crystal packing and hydrogen bonding

The principal hydrogen bonding interactions in DL4CIT are shown in Figure 23 and the corresponding bond lengths and angles are listed in Table 8. The N15–H15•••O35 and N17–H17A•••O36 interactions between the DL4 cation and the citrate anion generate a $R_2^2(8)$ hydrogen bonding motif (**1**). The three interactions N17–H17A•••O36, N17–H17B–O37^a (a = 2-x, 2-y, 1-z) and O38^a–H38•••O36 between the DL4 cation and the citrate anion form a hydrogen bonding motif (**2**) with graph-set notation $R_3^2(8)$. The citrate anions interact via the O31–H31•••O32^a hydrogen bond and the centre of inversion at 0, ½, ½ generates a hydrogen bonded

dimer (**3**) with graph-set notation $R_2^2(8)$. There is also an O33–H33•••O36 intramolecular hydrogen bonding interaction in the citrate anion.

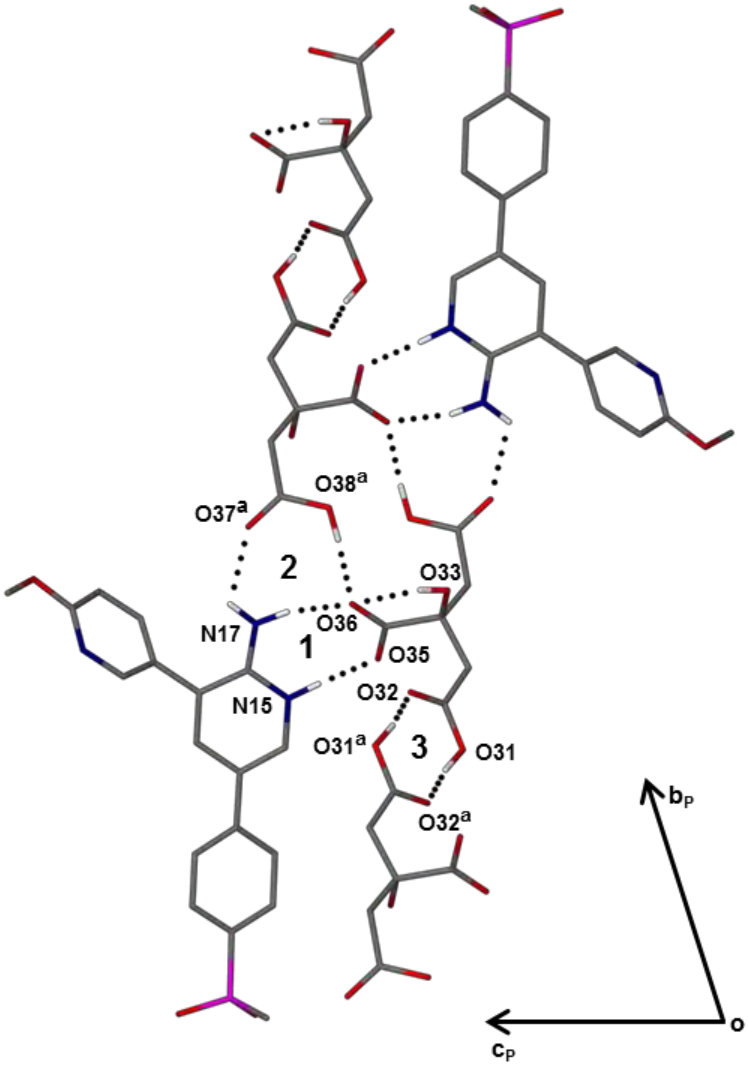

Figure 23: Hydrogen bonding interactions in DL4CIT (Only the H atoms relevant in principal H-bonding have been included). Symmetry operator: a = 2-x, 2-y, 1-z.

Table 8: Principal hydrogen bonding interactions in DL4CIT.

Interaction	D–H (Å)	H•••A (Å)	D•••A (Å)	D–H•••A (°)
N15–H15•••O35	0.88	1.74	2.614(2)	172
N17–H17A•••O36	0.88	2.00	2.806(2)	152
N17–H17B•••O37[a]	0.88	2.35	2.860(2)	117
O31–H31•••O32[a]	0.95	1.67	2.608(2)	167
O38[a]–H38•••O36	0.90	1.81	2.708(1)	174
O33–H33•••O35[b]	0.83	2.06	2.823(1)	152
O33–H33•••O36	0.83	2.27	2.708(1)	113

[a] 2-x,1-y,1-z; [b] 1+x, y, z

When viewed down [0 1 0] the asymmetric units in DL4CIT display a zig-zag packing arrangement (Figure 24).

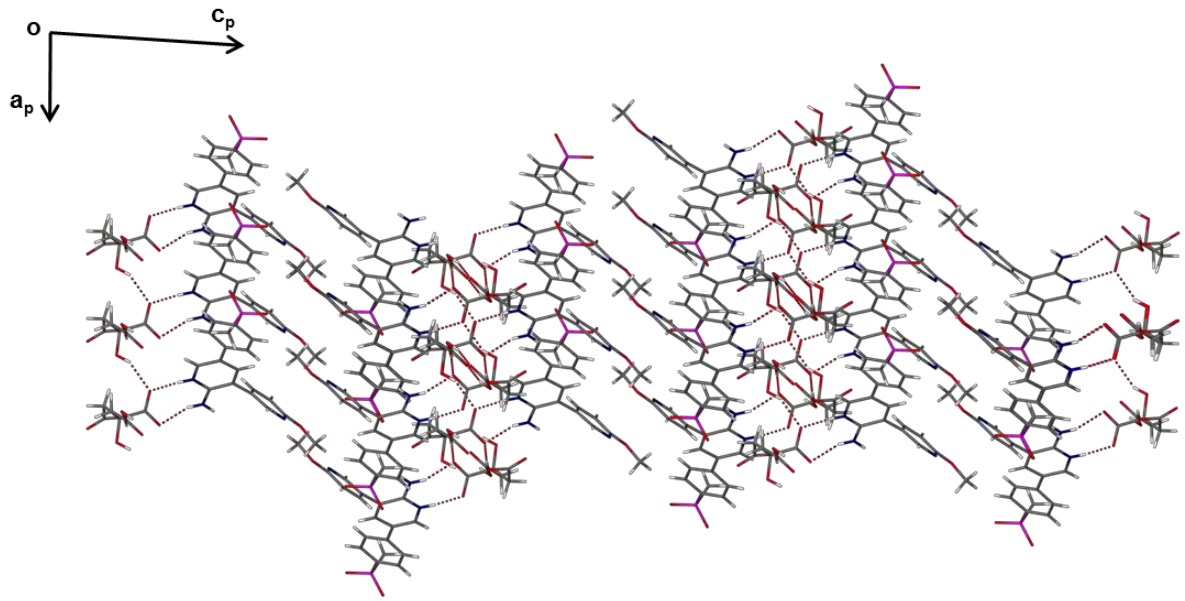

Figure 24: Packing diagram of DL4CIT viewed along [0 1 0].

Comparative PXRD

The experimental and calculated PXRD traces for DL4CIT are shown in Figure 25. The traces are practically identical, confirming that the single crystal that was analysed is representative of the bulk material.

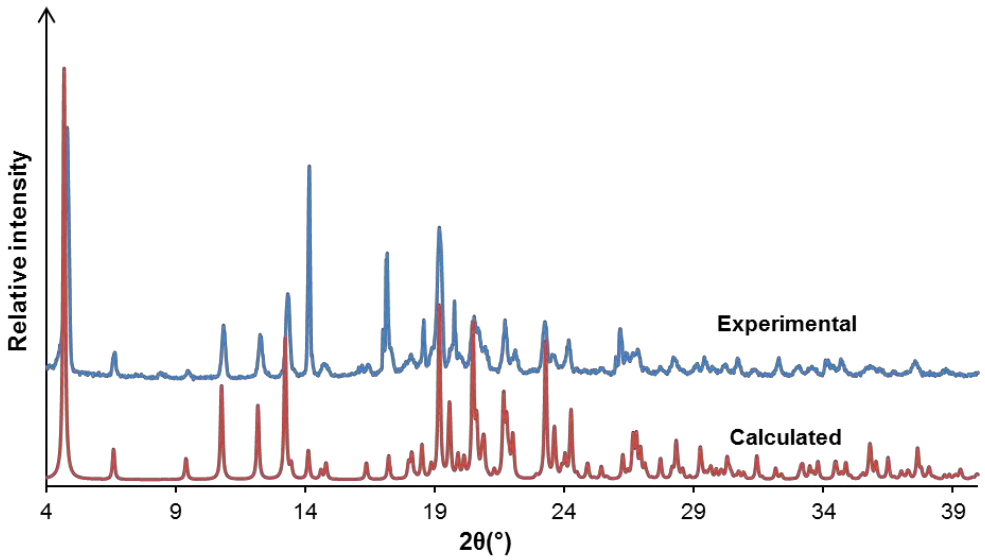

Figure 25: Calculated and experimental PXRD traces for DL4CIT.

Solubility assessment

DL4CIT could be prepared by LAG, which proved to be a quick and easy method of scaling up the material for solubility analysis. Values for the equilibrium solubility of DL4 and DL4CIT were obtained using the methodology described in Chapter 2. Excess amount of material was added to 5 cm^3 of a 1% ethanol-water (v/v) solution with stirring at constant temperature (25 ± 0.5 °C). After 72 hours the solutions were filtered and the concentration of DL4 was determined using UV-visible spectroscopy. The values for the apparent solubility of DL4 and DL4CIT were found to be 0.033 mM and 1.61 mM respectively and were based on triplicate measurements. The results demonstrate that the citrate salt form of DL4 had an apparent solubility that was 48 times greater than that of untreated DL4.

DL4ORO: DL4-orotic acid 1:1 salt

LAG and single crystal preparation

The LAG experiment between DL4 and orotic acid resulted in a product with a PXRD trace as shown in Figure 26. There are prominent new peaks that emerge in the trace of the product between 2θ-positions 7.6° and 15.2°. This gave strong evidence that a new phase had resulted from the LAG experiment. Single crystals were prepared by co-precipitation using a 50% ethanol-water (v/v) mixture. A mixed solvent system was required, because orotic acid is insoluble in common organic acids, but sparingly soluble in water at 25 °C while DL4 is soluble in ethanol, but insoluble in water. The components were each dissolved separately in 1 cm^3 of 50% ethanol-water (v/v) at elevated temperature (~50 °C). The solutions were combined while stirring and filtered through a 0.45 µm nylon filter into a clean vial. The vial was left uncapped on the benchtop and needle-like crystals with a slightly yellow colour appeared after 4-6 days. The vial was sealed after the crystals appeared.

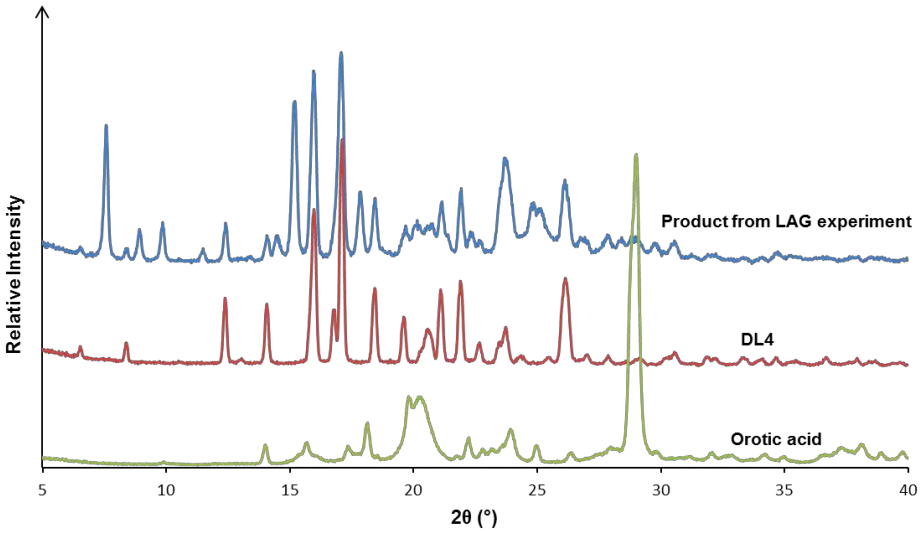

Figure 26: PXRD traces for orotic acid, DL4 and the product of the LAG experiment with DL4 and orotic acid.

Stoichiometry

Crystals of DL4ORO were dissolved in DMSO-d_6 and analysed using ^{1}H NMR spectroscopy. The partial spectrum and integration of the proton signals are shown in Figure 27 and Table 9. H_h in DL4 was used as a reference integral and set to 1.00. The proton signal for H_a in orotic acid integrated for 1.06, indicating a 1:1 DL4: orotic acid stoichiometry.

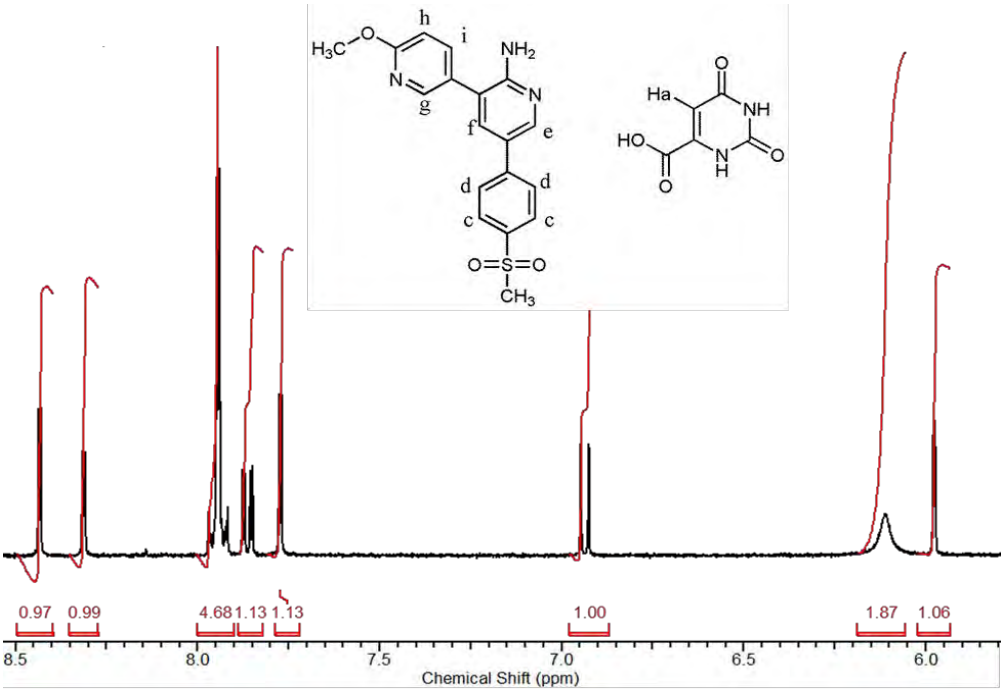

Figure 27: Partial ^{1}H NMR spectrum of DL4ORO.

Table 9: ^{1}H NMR integration for DL4ORO.

Proton	δ (ppm)	Multiplicity	J (Hz)	Integration	Experimental/ Theoretical
C-H_e	8.44-8.43	d	2.45	0.97	0.97
C-H_g	8.31	d	2.45	0.99	0.99
C-H_c + C-H_d	7.92-7.97	m		4.68	1.2
C-H_i	7.85-7.88	d of d	2.45, 6.11	1.13	1.1
C-H_f	7.78	d	2.45	1.13	1.1
C-H_h	6.92-6.95	d	8.56	*1.00	1.00
2 x N-H_2	6.11	s (br)		1.87	0.94
C-H_a	5.98	d	1.96	1.06	1.1

*reference integral.

IR spectroscopy

There are sharp peaks in the IR spectrum of DL4ORO (Figure 28) associated with the carboxylate stretching (1409, 1486 and 1596 cm^{-1}). This indicates that an acid-base reaction occurred between DL4 and orotic acid and that the product is therefore a salt and not a co-crystal.

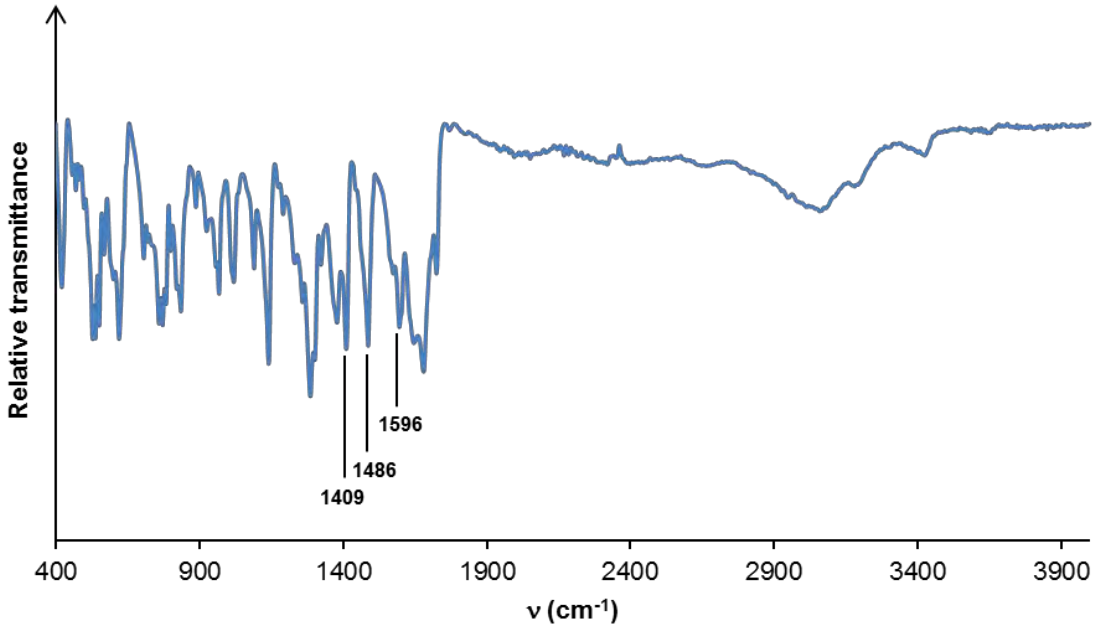

Figure 28: IR spectrum of DL4ORO.

Thermal analysis

HSM

Representative HSM photographs for DL4ORO are shown in Figure 29. The crystals start to change colour at 160 °C and melting occurs concurrently with decomposition as can be seen in the photographs taken at 244 °C and 250 °C.

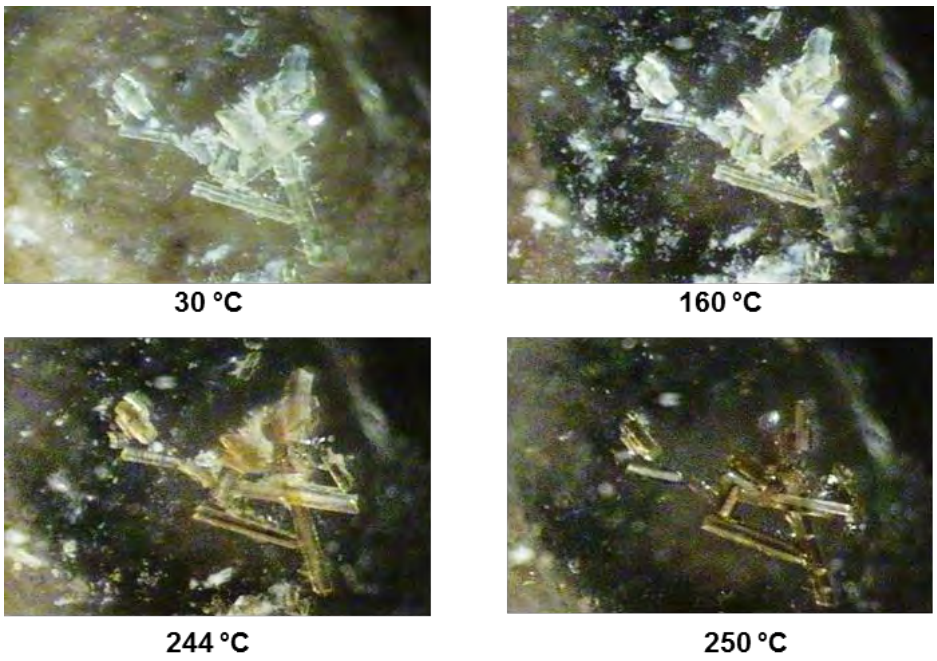

Figure 29: Representative HSM photographs of DL4ORO.

TGA and DSC

The TGA trace for DL4ORO (Figure 30) shows a mass loss of 0.4 ± 0.1% (n = 2) between 30 °C and 50 °C. This is consistent with the loss of 0.11 – 0.12 water molecules (calculated 0.4% for a 1:1:0.11 DL4:orotic acid:water composition). The onset of decomposition occurs at 231 °C and this is consistent with the thermal events observed during the HSM experiment. The second mass loss of 30.7% between 260 °C and 286 °C is attributed to the loss of the orotic acid molecule (calculated 30.4%).

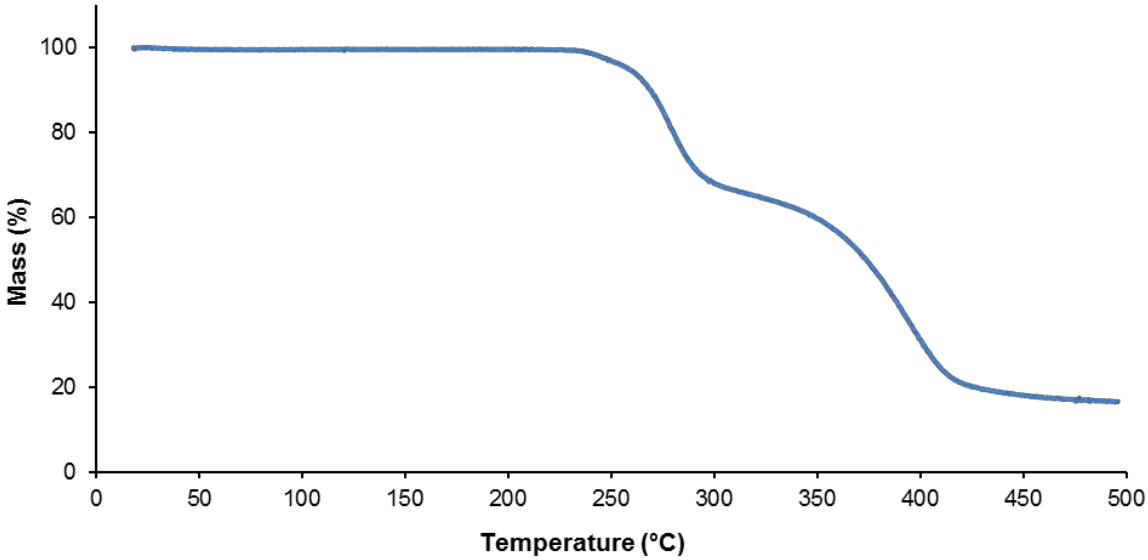

Figure 30: TGA trace for DL4ORO.

The DSC trace for DL4ORO (Figure 31) shows an endotherm spanning the temperature range 235 – 249 °C (peak 243 °C) corresponding to the melting of the salt (ΔH_{fus} = 55.0 kJ mol^{-1}). There is an exotherm that occurs immediately after fusion and this is attributed to the decomposition of DL4ORO. The estimated value of ΔH_{fus} is compromised by the shift in the baseline caused by this exotherm.

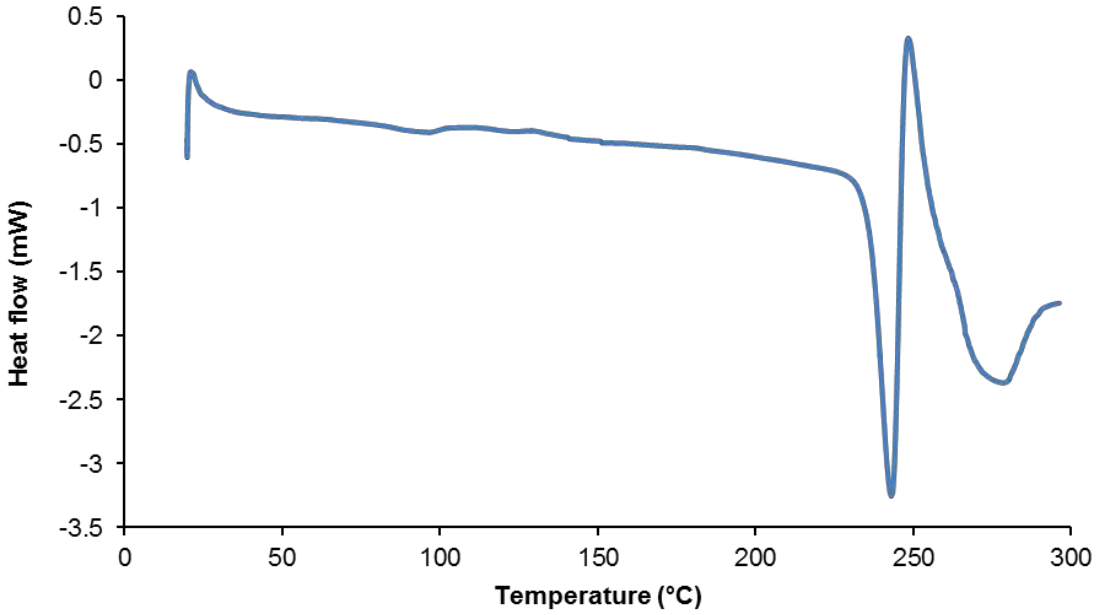

Figure 31: DSC trace for DL4ORO.

Crystal structure analysis

Data-collection and space group determination

Crystal intensity data were collected on a Bruker KAPPA APEX II DUO single crystal X-ray diffractometer. Lorentz-polarization corrections were applied using the program SAINT[5] and the data were corrected for absorption effects using the program SADABS.[4] The Laue symmetry was found to be 2/m indicating the monoclinic crystal system and the space group $P2_1/c$ was identified from the systematic absences.

Structure solution and refinement

The structure of DL4ORO was solved by direct methods using program SHELXS-97,[7] revealing all of the non-hydrogen atoms in DL4 and orotic acid. Following isotropic refinement, these atoms were refined anisotropically using SHELXH-97.[7] Following location of H atoms in difference Fourier syntheses, they were placed in idealised positions using a riding model and were refined isotropically with U_{iso} values 1.2 – 1.5 times those of their parent atoms. The hydrogen on the pyridine nitrogen of DL4 was located in the difference Fourier map, indicating the formation of a salt. The CO bond lengths in the co-former were found to be 1.241(2) and 1.252(2) Å, also consistent with a proton transfer between DL4 and orotic acid. Data-collection and refinement parameters for DL4ORO are listed in Table 10. The difference Fourier maps revealed a low electron density peak that was assumed to be a partially occupied oxygen atom, which was located within hydrogen bonding distance of the orotate ion. As indicated above, TGA had shown a mass loss of 0.4 ± 0.1% (n = 2), confirming the presence of 0.11 water molecules. The oxygen atom was thus assigned a site-occupancy factor of 0.11 and refined isotropically (final value: U_{iso} = 0.058 Å^2).

Table 10: Data-collection and refinement parameters for DL4ORO.

Molecular formula	$(C_{18}H_{18}N_3O_3S)^+ \bullet (C_5H_3N_2O_4)^+ \bullet (H_2O)_{0.11}$
Formula weight (g mol^{-1})	513.49
Crystal system	Monoclinic
Space group	$P2_1/c$
a (Å)	4.7043(4)
b (Å)	12.237(1)
c (Å)	39.836(3)
α (°)	90
β (°)	92.999(2)
γ (°)	90
V (Å)^3	2290.1(3)
Z	4
D_c (g cm^{-3})	1.489
μ (Mo Kα) (mm^{-1})	0.199
F(000)	1068
Data collection temp. (K)	173(2)
Crystal size (mm^3)	0.10 × 0.10 × 0.36
Range scanned θ (°)	1.7 – 27.6
Index ranges ±*h*, ±*k*, ±*l*	-6, 5; -15, 15; -51, 51
Reflections (total)	34880
Independent reflections	5294
Reflections with I>2σ(I)	4306
No. of parameters	331
R_{int}	0.040
S	1.03
R_1 [*I*>2σ(*I*)]	0.0383
Reflections omitted	2
wR_2	0.0969
a, b in w = 1/[σ^2(F_o^2)+(aP)^2+(bP)]	0.0435, 0.981
$(\Delta/\sigma)_{mean}$	<0.01
$\Delta\rho_{min,max}$ (e Å^{-3})	-0.40, 0.30

Molecular structure

The asymmetric unit and labelling scheme for DL4ORO are shown Figure 32. The ASU consists of one molecule of DL4 that has been protonated at N15 and one orotate anion. There is also a partial oxygen atom (O1W) attributed to the 0.11 molecules of water. Due to the low occupancy of the water oxygen atom, no attempt was made to place H atoms on the partial water molecule.

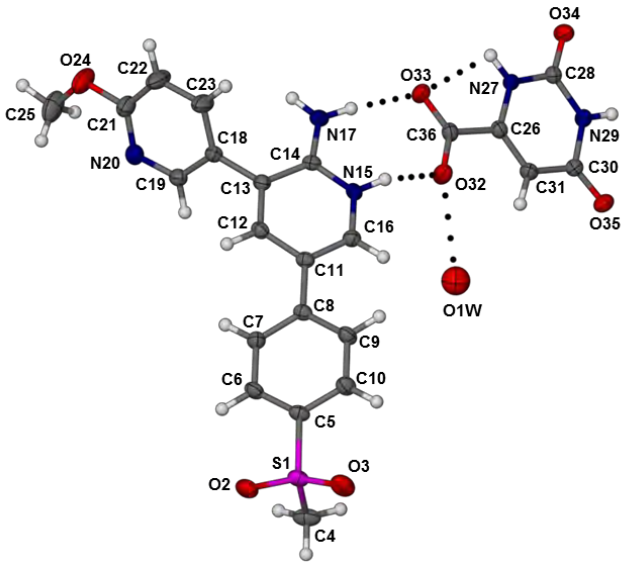

Figure 32: Asymmetric unit of DL4ORO showing thermal ellipsoids at the 50% probability level.

Crystal packing and hydrogen bonding

There is a $R_2^2(8)$ hydrogen bonding motif (**1** in Figure 33) that is generated by the N15–H15•••O32 and N17–H17A•••O33 interactions between the DL4 cation and the orotate anion. There is also a $R_3^2(8)$ hydrogen bonding motif (**2**) resulting from the N17–H17B•••O34[a] (a = -1-x, ½+y, ½-z), N27–H27•••O35[a] and N17–H17A•••O33 interactions. The orotate anions form $R_2^2(9)$ hydrogen bonded dimers (**3**) via the N27–H27•••O35[a] and N29–H29•••O33[b] (b = -1-x, -½+y, ½-z) interactions. The principal hydrogen bonding interactions are listed in Table 11. The partially occupied water molecule forms a strong hydrogen bonding interaction with the orotate ion, as evidenced by the O1W•••O32 distance of 2.89(2) Å. The O1W•••O24[c] (c = x, -1+y, z) and O1W•••O24[d] (d = 1+x, -1+y, z) distances are 3.06(2) Å and 3.12(2) Å respectively, indicating weak hydrogen bonding between the partial water molecule and DL4 cations related by the pseudo-translation of ~ a/2.

Table 11: Principal hydrogen bonding interactions in DL4ORO.

Interaction	D–H (Å)	H•••A (Å)	D•••A (Å)	D–H•••A (°)
N27–H27•••O33	0.88	2.37	2.710(2)	103
N27–H27•••O35[a]	0.88	2.12	2.920(2)	151
N29–H29•••O33[b]	0.88	1.92	2.801(2)	177
N15–H15•••O32	0.88	1.79	2.620(2)	156
N17–H17A•••O33	0.88	1.96	2.839(2)	173
N17–H17B•••O34[a]	0.88	2.19	2.780(2)	124

[a] -1-x, ½+y, ½-z; [b] -1-x, - ½+y, ½-z

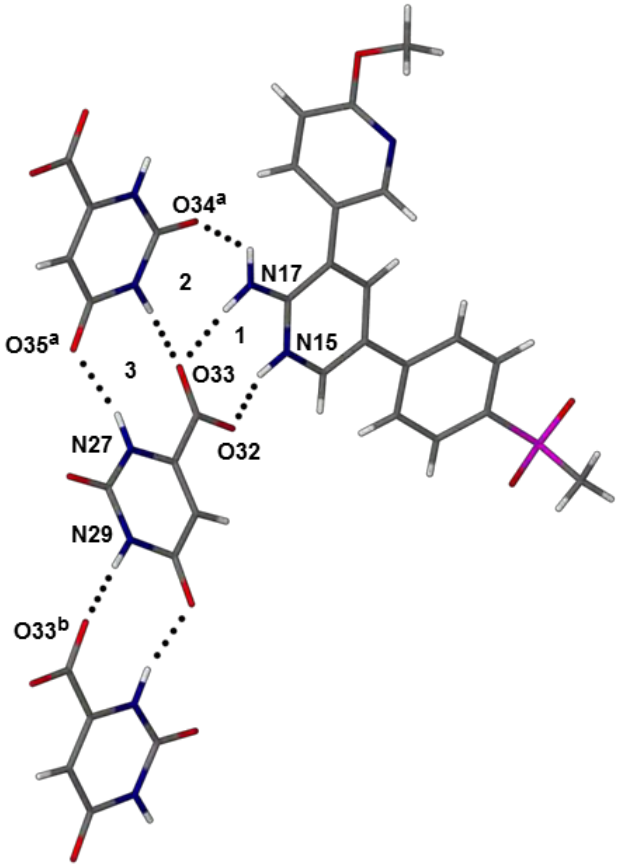

Figure 33: Hydrogen bonding interactions in DL4ORO (Only H atoms involved in hydrogen bonding have been included). Symmetry operators: a = -1-x, ½+y, ½-z ; b= -1-x, -½+y, ½-z.

The hydrogen bonding interactions in DL4ORO resemble those seen in DL4CIT. In both structures the amino-pyridinium moiety of the DL4 cation forms a $R_2^2(8)$ hydrogen bonding motif (**1**) with the carboxylate group of the co-former anion. Another feature that is common to both salts is the $R_3^2(8)$ hydrogen bonding motif (**2**) that is generated by the interaction between the amino-pyridinium group and the carboxylate groups of two co-former anions. Furthermore, the co-former anions in both salts also form hydrogen bonded dimers (synthon **3**).

When viewed along [0 1 0] the DL4 cations and orotate anions pack in alternating rows that run diagonally along the *b*-axis (Figure 34).

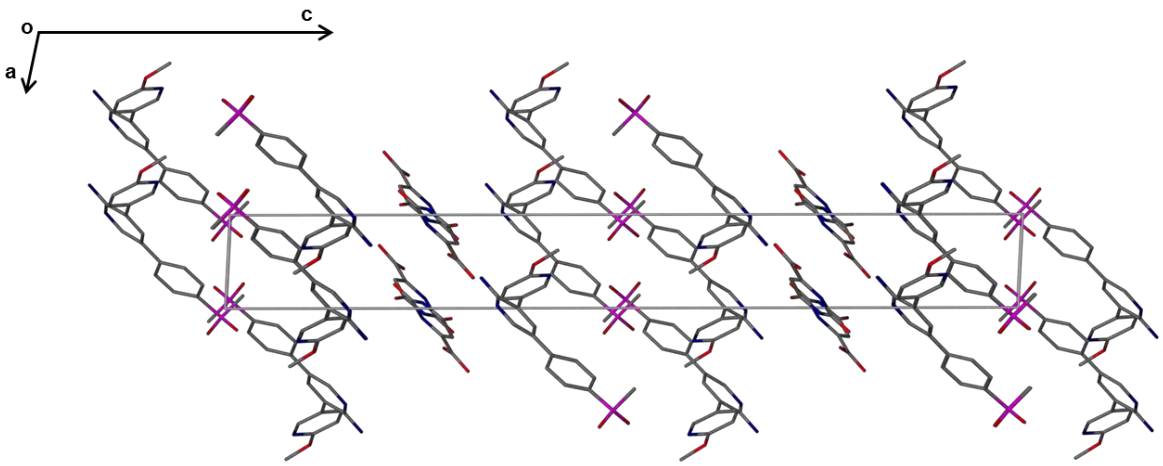

Figure 34: Packing diagram of DL4ORO viewed along [0 1 0]. Hydrogens have been omitted for clarity.

The crystal packing arrangements that are observed for DL4CIT and DL4ORO are very similar: both salts have the DL4 cations and co-former anions packing in alternate rows, with the co-formers acting as hydrogen bonded “links” between the rows. This observation suggests that small co-former molecules with carboxylic acid functional groups could potentially form salts of DL4 that have the same hydrogen bonding and crystal packing features.

Comparative PXRD

The high level of agreement between the calculated and experimental PXRD traces of DL4ORO (Figure 35) confirms that the single crystal that was analysed is representative of the bulk material. Significant differences in several corresponding peak intensities are attributed to preferred orientation of the crystallites in the experimental sample, which could be due to the acicular morphology of DL4ORO crystals observed in HSM.

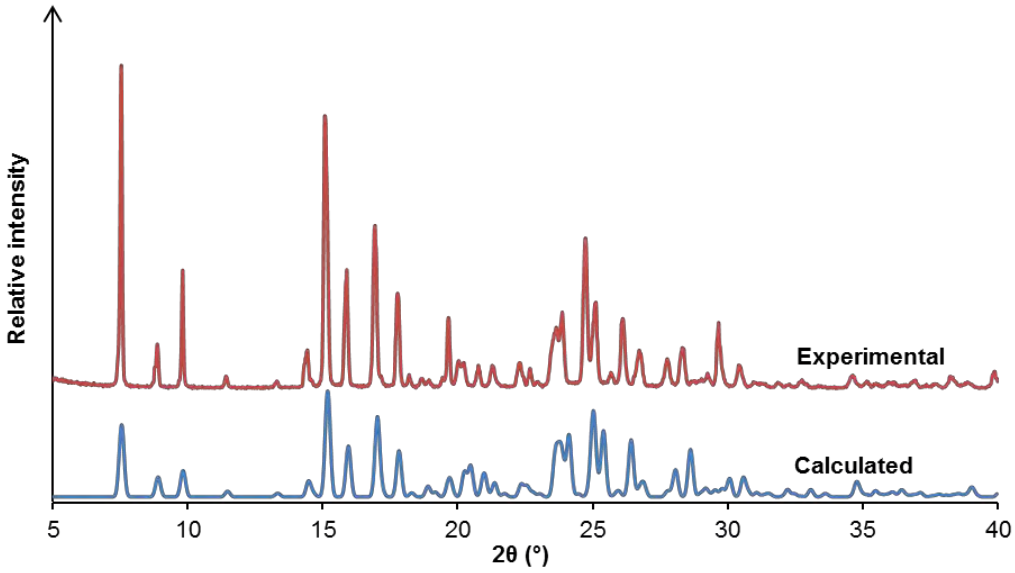

Figure 35: Calculated and experimental PXRD traces for DL4ORO.

In summary, only one of the salts of DL4 showed a significant improvement in the apparent solubility of DL4. This highlighted the need to explore alternative strategies for enhancing the solubility of this compound. The next chapter will present the results of CD inclusion experiments conducted with DL4, leading to superior solubility enhancement and biological activity.

References

1. Y. Younis, F. Douelle, T. Feng, D. G. Cabrera, C. Le Manach, A. T. Nchinda, S. Duffy, K. L. White, D. M. Shackleford, J. Morizzi, J. Mannila, K. Katneni, R. Bhamidipati, K. M. Zabiulla, J. T. Joseph, S. Bashyam, D. Waterson, M. J. Witty, D. Hardick, S. Wittlin, V. Avery, S. A. Charman and K. Chibale, *J. Med. Chem.,* 2012, **55**, 3479-3487.
2. D. L. Cruickshank, Y. Younis, N. M. Njuguna, D. S. B. Ongarora, K. Chibale and M. R. Caira, *CrystEngComm.*, 2014, **16**, 5781- 5792.
3. J. A. Bis and M. J. Zaworotko, *Cryst. Growth Des.*, 2005, **5**, 1169-1179.
4. G. M. Sheldrick, Program SADABS, Version 2.05, University of Göttingen, Germany, 2007.
5. Bruker AXS Inc., Program SAINT, Version 7.60a, Bruker AXS Inc., Madison, WI, USA, 2006.
6. Bruker AXS Inc., XPREP, Version 5.1, Bruker AXS Inc., Madison, WI, USA, 1997.
7. G. M. Sheldrick, *Acta Crystallogr. A.,* 2008, **64**, 112-122.
8. L. J. Barbour, *J. Supramol. Chem.,* 2001, **1**, 189-191.
9. L. J. Barbour, *J. Appl. Crystallogr.*, 1999, **32**, 351-352.
10. J. Pérez, C. Díaz, I. G. Salado, D. L. Pérez, F. Paláez, O. Genilloud and F. Vicente, *Adv. Biosci. Biotechnol.*, 2013, **4**, 628-639.
11. A. L. Spek, *Acta Crystallogr.*, 2009, **D65**, 148-155.

CHAPTER 6: Cyclodextrin inclusion of 3-(6-methoxy-pyridin-3-yl)-5-(4-methylsulfonylphenyl)-pyridin-2-amine (DL4): a novel antimalarial drug lead

Introduction

As mentioned in the previous chapter, DL4 (Figure 1) has displayed very potent *in vitro* and *in vivo* antiplasmodial and antimalarial activity respectively, but poor aqueous solubility (0.121 mg cm^{-3} at pH 6.5).[1] Five novel salts and a co-crystal of DL4 were reported in the literature and it has been shown that the aqueous solubility of DL4 could be improved using this strategy.[2] However, to date no cyclodextrin (CD) inclusion complexes of DL4 have been reported. The use of CDs as a means of solubilizing poorly soluble compounds has been reported extensively in the literature[3] and this chapter will discuss the CD inclusion experiments that were carried out with DL4 in an attempt to improve its physicochemical properties.

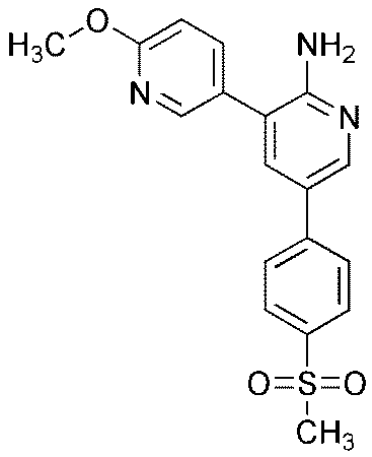

Figure 1: Structure of DL4.

CD inclusion experiments with DL4

Kneading experiments were performed with DL4 and each of the native CDs (α-CD, β-CD and γ-CD) to identify any possible CD inclusion complexes. DL4 was kneaded with each CD in a 1:1 molar ratio for 20 minutes using a mortar and pestle. Small amounts of water were added to allow the kneaded material to maintain a paste-like

consistency. The samples were analysed using PXRD and the traces were compared with a series of patterns for isostructural complexes of the CDs.[4]

Kneading experiments with DL4 and α-CD or β-CD did not produce any inclusion complexes. However, the PXRD trace from the kneading experiment with DL4 and γ-CD indicated that a mixture of an inclusion complex and DL4 had formed. The PXRD trace (Figure 2) for the product showed peaks at 2θ positions 7.5, 10.5, 14.2, 14.9, 15.8, and 16.6° that coincided with peaks from the trace for isostructural γ-CD inclusion complexes.[4] The PXRD trace of the product also shows peaks from the PXRD trace for DL4, which indicates that a mixture of an inclusion complex and DL4 had formed. The product was recrystallized, but pure crystals of the inclusion complex were not obtained. Co-precipitation experiments with the native CDs and DL4 did not produce any inclusion complexes.

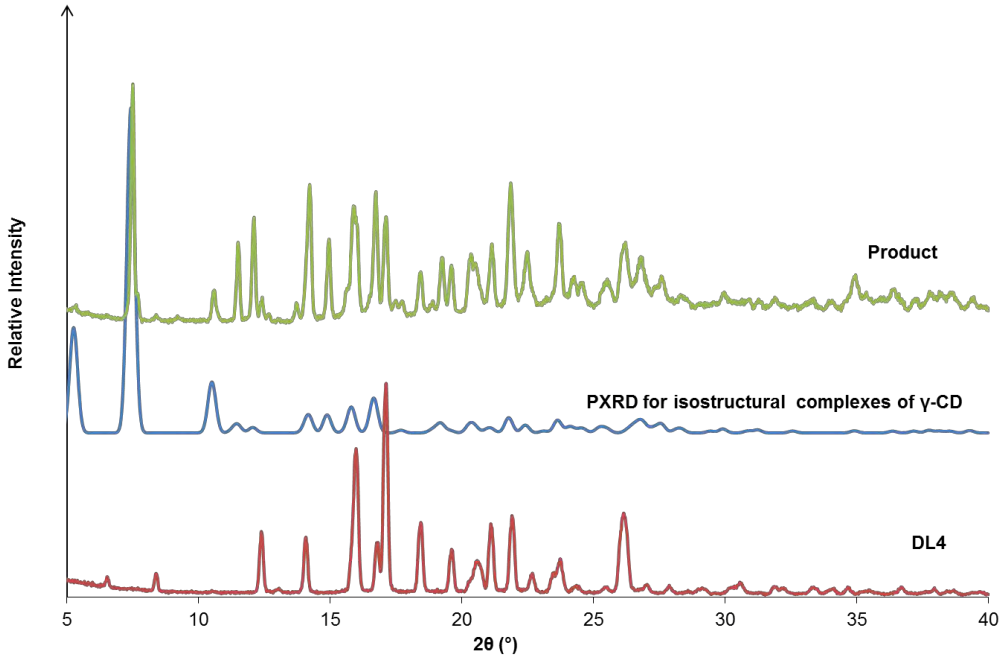

Figure 2: PXRD traces for DL4, isostructural complexes of γ-CD and the product of kneading DL4 and γ-CD.

Co-precipitation experiments were performed using three derivatised CDs, namely heptakis(2,6-di-*O*-methyl)-β-cyclodextrin (DIMEB), heptakis(2,3,6-tri-*O*-methyl)-β-cyclodextrin (TRIMEB) and hexakis(2,3,6-tri-*O*-methyl)-α-cyclodextrin (TRIMEA). The unit cell of the crystal obtained from co-precipitation with TRIMEA and DL4 was checked and it matched the unit cell of pure TRIMEA. Co-precipitation with TRIMEB

and DL4 did not produce any crystals. An inclusion complex of DIMEB and DL4 was prepared and is henceforth denoted DMBDL4.

DMBDL4: A DIMEB•DL4 inclusion complex

Complex preparation

DMBDL4 was prepared by adding 5 mg (0.014 mmol) of DL4 to a saturated aqueous solution containing an equimolar amount of DIMEB. The solution was stirred for 24 hours while the temperature was cycled between 25 and 40 °C. The solution was filtered through a 0.45 µm filter into a clean vial and placed in the oven at 60 °C. Crystals appeared after 4 - 7 days.

The inclusion complex could not be prepared in highly crystalline form by kneading. PXRD analysis showed that kneading produced a mixture of DL4 and an amorphous phase. All samples of DMBDL4 intended for final use were prepared using a modified version of the co-precipitation method described above. The DIMEB was dissolved in 1 cm^3 of Milli-Q^5 water at room temperature and DL4 was dissolved separately in 1 cm^3 of ethanol at 40 - 50 °C. The two components were combined while stirring at room temperature and then filtered through a 0.45 µm nylon filter into a clean vial. The open vial was placed in an oven at 60 °C for two hours to allow some of the ethanol to evaporate and after two hours the vial was capped and sealed. Crystals appeared after 4 - 7 days.

Confirmation of stoichiometry

The host-guest stoichiometry for the DMBDL4 complex was confirmed using ^1H NMR spectroscopy (Figure 3). The proton signals from DL4 and DIMEB were integrated (Table 1) and the results confirm that the host-guest ratio is 1:1.

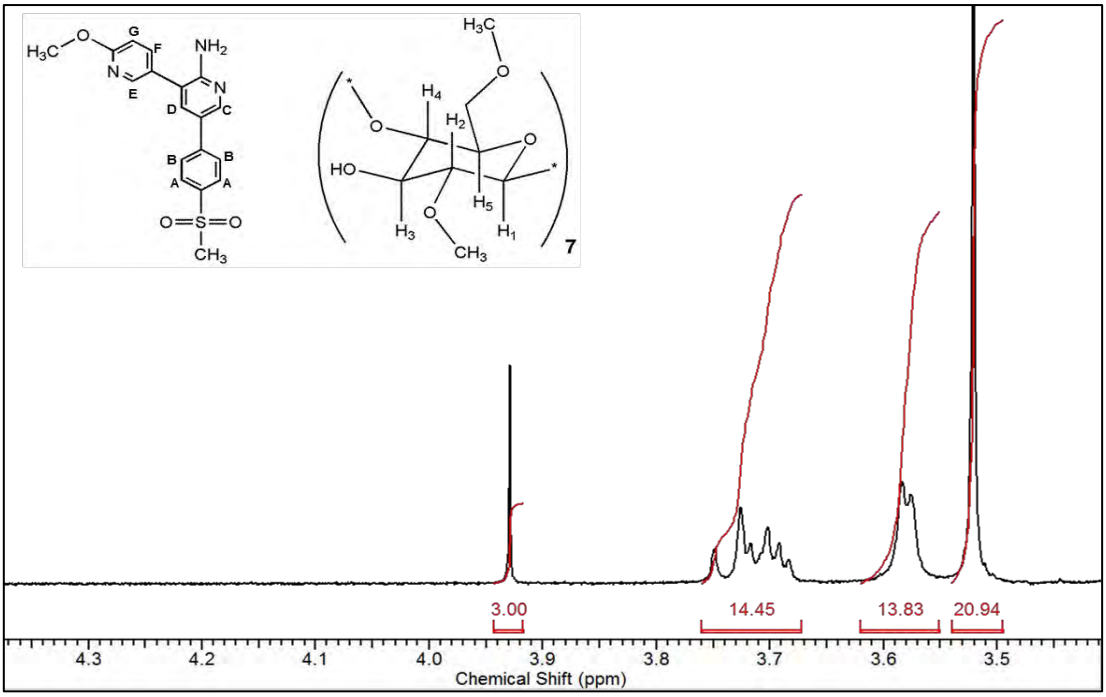

Figure 3: Partial ^{1}H NMR spectrum of DMBDL4 confirming 1:1 host-guest stoichiometry.

Table 1: ^{1}H NMR integration for the DMBDL4 inclusion complex

Proton	δ (ppm)	Multiplicity	J (Hz)	Integration	Experimental/ Theoretical
C-H_C	8.44	d	2.57	0.93	0.93
C-H_E	8.32	d	3.12	0.89	0.89
C-H_A + C-H_B	7.95	d	2.75	3.88	0.97
C-H_F	7.85-7.88	d of d	8.23, 2.57	0.82	0.82
C-H_D	7.75	d	2.38	0.92	0.92
C-H_G	6.94	d	8.60	0.89	0.89
2 x N-H_2	6.04	s (br)		1.82	0.91
3 x O-CH_3	3.93	s		*3.00	1.00
3 x O-CH_3	3.24	s		3.09	1.03
C-H_1 + C-OH	4.98	m		14.05	1.00
C-H_3 + C-H_5	3.70	m		14.45	1.03
2 x C-H_6	3.58	d	3.30	13.83	0.99
3 x O-CH_3	3.52	s		20.94	1.00
3 x O-CH_3	3.27	s		21.85	1.04
C-H_2	3.19-3.23	d of d	10.36, 3.67	7.02	1.00

*Reference integral

Thermal analysis

HSM

Crystals of DMBDL4 were heated at a rate of 10 K min^{-1} during a HSM experiment and photographs of thermal events were recorded. Small bubbles started to appear from 150 °C and the photograph taken at 170 °C (Figure 4) shows two large bubbles (highlighted by a red arrow). The crystals melted at 220 °C. The temperatures at which thermal events take place during HSM are higher compared to the TGA and DSC experiments. This difference is caused by the different sample sizes and conditions used during the TGA and DSC experiments.

Figure 4: Representative HSM photographs of DMBDL4.

TGA and DSC

TGA was used to quantify the water content of DMBDL4 and the results (Figure 5) confirmed the presence of two water molecules per inclusion complex unit in the crystal. The TGA traces were recorded in triplicate and an average mass loss of 2.1 ± 0.1 % was observed between 50 °C and 100 °C corresponding to the loss of two water molecules (calculated 2.09 %). TG analysis did not reveal any guest loss before the onset of decomposition at 229 °C.

The baseline of the DSC trace (Figure 5) is slightly sloped and this is most probably due to an irregularity with the DSC instrument at the time of recording. However, it is still possible to observe all of the significant thermal events. There is a broad

endotherm between 50 °C and 130 °C corresponding to the loss of the two water molecules. A small exotherm at 179 °C indicates a phase transition which, was confirmed using variable temperature PXRD analysis (Figure 14). A sharp endotherm at 218 °C indicates the melting point of the complex.

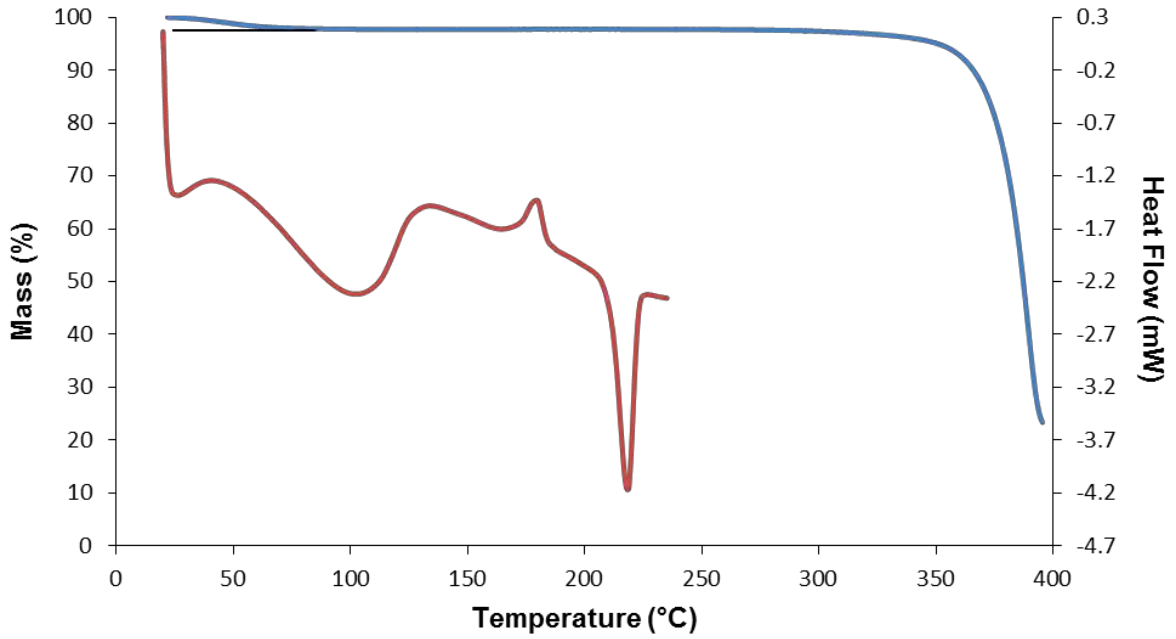

Figure 5: Representative TGA (blue) and DSC (red) traces for DMBDL4.

Crystal structure analysis

Data-collection and space group determination

Crystal intensity data were collected on a Bruker KAPPA APEX II DUO single crystal X-ray diffractometer. Lorentz-polarization corrections were applied with program SAINT[6] and absorption corrections were applied using the program SADABS.[7] The Laue symmetry was found to be 2/m which is consistent with the monoclinic crystal system and the space group $P2_1$ was identified from the systematic absence of reflections *0k0* with $k = 2n+1$. The chiral space group of the complex is consistent with the chiral nature of DIMEB. The crystal system and space group were confirmed by the program XPREP.[8]

Structure solution and refinement

Crystal and refinement data for DMBDL4 are shown in Table 2 below. The structure was solved by direct methods using program SHELXS-97[9] within the XSEED interface.[10] This revealed all of the host and guest atoms as well as the oxygen atoms of two water molecules. These atoms were refined using full-matrix least-squares with SHELXH-97.[9] Remarkably, all of the hydrogen atoms, including those of the two water molecules, were located in difference Fourier maps. This attests to exceptionally high crystal quality and consequently excellent X-ray intensity data, which is somewhat unusual for cyclodextrin inclusion complexes. All ordered non-hydrogen atoms were refined anisotropically. Atom C8 of the glucose unit G3 was found to be disordered over two positions and the disordered components C8G3 and C832 were included with assigned site occupancy factors *x* and *1-x* (initially set at 0.6 and 0.4 respectively). The refined final value of *x* was 0.55. Following their location, hydrogen atoms for the host and guest were placed in idealised positions using a riding model. The hydrogen atoms of the water molecules were restrained using a DFIX command with the O-H bond lengths fixed at 0.96(1) Å.

Table 2: Data-collection and refinement parameters for DMBDL4.

Abbreviated Formula	DMB•DL4•2H_2O
Complex Formula	$C_{56}H_{98}O_{35}$•$C_{18}H_{17}N_3O_3S$•2H_2O
Formula weight (g mol^{-1})	1722.78
Crystal system	Monoclinic
Space group	$P2_1$
a (Å)	11.3127(6)
b (Å)	14.5968(7)
c (Å)	26.187(1)
α (°)	90.0
β (°)	96.579(1)
γ (°)	90.0
V $(Å)^3$	4295.8(4)
Z	2
D_c (g cm^{-3})	1.332
μ (Mo Kα) (mm^{-1})	0.131
F(000)	1840
Data collection temp. (K)	173(2)
Crystal size (mm^3)	0.10 × 0.23 × 0.30
Range scanned θ (°)	1.6 - 28.3
Index ranges ±*h*, ±*k*, ±*l*	-15, 15 ; -19, 19 ; -34, 34
Reflections (total)	48106
Independent reflections	21356
Reflections with I>2σ(I)	17693
No. of parameters	1090
R_{int}	0.025
S	1.02
R_1 [*I*>2σ(*I*)]	0.0388
Reflections omitted	2
wR_2	0.0911
a, b in w = $1/[\sigma^2(F_o^2)+(aP)^2+(bP)]$	0.0460, 0.4027
$(\Delta/\sigma)_{mean}$	<0.001
$\Delta\rho_{min,max}$ (e $Å^{-3}$)	-0.38 and 0.28

Description of the structure

The asymmetric unit of the DMBDL4 structure (Figure 6) consists of a single DIMEB molecule, one DL4 molecule and two water molecules. The DL4 molecule is positioned within the DIMEB cavity with the hydrophobic 4-(methylsulfonyl)phenyl ring extending into the cavity as far as the primary rim and the more polar 2-methoxypyridinyl “tail” protruding from the secondary rim into interstitial spaces in the crystal structure.

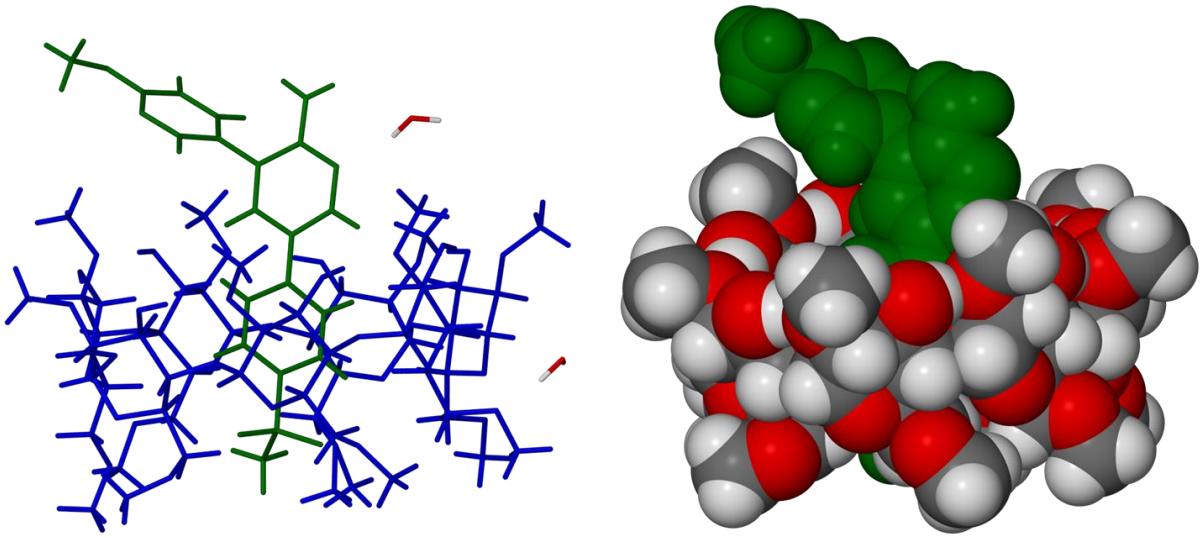

Figure 6: Asymmetric unit of DMBDL4 with host shown in blue and the guest in green (left) and space-filling view of DMBDL4 with the guest shown in green (right). Water molecules have been omitted in the space-filling diagram.

Host conformation

The geometric parameters of the O4-heptagon of the host molecule in DMBDL4 are listed in Table 3. The l parameter measures the distance of each O4 atom to the centroid of the heptagon and in a regular heptagon the values would all be equal. The values are not all the same for the host molecule, indicating that complexation has led to some distortion. The deviations (α) of the O4 atoms from the O4 mean plane are very small, indicating a fairly high degree of planarity of the O4-heptagon. The D_3 parameter, which is not directly defined by the O4-heptagon, measures the O•••O distances of the O2n-H•••O(3n-1) hydrogen bonds that link the contiguous glucose rings. D_3 values for DMBDL4 range from 2.793(2) to 3.004(2) Å, which is consistent with these hydrogen bonding interactions. The values for τ_2 (tilt angles) show that the primary sides of G3 and G6 are tilted to a greater extent towards the centre of the cavity of the DIMEB molecule than the other glucose units in the macrocycle.

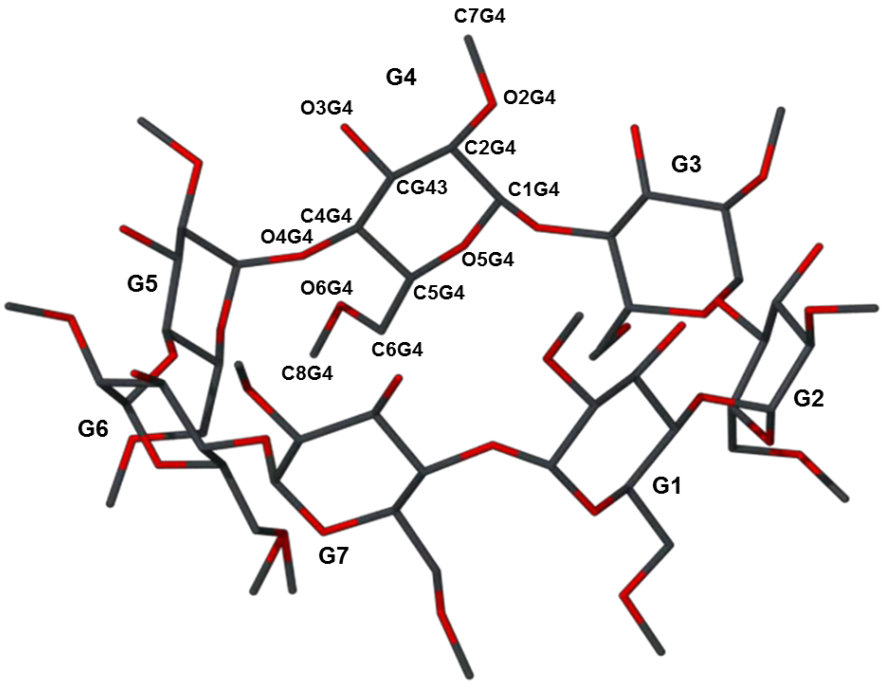

Figure 7: Macrocyclic structure of DIMEB in the inclusion complex (hydrogens have been omitted for clarity). The glucoside units are labelled G1-G7 and the atom numbering scheme for a representative glucose ring is indicated.

Table 3: Geometric parameters of the host molecule in DMBDL4.

Residue	*l* (Å)	D (Å)	ϕ (°)	d (°)	α[a] (Å)	D_3[b] (Å)	τ_2 (°)[c]
G1	4.936	4.236	130.7	-1.6	0.0728	2.793	2.93
G2	5.415	4.288	119.5	-10.9	-0.1875	2.912	15.77
G3	4.921	4.481	131.2	10.4	-0.0487	3.004	25.28
G4	4.688	4.455	134.7	4.1	0.2511	2.817	10.91
G5	5.263	4.199	123.5	-14.5	-0.0858	2.792	4.67
G6	5.269	4.382	123.0	7.0	-0.2199	2.948	22.15
G7	4.664	4.550	135.6	4.7	0.2180	2.843	15.00

[a] mean esd 0.0009 Å; [b] esd = 0.002 Å; [c] mean e.s.d. 0.002

Guest inclusion

The bond lengths and angles of the guest molecule are consistent with those for the uncomplexed molecule.[2] However, the angles between the aromatic rings of the guest molecule do change upon complexation. The angle between the 2-methoxypyridine ring and the 2-aminopyridine ring changes from 53.03(8)° to 61.23(9)° in the complex. Similarly, the angle between the 2-aminopyridine ring and the 4-(methylsulfonyl)phenyl ring changes from 27.46(8)° to 34.1(1)° when the complex is formed. The orientation of the methylsulfonyl group also changes

significantly when the molecule is included in DIMEB (Figure 8). These changes indicate that the guest is distorted upon complexation due to interactions with the DIMEB molecule in its attempt to be accommodated optimally.

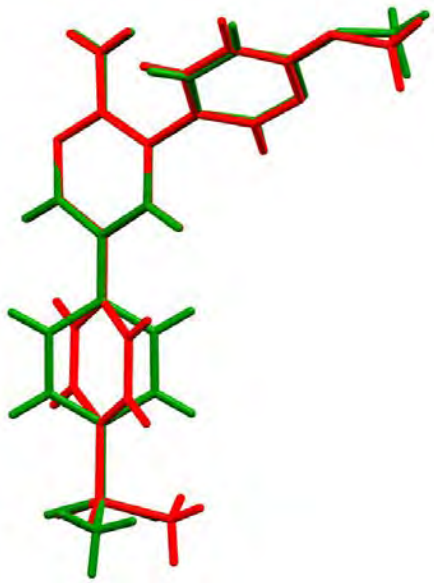

Figure 8: Overlay of the uncomplexed (green) and complexed (red) DL4 molecues.

Two structures for uncomplexed DIMEB (a hydrated molecule of DIMEB) were accessed from the CSD,[11] namely BOYFOK04[12] and CEQCUW.[13] Program Mercury[14] was used to calculate the values for τ_2 (Table 4). BOYFOK04 was considered to be a representative structure for the uncomplexed DIMEB molecule, because the τ_2 values for this structure are closer to those for DMBDL4 than are the values for CEQCUW. Although most of the values for τ_2 in DMBDL4 and BOYFOK04 appear to be very similar, there is a significant difference for each of G2, G5 and G6. These differences can be explained by viewing the orientation of the guest inside the host molecule (Figure 9). The 4-(methylsulfonyl)phenyl ring of DL4 extends towards the primary rim of the host and it is orientated in the direction of the G2, G5 and G6 glucose units, causing these glucoside units to distort. The inclusion of the 4-(methylsufonyl)phenyl ring into the DIMEB cavity causes the host molecule to take on an elliptical shape. This distortion is also reflected in the values of parameter l (Table 4), the longest being those for the G2, G5 and G6 glucose residues.

Table 4: τ_2 values for DMBDL4, BOYFOK04 and CEQCUW.

Glucosides unit	DMBDL4[a]	BOYFOK04	CEQCUW
G1	2.93	2.8	3.6
G2	15.77	18.0	16.4
G3	25.28	27.6	24.3
G4	10.91	11.0	10.3
G5	4.67	11.0	6.9
G6	22.15	14.1	16.6
G7	15.00	18.6	19.6

[a] mean e.s.d 0.01 Å

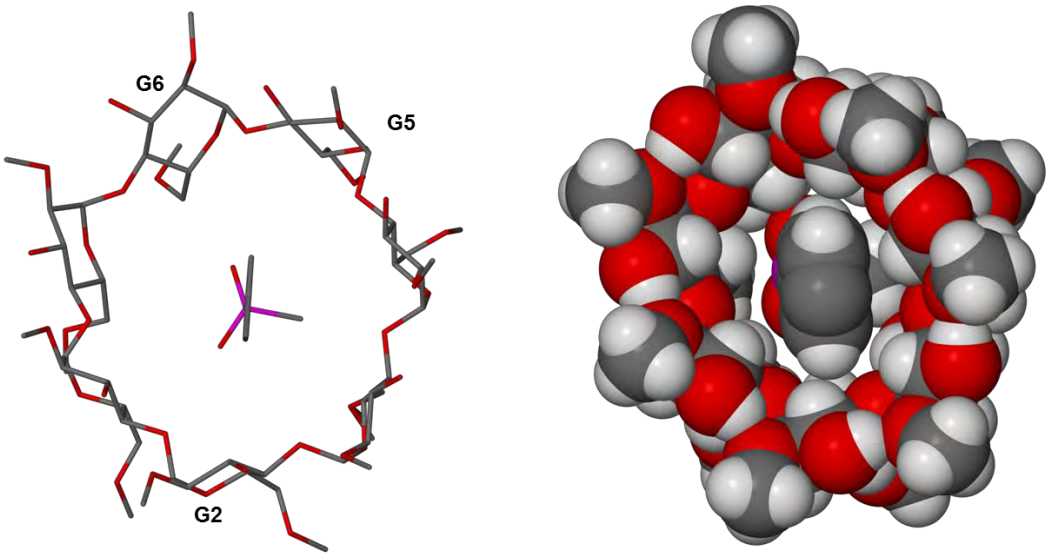

Figure 9: View from the secondary rim of DMBDL4. The left image shows the 4-(methylsulfonyl)phenyl ring extended towards G2, G5 and G6. The image on the right shows a space-filling view from the secondary rim.

The differences in the tilt angles for DMBDL4 and BOYFOK04 as well as the conformational changes in the guest molecule thus indicate that on complexation there are simultaneous conformational changes of DIMEB and DL4 to optimise inclusion geometry i.e. a mutually induced fit.

Hydrogen bonding

There are seven O2n–HO(3n-1) intramolecular hydrogen bonds which cause the DIMEB molecule to adopt a 'round' shape (Figure 10).

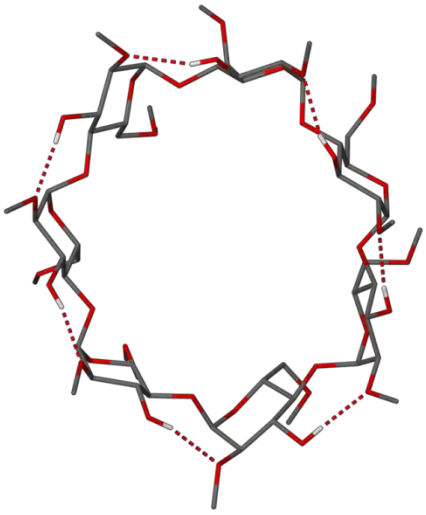

Figure 10: Intramolecular hydrogen bonding interactions in the host molecule of DMBDL4.

Figure 11 has been drawn in stereoview to illustrate that the guest forms hydrogen bonding interactions with both of the water molecules as well as another guest molecule.

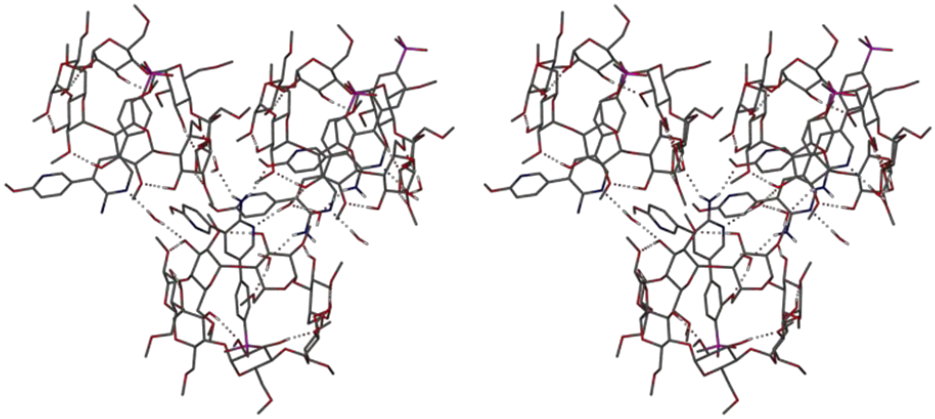

Figure 11: Stereoview of the primary hydrogen bonding interactions in DMBDL4. The complex molecule in the foreground shows hydrogen bonding interactions emanating from the amine group to the water molecules and to another guest molecule (the host molecule of this guest has been omitted for clarity). The diagram also shows the water molecules creating hydrogen bonding "bridges" between the complex molecules.

Table 5 lists the principal hydrogen bonding interactions that occur within DMBDL4 with their respective distances and angles.

Table 5: Hydrogen bonding interactions in the DMBDL4 inclusion complex.

Interaction	D-H (Å)	H•••A (Å)	D•••A (Å)	D-H•••A (°)
Intramolecular				
O3G1−H31B•••O2G2	0.84	2.11	2.912(2)	161
O3G2−H32B•••O2G3	0.84	2.20	3.004(2)	160
O3G3−H33B•••O2G4	0.84	1.98	2.817(2)	174
O3G4−H34B•••O2G5	0.84	1.96	2.792(2)	169
O3G5−H35B•••O2G6	0.84	2.12	2.948(2)	168
O3G6−H36B•••O2G7	0.84	2.01	2.843(2)	172
O3G7−H37B•••O2G1	0.84	1.96	2.793(2)	171
Intermolecular				
O26−H26A•••N15	0.90	2.06	2.914(2)	159
O27−H27A•••O6G2	0.89	2.07	2.953(2)	167
N17−H17B•••O27[a]	0.88	2.23	3.007(3)	147
O26−H26B•••O3G3[b]	0.84	2.13	2.972(2)	172
O27−H27B•••O26[c]	0.96	1.88	2.831(2)	172
N17−H17A•••O24[d]	0.84	2.13	2.972(2)	172

[a] 1–x, ½+y, -z; [b] 1–x, -½+y, -z; [c] -1+x, y, z; [d] 2–x, -½+y, -z

Crystal packing

The DMBDL4 structure has a cage-type packing arrangement, as seen in Figure 12. The 2-methoxypyridinyl “tail” of the guest and the two water molecules are located in the interstitial spaces, preventing the host molecules from forming a channel-packing arrangement.

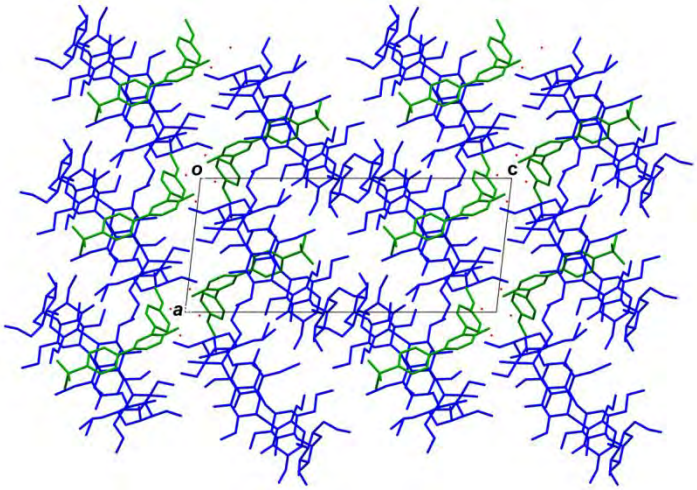

Figure 12: Packing diagram for DMBDL4 viewed along [0 1 0]. The host molecules are shown in blue and the guest in green (hydrogens have been omitted for clarity).

Comparative PXRD

The high level of agreement between the experimental and calculated PXRD traces for DMBDL4 (Figure 13) confirms that the single crystal which was analysed is representative of the bulk material. When more material for further analysis of DMBDL4 was required, the inclusion complex was grown by co-precipitation and the PXRD traces of the samples were recorded and compared with the calculated trace to confirm their purity.

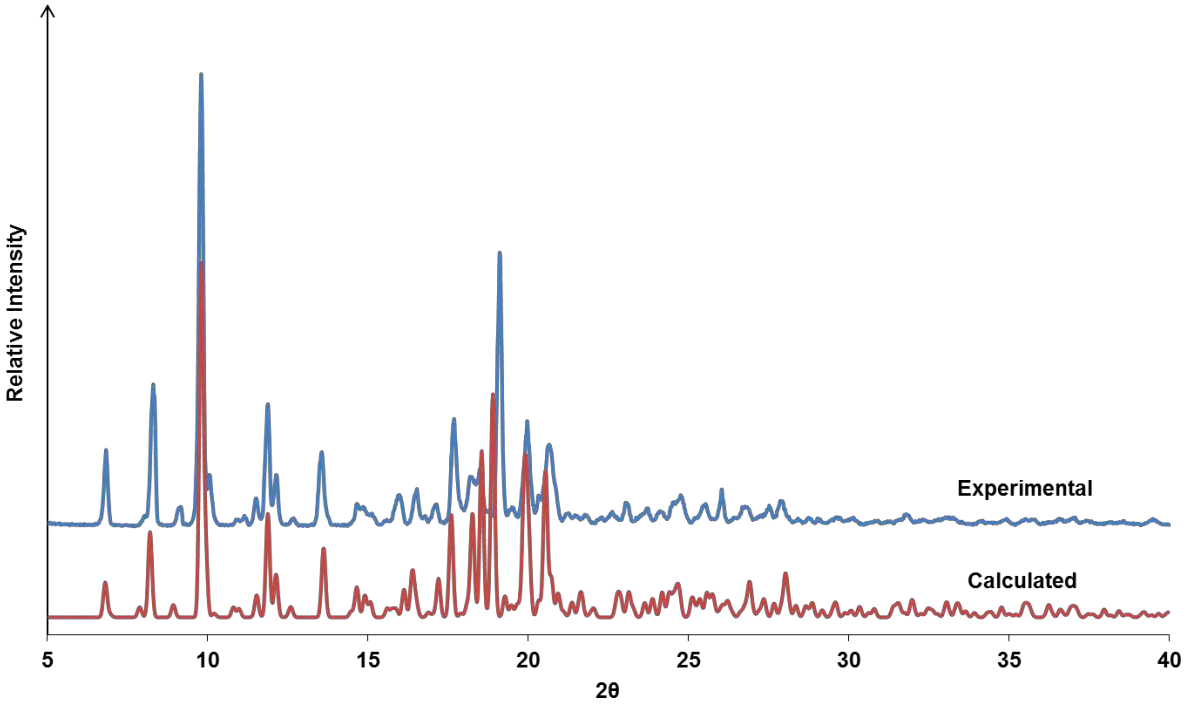

Figure 13: Calculated and experimental PXRD traces for DMBDL4.

Variable temperature PXRD

Variable temperature PXRD analysis was used to investigate the phase transition that was indicated by the exothermic peak between 165 °C and 187 °C in the DSC trace of DMBDL4. The PXRD pattern for a sample of DMBDL4 was recorded at 30 °C, 165 °C, 175 °C and 185 °C. A comparison of the PXRD traces (Figure 14) shows that the PXRD trace at 30 °C is practically identical to the calculated trace. However, the PXRD traces recorded at 165 °C, 175 °C and 185 °C are identical and clearly different from the trace recorded at 30 °C. This indicates that a phase

transition takes place at ~165 °C, resulting in a different PXRD trace. This is consistent with the exothermic peak that was observed between 165 °C and 187 °C in the DSC trace.

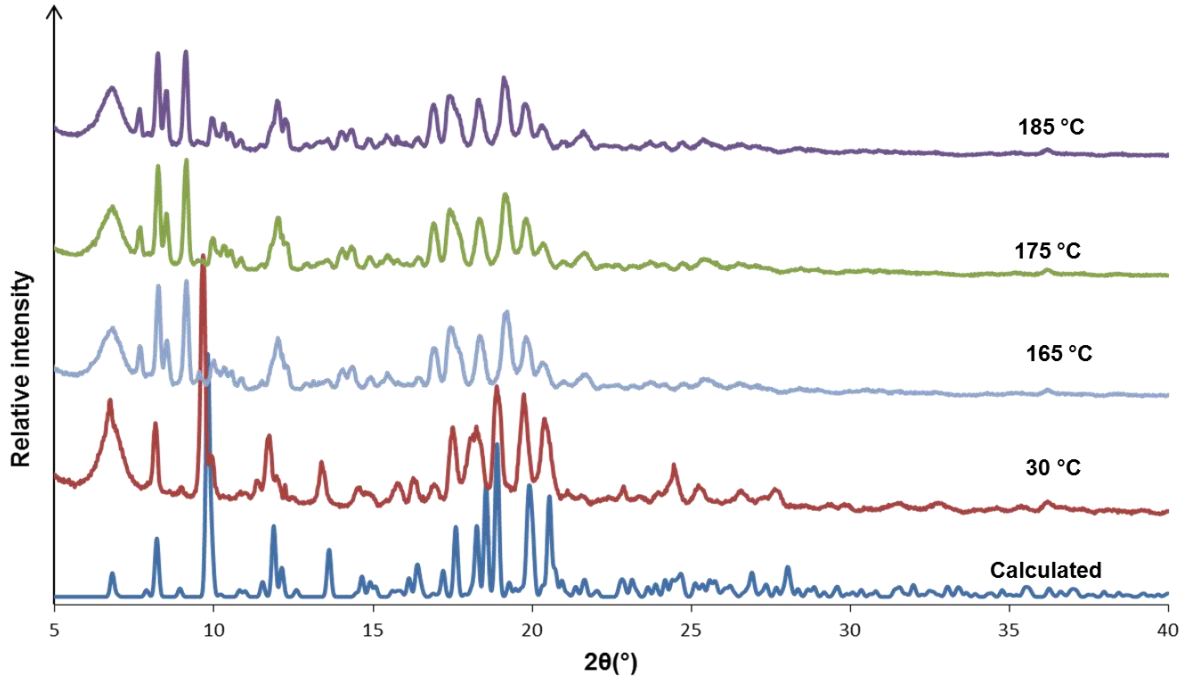

Figure 14: Variable temperature PXRD traces for DMBDL4.

Phase solubility studies

Phase solubility studies were carried out with DL4 and seven different CDs, namely α-, β- and γ-CD, partially methylated β-CD (DIMEB), randomly methylated β-CD (RAMEB), hydroxypropyl β-CD (HPβCD) and sulfobutyl β-CD sodium salt (SBβCD). The phase solubility studies with α-CD, γ-CD, RAMEB and SBβCD produced erratic results that were not reproducible and these are therefore not reported. A possible reason for the unreliable results with α-CD and γ-CD could be aggregation of these host molecules in solution, which would have resulted in significant scattering of UV-visible radiation.

The phase solubility experiments were performed according to the method described by Higuchi and Connors.[15] Serial dilutions of each CD solution were prepared and an excess amount of DL4 was added to a polytop vial containing 5 cm^3 of the CD solution. The vials were stirred (500 rpm) at constant temperature (25 ± 0.5 °C) for

72 hours. The solutions were filtered through a 0.45 µm nylon filter and diluted appropriately before their UV-visible spectra were recorded. The concentration of DL4 was determined from a calibration curve (Figure 15) obtained as described in Chapter 2.

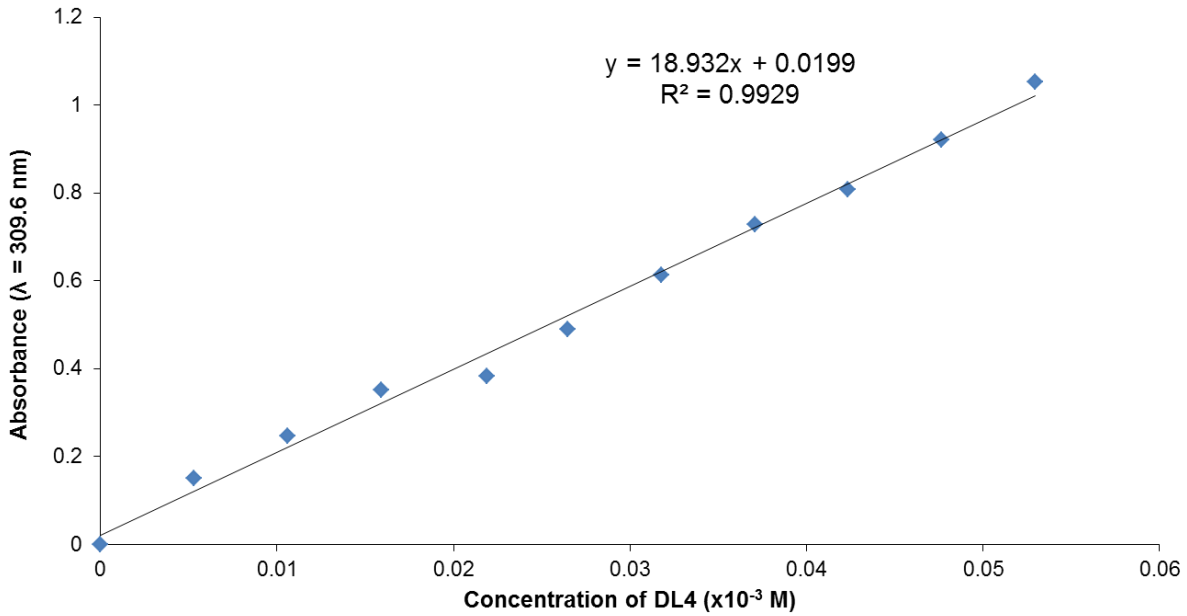

Figure 15: Calibration curve for DL4.

As described in Chapter 4, there are two types of phase solubility profile, namely A- and B-type. The former is characterized by an increase in substrate solubility with increasing CD concentration while the latter indicates the formation of insoluble complexes in solution. The subtypes A_L, A_P, A_N, B_S and B_L were also defined previously.

Figure 16 shows the phase solubility results for DL4 with β-CD. This phase solubility profiles has A_N-type behaviour, with the solubility of DL4 increasing to a plateau. The negative deviation in the solubility of DL4 at the higher concentrations of β-CD could be caused by aggregation of β-CD molecules in solution or changes in the solubility of the complex in solution. Aggregation of β-CD molecules in solution would cause scattering of UV-visible light, resulting in a decrease in the absorbance that is detected. The apparent solubility of DL4 (12.08 mg cm^{-3}, equivalent to 0.034 mM at 25 °C) increased by a factor of 30 at the highest concentration of β-CD investigated.

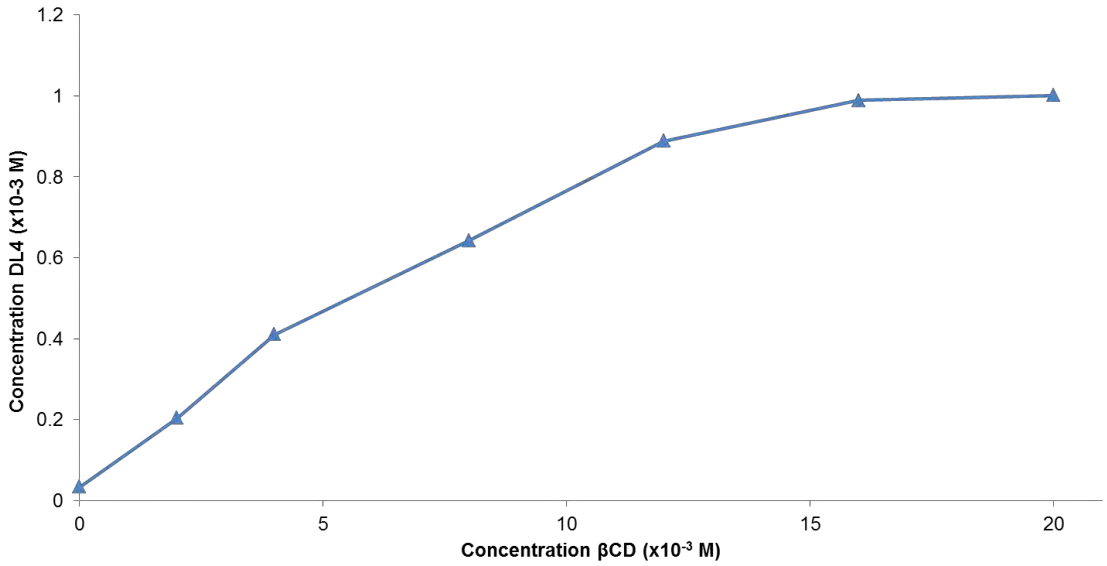

Figure 16: Solubility of DL4 as a function of [β-CD] at 25°C.

The phase solubility profiles for the experiments involving DIMEB and HPβCD both displayed A_L-type behaviour (Figure 17 and Figure 18). The solubility of DL4 increased with increasing concentration of the CD. At the highest concentration of HPβCD used, the apparent solubility of DL4 increased by a factor of more than 80. More significantly, the solubility enhancement for DL4 at the highest concentration of DIMEB used was more than 100-fold.

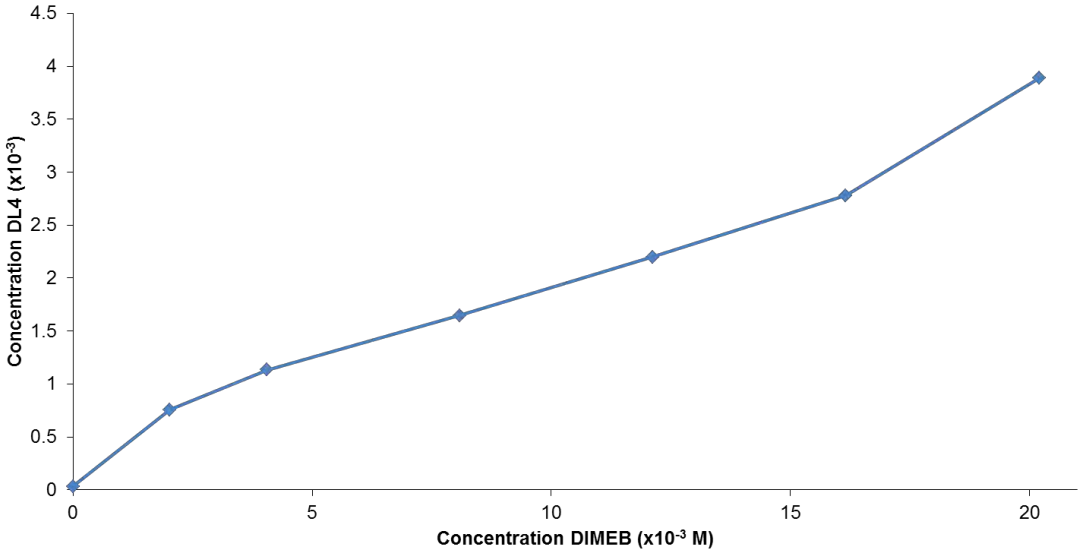

Figure 17: Solubility of DL4 as a function of [DIMEB] at 25°C.

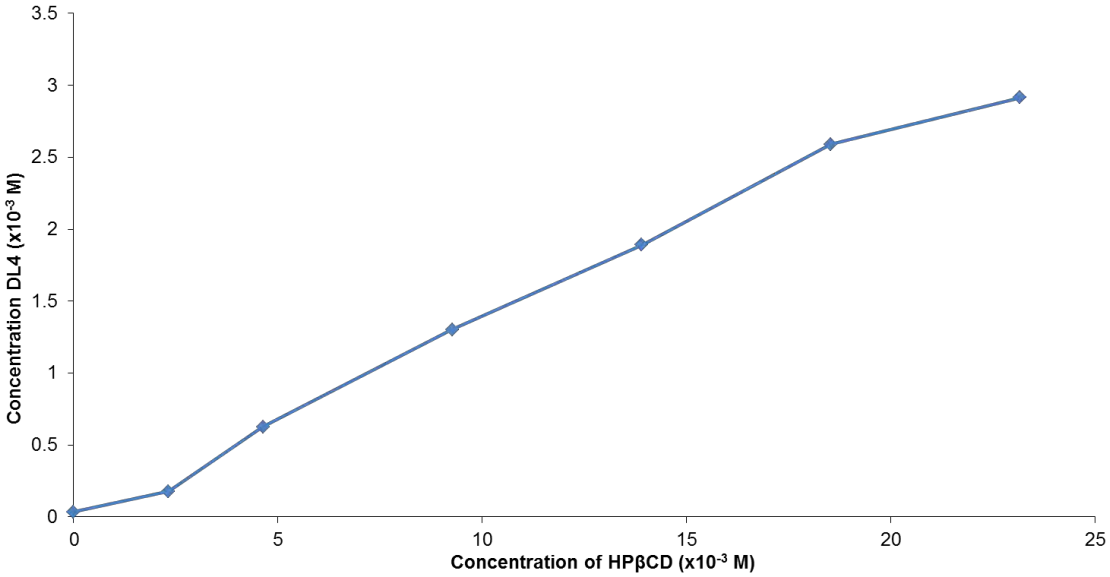

Figure 18: Solubility of DL4 as a function of [HPβCD] at 25 °C.

Using equation (1), it was possible to calculate the association constants for complex formation by using the slopes of the phase solubility profiles. Equation (1), where S_0 is the intrinsic solubility of DL4 at 25 °C, only applies to 1:1 host-guest complexes with the slope of the plot being less than 1. The initial slope was used to calculate K_C for the host β-CD (up to 12 mM). The estimated values for K_C are shown in Table 6.

$$K_C = \frac{slope}{S_0(1-slope)} \qquad (1)$$

Table 6: The apparent stability constants for complexation between DL4 and three CDs.

Cyclodextrin	K_C (M^{-1})
β-CD	2224
HPβCD	4477
DIMEB	6054

The values obtained for the association constants indicate moderately strong binding between DL4 and β-CD and strong binding between DL4 and HPβCD. The value of K_C obtained for the association between DIMEB and DL4 indicates the formation of a very stable complex.

Biological testing

Phase solubility studies showed that complexation with DIMEB had an enhancing effect on the aqueous solubility of DL4. The DMBDL4 inclusion complex was subsequently submitted for *in vivo* pharmacokinetic (PK) and efficacy testing to establish whether the inclusion of DL4 in DIMEB had any effect on the *in vivo* PK properties and the efficacy of DL4. While the biological tests were performed by specialists in this area, the author of this dissertation was responsible for preparing pure samples of DL4 and its inclusion complex in the required form and particle size range, for packing microcapsules with these materials, and for establishing the appropriate composition of the suspension vehicle for efficacy testing. She also engaged closely with the specialists to discuss the interpretation of the results.

Pharmacokinetic studies

In vivo pharmacokinetic testing was carried out by Dr Natasha Strydom and colleagues from the Division of Pharmacology at the University of Cape Town (South Africa). Nine 6-week-old C57BL/6 mice were divided into an intravenous and two oral dosage groups (n = 3).

For the intravenous group, a single 2.5 mg kg^{-1} dose (formulation: DMSO, PEG, EtOH, PPG [2:6:1:7, v/v]) was injected into the penile dorsal vein. Oral dosing was achieved using a Torpac capsule loaded with either DL4 or DMBDL4 with a particle size range of 100-150 µm. Pure DL4 and the complex DMBDL4 were collected separately between a 150 micron and 100 micron sieve to achieve the desired particle size range. A single Torpac capsule containing 5 mg kg^{-1} active dose of either DMBDL4 or DL4 was administered orally to groups A and B respectively. Blood samples were collected at 0.5, 1, 3, 5, 8 and 24 hours after administration and the whole blood concentration of DL4 was determined using a LC-MS assay.[16]

Table 7 shows the pharmacokinetic parameters for the three groups of mice and the mean plot of the DL4 exposure in the three groups is shown in Figure 19. DL4 was detectable for the duration of the experiment in all groups. The capsule dosage form

caused higher variance in absorption and subsequent pharmacokinetic parameters due to the added variability of capsule and compound dissolution. The rate of absorption for the DMBDL4 inclusion complex was slower with a significant lag in absorption and a longer T_{max} of 5 hours compared to 3.7 hours for DL4. Mean bioavailability suggests higher bioavailability was observed for DMBDL4, but the variance observed between animals makes this inconclusive. However, the DMBDL4 complex did show less variance compared to DL4, suggesting its absorbance to be more consistent and predictable. The apparent half-life of DL4 increased from 3.82 h to 6.12 h when DMBDL4 was administered and at 24 hours much higher levels of DL4 were observed for the complex (0.3 µM for DMBDL4 compared to 0.06 µM for untreated DL4).

Table 7: Pharmacokinetic parameters for the intravenous and capsule dosage groups.

Parameter	IV (2.5 mg kg^{-1})	DMBDL4 (5 mg kg^{-1} active)	DL4 (5 mg kg^{-1})
$t_{1/2}$ (h)[a]	4.58	6.12	3.82
C_{max} (µM)[b]	11.4	3.00	2.47
t_{max} (hr)[c]	-	5.00	3.70
V_d (L kg^{-1})[d]	0.74	-	-
Cl_{tot} (cm^3 min^{-1} kg^{-1})[d]	1.94	-	-
AUC (min µmol L^{-1})[e]	3666	2131	1548
Bioavailability (%)	-	29 (23 – 35)	22 (4 – 36)
Conc. at 24 hr (µM)	0.25	0.30	0.06

[a] Half-life of DL4, [b] Maximum concentration of DL4, [c] Time taken to reach maximum concentration of DL4, [d] Volume of distribution, [e] Area under the curve.

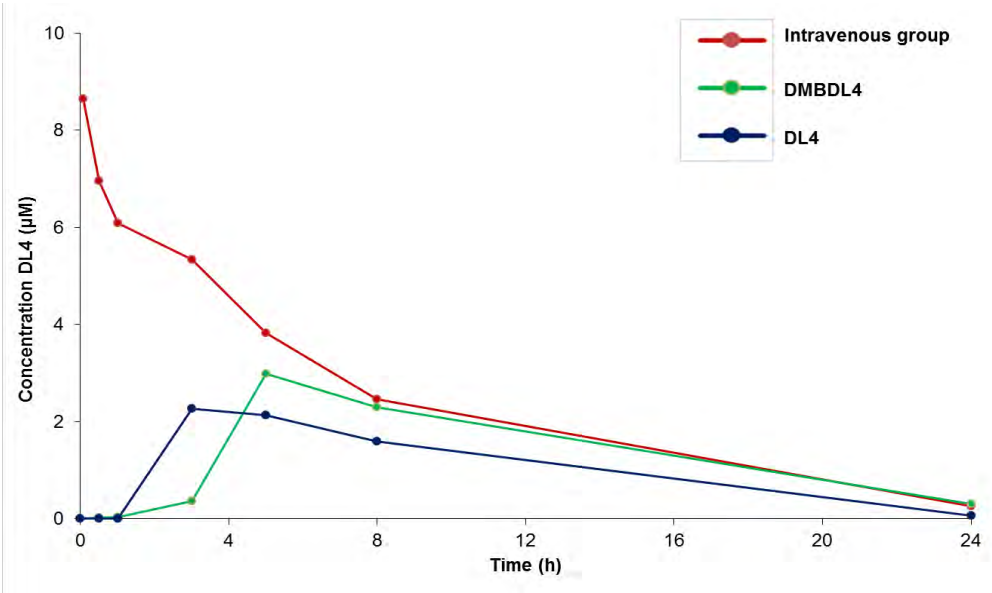

Figure 19: Mean plot of the exposure of DL4 in C57Bl6 mice at a dose of 2.5 mg kg^{-1} (intravenous group) and 5 mg kg^{-1} (oral dosage groups).

The pharmacokinetic results are consistent with a slow release of the DL4 from the inclusion complex, resulting in a longer sustained concentration of DL4 over time as seen from the increase in apparent half-life. The lag in absorption suggests that the DMBDL4 inclusion complex dissociates after gastric emptying and that it is absorbed in the duodenum and jejunum, while the more rapid absorption for DL4 suggests that its site of absorption is the stomach. Absorption in the duodenum and jejunum is more favourable than absorption in the stomach since the capsule spends only a short time in the stomach and there is considerable variance in gastric emptying. A pH-dependent change in the dissolution for DMBDL4 and DL4 would explain the increased variance and the change in apparent half-life. Kinetic solubility studies were performed for DL4 and the results (Table 8) show that DL4 has a maximum absorption at pH 2, which is consistent with the site of absorption being the stomach. To verify the pH-dependent absorption of the DMBDL4 inclusion complex, kinetic solubility studies should be performed in different pH media. The data for DMBDL4 should further be analysed using non-linear mixed effects modelling to account for the lag in absorption and observed variance.

Table 8: Kinetic solubility data for DL4.

pH	Equilibrium solubility
2	4422 µg cm^{-3}
10.7	10.7 µg cm^{-3}
11.7	11.7 µg cm^{-3}

In vivo efficacy testing

In vivo efficacy testing was carried out by Dr Sergio Wittlin and colleagues at the Swiss Tropical and Public Health Institute (Basel, Switzerland). Mice (*n* = 3) were infected with a GFP-transfected *P. berghei* ANKA strain of malaria and parasitemia was determined using standard flow cytometry techniques. The activity of the drug lead or inclusion complex was calculated as the difference between the mean percentage parasitemia for the control and treated groups expressed as a percentage relative to the control group. Compounds were suspended in a 4% Tween80 and 9% ethanol [v/v] suspension vehicle and orally administered once per day on four consecutive days (4, 24, 48, and 72 h after infection).[17]

The results (Table 9) show that there is no significant difference between the antimalarial activity of DL4 and DMBDL4 at the 30 mg kg^{-1} and 10 mg kg^{-1} dosages. This is because the DL4 already has very high antimalarial activity at these dosages (>97% activity reduction in parasitemia) and any increase would be insignificant. However, there is a noticeable increase in the antimalarial activity of the DMBDL4 inclusion complex at the 3 mg kg^{-1} dosage with a 54.44% reduction in parasitemia. This is more than double the antimalarial activity for DL4 at the same dosage (20.83% parasitemia reduction). This increase is consistent with the results of the PK studies, which suggest that the slow-release action of the DMBDL4 inclusion complex results in a longer sustained concentration of DL4 over time.

The results of the *in vivo* studies showed that the inclusion complex DMBDL4, a new solid form of DL4, exhibited improved PK properties and increased antimalarial activity at low doses (3 mg kg^{-1}) compared to DL4.

Table 9: *in vivo* efficacy results for DL4 and DMBDL4.

Substance	Dosage (mg kg^{-1})	Parasitized RBC over 100[a]			Average	% of control	% Activity	Average mouse survival (days)
		Mouse 1	Mouse 2	Mouse 3				
DL4	30	0.40	0.40	0.40	0.40	1.28	98.72	8.3
DL4	10	1.00	0.50	0.60	0.70	2.24	97.76	7.0
DL4	3	18.40	27.40	28.40	24.73	79.14	20.83	3.0
DMBDL4	30	0.20	0.20	0.20	0.20	0.64	99.36	9.0
DMBDL4	10	0.50	0.30	0.50	0.43	1.39	98.61	7.0
DMBDL4	3	12.90	14.60	15.20	14.23	45.56	54.44	7.0
Control	-	28.70	28.50	20.90	26.03	83.33	16.67	3.0

[a]This is the number of parasitized red blood cells divided by 100.

References

1. Y. Younis, F. Douelle, T. Feng, D. G. Cabrera, C. Le Manach, A. T. Nchinda, S. Duffy, K. L. White, D. M. Shackleford, J. Morizzi, J. Mannila, K. Katneni, R. Bhamidipati, K. M. Zabiulla, J. T. Joseph, S. Bashyam, D. Waterson, M. J. Witty, D. Hardick, S. Wittlin, V. Avery, S. A. Charman and K. Chibale, *J. Med. Chem.,* 2012, **55**, 3479-3487.
2. D. L. Cruickshank, Y. Younis, N. M. Njuguna, D. S. B. Ongarora, K. Chibale and M. R. Caira, *CrystEngComm.*, 2014, **16**, 5781- 5792.
3. T. Loftsson, M. E. Brewster and M. Másson, *A. J. Drug Deliv.,* 2004, **2**, 261-275.
4. M. R. Caira, *Rev. Roum. Chim.,* 2001, **46**, 371-386.
5. Milli-Q water, Millipore Corporation, Billerica, Massachusetts, USA.
6. Bruker AXS Inc., Program SAINT, Version 7.60a, Bruker AXS Inc., Madison, WI, USA, 2006.
7. G. M. Sheldrick, Program SADABS, Version 2.05, University of Göttingen, Germany, 2007.
8. Bruker AXS Inc., XPREP, Version 5.1, Bruker AXS Inc., Madison, WI, USA, 1997.
9. G. M. Sheldrick, *Acta Crystallogr. A.,* 2008, **64**, 112-122.
10. L. J. Barbour, *J. Supramol. Chem.,* 2001, **1**, 189-191.
11. F. H. Allen, *Acta Crystallogr.*, 2002, **B58**, 380-388.
12. T. Aree, H. Hoier, B. Schulz, G. Reck and W. Saenger, *Angew. Chem. Int. Ed.*, 2000, **39**, 897-899.
13. T. Aree, W. Saenger, P. Leibnitz and H. Hoier, *Carbohydr. Res.*, 1999, **315**, 199-205.
14. C. F. Macrae, I. J. Bruno, J. A. Chisholm, P. R. Edgington, P. McCabe, E. Pidcock, L. Rodriguez-Monge, R. Taylor, J. van de Streek and P. A. Wood, *J. Appl. Cryst*., 2008, **41**, 466-470.
15. T. Higuchi and K. A. Connors, *Adv. Anal. Chem. Instrum.,* 1965, **4**, 117-212.
16. P. Melariri, L. Kalombo, P. Nkuna, A. Dube, R. Hayeshi, B. Ogutu, L. Gibhard, C. deKock, P. Smith, L. Wiesner, H. Swai, *Int. J. Nanomedicine*, 2015, **10**, 1493-1503.

17. C. Le Manach, T. Paquet, D. G. Cabrera, Y. Younis, D. Taylor, L. Wiesner, N. Lawrence, S. Schwager, D. Waterson, M. J. Witty, S. Wittlin, L. J. Street, K. Chibale, *J. Med. Chem.*, 2014, **57**, 8839-8848.

CHAPTER 7: Conclusion

This chapter presents a summary of the most significant outcomes of the study, with comments on the possible implications for the future development of the drug leads investigated and suggestions for further work. Single crystal X-ray structures were determined for two novel antimalarial drug leads. Three salts and one cyclodextrin (CD) inclusion complex of a novel antimalarial drug lead were isolated, fully characterized and their single crystal X-ray structures determined.

DL1

No suitable single crystals of DL1 were isolated, precluding the possibility of full structural analysis. No supramolecular derivatives of DL1 were obtained from the co-crystal screening or CD inclusion experiments and this compound proved to be very challenging to work with. The lack of positive results of the experiments with DL1 demonstrates the ability of early supramolecular intervention to streamline the drug discovery and design process by identifying compounds that may not be amenable to beneficiation via supramolecular derivatisation.

DL2

Single crystals of DL2 were prepared by recrystallization from acetone and the X-ray crystal structure was determined. A search of the Cambridge Structural Database[1] revealed that functional groups that were most likely to form supramolecular heterosynthons with the functional groups in DL2 could be provided by carboxylic acid and amide co-formers. Nine compounds from these classes were selected for co-crystal screening with DL2.

Equimolar amounts of DL2 and each co-former were ground with a mortar and pestle for 15 minutes and the products were analysed using PXRD. The results indicated that all of the experiments resulted in physical mixtures only. The next stage of the co-crystal screening was liquid-assisted grinding (LAG) which involved grinding equimolar amounts of DL2 and co-former for 15 minutes while adding small drops of

ethanol or acetonitrile. The products of the LAG experiments were analysed using PXRD and the results show that only physical mixtures of DL2 and the co-former were obtained.

CD inclusion with DL2 was attempted using the kneading and co-precipitation methods. DL2 and an equimolar amount of either α-, β- or γ-CD were co-ground for 20 minutes while drops of water were added to maintain a paste-like consistency. The PXRD traces of the products were compared with known powder patterns for common isostructural complexes. The PXRD traces of the products did not match any of the isostructural patterns and it was found that all of the kneading experiments had resulted in physical mixtures of DL2 and the corresponding CD.

The fact that none of the desired products (co-crystals or inclusion complexes) could be isolated indicates that DL2 may not be a favourable candidate for further drug development. The poor solubility of this compound may be a result of the strong intramolecular and intermolecular hydrogen bonding systems in DL2 that could preclude its ability to form new hydrogen bonds with other molecules.

DL3

The X-ray crystal structure of DL3 was determined after suitable single crystals were prepared by recrystallization of DL3 from acetone. DL3 displayed poor solubility in both aqueous and organic media and it was therefore necessary to explore alternative methods of enhancing its solubility. Phase solubility studies were performed with DL3 and both β-CD and HPβCD using the methodology described by Higuchi and Connors.[2] The phase solubility profiles for β-CD and HPβCD displayed A_P- and A_L-type behaviour respectively. In both cases the apparent solubility of DL3 increased by a factor of more than 350 at the highest concentration of CD used. The results of the phase solubility studies demonstrate that it is possible to significantly enhance the apparent solubility of DL3 through CD inclusion. This is an encouraging result indicating that aqueous cyclodextrin solutions could have applications as media for alternative modes of delivery as well as further biological testing of this poorly soluble drug lead.

DL4

Co-crystal screening was carried out with DL4, a novel antimalarial drug lead that has been reported in the literature.[3] Based on the success of published co-crystal studies with DL4 (five salts and one novel co-crystal were reported),[4] another series of co-formers was selected for co-crystal screening with this drug lead. Three hits were identified from liquid-assisted grinding (LAG) experiments and co-precipitation experiments were performed in each case.

Three novel salts of DL4 were prepared, namely DL4ADI, DL4CIT and DL4ORO. The salts were fully characterised using spectroscopic and thermal techniques and the X-ray crystal structure of each salt was determined. It was observed that for each of the salts a $R_2^2(8)$ hydrogen bonding motif formed between the amino-pyridinium group of the DL4 cation and the carboxylate group of the co-former anion. Furthermore, the crystal packing and principal hydrogen bonding interactions in DL4CIT and DL4ORO were found to be very similar. This suggests that co-formers with a similar size and structure to orotic acid and citric acid could potentially form salts of DL4 that have the same crystal packing and hydrogen bonding interactions occurring in DL4CIT and DL4ORO.

A turbidimetric solubility test showed that DL4ADI had an apparent solubility that was less than that of DL4. The equilibrium solubility for DL4CIT at 25 ± 0.5 °C was determined to be 48 times greater than that of DL4.

Kneading and co-precipitation experiments were carried out with DL4 in an attempt to isolate inclusion complexes with CDs. An inclusion complex between DIMEB and DL4 (DMBDL4) was isolated and fully characterized. Phase solubility studies were performed with DL4 and β-CD, HPβCD and DIMEB. The results revealed that the apparent solubility of DL4 increased by factors of 30, 80 and 100 respectively at the highest concentrations of β-CD, HPβCD and DIMEB employed.

DMBDL4 was submitted for biological testing to establish whether inclusion of DL4 in DIMEB might have any effect on the *in vivo* pharmacokinetic (PK) properties and

efficacy of DL4. The results of *in vivo* PK studies with DMBDL4 were consistent with a slow-release of DL4 from the inclusion complex, as evidenced by the increased half-life and T_{max} compared to uncomplexed DL4. The results also suggested that DMBDL4 dissociated after gastric emptying and that DL4 was absorbed in the duodenum and jujenum and not the stomach, as was the case with untreated DL4. *In vivo* efficacy testing showed that the antimalarial activity of DMBDL4 at the 3 mg kg^{-1} dose was more than double that of DL4 at the same dosage (54.4% and 20.8% respectively). These results demonstrate that CD inclusion was able to produce a new solid form of DL4 that exhibited enhanced aqueous solubility and antimalarial activity at low doses compared to DL4.

This study demonstrates that supramolecular modification of poorly soluble compounds can result in new solid forms with superior physicochemical properties. It also highlights the effectiveness of employing supramolecular intervention in parallel with the drug discovery process as a tool for selecting suitable candidates for further development, ultimately reducing preclinical candidate attrition. [5,6]

Future work

Phase solubility studies showed that DL3 forms 1:1 complexes with β-CD and HPβCD in solution. Solid-state kneading and co-precipitation experiments with cyclodextrins should be performed in an attempt to isolate inclusion complexes between DL3 and these host compounds.

If the inclusion complex DMBDL4 dissociates after gastric emptying and DL4 is absorbed in the duodenum and the jujenum, then the solubility of DMBDL4 would be greatest at pH 7.4. Kinetic solubility studies should be carried out with DMBDL4 to determine whether there is a pH-dependent change in the absorption of DMBDL4 and thereby determine its site of absorption.[7]

References

1. Cambridge Structural Database and Cambridge Structural Database system, Version 5.36 (updates to May 2015), Cambridge Crystallographic Data Centre, University Chemical Laboratory; Cambridge, England, 2014.
2. T. Higuchi and K. A. Connors, *Adv. Anal. Chem. Instrum.,* 1965, **4**, 117-212.
3. Y. Younis, F. Douelle, T. Feng, D. G. Cabrera, C. Le Manach, A. T. Nchinda, S. Duffy, K. L. White, D. M. Shackleford, J. Morizzi, J. Mannila, K. Katneni, R. Bhamidipati, K. M. Zabiulla, J. T. Joseph, S. Bashyam, D. Waterson, M. J. Witty, D. Hardick, S. Wittlin, V. Avery, S. A. Charman and K. Chibale, *J. Med. Chem.,* 2012, **55**, 3479-3487.
4. D. L. Cruickshank, Y. Younis, N. M. Njuguna, D. S. B. Ongarora, K. Chibale and M. R. Caira, *CrystEngComm.*, 2014, **16**, 5781- 5792.
5. M. Palucki, J. D. Higgins, E. Kwong and A. C. Templeton, *J. Med. Chem.*, 2010, **53**, 5897-5905.
6. S. Balbach and C. Korn, *Int. J. Pharm.*, 2004, **275**, 1-12.
7. P. A. Shore, B. B. Brodie and C. A. M. Hogben, *J. Pharmocol. Exp. Ther.*, 1957, **119.3**, 361-369.

Appendix

Crystallographic data files

This document contains all of the PXRD traces from the co-crystal and CD inclusion experiments that were not included in the dissertation.

The crystallographic data files and checkcif reports for all of the X-ray crystal structures have been included in the folders listed in Table 1. The crystallographic files included in each folder have the extensions .res, .hkl, .cif, .fcf, .xl, .sup and .lis. A checkcif document for each structure has also been included in .pdf format. All of the folders listed in Table 1 are contained in one folder labelled “Appendix”.

Table 1: The names and contents for each of the folders included in the Appendix folder.

Folder Name	Contents
DL2	Crystallographic data files for DL2
DL3	Crystallographic data files for DL3
DL4ADI	Crystallographic data files for DL4ADI
DL4CIT	Crystallographic data files for DL4CIT
DL4ORO	Crystallographic data files for DL4ORO

DL1

This section includes LC-MS, ^{1}H NMR and ^{13}C NMR data for DL1. It also includes a detailed account of experiments that were performed with DL1.

Liquid chromatography-mass spectrometry (LC-MS)

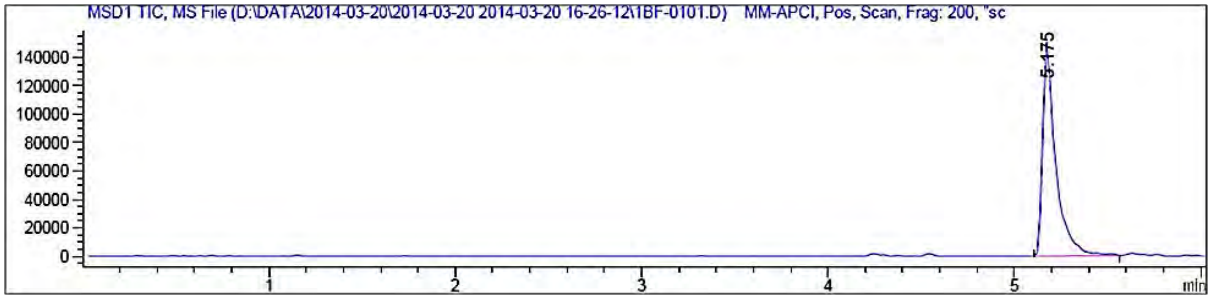

Figure 1: LC chromatogram of DL1.

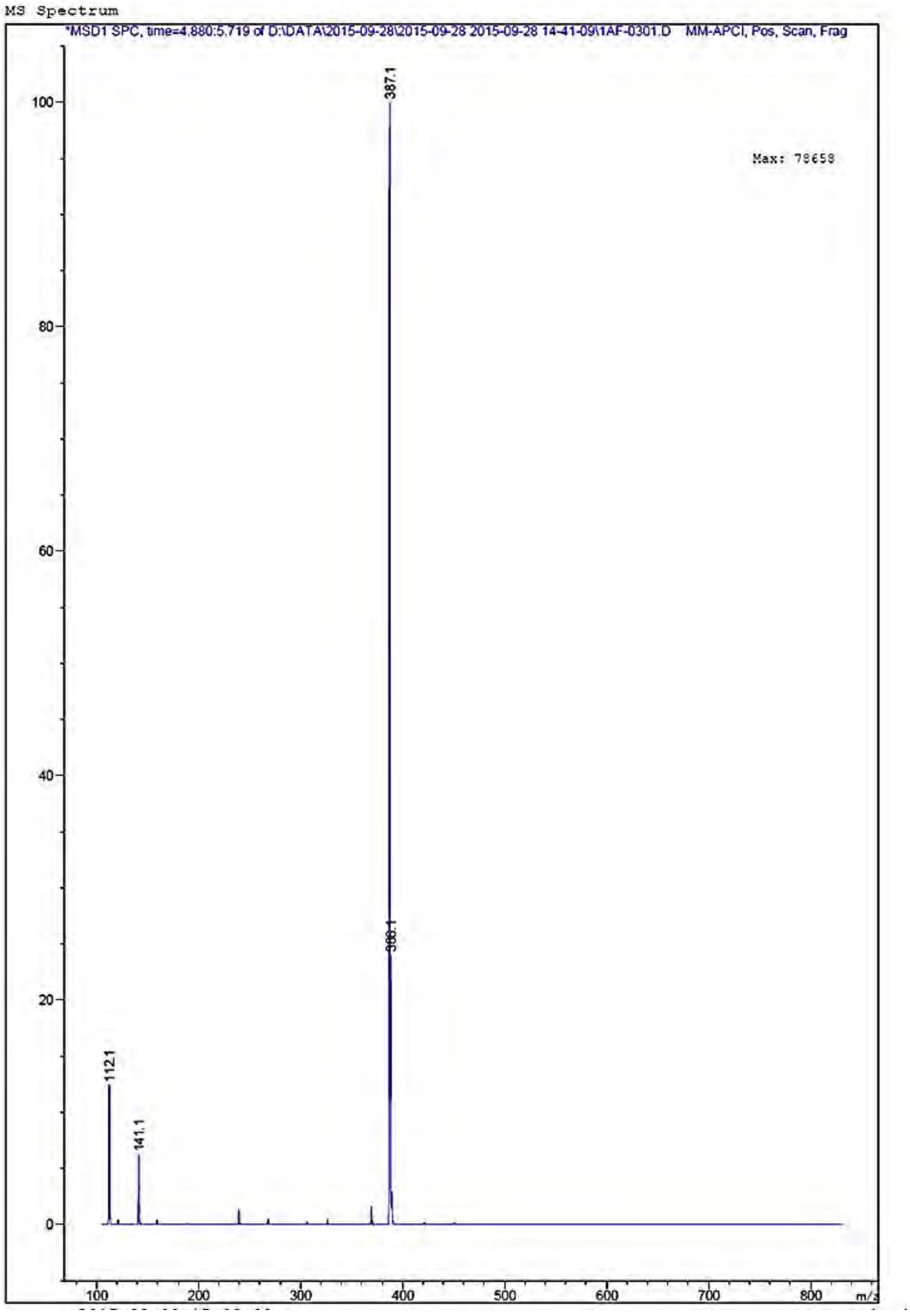

Figure 2: Mass spectrum of DL1.

^{1}H NMR

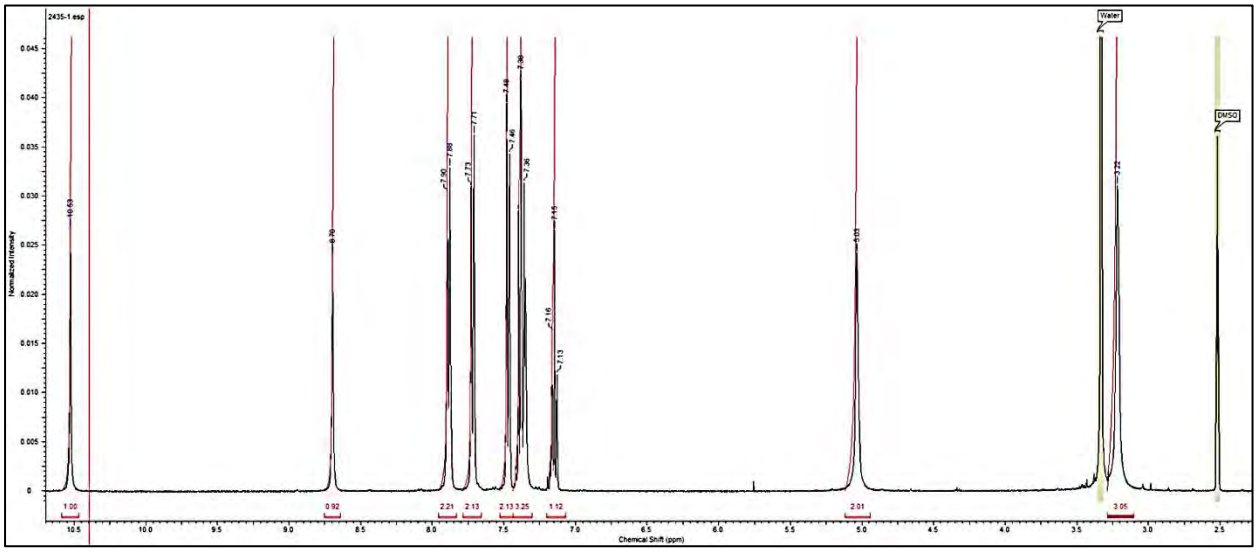

Figure 3: ^{1}H NMR spectrum of DL1in DMSO-d_6.

^{13}C NMR

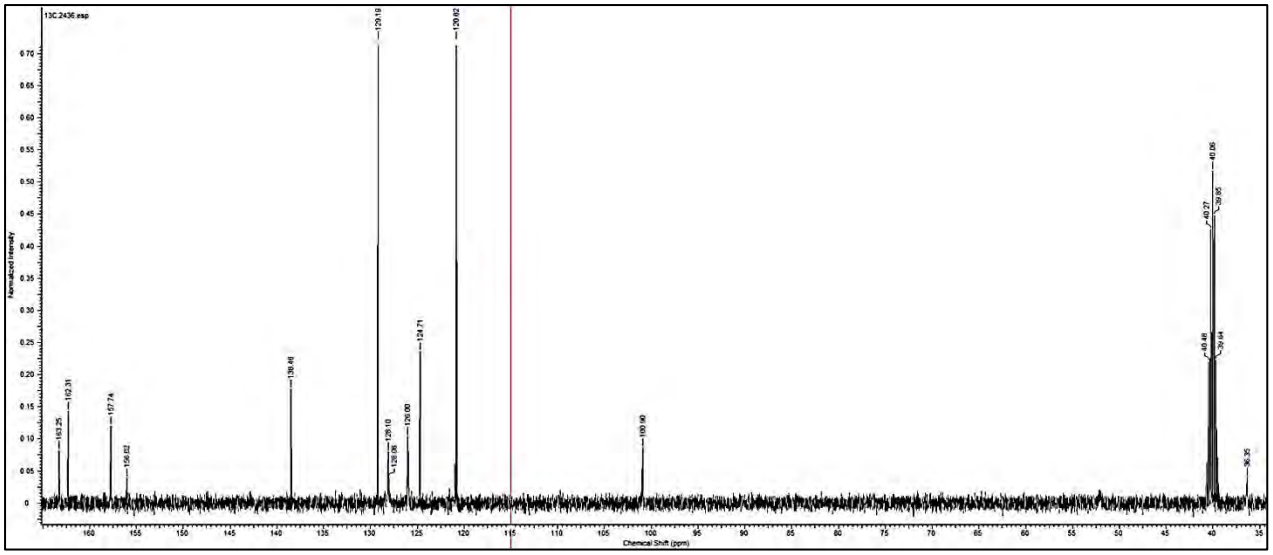

Figure 4: ^{13}C NMR spectrum of DL1 in DMSO-d_6.

Recrystallizations

DL1 was recrystallized from eight solvents as summarized in Table 2. In general, 10 mg of the compound was dissolved in a minimum of solvent while heating to ~50 °C. The solutions were filtered through a 0.45 µm nylon filter into a clean vial

and left on the bench to crystallize. In the case of recrystallization from isopropanol, the vial was maintained at a temperature of 40 °C to allow the solvent to evaporate slowly. For vapour diffusion, 10 mg of DL1 was dissolved in dichloromethane and the vial was placed inside a larger vial containing ethyl acetate. None of the crystallization attempts resulted in crystals that were suitable for SCXRD.

Table 2: Recrystallization experiments with DL1.

Solvent	Crystallization method
Methanol	Slow evaporation at ambient temp.
Ethanol	Slow evaporation at ambient temp.
Diethyl ether	Slow evaporation at ambient temp.
Ethyl acetate	Slow evaporation at ambient temp.
Acetonitrile	Slow evaporation at ambient temp.
Hexane	Slow evaporation at ambient temp.
Isopropanol	Slow evaporation at 40 °C
Dichloromethane/ethyl acetate	Vapour diffusion

Co-crystal screening

10 mg of DL1 was co-ground with an equimolar amount of the co-former for 15 minutes while small drops of ethanol were added. The products of the experiments were analysed by PXRD and the results show that all of the products were physical mixtures of DL1 and the co-former (Table 3). The products of the LAG experiments were recrystallized, but no single crystals were obtained using this method.

Table 3: Co-formers, molar ratios and experimental outcomes for LAG experiments with DL1.

Co-former	Molar ratio	Experimental outcomes	Recrystallization of LAG product
Adipic acid	1:1	Physical mixture	No single crystals
Uracil	1:1	Physical mixture	No single crystals
Benzamide	1:1	Physical mixture	No single crystals
Isonicotinamide	1:1	Physical mixture	No single crystals
L-ascorbic acid	1:1	Physical mixture	No single crystals
L-tartaric acid	1:1	Physical mixture	No single crystals
Orotic acid	1:1	Physical mixture	No single crystals
Uric acid	1:1	Physical mixture	No single crystals
Citric acid	1:1	Physical mixture	No single crystals
Nicotinic acid	1:1	Physical mixture	No single crystals
L-malic acid	1:1	Physical mixture	No single crystals
Propionamide	1:1	Physical mixture	No single crystals

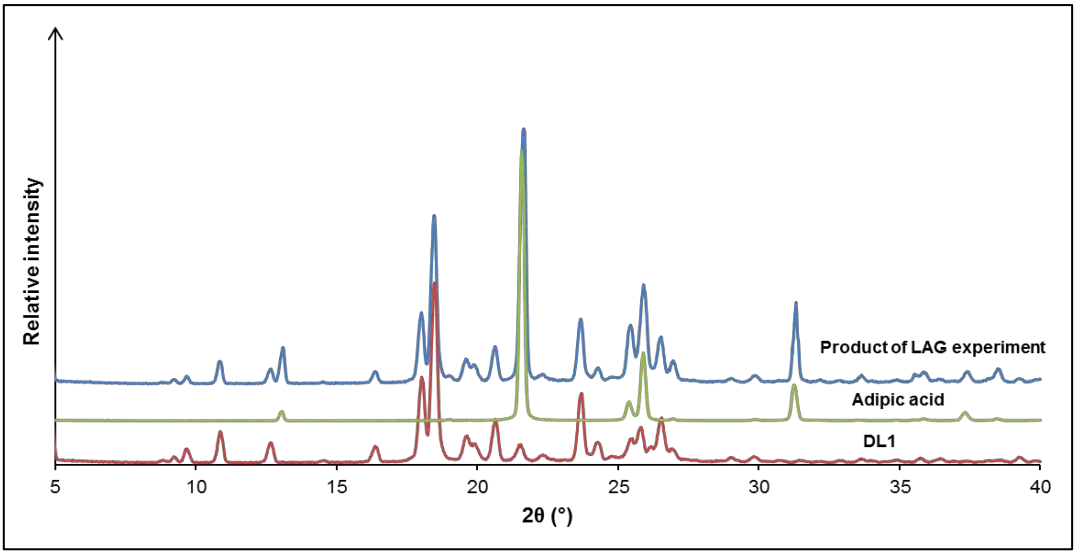

Figure 5: PXRD traces of DL1, adipic acid and the product of LAG.

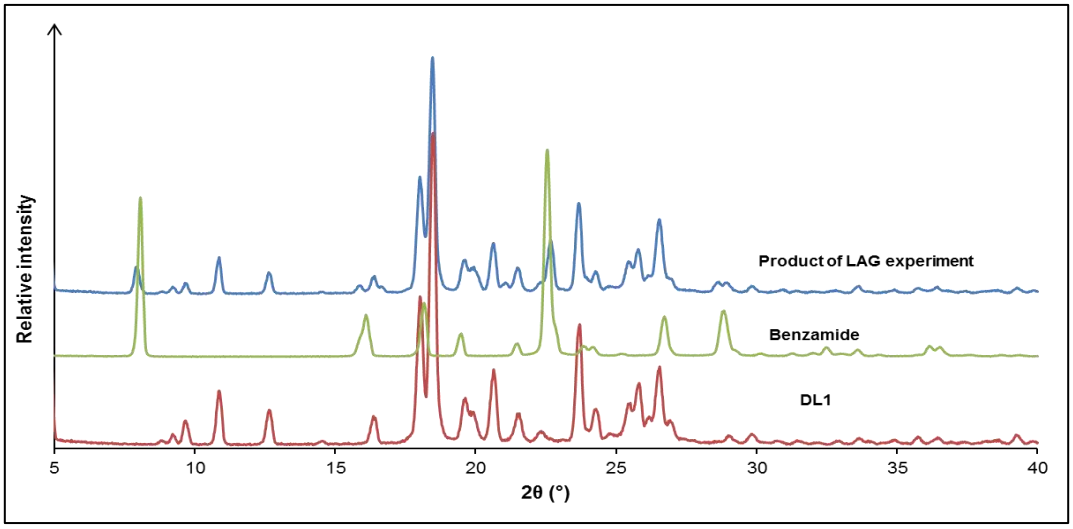

Figure 6: PXRD traces of DL1, benzamide and the product of LAG.

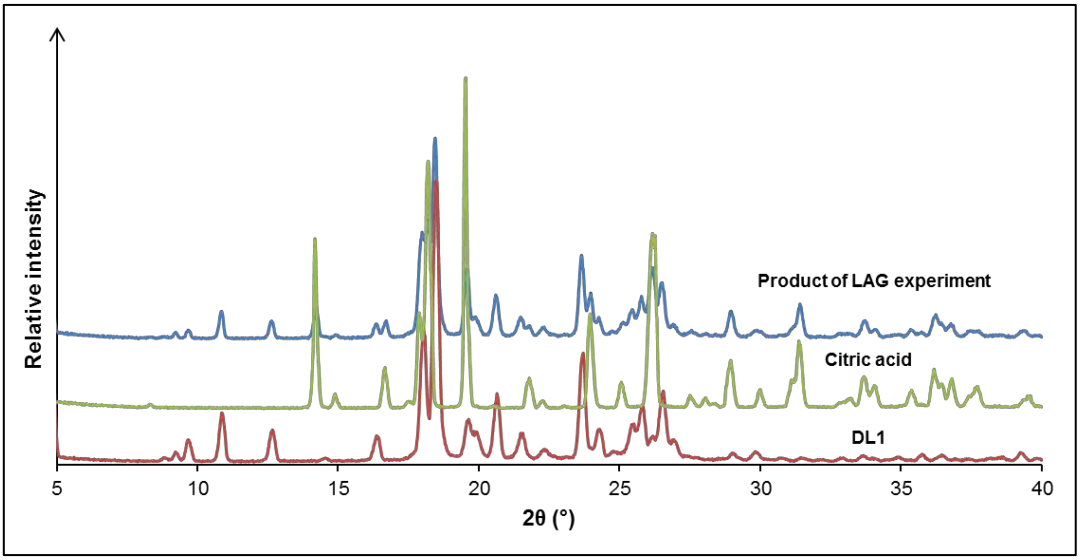

Figure 7: PXRD traces of DL1, citric acid and the product LAG.

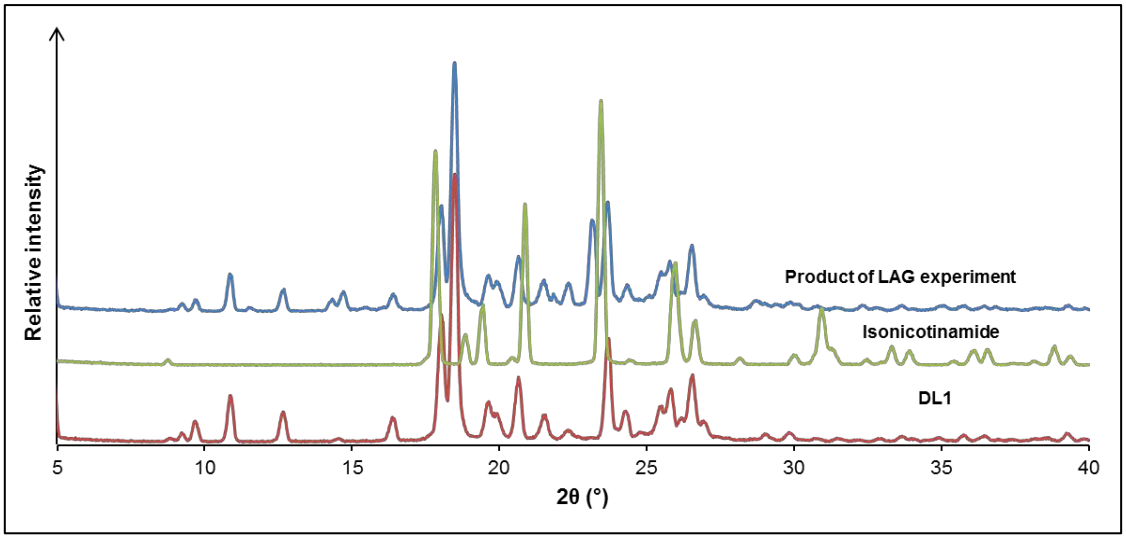

Figure 8: PXRD traces of DL1, isonicotinamide and the product of LAG.

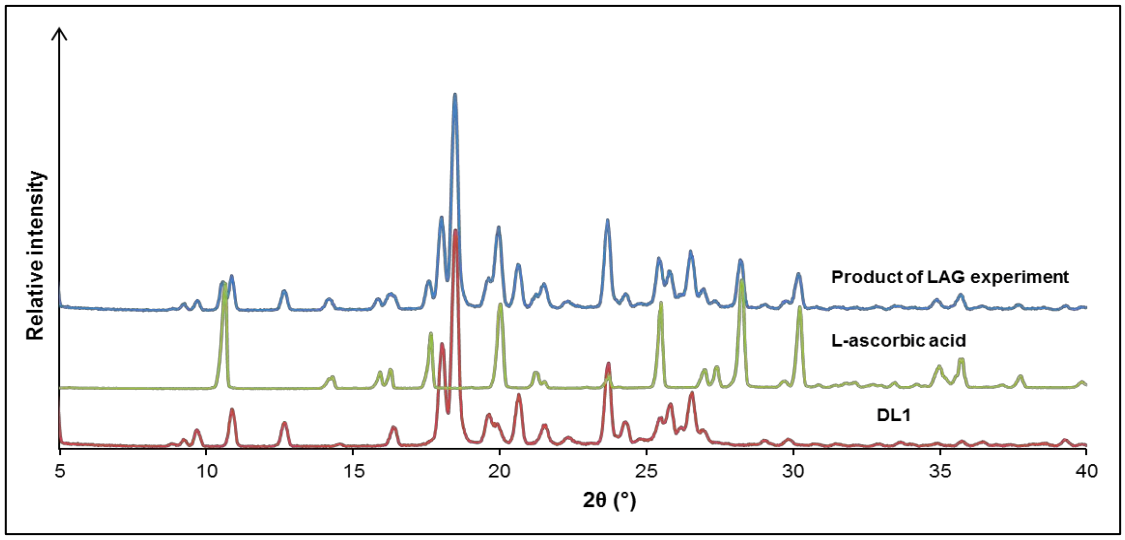

Figure 9: PXRD traces of DL1, L-ascorbic acid and the product of LAG.

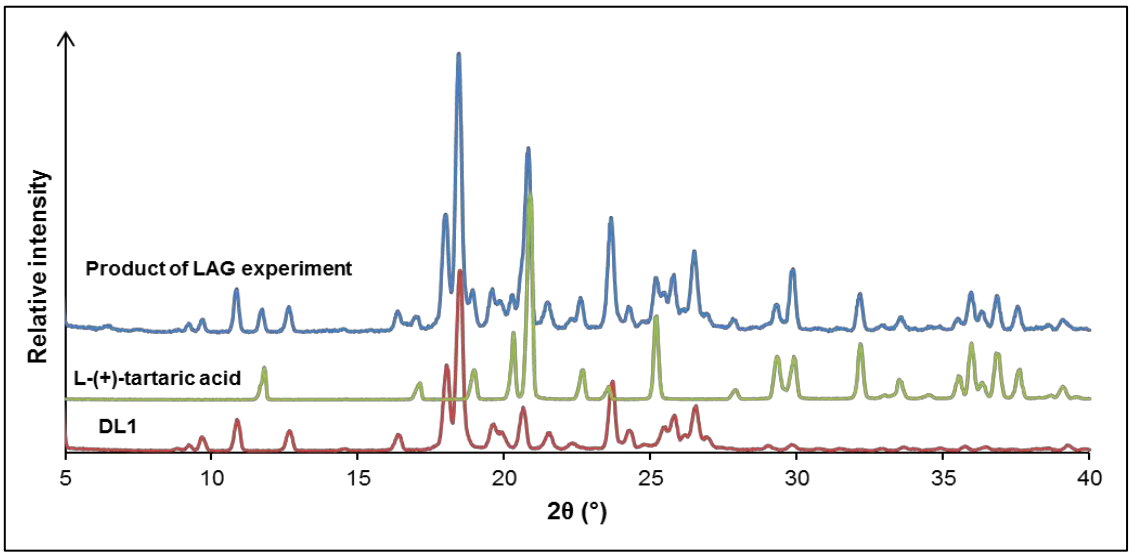

Figure 10: PXRD traces of DL1, L-(+)-tartaric acid and the product of LAG.

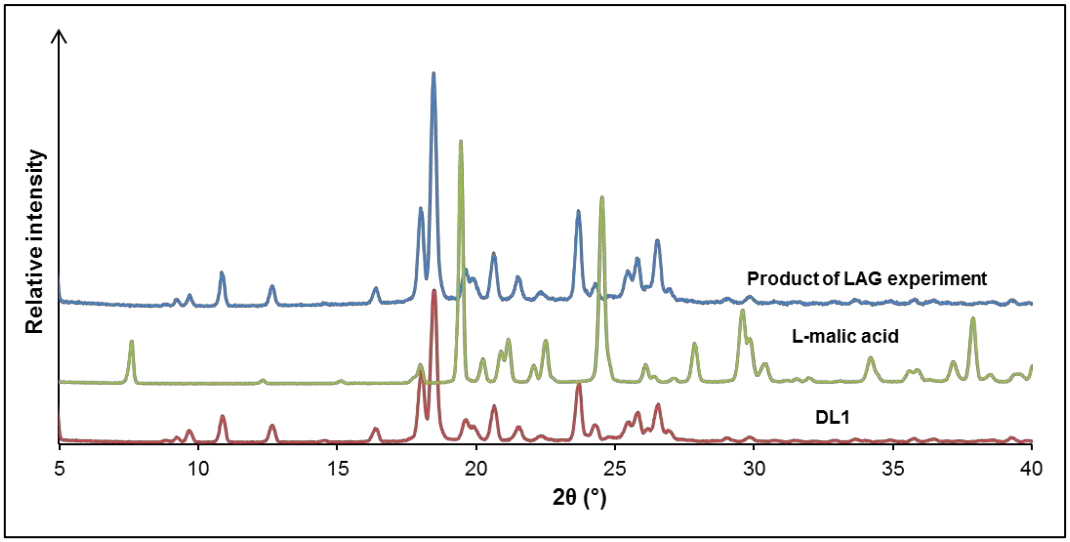

Figure 11: PXRD traces of DL1, L-malic acid and the product of LAG.

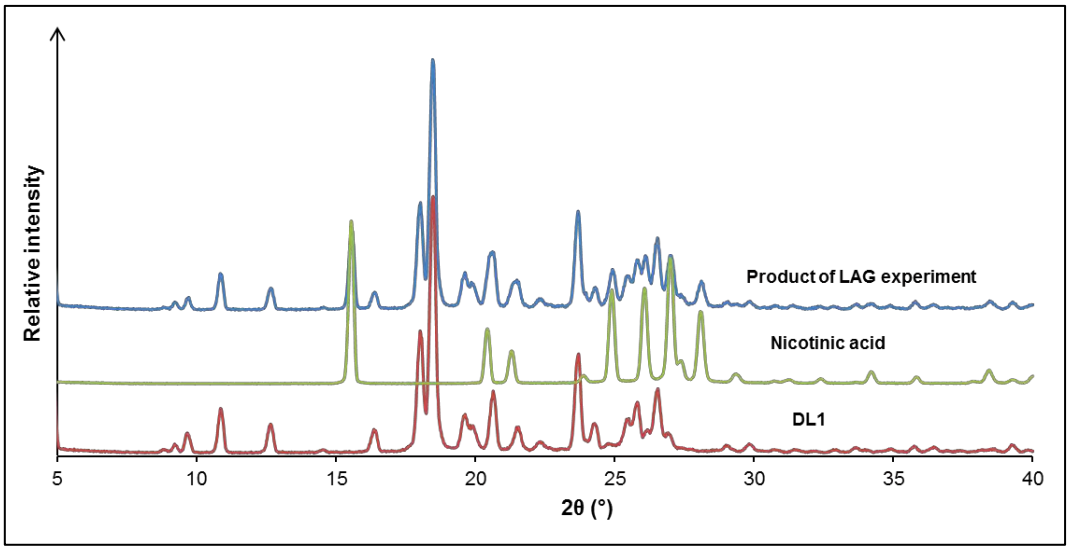

Figure 12: PXRD traces of DL1, nicotinic acid and the product of LAG.

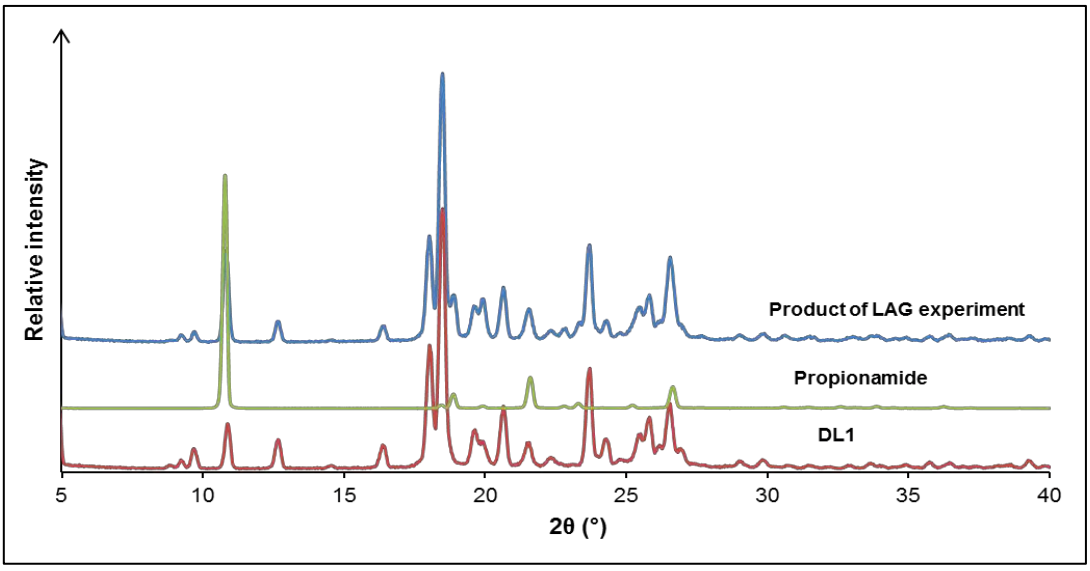

Figure 13: PXRD traces of DL1, propionamide and the product of LAG.

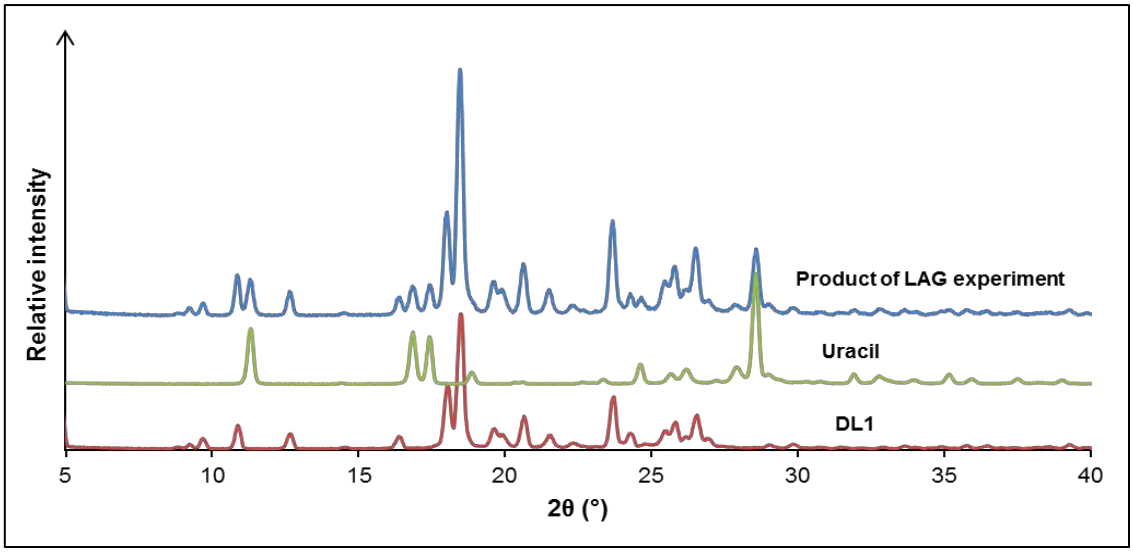

Figure 14: PXRD traces of DL1, uracil and the product of LAG.

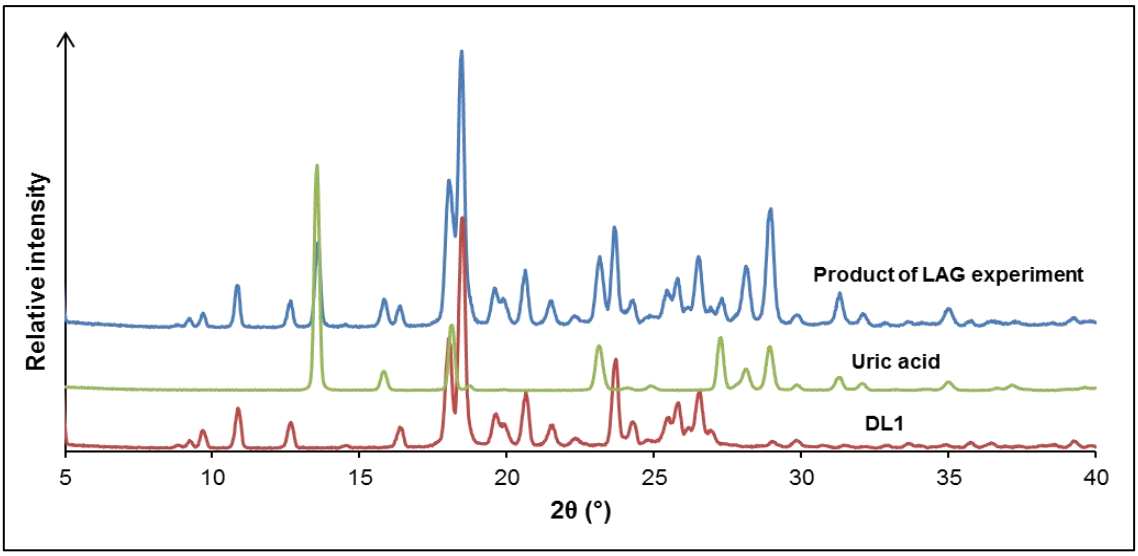

Figure 15: PXRD traces of DL1, uric acid and the product of LAG.

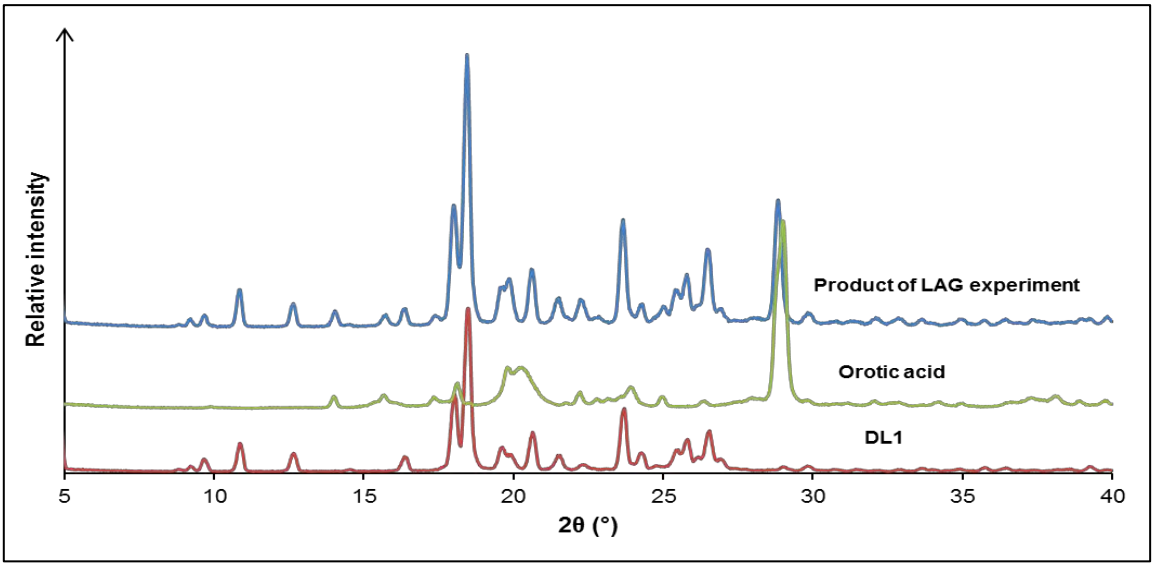

Figure 16: PXRD traces of DL1, orotic acid and the product of LAG.

CD inclusion

10 mg of DL1 was co-ground with an equimolar amount of α-CD, β-CD or γ-CD for 15 minutes. Drops of water were added to maintain a paste-like texture during the kneading experiment. The products were analysed using PXRD and the results show that a complex formed between DL1 and γ-CD. Kneading α-CD and DL1 and γ-CD and DL1 resulted in physical mixtures of the components.

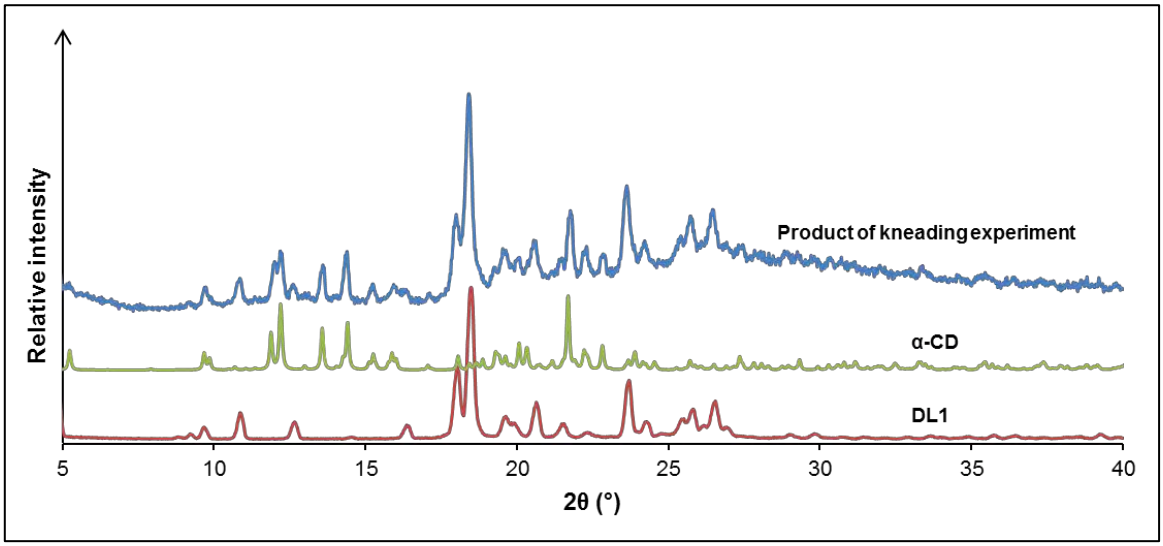

Figure 17: PXRD traces of DL1, α-CD and the product of kneading α-CD and DL1.

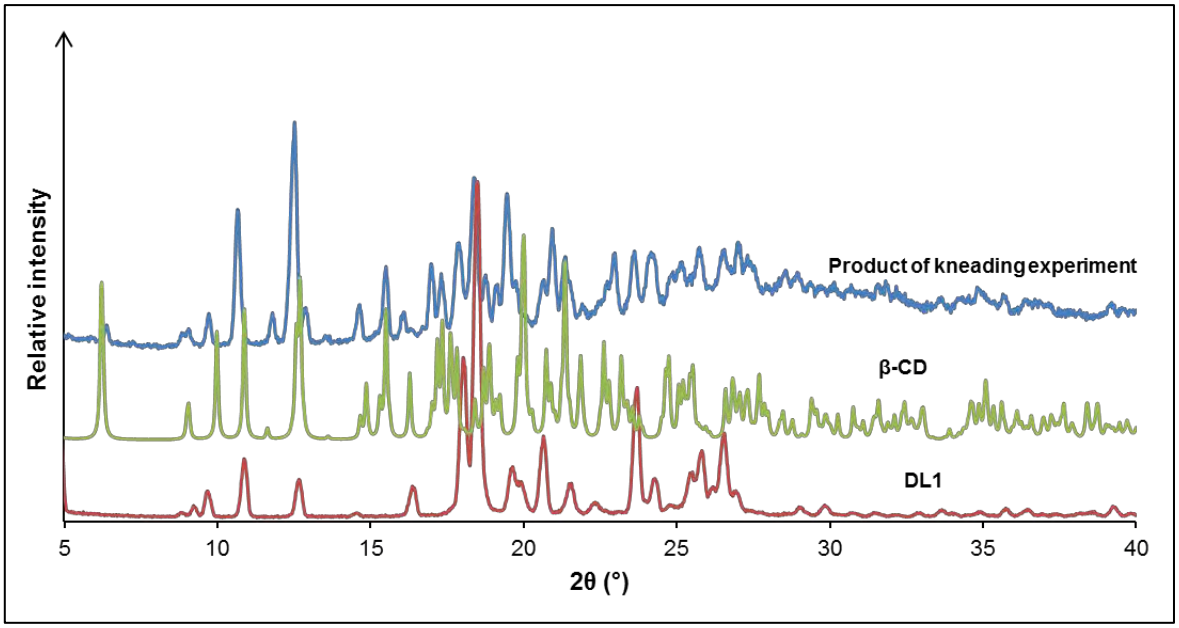

Figure 18: PXRD traces of DL1, β-CD and the product of kneading DL1 and β-CD.

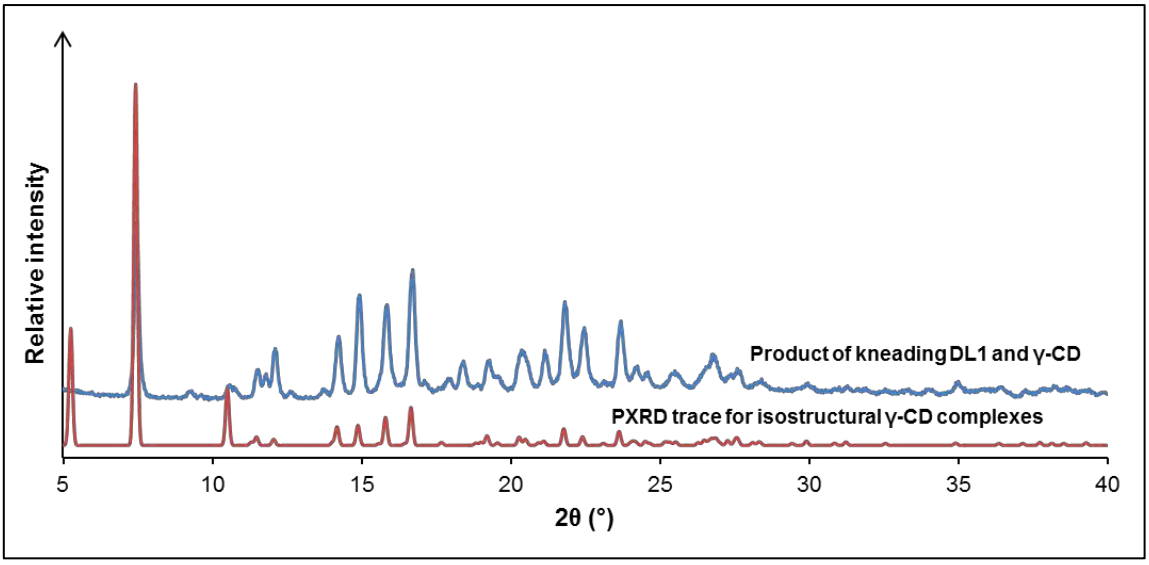

Figure 19: PXRD traces of isostructural γ-CD complexes and the product of kneading γ-CD and DL1.

DL2

The LC-MS, ^{1}H NMR and ^{13}C NMR spectra for DL2 were provided by H3D and are shown below.

LC-MS

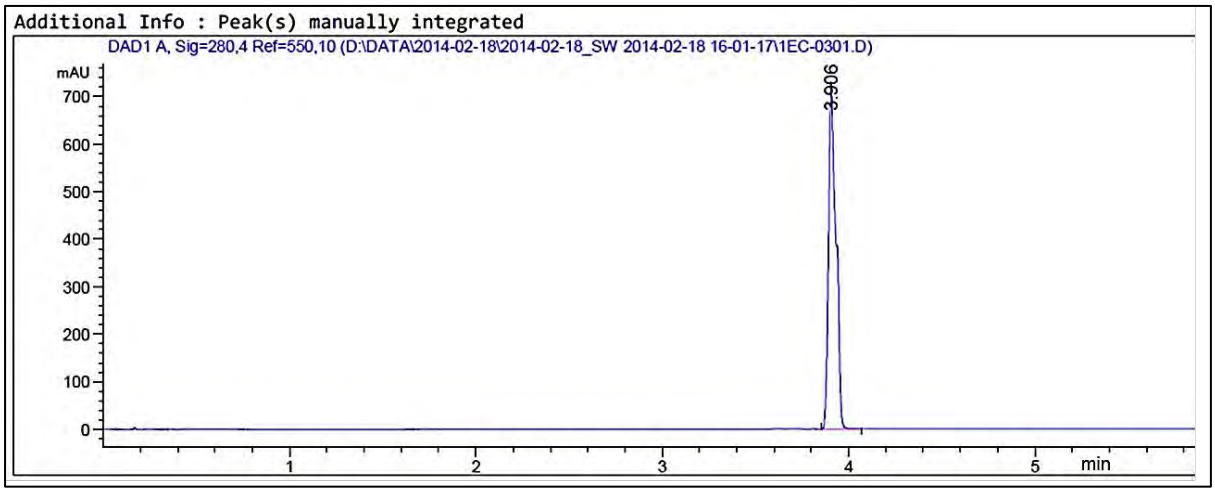

Figure 20: LC chromatogram of DL2.

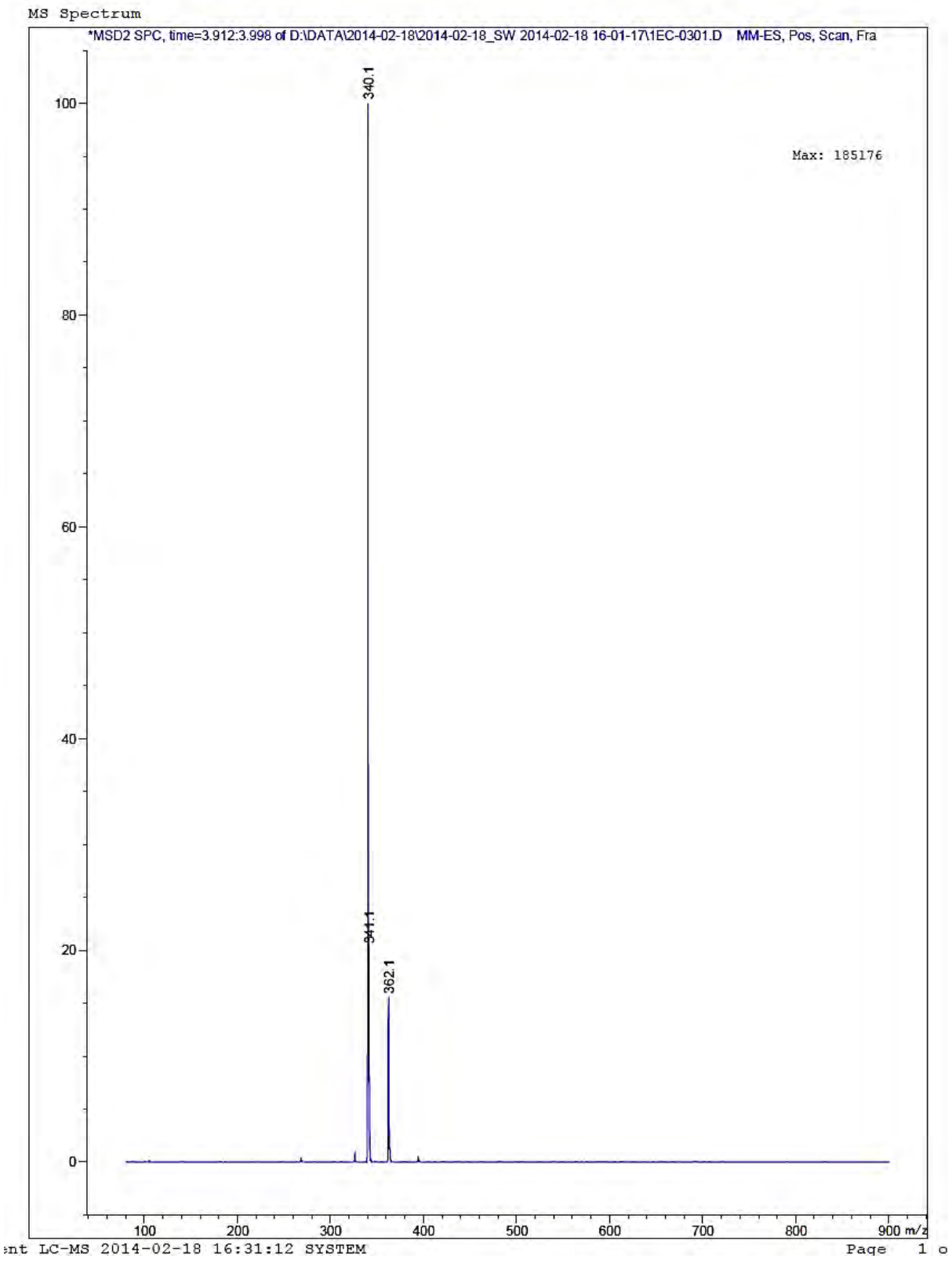

Figure 21: Mass spectrum of DL2.

^{1}H NMR

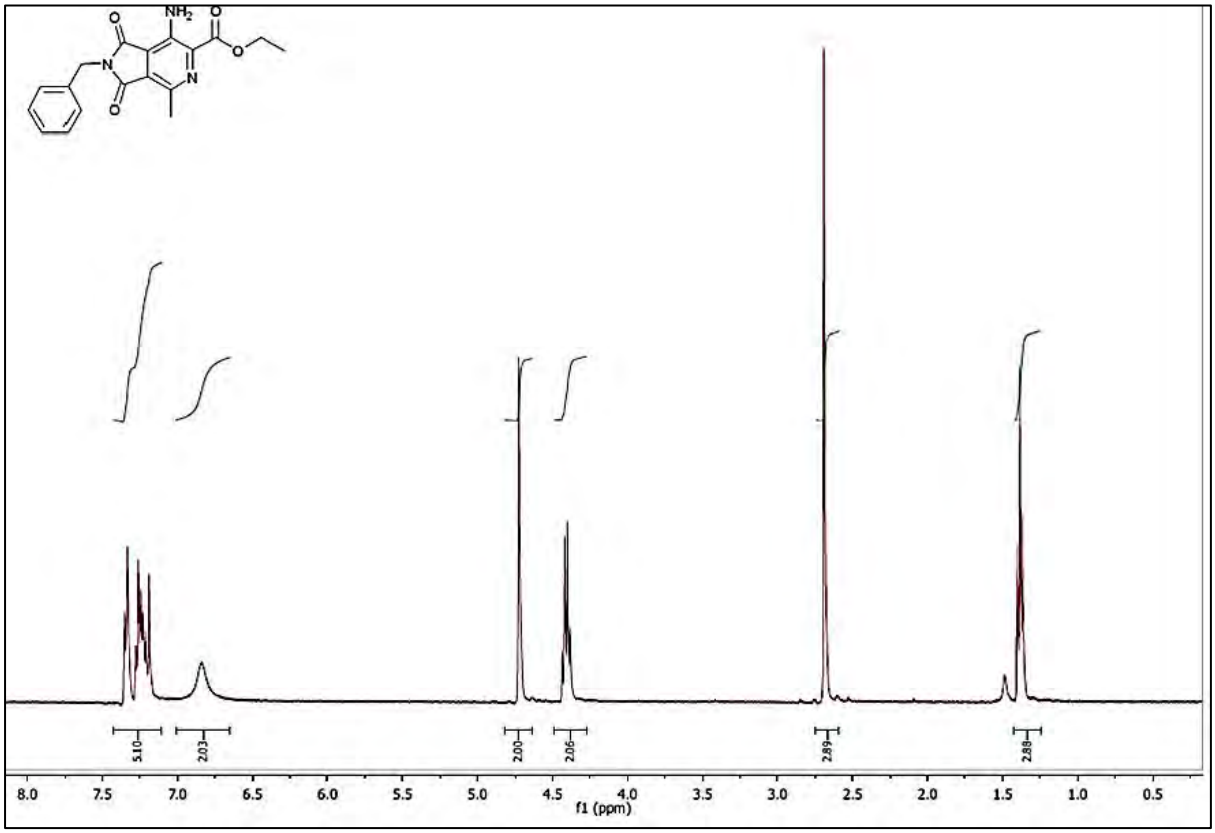

Figure 22: ^{1}H NMR spectrum of DL2 in $CDCl_3$.

PXRD traces for dry co-grinding experiments

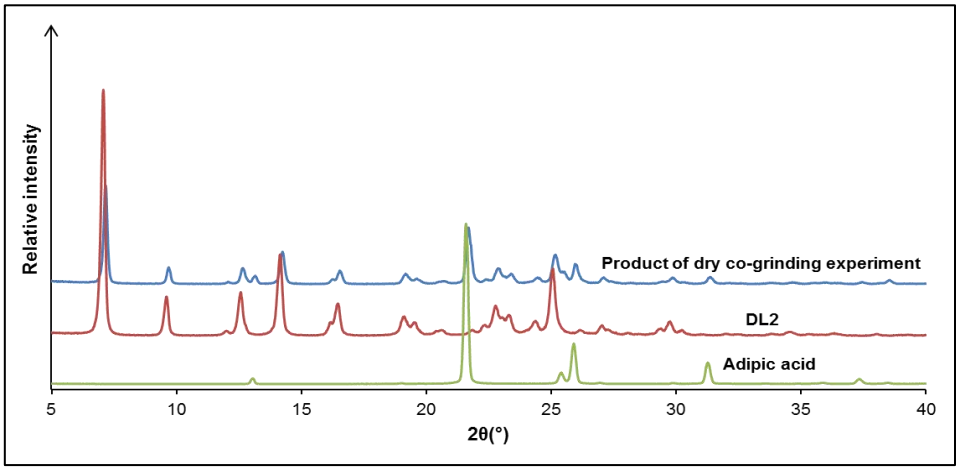

Figure 23: PXRD traces of adipic acid, DL2 and the product of the dry co-grinding experiment.

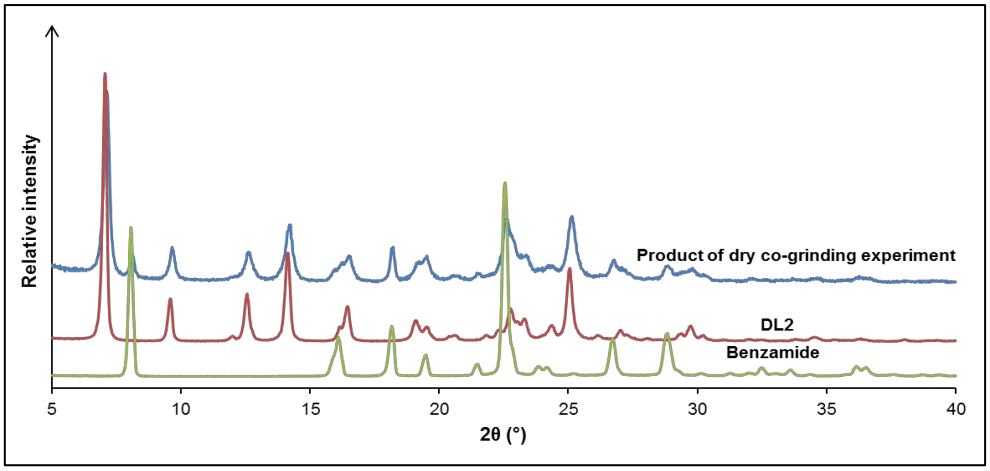

Figure 24: PXRD traces of benzamide, DL2 and the product of the dry co-grinding experiment.

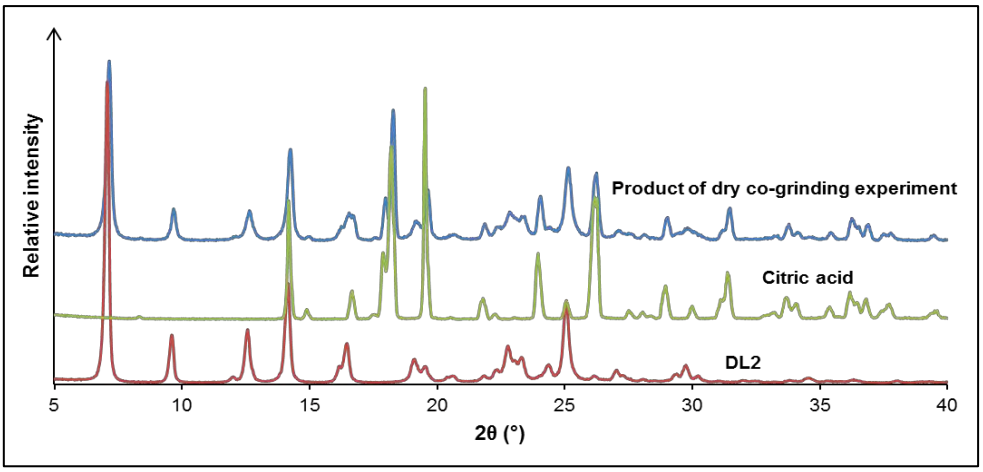

Figure 25: PXRD traces of DL2, citric acid and the product of the dry co-grinding experiment.

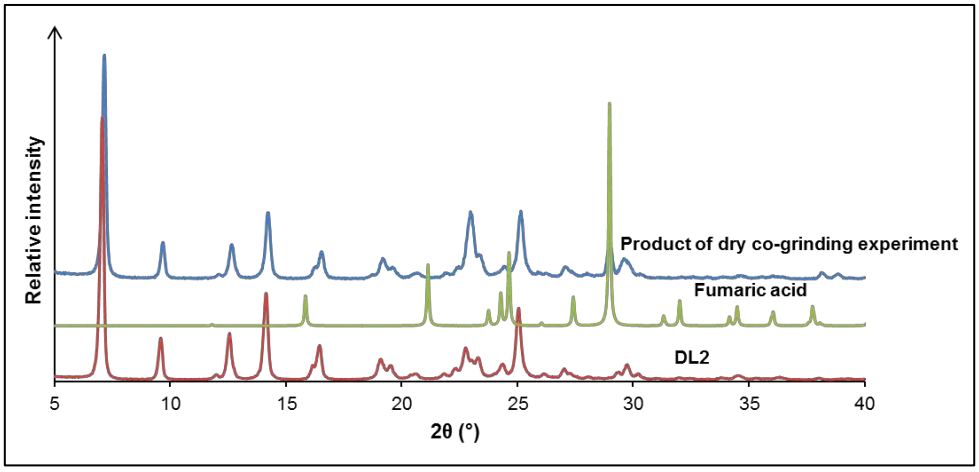

Figure 26: PXRD traces of DL2, fumaric acid and the product of the dry co-grinding experiment.

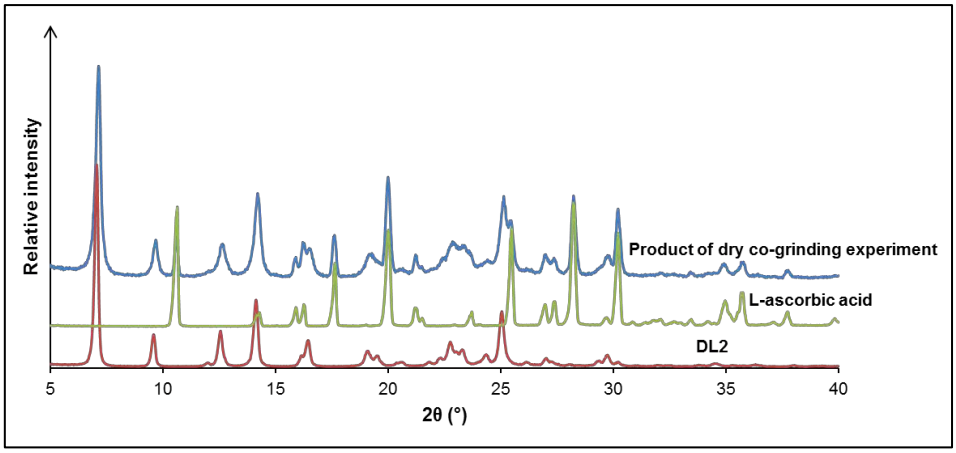

Figure 27: PXRD traces of DL2, L-ascorbic acid and the product of the dry co-grinding.

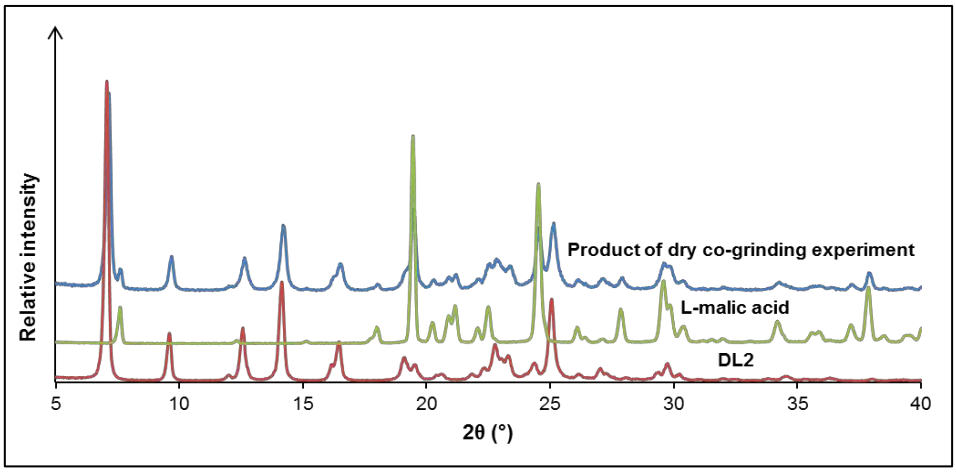

Figure 28: PXRD traces of DL2, L-malic acid and the product of the dry co-grinding experiment.

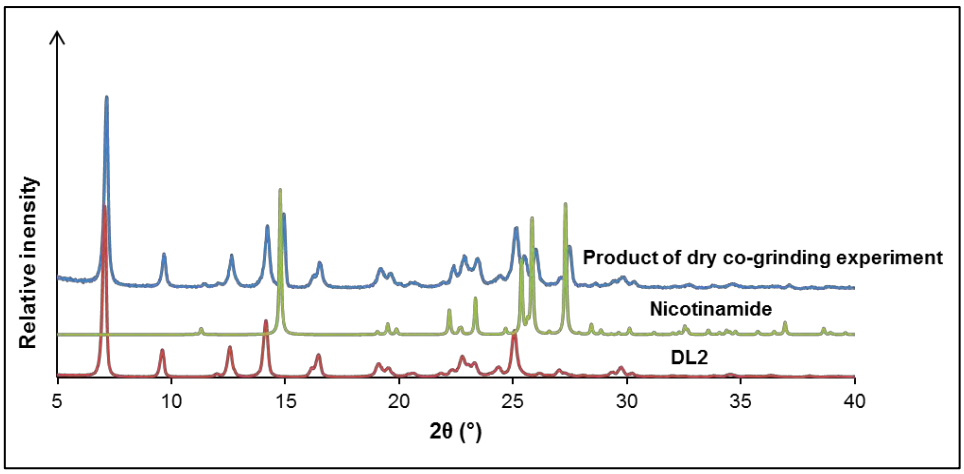

Figure 29: PXRD traces of DL2, nicotinamide and the product of the dry co-grinding experiment.

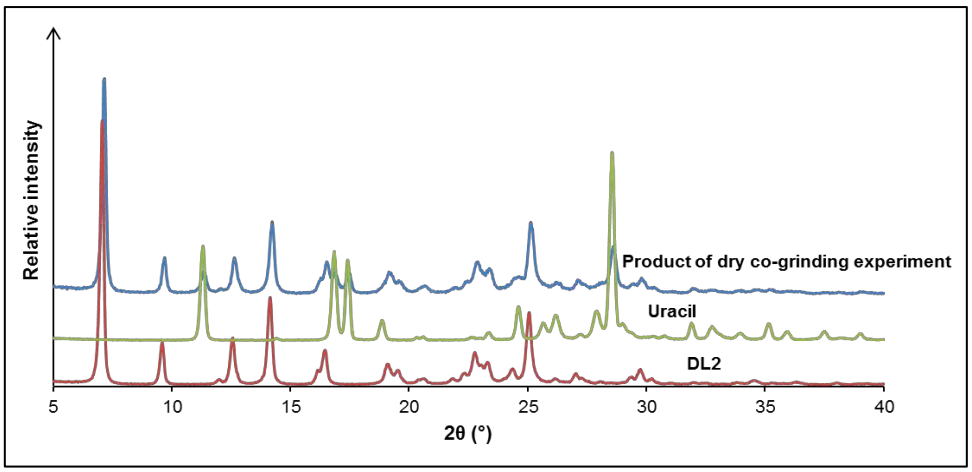

Figure 30: PXRD traces of DL2, uracil and the product of the dry co-grinding experiment.

PXRD traces from LAG experiments

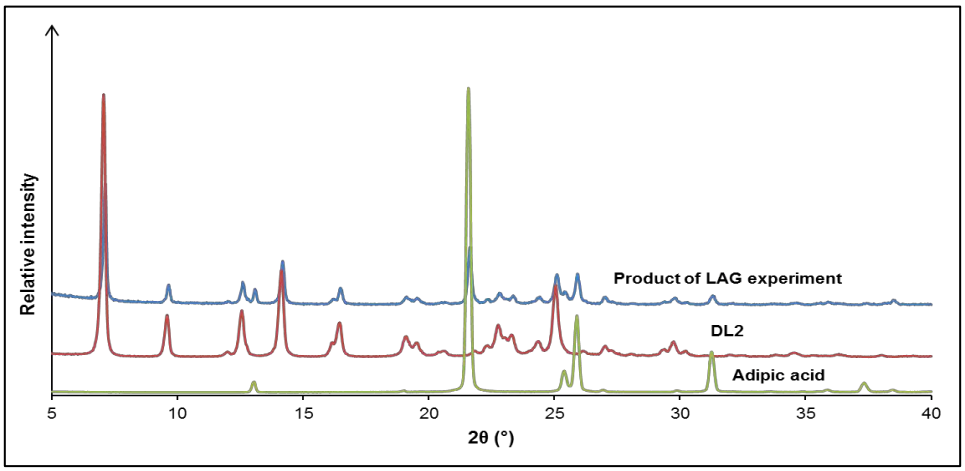

Figure 31: PXRD traces of adipic acid, DL2 and the product of LAG.

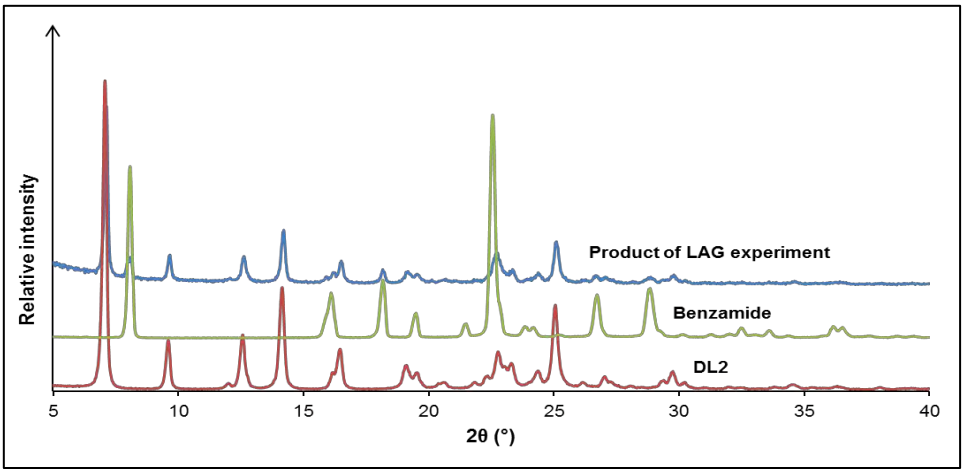

Figure 32: PXRD traces of DL2, benzamide and the product of LAG.

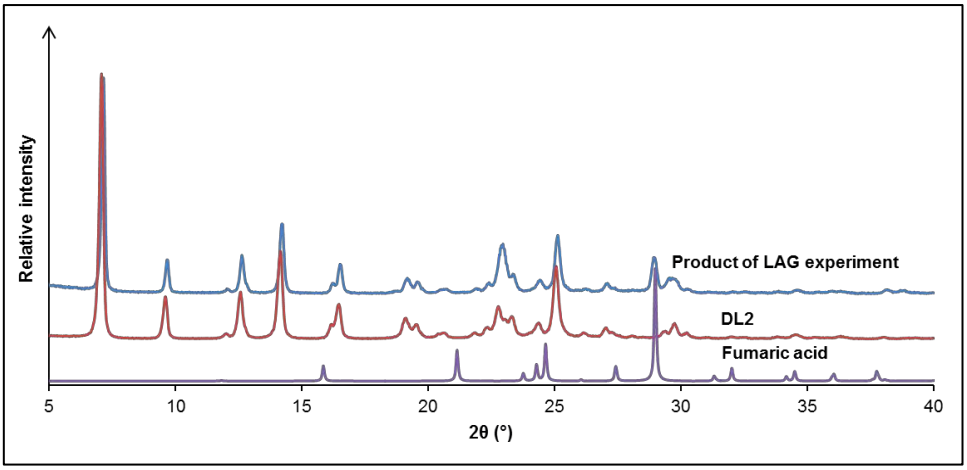

Figure 33: PXRD traces of fumaric acid, DL2 and the product of LAG.

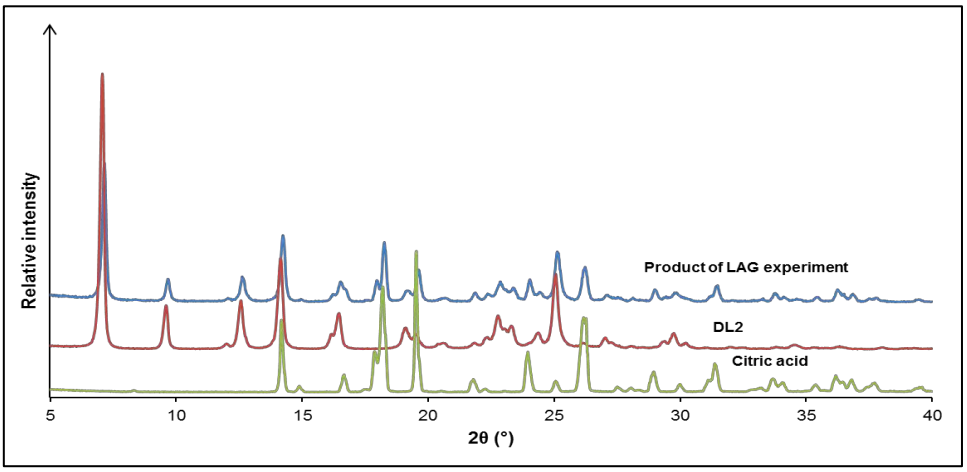

Figure 34: PXRD traces of citric acid, DL2 and the product of LAG.

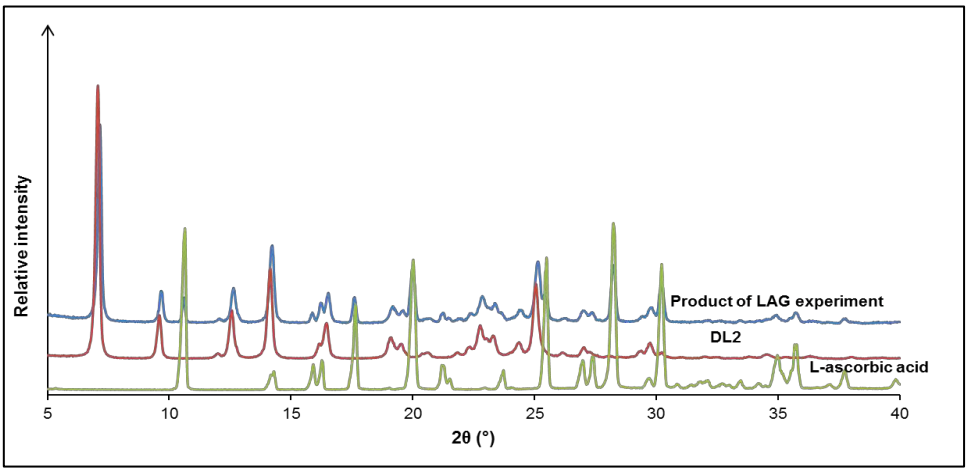

Figure 35: PXRD traces of L-ascorbic acid, DL2 and the product of LAG.

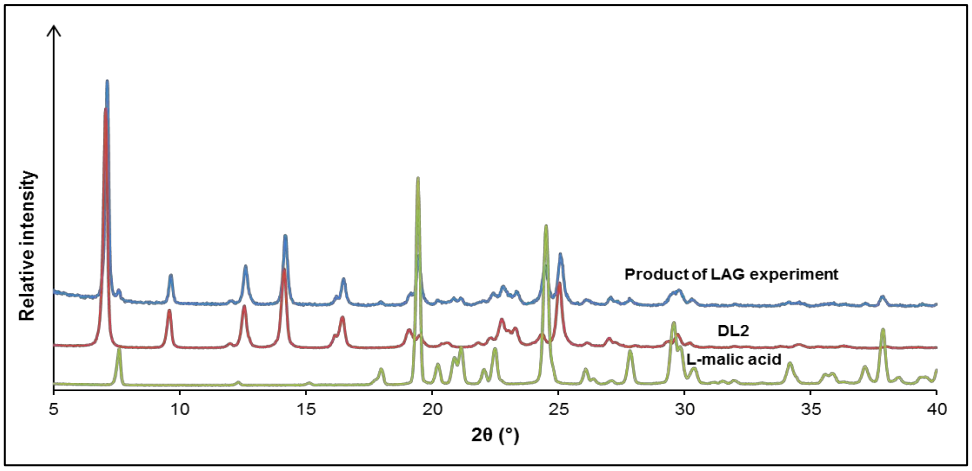

Figure 36: PXRD traces of L-malic acid, DL2 and the product of LAG.

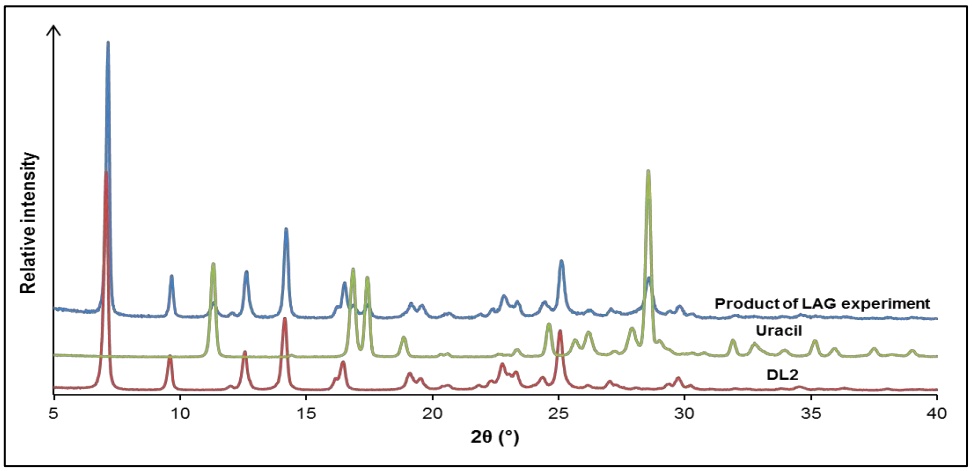

Figure 37: PXRD traces of DL2, uracil and the product of LAG.

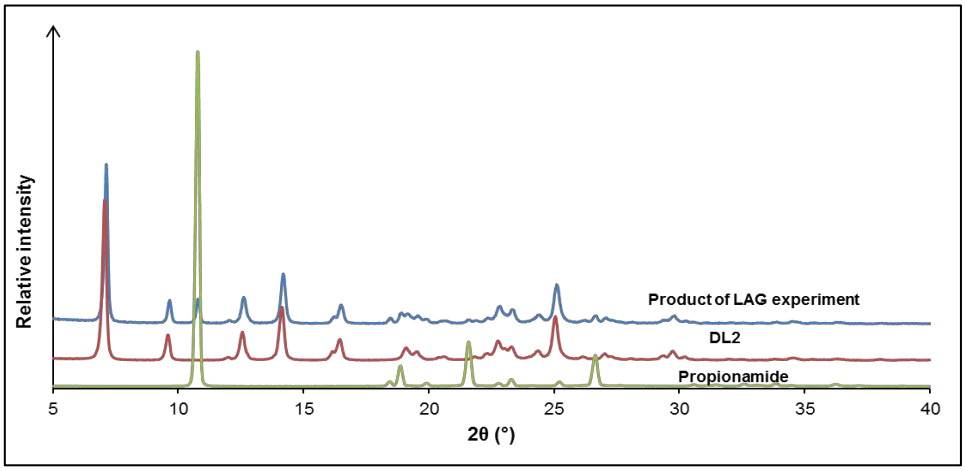

Figure 38: PXRD traces of propionamide, DL2 and the product of LAG.

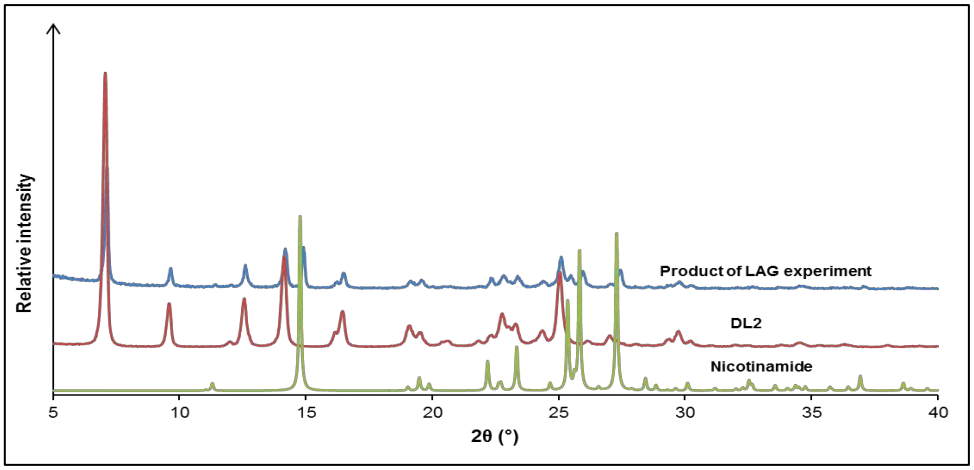

Figure 39: PXRD traces of nicotinamide, DL2 and the product of LAG.

PXRD traces for kneading experiments

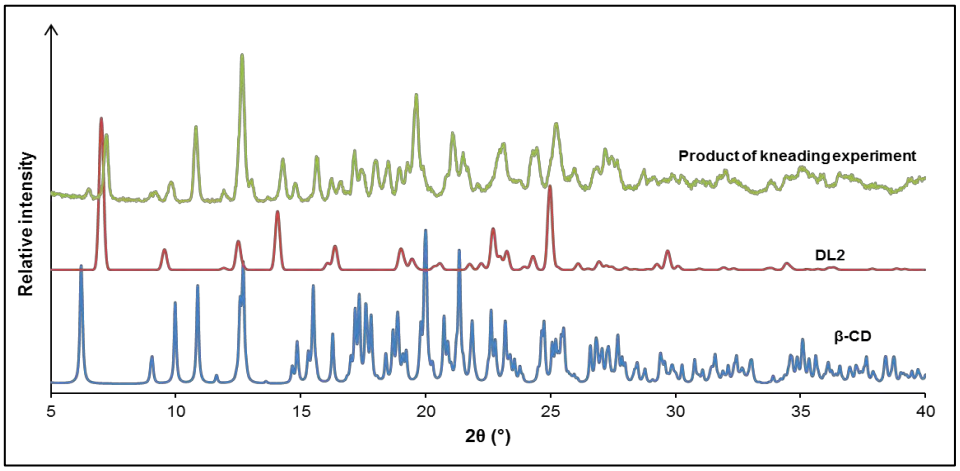

Figure 40: PXRD traces of β-CD, DL2 and the product of the kneading DL2 and β-CD.

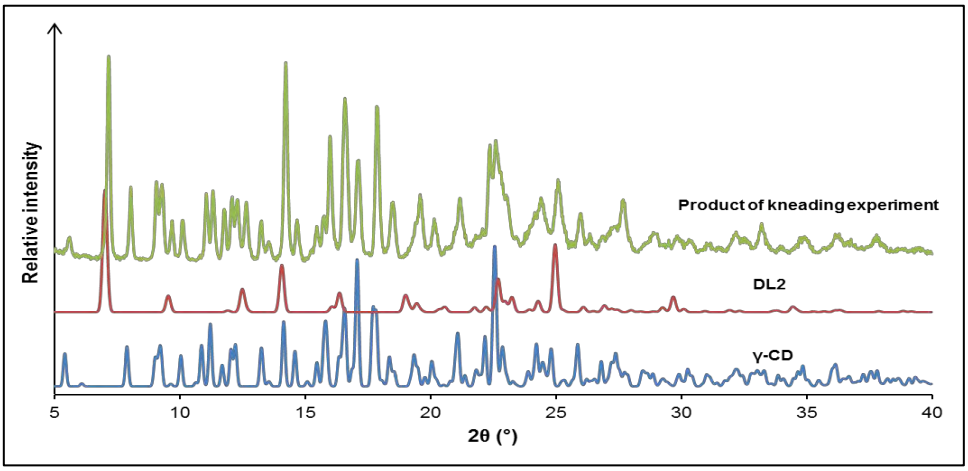

Figure 41: PXRD traces of γ-CD, DL2 and the product of the kneading DL2 and γ-CD.

DL3

The LC-MS, ^{1}H NMR and ^{13}C NMR spectra for DL3 were provided by H3D and are shown below.

LC-MS

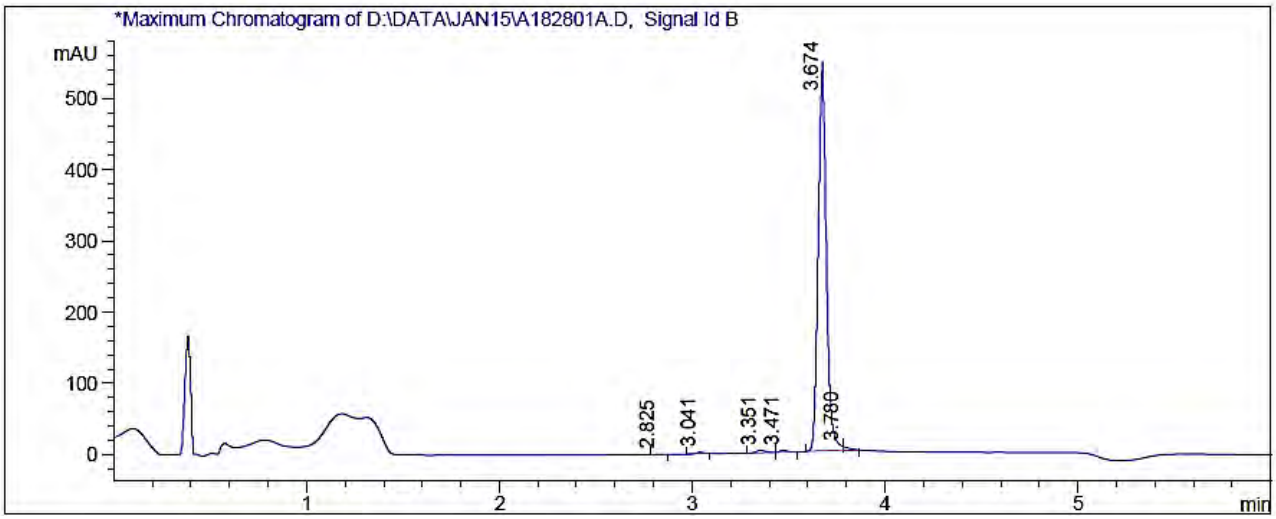

Figure 42: LC chromatogram of DL3.

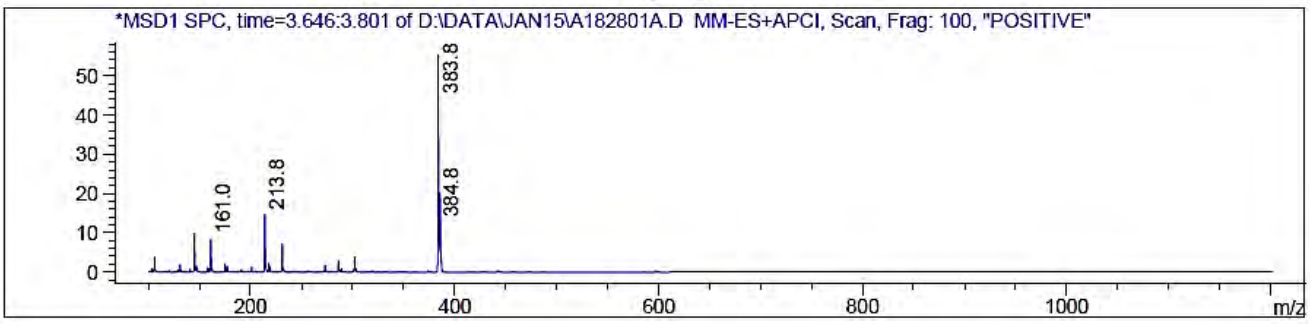

Figure 43: Mass spectrum of DL3.

^{1}H NMR

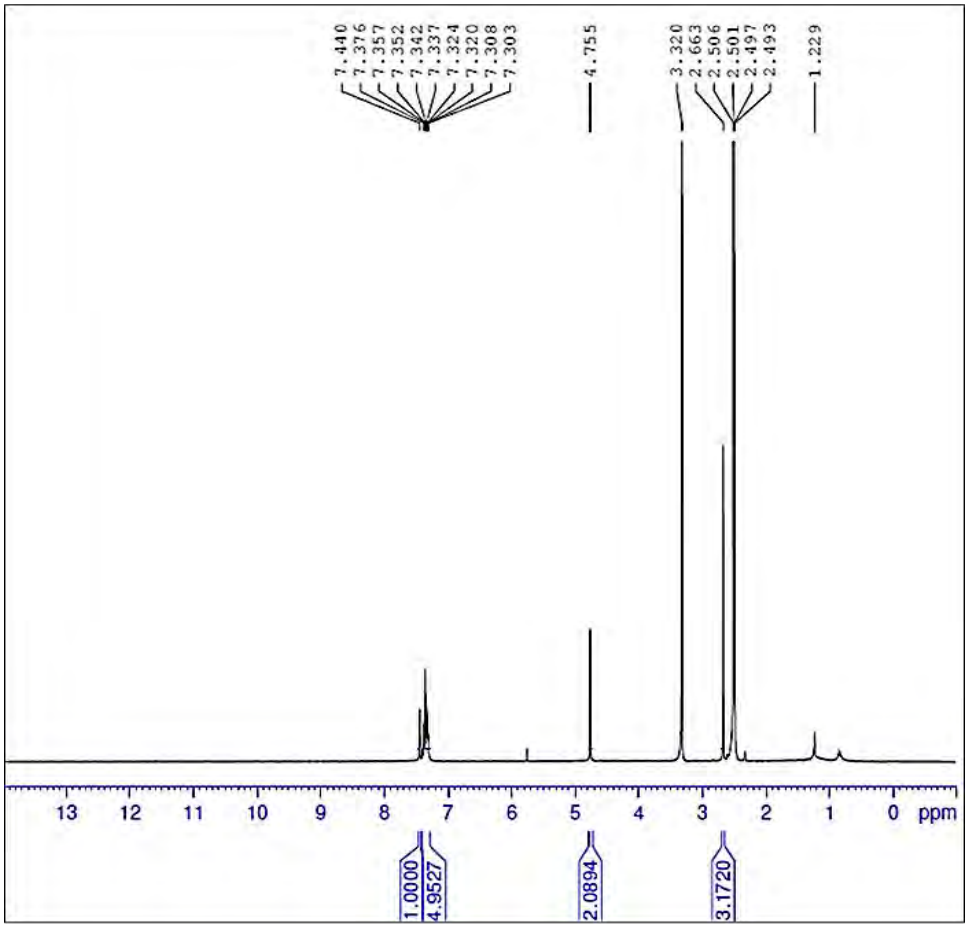

Figure 44: Partial ^{1}H NMR spectrum of DL3 in DMSO-d_6.

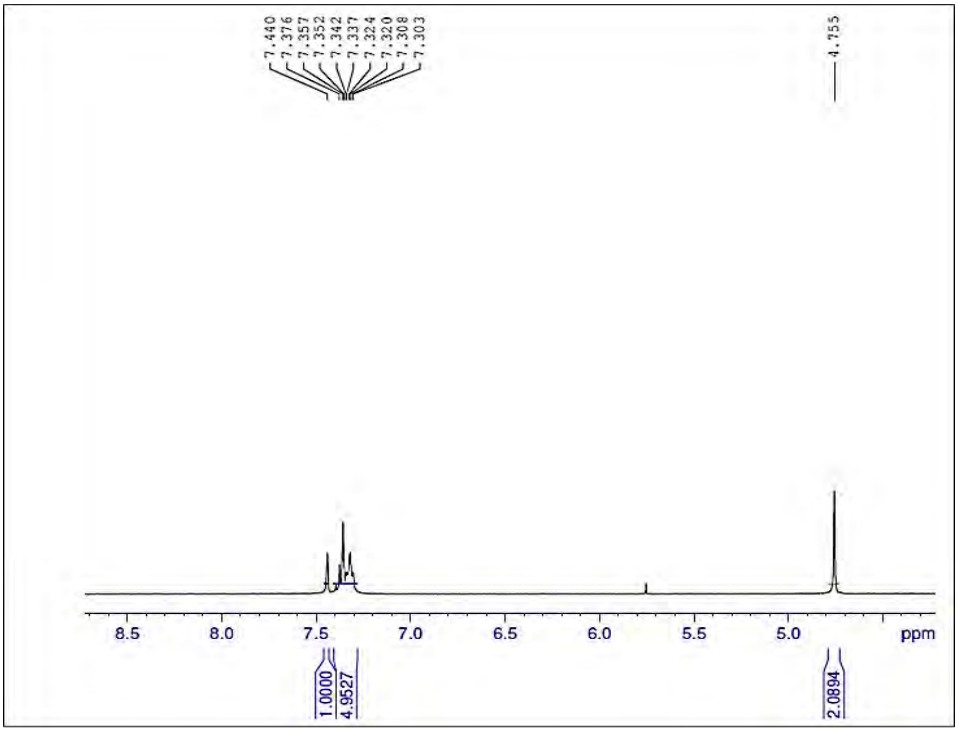

Figure 45: Partial ^{1}H NMR spectrum of DL3 in DMSO-d_6.

^{13}C NMR

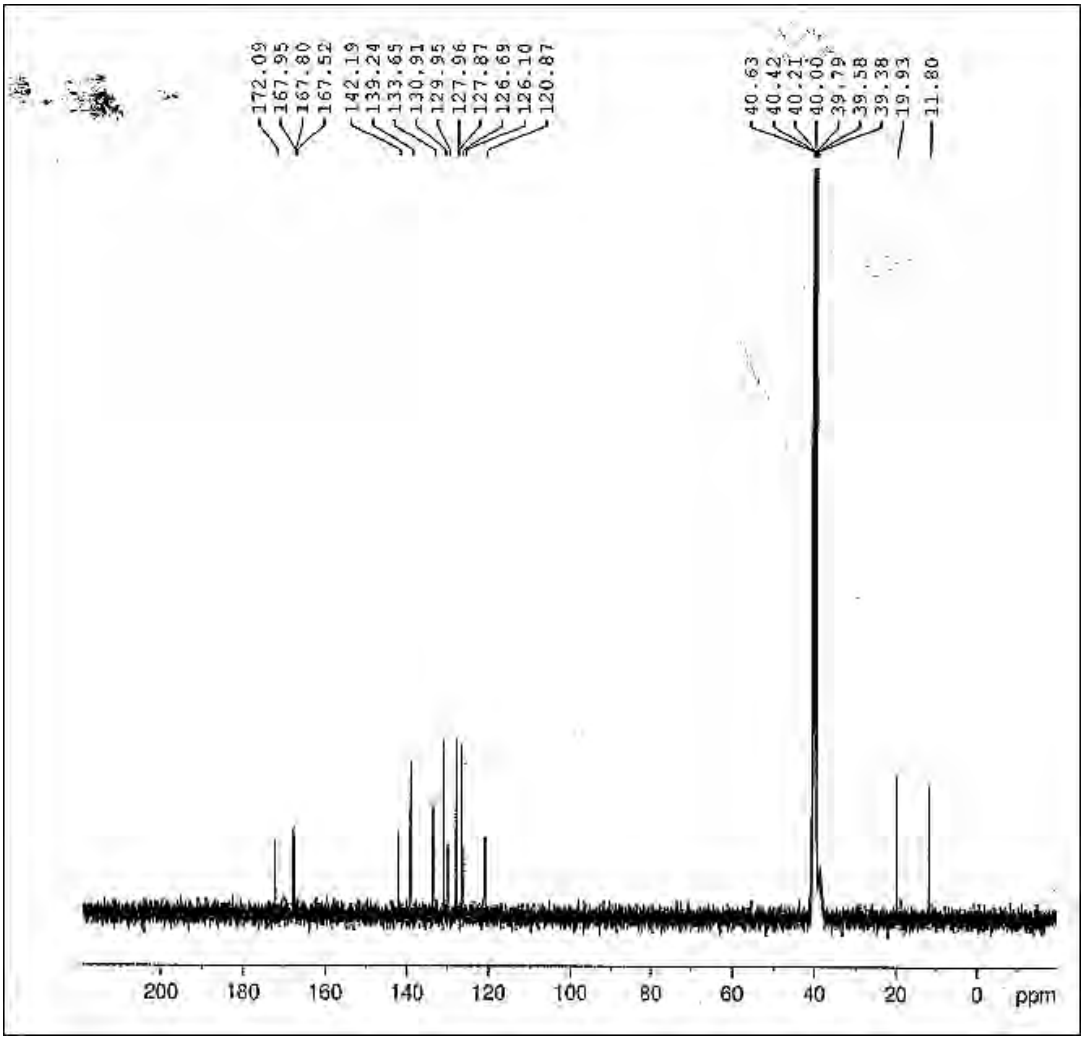

Figure 46: ^{13}C NMR spectrum of DL3 in DMSO-d_6.

DL4

PXRD traces for LAG experiments

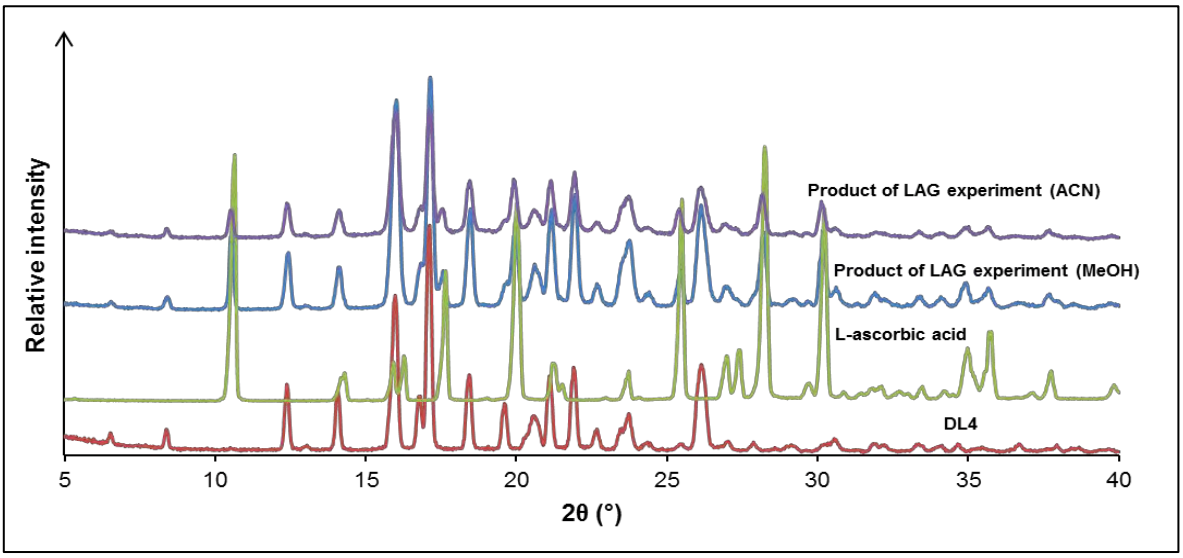

Figure 47: PXRD traces of DL4, L-ascorbic acid and the products of the LAG experiments.

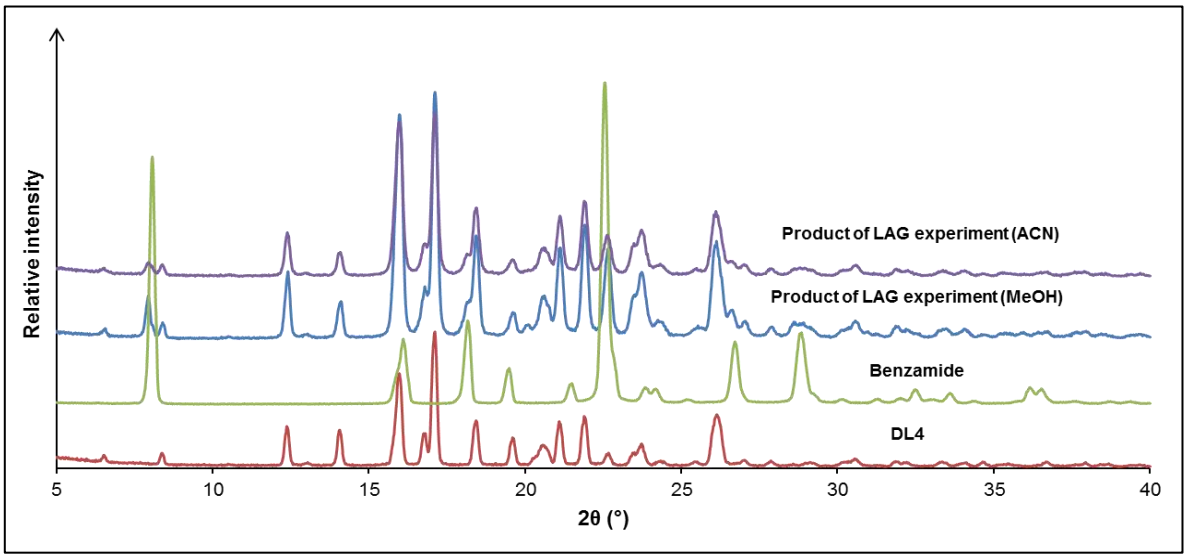

Figure 48: PXRD traces of DL4, benzamide and the products of the LAG experiments.

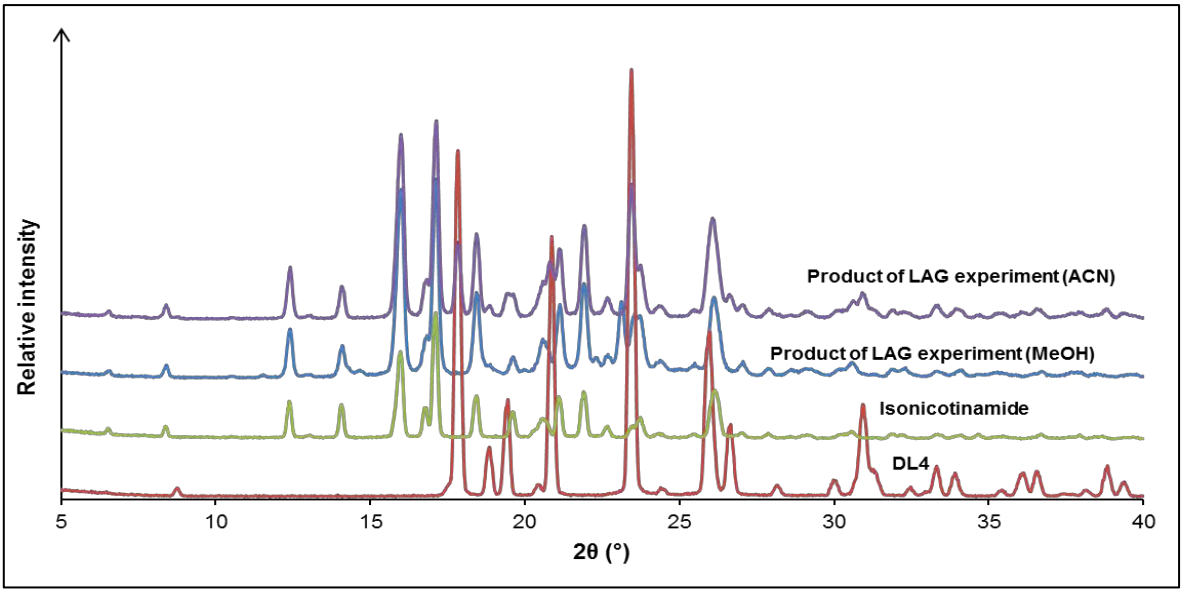

Figure 49: PXRD traces of DL4, isonicotinamide and the products of LAG experiments.

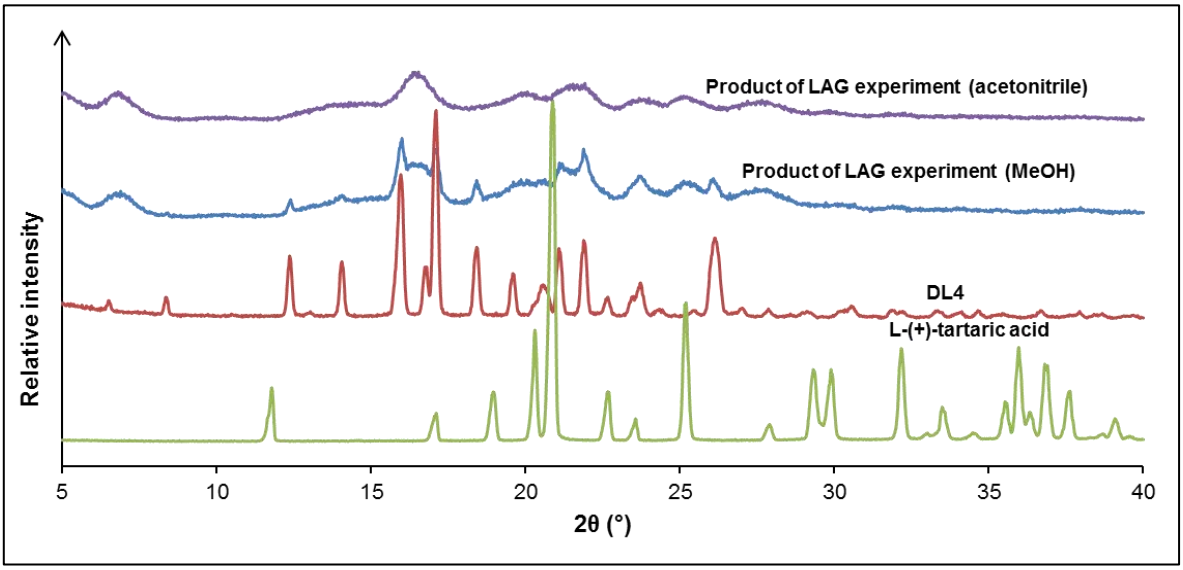

Figure 50: PXRD traces of L-(+)-tartaric acid, DL4 and the products of the LAG experiments.

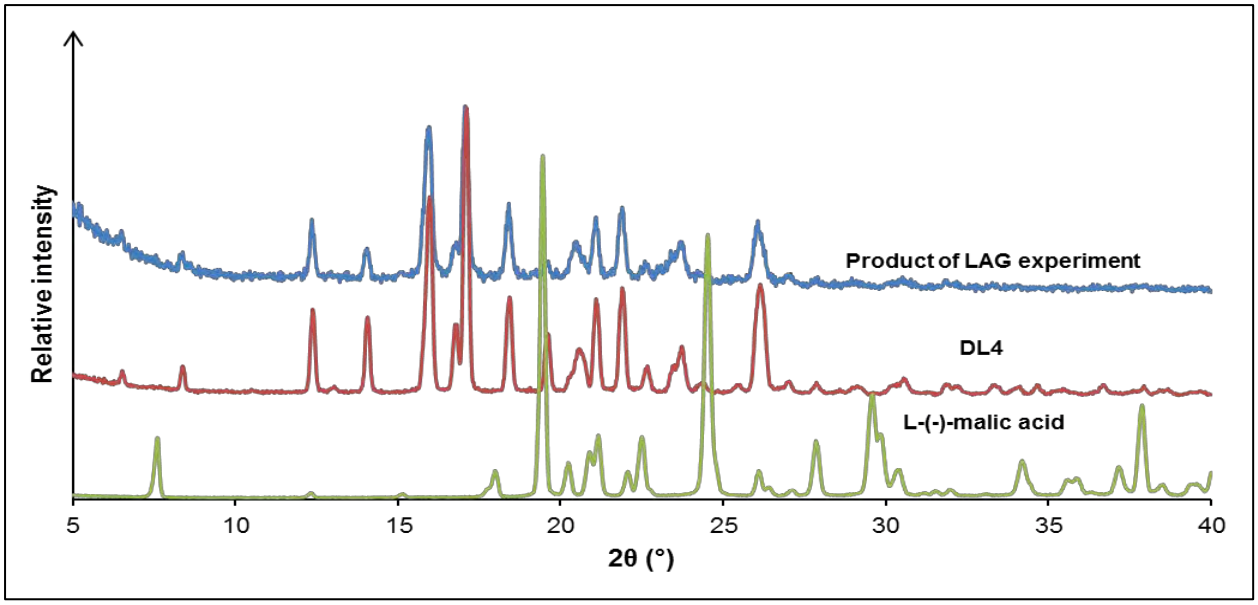

Figure 51: PXRD traces of L-(-)-malic acid, DL4 and the product of LAG.

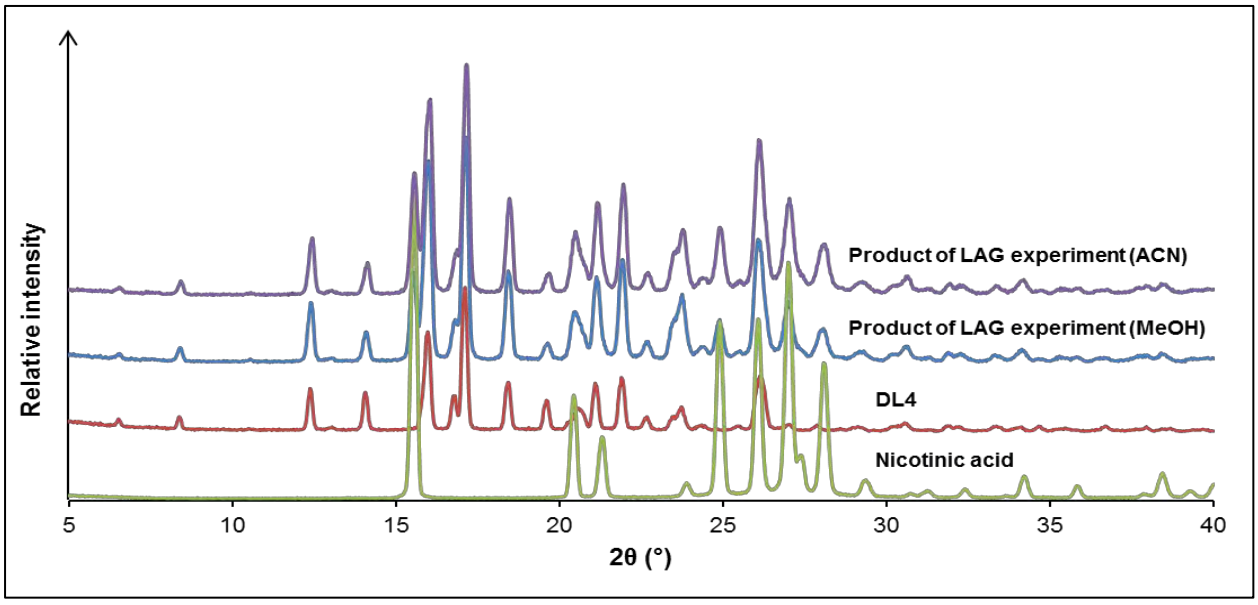

Figure 52: PXRD traces of nicotinic acid, DL4 and the products of the LAG experiments.

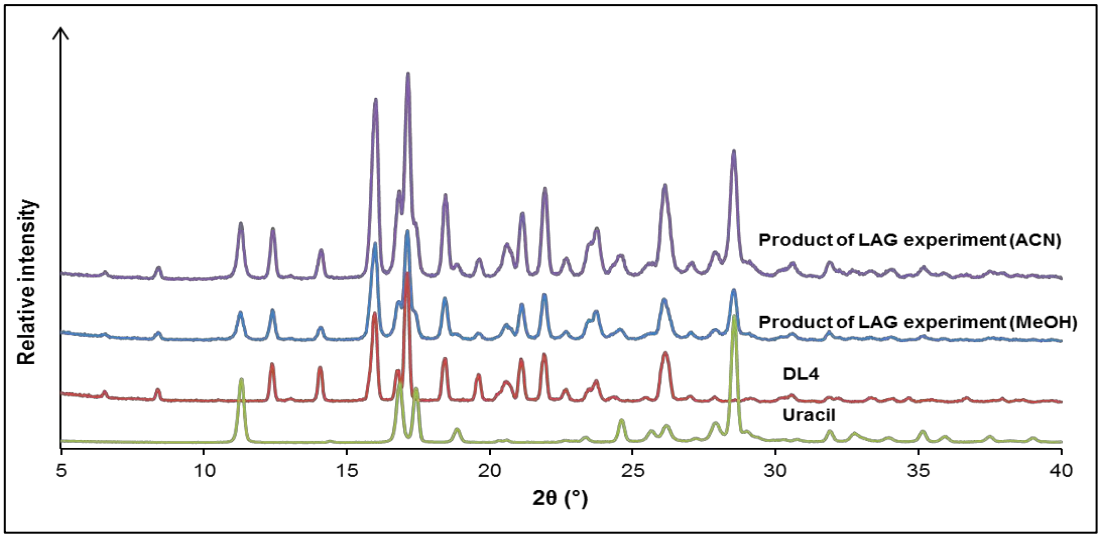

Figure 53: PXRD traces of uracil, DL4 and the products of the LAG experiments.

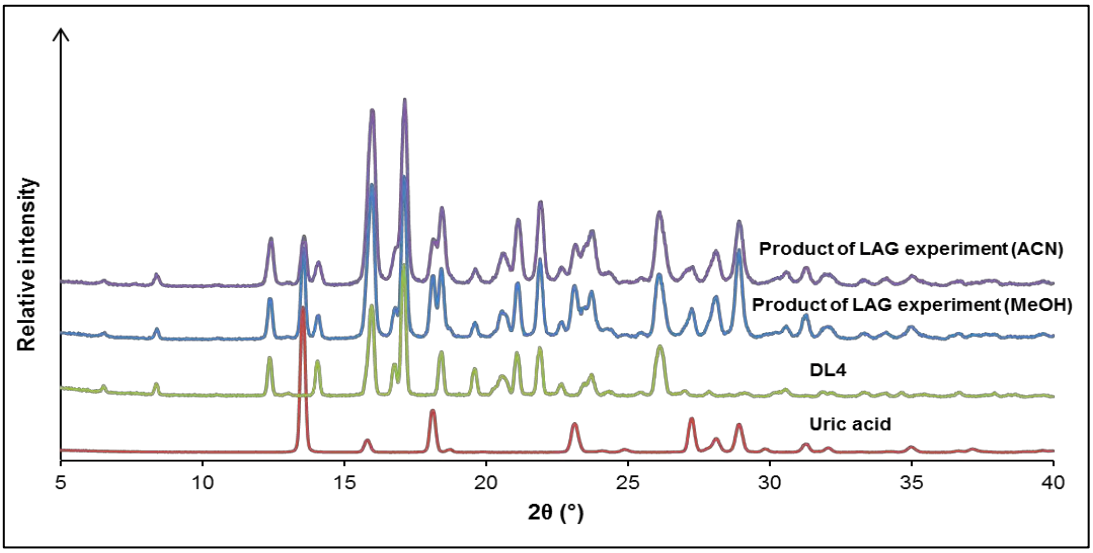

Figure 54: PXRD traces of uric acid, DL4 and the products of the LAG experiments.

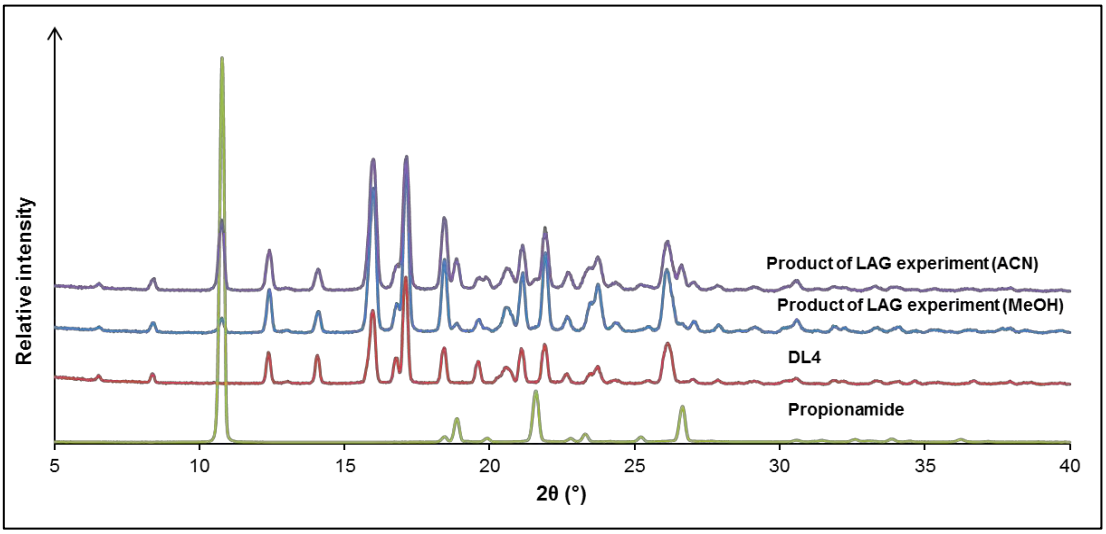

Figure 55: PXRD traces of propionamide, DL4 and the products of the LAG experiments.

PXRD traces for kneading experiments

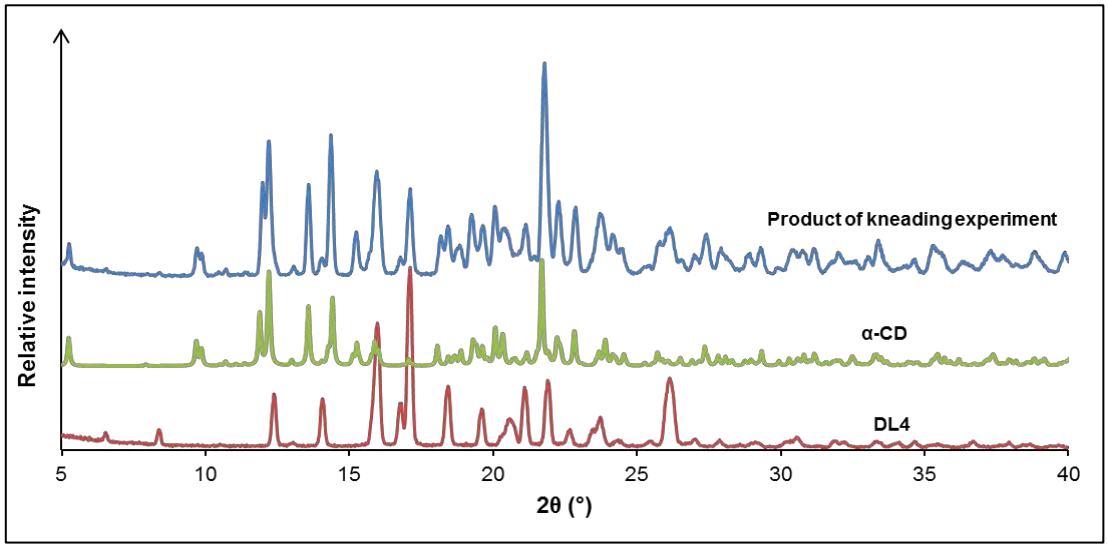

Figure 56: PXRD traces of DL4, α-CD and the product of kneading DL4 and α-CD.

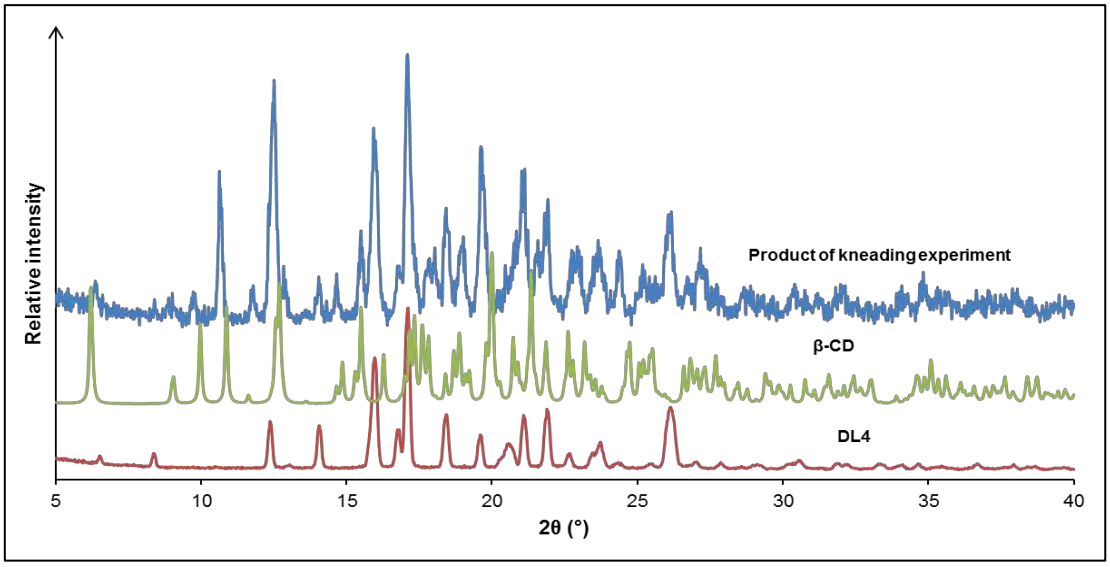

Figure 57: PXRD traces of DL4, β-CD and the product of kneading DL4 and β-CD.